Technische Universität München
Fakultät für Physik

Neutron Scattering Studies of Pyrochlore Quantum Magnets

Viviane Peçanha Antonio

Vollständiger Abdruck der von der Fakultät für Physik der Technischen Universität München zur Erlangung des akademischen Grades eines Doktors der Naturwissenschaften (Dr. rer. nat.) genehmigten Dissertation.

Vorsitzender: Prof. Dr. Frank Pollmann
Prüfer der Dissertation:
1. Priv.-Doz. Dr. Joachim Wuttke
2. Prof. Dr. Peter Müller-Buschbaum

Die Dissertation wurde am 04.06.2019 bei der Technischen Universität München eingereicht und durch die Fakultät für Physik am 17.07.2019 angenommen.

Valeu a pena?
Tudo vale a pena,
Se a alma não é pequena.
Quem quer passar além do Bojador,
Tem de passar além da dor.
Deus ao mar o perigo e o abismo deu,
Mas nele é que espelhou o céu.

Was it worthwhile?
Everything is worthwhile,
When the soul is not small.
Those who want to go beyond the Bojador,
Must go beyond the pain.
God gave the sea the danger and the abyss,
But was in it that He mirrored the sky.

Lohnt' es die Müh'?
Die Müh' ist nie verloren,
wenn nur die Seele groß geboren.
Willst du Kap Bojador bezwingen,
muss du den Schmerz erst niederringen.
Gott gab dem Meer Gefahr und Tiefe,
und ließ es doch den Himmel spiegeln.

Fernando Pessoa, *Mar Português*

Contents

Abstract

This thesis presents experimental studies of the geometrical frustration manifested in three different magnetic pyrochlore oxides. An overview of theory surrounding the main scientific topic of this work, as well as that supporting the data analysis, is detailed in the introductory chapters.

Initially, bulk and neutron scattering measurements performed on the isotopically enriched Sm-based pyrochlores $^{154}Sm_2Ti_2O_7$ (titanate) and $^{154}Sm_2Sn_2O_7$ (stannate) powder samples are presented. High resolution neutron diffraction is used to determine the precise stoichiometry of the compounds. Titanate and stannate are shown to display sharp heat capacity anomalies, at 350 mK and 440 mK, respectively, which signalise phase transitions to a possible magnetic long-range order.

Inelastic neutron scattering measurements are employed to determine the crystalline electric field (CEF) level scheme of the Sm-based pyrochlores. The analysis includes transitions between the ground-state and first excited J multiplets of the Sm^{3+} ion. To further validate those results, the single-ion magnetic susceptibility of the compounds is calculated and compared with the experimental DC-susceptibility measured in low applied magnetic fields. It is demonstrated that the inclusion of intermultiplet transitions in the CEF analysis is fundamental to the understanding of the intermediate and, more importantly, low temperature magnetic behaviour of the Sm-based pyrochlores.

Neutron diffraction performed at very low temperatures correlates the heat capacity anomaly of the Sm-based pyrochlores with the onset of an all-in-all-out long-range order in the stannate sample, while in the titanate a dipolar long-range order can be only indirectly inferred. In order to investigate possible magnetic dynamics in the ground-state of those compounds, we also performed high resolution inelastic neutron scattering and μSR experiments on both samples. The results seem to be inconclusive, since the data present no indication of spin dynamics at low temperatures. Finally, the reasons for this strange behaviour are speculated.

Next, the focus is switched to another pyrochlore compound. Extensive studies on the zero field ground-state of a powder sample of the pyrochlore $Yb_2Ti_2O_7$ are reported. The sharp heat capacity anomaly, which labels a low temperature phase transition in this material, is observed at $T_c = 280$ mK. In disagreement with many results reported previously on the compound, polarised and unpolarised neutron diffraction demonstrate that a long-range, *quasicollinear* ferromagnetic order, with a magnetic moment of $0.87(2)\mu_B$, develops below T_c.

High resolution inelastic neutron scattering measurements are used to explore coherent and incoherent dynamics below the phase transition temperature. Sharp gapped low lying magnetic excitations coexisting with a remnant quasielastic contribution, likely associated with persistent spin fluctuations, are present at temperatures $T < T_c$. Moreover, a broad inelastic continuum of excitations at ~ 0.6 meV is observed from the lowest measured temperature up to at least 2.5 K. At 10 K, the continuum has vanished and a broad quasielastic conventional paramagnetic scattering takes place at the observed energy range. Eventually, it is shown that the exchange parameters obtained within the framework of linear spin wave theory do not accurately describe the observed zero field inelastic neutron scattering data.

Kurzfassung

Diese Arbeit befasst ich mit der experimentellen Untersuchung der geometrischen Frustration in drei verschiedenen magnetischen Pyrochloroxiden. Die zugrundeliegende Theorie der drei Hauptthemen, sowie die Datenanalyse, ist im Einleitungskapitel dargestellt.

Labor und Neutronendiffraktometriemessungen an isotopisch angereicherten Sm-basierenden Pyrochlorpulverproben $^{154}Sm_2Ti_2O_7$ (Titanat) und $^{154}Sm_2Sn_2O_7$ (Stannat) werden erläutert. Hochauflösende Neutronendiffraktion wurde benutzt, um die genaue Stöchiometrie der Proben zu bestimmen. Titanat und Stannat zeigen eine abrupte Wärmekapazitätsanomalie bei 350 mK bzw. 440 mK, was einen Phasenübergang zu einer möglichen langreichweitigen magnetischen Ordnung andeutet.

Inelastische Neutronenstreuung wurde verwendet um die Kristallfeldlevel (CEF) der Sm-basierenden Pyrochlore zu bestimmen, durch die Analyse der Übergänge zwischen Grundzustand und des erstem angeregten J Multiplets des Sm^{3+} Ions. Um die Resultate weiter zu bestätigen wurde die magnetische Einzelionensuszeptibilität der Stoffe berechnet und mit der experimentell bestimmten DC-Suszeptibilität in schwachen magnetischen Feld verglichen. Die Berücksichtigung der Intermultipet Übergänge in der CEF Analyse ist hierbei höchst wichtig um das Verhalten der Sm-basierenden Pyrochlore bei mittleren und besonders bei tiefen Temperaturen zu verstehen.

Die Anomalie in der Wärmekapazität konnte mit dem Anfang einer langreichweitigen *all-in-all-out* Ordnung in der Stannat Probe in Verbindung gebracht werden, wohingegen in der Titanat Probe eine langreichweitige, dipolare Ordnung nur indirekt ermittelt werden konnte. Um mögliche magnetische Anregungen im Grundzustands der Sm-basirenden Pyrochlore zu untersuchen wurden inelastische Neutronenstreuung und μSR Experimente an beiden Proben durchgeführt. Es konnten keine Hinweise auf Anregungen festgestellt werden, aber die Resultate scheinen nicht eindeutig. Über mögliche Gründe für dieses seltsame Verhalten wird spekuliert.

Als nächstes wird eine extensive Studie über den Null-Feld Grundzustand einer Pulverprobe des Pyrochlors $Yb_2Ti_2O_7$ vorgestellt. Eine abrupte Wärmekapazitätsanomalie, die einen Phasenübergang bei tiefer Temperatur markiert, existiert bei $T_c = 280$ mK. Neutronendiffraktionsmessungen zeigen, dass sich eine *quasi-kollineare*, langreichweitige, ferromagnetische Ordnung, mit einem magnetischen Moment von $0,87(2)\mu_B$, unterhalb T_c einstellt. Hochauflösende, inelastische Neutronenmessungen zeigen, dass unterhalb der Phasenübergangstemperatur eine scharfer, getrennter, magnetischer Anregungszustand mit einem remanenten quasielastischen Untergrund, verursacht durch anhaltende Spin-Fluktuationen, koexistiert. Darüber hinaus sind breite inelastisches Kontinuumsanregungen bei $\sim 0,6$ meV beobachtbar, von den tiefsten Temperaturen bis mindestens 2,5 K. Bei 10 K ist das Kontinuum nicht mehr messbar und eine breite, quasielastische, konventionelle paramagnetische Streuung ist sichtbar. Zuletzt zeigen wir, dass die Austauschparameter, die durch lineare Spinwellentheorie ermittelt wurden, die gemessenen Null-Feld inelastischen Neutronenstreudaten nicht akkurat beschreiben.

Chapter 1

Introduction

1.1 The meaning of frustration

The term *frustration* was employed for the first time by P. W. Anderson, as the own author would state, "to describe in a vague way the essential feature of true models of the spin glass phenomenon, involving the impossibility of satisfying a large fraction of the exchange interactions with any spin structure" [1]. This word, without exaggerations, was so well employed as the definition of a physical mechanism that, in the present years, the study of frustration, or rather, of its consequences, has become one of the pillars of the research in condensed matter physics.

As the quotation by Anderson clarifies, frustration is the key concept for the occurrence of the spin glass phase. In those early years, this static random magnetic order, developed in some systems below a certain critical temperature, was generically attributed to disorder. More specifically, spin glass behaviour is believed to be directly associated with bond disorder introduced by non-magnetic impurities randomly diluted in a magnetic matrix [2].

If the last statement in the latter paragraph was absolutely correct, probably you would not be reading this thesis. Turns out that geometrical disorder is far from being the most important ingredient in the physics presented by spin glasses. A counter example could be the pyrochlore $Y_2Mo_2O_7$. This compound presents a glassy ground-state even in the absence of any apparent bond disorder or magnetic dilution [3, 4]. As Anderson correctly predicted, disorder is not as fundamental for spin glasses as frustration is.

The crystallographic lattice, hold together by Coulombic forces, and its symmetry are the only real constraints to the magnetic atoms. Sometimes, its geometry precludes the formation of a state in which the free energy of all the magnetic interactions between the composing ions can be simultaneously minimised. The most trivial exemple, and in fact the subject of the earliest work reporting on a model of a frustrated system, would be the Ising antiferromagnet in the 2D triangular lattice [5]. In this lattice, neither an ordinary ferromagnet or a Heisenberg antiferromagnet are frustrated. However, if two out of three Ising spins, located at the vertices of regular triangles, couple and display an antiparallel arrangement, how would the third solitary spin behave?

This is a very pragmatic example, which the author of this thesis particularly dislikes. Indeed, the canonical frustrated pyrochlore is, unexpectedly, a effective ferromagnet (see the Section 1.4 below). However, even though the model of Wannier *et al.* [5] unlikely describes any real condensed matter system, it is useful to illustrate in simple terms the problematics surrounding frustration.

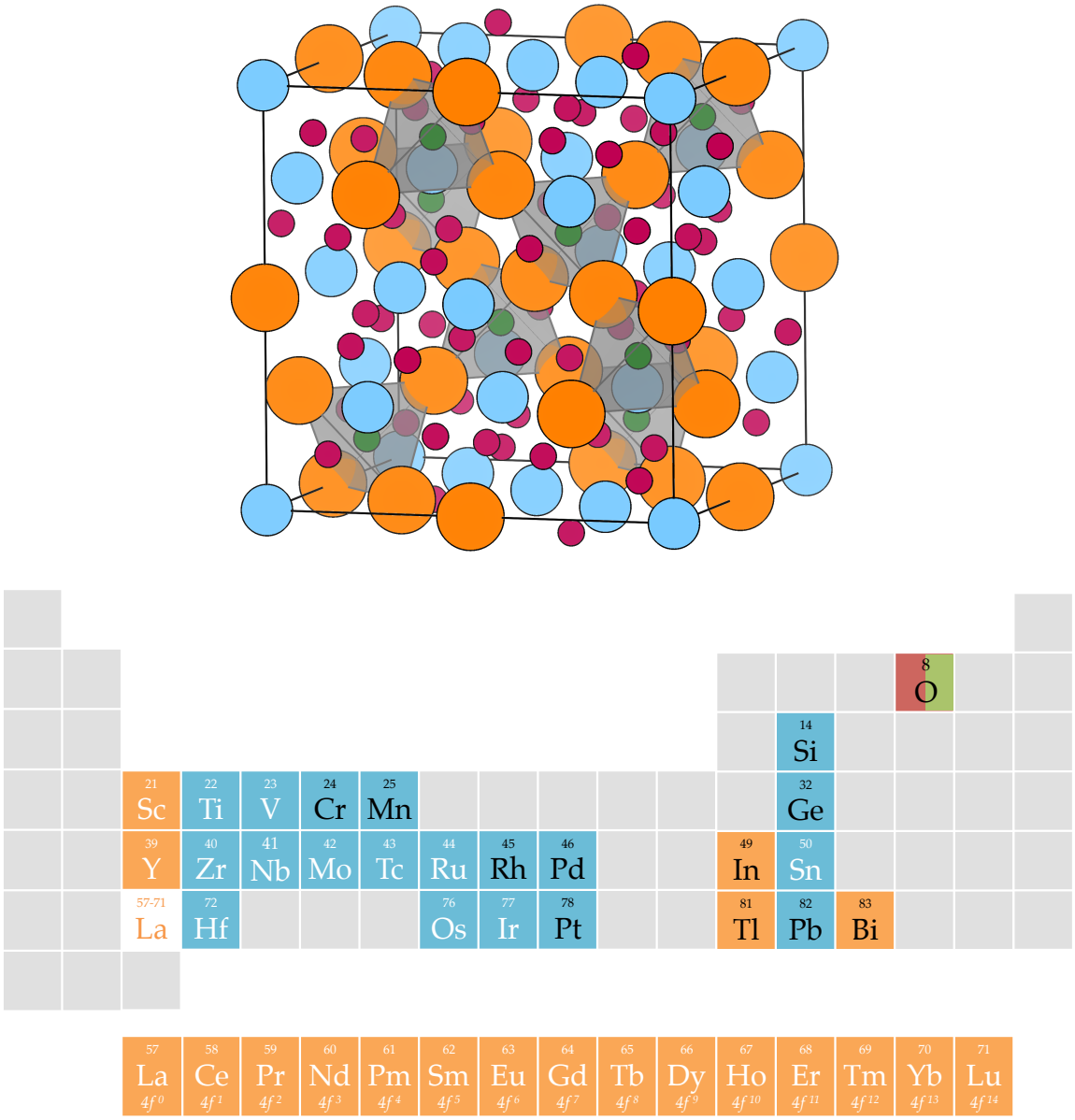

Figure 1.1: Top: cubic unit cell representing the pyrochlore structure. Two tetrahedra (grey) are connected by each rare-earth atom (orange). The transition metal (light blue) atoms, which form themselves an interpenetrating lattice of corner-sharing tetrahedra, are chosen to lay at the origin of the unit cell. Oxygens (dark magenta and green) occupy two distinct symmetry positions. The O^{2-} at the 8*b* sites are located at the centre of the rare-earth tetrahedra. Bottom: schematic periodic table showing the possible occupation at *A* and *B* sites. Elements written in black require high pressure synthesis for the cubic pyrochlore phase formation. All the elements in white, with exception of tin (Sn), require high pressure synthesis for some choices of rare-earth. The electronic configuration of the trivalent rare-earths is shown below each lanthanide element.

1.2 The pyrochlore lattice

Pyrochlores are cubic compounds forming in the cubic $Fd\bar{3}m$ (227) space group with chemical formula $A_2B_2O_7$, where A^{3+} is a rare-earth and B^{4+} is a transition metal. The pyrochlore structure may be represented using two origin choices. The second origin choice is the most common in the representations of the unit cell composition, and in this work it will also be used in the sections dealing with sample characterisation. Rare-earth and transition metal occupy the 16*c* and 16*d* Wyckoff positions, respectively. As oxygens are hosted at the two inequivalent 48*f* and 8*b* positions, the chemical formula can also be written as $A_2B_2O_6O'$.

The pyrochlore unit cell and its contents are depicted in Figure 1.1. The periodic table below it displays the series of elements that may occupy either *A* (orange) or *B* sites (light blue). For some choices of transition metal (black), the perfect pyrochlore structure is only formed with high pressure synthesis. Most commonly, for bigger ionic radius the resulting compounds present mixed defective fluorite phases and anti-site $A-B$ mixing [6,7]. Each rare-earth atom is shared between two corner linked tetrahedra. The oxygen O' (green) is positioned at the geometric centre of each of them. The distance between the 8*b* and 16*d* elements is remarkably short in pyrochlores, of about 2.2 Å [7]. The removal of the 8*b* oxygen exposes the rare-earth cations to each other, and the resulting Coulomb repulsion tends to destabilise the pyrochlore structure [6]. As described below, the electrostatic field created by the oxygen atoms is not only important for the stability of pyrochlore lattice, but also plays an important role in the magnetism presented by the rare-earth.

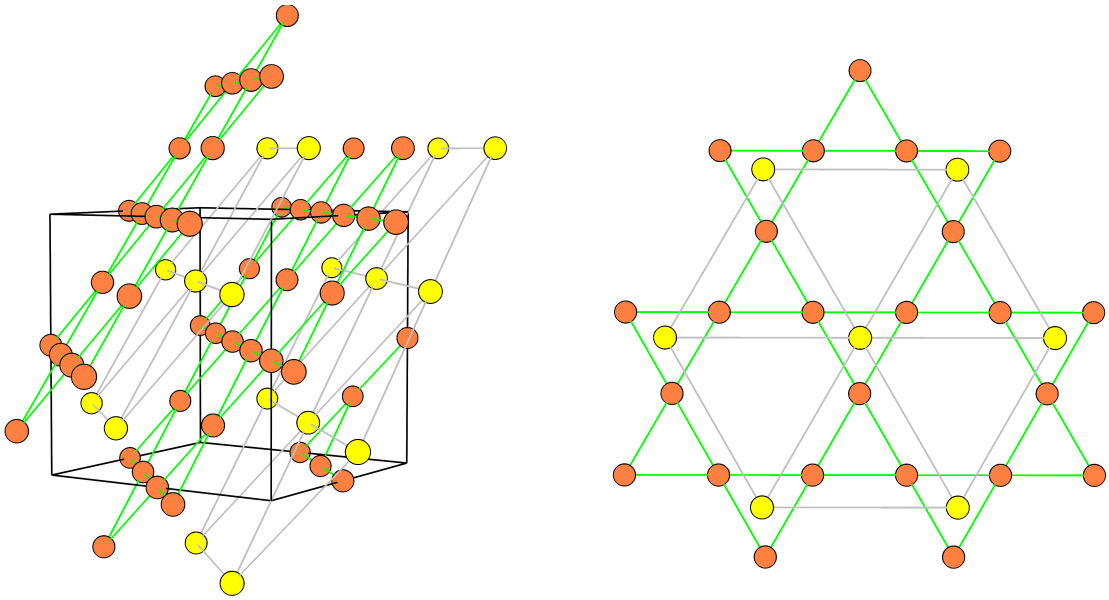

Figure 1.2: Representation of the pyrochlore rare-earth sublattice as an arrangement of triangular (yellow circles connected by grey lines) and Kagomé (orange circles connected by green lines) planes along the cubic ⟨111⟩ directions. On the left, the alternating stacking of planes inside the conventional unit cell, and, on the right, the top view along ⟨111⟩.

In this thesis, the transition metals that occupy the *B* sites, Ti^{4+} and Sn^{4+}, are non-magnetic. Hence, we will be concerned mostly with the geometry of the underlying rare-earth sublattice. The most common way of representing it was already shown in Figure 1.1. Additionally, some alternative views will be discussed in this chapter, especially those directly related with

the frustration mechanism. For example, the rare-earth arrangement can be viewed as an alternating stacking of triangular and Kagomé planes along the three-fold $\langle 111 \rangle$ directions [8]. This representation, depicted in Figure 1.2, is usually used to demonstrate the similar topology of pyrochlores and perovskites [7]. It is also noteworthy to emphasise the large distance difference between nearest neighbours within Kagomé and triangular planes, as clear on the right panel of Figure 1.2. From the point of view of magnetism, differently from what it could be expected, the nearest neighbour interactions displayed in pyrochlores differ remarkably from those presented in the two-dimensional Kagomé lattice [7].

Other alternative views of the pyrochlore lattice will be explored below, along with a more detailed description of the single ion and collective magnetic properties of those compounds.

1.3 Hierarchy of interactions: the frustration mechanism

As frustration requires dissatisfaction, several interactions may compete in a compound for the phenomenon to occur. In this section, single ion properties and exchange interactions, central to the thematics of this work, will be treated in more detail. Dipolar interaction is mentioned for completeness and also for its fundamental importance in the earlier research of frustrated pyrochlores.

1.3.1 Crystalline electric field anisotropy

While a magnetic atom is isolated, the spin S and orbital L degrees of freedom are coupled. The angular momentum resultant from this coupling is simply $\boldsymbol{J} = \boldsymbol{L} + \boldsymbol{S}$. At zero external magnetic field, each level J possesses $(2J+1)$ degenerated substates, classified according to their projection $m_J = -J, -J+1, ..., J$ along the quantisation axis defined, until now, by the direction of the applied magnetic field.

In condensed matter, no atom is isolated. It is very reasonable, thus, to assume that the localised f electron cloud of the rare-earth atom reacts strongly to its environment. The splitting of each one of the $(2J+1)$-degenerate multiplets is the general consequence of the perturbation, over the lanthanide, caused by the other ions in the crystallographic lattice. Its magnetic moment, that before could point along any direction, will be subject to what is called *crystalline electric field anisotropy*, or, in short, crystal field anisotropy (CEF).

Symmetry considerations may be used to determine the number of levels in which each J multiplet will be splitted. It is interesting, then, to reinterpret the pyrochlore crystallographic structure in a way particularly suitable for the analysis that follows. Figure 1.3 presents a zoom-in view of the eight-oxygen puckered crown surrounding the rare-earth ion. We have already mentioned in Section 1.2 that two different sites of the pyrochlore lattice are occupied by O^{2-}: the $8b$ (green balls) and the $48f$ (dark magenta balls) Wickoff positions. The former is situated closer to the the rare-earth than the latter. Intentionally, we are going to define a new z axis, which is parallel to the line that connects the rare-earth to its neighbouring O'. This new z direction, called from now on of *local-z*, is going to be the new quantisation axis. Clearly, the local-z does not coincide with the crystallographic, or *global*, c axis. It is in reality parallel to the equivalent cubic three-fold $\langle 111 \rangle$ directions.

An interesting consequence of the global-to-local coordinate transformation is that, now, each rare-earth atom will have stuck to itself its own coordinate system. When we say that the single ion anisotropy forces the ordered moment to point along z, we mean that the crystal field constraints the magnetic moment to point along the atom own local-z axis. The same is true for

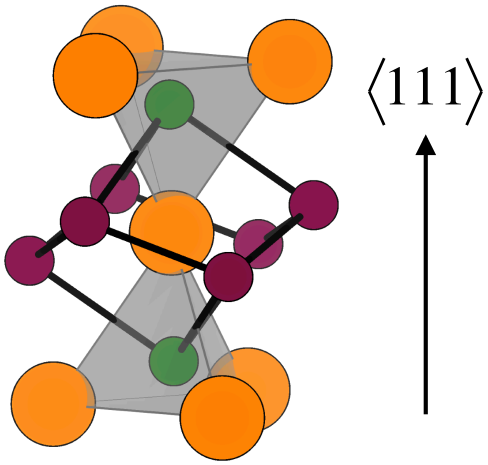

Figure 1.3: Ball-and-stick model of the oxygen environment surrounding the rare-earth atom (orange). The 8*b* oxygens are shown in green and the 48*f* oxygens in dark magenta. The local-*z* axis is parallel to the line that connects the *A* site with the O' oxygens. This direction coincides with the crystallographic cubic three-fold axis.

the *xy* anisotropy, for which, as the name suggests, the CEF constrains the moment to lie on the plane perpendicular to the local-*z* axis.

Both types of anisotropy are represented in Figure 1.4. On the left, where the magnetic moments are constrained to point along their local-*z* axis, we have an example of axial anisotropy, in which each spin can have two states (referred hear as *in* or *out*) along one direction. In other words, this system satisfies the Ising model in three dimensions, and the pyrochlores presenting this anisotropy are called *Ising pyrochlores*. On the right, the ellipsoids around the rare-earth atom correspond to the local plane perpendicular to each one of the local-*z* axis. Compounds displaying this anisotropy are referred to as *XY pyrochlores*. This class of materials is said to have an *U(1) accidental degeneracy* [9]. Interestingly, at very low temperatures one out of many ground-states may actually be selected via the order-by-disorder mechanism [10, 11].

1.3.1.1 The point charge model

The CEF acting on the magnetic atom is treated as a perturbation H_{CEF} to the single ion H_0 Hamiltonian. The *point charge model* is the standard method used to determine H_{CEF}. Basically, one has to evaluate the electrostatic potential $V(r,\theta,\phi)$ generated by a charge located at a point separated by a distance $\boldsymbol{r}$ from the magnetic atom [12]. The crystalline potential $V(r,\theta,\phi)$ can be readily calculated in terms of spherical harmonics $Y_{k,q}(\theta,\phi)$, which are finally combined in the form of tensor operators.

Generically, H_{CEF} can be expressed as

$$H_{CEF} = \sum_{k=0}^{2l} \sum_{q=-k}^{k} B_q^k \boldsymbol{C}_q^k, \tag{1.1}$$

where B_q^k are the *crystal field parameters* and $\boldsymbol{C}_q^k$ are the *Wybourne tensor operators*, here defined

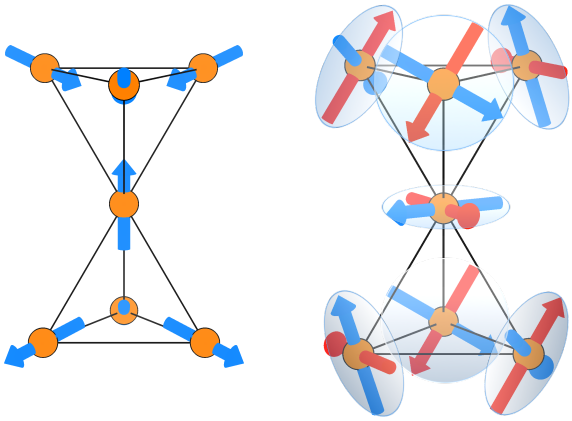

Figure 1.4: Left: Ising spins in the corner-sharing tetrahedra, constrained to point along one direction, the local-z axis. In the commonly used pyrochlore terminology, the *up* and *down* are substituted by the *in* and *out*, referring to whether the four magnetic moments point to (upper tetrahedron) or away of (bottom tetrahedron) the centre of one motif. Right: xy spins lying on the plane perpendicular to the local-z. Note that the x and y axes can be defined as any two mutually perpendicular vectors contained in the plane. This infinite number of choices of x and y axis within one plane is termed $U(1)$ (accidental) degeneracy.

as [13][1]

$$C_q^k = \sqrt{\frac{4\pi}{2k+1}} Y_{k,q}(\theta, \phi) \tag{1.2}$$

For rare-earth atoms, the orbital quantum number $l = 3$ implies that $0 \leq k \leq 6$. Moreover, $|q| \leq k$. The tensor operators with matrix elements different of zero in the expansion of Equation (1.1) depend only upon the point symmetry of the magnetic atom in the lattice [14, 15]: the higher the symmetry, the smaller the number of independent terms.

In first analysis, the B_q^k are not expected to be simply coefficients of the expansion in Equation (1.1). The minimal assumption of the point charge model is that the eigenstates of H_{CEF} can be factorised as the product of *i.* angular and *ii.* radial contributions [13]. The former is given by the spherical harmonics combination in the form of tensor operators, and depends upon the point symmetry of the magnetic ion. The angular part should be, therefore, the same for those compounds belonging to one specific family (for example, for all the pyrochlore titanates). The radial part is dependent on the k^{th} moment $\langle r^k \rangle$ of the $4f$ electron distribution of the particular rare-earth ion.

The statements in the preceding paragraph would imply that the replacement of a rare-earth atom within the same series of compounds would simply introduce a difference, in the crystal field parameters, given by the multiplicative factor $\langle r^k \rangle$. This is a quantity determined, more or less robustly, from first principles [16]. It could be thus assumed that B_q^k can be predicted or calculated — without the requirement of the explicit diagonalisation of H_{CEF} — for all those pyrochlores whose unique difference is the occupation of the A site. In practice, however, the crystal field parameters are seen to not obey precisely this presumed "scaling law" between isomorphic compounds [13].

Nevertheless, the point charge model can still be used to solve the CEF scheme of the f electron shells. The series expansion character of Equation (1.1) allows us to diagonalise H_{CEF}

[1] One drawback of the point charge model is that the precise conventions used in the construction of the tensor operators have to be taken into consideration, because, in general, they are not unique.

using the parameters B_q^k as the fitting coefficients. The CEF excitations of a compound can thus be perfectly modelled, as long as the eigenvalues of H_{CEF} are empirically determined. This is the procedure we are going to follow in this work.

1.3.1.2 Crystal field excitations in pyrochlores

When in the pyrochlore lattice, the full-rotation symmetry of the free ion is reduced to the point group D_{3d}. Group theoretical considerations can be used to show that, in this geometry, the trigonal charge environment around the rare-earth splits each of its $(2J+1)$-fold degenerated multiplets into a series of singlets or doublets. The lanthanides studied in this work (Sm^{3+} and Yb^{3+}) possess an odd number of electrons in their unfilled $4f$ orbital. Consequently, all possible J's will be half-integers and each multiplet can be shown to split into $(J+\frac{1}{2})$ *Kramers doublets* [12]. The analysis used to deduce the level splitting of each J multiplet is detailed in the Appendix A.

We want to define the H_{CEF} pertinent to the magnetic ion in the pyrochlore lattice. First of all, the Hamiltonian (1.1) must be Hermitian. As, for a generic tensor operator $\boldsymbol{T}_q^k$,

$$(\boldsymbol{T}_q^k)^\dagger = (-1)^{-q}\boldsymbol{T}_{-q}^k, \tag{1.3}$$

it can be easily seen that $B_q^k = (-1)^{-q}B_{-q}^k$ [14]. Next, H_{CEF} must be invariant under time reversal symmetry. The action of time reversal ($\boldsymbol{\theta}$) over a tensor operator is [14,15,17]

$$\boldsymbol{\theta}\boldsymbol{T}_q^k\boldsymbol{\theta}^{-1} = (-1)^k\boldsymbol{T}_q^k, \tag{1.4}$$

which automatically implies that k is even. Finally, the point symmetry of the A site comes into play. Especially for the D_{3d} point group, only the invariance of the Hamiltonian under C_3 rotations must be considered [17] in order to obtain

$$\frac{2q}{3} = 2n,$$

where n is an integer.

After those considerations, we obtain the minimal single ion Hamiltonian relevant to pyrochlores, which is given by [18]

$$H_{CEF} = B_0^2\boldsymbol{C_0^2} + B_0^4\boldsymbol{C_0^4} + B_3^4(\boldsymbol{C_{-3}^4} - \boldsymbol{C_3^4}) + B_0^6\boldsymbol{C_0^6} + B_3^6(\boldsymbol{C_{-3}^6} - \boldsymbol{C_3^6}) + B_6^6(\boldsymbol{C_{-6}^6} + \boldsymbol{C_6^6}). \tag{1.5}$$

Making slightly different considerations about the symmetries of H_{CEF}, one can engineer several different ways of arriving at the very same Hamiltonian [14,15,17].

The choice of basis for the matrix representation of Equation (1.5) is not unique. The most straightforward restriction, largely used in the investigation of CEF levels in pyrochlores, results in the well known *Stevens' operator formalism*. In simple terms, the Stevens' formalism consists in limiting the basis of states to a single $|L,S,J,m_J\rangle$ level. This is the state preponderant in the ground-state wave function, found considering the Hund's rules. This simplification allows the replacement of the tensor operators $\boldsymbol{C}_q^{(\pm k)}$ by the Stevens' operator equivalents [19,20]. The change in the basis of states naturally induces a renormalisation of the parameters B_q^k. The values obtained in this work and the ones calculated using the Stevens' operator formalism, which we call here S_k^q, can be related by

$$S_k^q = \lambda_{kq}\theta_k B_q^k, \tag{1.6}$$

where the θ_k are the Stevens' multiplicative factors listed in Reference [12]. The constants $\lambda_{20} = \frac{1}{2}$ and $\lambda_{40} = \frac{1}{8}$ are given in Reference [21].

The fact that, due to the crystal field anisotropy, the ground-state of most of the rare-earth ions in the pyrochlore lattice is not a highly degenerated J multiplet, but a doublet consisting of time reversed partners $\left|\Gamma_0^{\pm}\right\rangle$[2], deeply affects the magnetism of the compounds, especially at low temperatures. Since the ground-state doublet is well separated (by a large energy difference E_i) from the excited crystal field levels, at temperatures $T \ll E_i/k_B$, where k_B is the Boltzmann constant, pyrochlores behave as *effective spin-*$\frac{1}{2}$ systems.

Particularly, we are concerned with the transformation properties of the doublet ground-states. For example, the spin components of the operator $\boldsymbol{S}$ for spin-$\frac{1}{2}$ states can be defined as [23]

$$\begin{aligned} \tilde{\boldsymbol{S}}_x &= |+\rangle\langle -| + |-\rangle\langle +|, \\ \tilde{\boldsymbol{S}}_y &= -i\,|+\rangle\langle -| + i\,|-\rangle\langle +|, \\ \tilde{\boldsymbol{S}}_z &= |+\rangle\langle +| - |-\rangle\langle -|, \end{aligned} \tag{1.7}$$

where

$$|+\rangle = \begin{pmatrix} 1 \\ 0 \end{pmatrix}, \quad \langle +| = |+\rangle^{\dagger} \quad \text{and} \quad |-\rangle = \begin{pmatrix} 0 \\ 1 \end{pmatrix}, \quad \langle -| = |-\rangle^{\dagger}. \tag{1.8}$$

As the doublet ground-state has the same transformation properties as the total angular momentum $\boldsymbol{J}$ under the D_{3d} point group operations, operators analogous to Equation (1.7) can be defined as

$$\begin{aligned} \boldsymbol{S}^x &= \left|\Gamma_0^+\right\rangle\left\langle\Gamma_0^-\right| + \left|\Gamma_0^-\right\rangle\left\langle\Gamma_0^+\right|, \\ \boldsymbol{S}^y &= -i\left|\Gamma_0^+\right\rangle\left\langle\Gamma_0^-\right| + i\left|\Gamma_0^-\right\rangle\left\langle\Gamma_0^+\right|, \\ \boldsymbol{S}^z &= \left|\Gamma_0^+\right\rangle\left\langle\Gamma_0^+\right| - \left|\Gamma_0^-\right\rangle\left\langle\Gamma_0^-\right|, \end{aligned} \tag{1.9}$$

where the doublet ground-state $\left|\Gamma_0^{\pm}\right\rangle$ is used as the new basis of the spin-$\frac{1}{2}$ operators.

The possibility of expressing the magnetic moments in the pyrochlore lattice using the operators in Equation (1.9) open an avenue for the investigation of magnetic interactions at low temperatures. Below, we detail the theory behind the intricate magnetic coupling between effective spins-$\frac{1}{2}$.

1.3.2 Exchange interaction

The Heisenberg exchange Hamiltonian can be generically written as [24]

$$H_{Ex} = \sum_{\langle ij \rangle} J'_{ij} \boldsymbol{J}^i \boldsymbol{J}^j, \tag{1.10}$$

where $\boldsymbol{J}^i$, $\boldsymbol{J}^j$ are the total angular momentum operators (see Appendix B) and J'_{ij} is the parameter which gives the strength of the coupling between spin i and spin j. We just mentioned that, due to the single ion properties of the rare-earth in the pyrochlore lattice, at temperatures $T \ll E_i/k_B$, $\boldsymbol{J}$ can be replaced by another set of effective spin-$\frac{1}{2}$ operators $\boldsymbol{S}_i = (\boldsymbol{S}_i^x, \boldsymbol{S}_i^y, \boldsymbol{S}_i^z)$ transforming identically to $\boldsymbol{J}$, so that

$$H_{Ex} = \sum_{\langle ij \rangle} J_{ij} \boldsymbol{S}_i \boldsymbol{S}_j. \tag{1.11}$$

[2]Note that this is true for either Kramers and non-Kramers ions [22].

The operators S^{α} in (1.9) and (1.11) can be scaled to have the same eigenvalues ($\pm \hbar/2$) as the $\tilde{S}_{\alpha}$ in (1.7). The coupling terms J_{ij} will then incorporate the expected values of J_{α}, since $\hbar S^{z} = 2\left\langle \Gamma_0^{\pm} \right| J_z \left| \Gamma_0^{\pm} \right\rangle J_z$ and $\hbar S^{\pm} = \left\langle \Gamma_0^{\pm} \right| J_x \pm i J_y \left| \Gamma_0^{\mp} \right\rangle (J_x \pm i J_y)$.

Interactions beyond first-nearest neighbours have been considered in several theoretical studies mainly because they can stabilise long-range order in highly frustrated configurations, as that of the antiferromagnetic Heisenberg spins in the corner-sharing tetrahedra lattice [25–28]. Yet, works that parametrise the exchange constants of pyrochlore magnets using neutron scattering measurements of spin waves successfully disregard next-nearest neighbour coupling [11,24,29,30]. Below, the first nearest neighbour Hamiltonian model used in the aforementioned experimental works, which is also relevant to the analysis performed in Chapter 7, is described in detail.

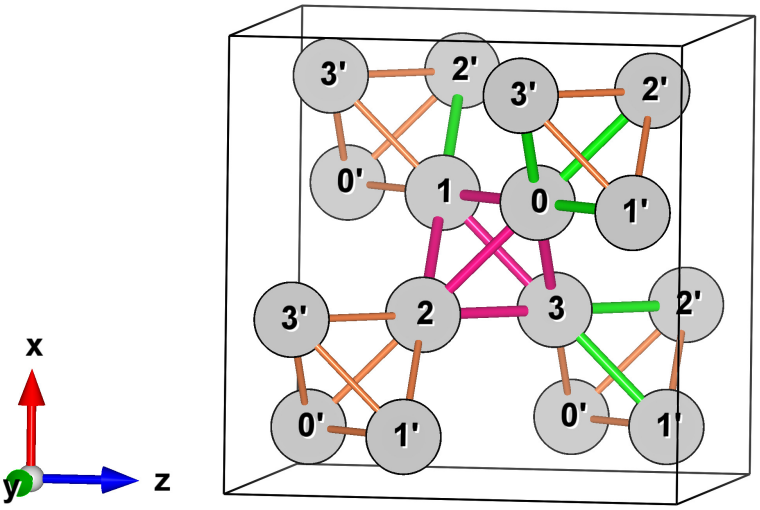

Figure 1.5: Pyrochlore rare-earth lattice represented using the coordinates of the first origin choice of the $Fd\bar{3}m$ space group. Atoms in the central tetrahedron, whose centre is also the origin of the coordinate system, are labeled 0 - 3. Equivalent atoms in any other tetrahedron are labeled 0′ - 3′. Inequivalent exchange paths in one unit cell are highlighted by green (between primed and unprimed ions) and magenta (between unprimed atoms) thick lines.

Each rare-earth cation in the pyrochlore lattice has six magnetic nearest neighbours. Using the first origin choice of the $Fd\bar{3}m$ space group, an alternative representation of the pyrochlore unit cell is drawn in Figure 1.5. Examination of this figure reveals twelve different exchange paths, marked with thick green and magenta lines. The atoms in the tetrahedron centred at the origin are numbered 0 - 3. The other symmetry equivalent atoms within the same unit cell, found performing the symmetry operations of the underlying FCC lattice, are labeled 0′ - 3′. The coordinates of the unprimed atoms are given in Table 1.1.

By definition, the exchange interaction must reflect the symmetry operations that leave the crystallographic lattice invariant. Mathematically, it means that

$$H_{Ex} = \sum_{\langle ij \rangle} S_i^{\dagger} J_{ij} S_j = \sum_{\langle ij \rangle} S_i^{\dagger} U^{\dagger} U J_{ij} U^{\dagger} U S_j, \tag{1.12}$$

where U is any unitary transformation, so that $U^{\dagger}U = \mathbb{1}$. The local symmetry of the magnetic ion (D_{3d}) is, once more, relevant in the determination of H_{Ex}. The symmetry elements of this point group are shown in the Table A.1 of Appendix A. Each of those operations can be

Atom	x	y	z
0	1	1	1
1	1	-1	-1
2	-1	1	-1
3	-1	-1	1

Table 1.1: Coordinates $\boldsymbol{r}_i$ (multiplied by $\frac{8}{a}$, where a is the lattice parameter) of the atoms belonging to the tetrahedron centred at the origin of the global coordinate system (unprimed set) in Figure 1.5.

represented by three-dimensional matrices, some of them explicitly given in the Appendix C. It is important to note that spins transform as axial vectors, so each one of the symmetry operation matrices is multiplied by its determinant (± 1).

In order to obtain the most general form of the coupling matrix for pyrochlores, we start defining a general 3×3 matrix

$$J_{01} = \begin{pmatrix} J_{01}^{xx} & J_{01}^{xy} & J_{01}^{xz} \\ J_{01}^{yx} & J_{01}^{yy} & J_{01}^{yz} \\ J_{01}^{zx} & J_{01}^{zy} & J_{01}^{zz} \end{pmatrix}, \tag{1.13}$$

which gives the coupling between the atoms 0 and 1 (see Figure 1.5). The hermiticity of the Hamiltonian is guaranteed when, for all the twelve different bounds,

$$J_{ij} = J_{ji}^{T}. \tag{1.14}$$

Equation (1.14) has profound consequences in the exchange interactions between nearest neighbours. The first is that, clearly, $J_{ij} \neq J_{ji}$. However, maybe the most important outcome of (1.14) is that the interactions within one unit cell can be completely determined by the spin configuration of a single tetrahedron [31], that formed by the unprimed atoms in Figure 1.5. The interaction between atoms connected by the green bounds is thus obtained using $J_{ij'} = J_{ij}^{\dagger}$. This characteristic of J_{ij} reduces to six the number of inequivalent exchange coupling matrices that need to be determined.

The *antisymmetric exchange* coupling between the magnetic atoms, also known as *Dzyaloshinskii-Moriya interaction*, must be considered. This interaction has its origin on the spin-orbit coupling [32], and can be expressed as

$$H_{Ex}^{Anti} = \boldsymbol{D}_{ij}(\boldsymbol{S}_i \times \boldsymbol{S}_j), \tag{1.15}$$

where $\boldsymbol{D}_{ij}$ is the Dzyaloshinskii-Moriya vector. The direction of $\boldsymbol{D}_{ij}$ is constrained (excepting for its sign) by symmetry, as stated in the *Moriya rules* [32]. The non-zero components in pyrochlores can be found simply by performing the cross product between the coordinates of the atoms i and j [3]. For example, for the bound $\langle 01 \rangle$, one obtains [33]

$$\hat{\boldsymbol{D}}_{01} = \begin{vmatrix} \hat{x} & \hat{y} & \hat{z} \\ 1 & 1 & 1 \\ 1 & -1 & -1 \end{vmatrix} = \frac{1}{\sqrt{2}} \begin{pmatrix} 0 \\ \hat{y} \\ -\hat{z} \end{pmatrix}, \tag{1.16}$$

[3]Note that this is not a Moriya rule, but the vector resulting from the cross product represents the Dzyaloshinskii-Moriya vector in pyrochlores due to the mirror plane that crosses the middle point of the rare-earth bounds [33].

a vector lying on the same plane, but with orientation perpendicular to the bound $\boldsymbol{r}_{01} = \boldsymbol{r}_0 - \boldsymbol{r}_1$. It is important to note that mirroring and rotations change the orientation of $\boldsymbol{D}_{ij}$. Consider for example the C_2^x operation that interchange the positions of the atoms 0 and 1 in Figure 1.5. If, for the bound $\langle 01 \rangle$, $\boldsymbol{D}_{ij} = \boldsymbol{D}_{01}$, the Dzyaloshinskii-Moriya vector for the bound $\langle 10 \rangle$ will be $\boldsymbol{D}_{10} = -\boldsymbol{D}_{01}$.

Using Equation (1.15), it is easy to show that, for the $\langle 01 \rangle$ bound, the Dzyaloshinskii-Moriya interaction will contribute to the exchange coupling terms $J_{01}^{xy}, J_{01}^{xz}, J_{01}^{yx}, J_{01}^{zx}$. In particular, $J_{01}^{xy} = -J_{01}^{yz}$ and $J_{01}^{xz} = -J_{01}^{zx}$. With this, we automatically guarantee that the condition of Equation (1.14) is satisfied.

Finally, we impose that both C_2^x and $\sigma^{[011]}$ operations have the same effect over the coupling matrix in (1.13), i.e, that $J_{10} = C_2^x J_{01} [C_2^x]^{-1} = \sigma_2^{[011]} J_{01} [\sigma^{[011]}]^{-1}$. So,

$$J_{10} = \begin{pmatrix} 1 & 0 & 0 \\ 0 & -1 & 0 \\ 0 & 0 & -1 \end{pmatrix} \cdot \begin{pmatrix} J_{01}^{xx} & J_{01}^{xy} & J_{01}^{xz} \\ -J_{01}^{xy} & J_{01}^{yy} & J_{01}^{yz} \\ -J_{01}^{xz} & J_{01}^{zy} & J_{01}^{zz} \end{pmatrix} \cdot \begin{pmatrix} 1 & 0 & 0 \\ 0 & -1 & 0 \\ 0 & 0 & -1 \end{pmatrix} \tag{1.17}$$

$$= \begin{pmatrix} -1 & 0 & 0 \\ 0 & 0 & 1 \\ 0 & 1 & 0 \end{pmatrix} \cdot \begin{pmatrix} J_{01}^{xx} & J_{01}^{xy} & J_{01}^{xz} \\ -J_{01}^{xy} & J_{01}^{yy} & J_{01}^{yz} \\ -J_{01}^{xz} & J_{01}^{zy} & J_{01}^{zz} \end{pmatrix} \cdot \begin{pmatrix} -1 & 0 & 0 \\ 0 & 0 & 1 \\ 0 & 1 & 0 \end{pmatrix}. \tag{1.18}$$

Finally,

$$\begin{pmatrix} J^{xx} & -J^{xy} & -J^{xz} \\ J^{xy} & J^{yy} & J^{yz} \\ J^{xz} & J^{zy} & J^{zz} \end{pmatrix} = \begin{pmatrix} J^{xx} & -J^{xz} & -J^{xy} \\ J^{xz} & J^{zz} & J^{zy} \\ J^{xy} & J^{yz} & J^{yy} \end{pmatrix} \quad \therefore \quad J_{01} = \begin{pmatrix} J^{xx} & -J^{xy} & -J^{xy} \\ J^{xy} & J^{yy} & J^{yz} \\ J^{xy} & J^{yz} & J^{yy} \end{pmatrix}, \tag{1.19}$$

where we drop the superfluous bound index. This coupling matrix possesses four different coupling terms and defines the most general exchange Hamiltonian for pyrochlores. To make it more familiar with the huge body of work performed on those magnets [11, 24, 31], we simply redefine J_{01} as

$$J_{01} = \begin{pmatrix} J_2 & J_4 & J_4 \\ -J_4 & J_1 & J_3 \\ -J_4 & J_3 & J_1 \end{pmatrix}, \tag{1.20}$$

Exchange matrices equivalent to (1.20) can be obtained using several different methods [23], but in the opinion of the author of this theses, this is the most clear. Once the most general exchange coupling matrix for one specific bound is defined, the exchange coupling for different bounds can be obtained using the symmetry operations of the D_{3d} point group. For example, a $C_3^{[111]}$ rotation (see Appendix C) transforms the bound $\langle 01 \rangle$ into the bound $\langle 03 \rangle$. Another $C_3^{[111]}$ rotation transforms $\langle 03 \rangle$ into $\langle 02 \rangle$. A S_4^x rotoinversion transforms $\langle 01 \rangle$ into $\langle 23 \rangle$. A S_4^y transforms $\langle 02 \rangle$ into $\langle 31 \rangle$ and, finally, S_4^z transforms $\langle 03 \rangle$ into $\langle 12 \rangle$. Each new coupling matrix is obtained doing $U J_{ij} U^\dagger$, where U is the symmetry operation matrix.

So far, the basis for the matrices representations we have used are the *global* x, y, z axis, which coincide with the crystallographic a, b, c. We can perform a transformation of basis to a different coordinate system using Equation (1.12), so that

$$J_{ij}^{local} = U_i J_{ij}^{global} U_j^\dagger. \tag{1.21}$$

Note that instead of transforming the J_{ij}^{global} to another global basis, now the matrices U_i and U_j will correspond to the local coordinates of the unprimed atom pair i, j. The z axis of each

local coordinate system will correspond to the local $\langle 111 \rangle$ direction. The x, y components can be any two vectors perpendicular to z and to each other. To keep this derivation equivalent to the performed in the literature [11,24,31], we choose the local coordinates described in the Appendix D.

The Hamiltonian after the *global* $\rightarrow$ *local* coordinates transformation is expressed as

$$\begin{aligned} H_{Ex} = \sum_{\langle ij \rangle} J_{zz} S_i^z S_j^z - J_{\pm}(S_i^+ S_j^- + S_i^- S_j^+) + J_{\pm\pm}(\gamma_{ij} S_i^+ S_j^- + \gamma_{ij}^* S_i^- S_j^-) \\ + J_{z\pm}[S_i^z(\zeta_{ij} S_j^+ + \zeta_{ij}^* S_j^-) + (\zeta_{ij}^* S_i^+ + \zeta_{ij} S_i^-) S_j^z], \end{aligned} \tag{1.22}$$

where $\gamma_{ij} = -\zeta_{ij}^*$ are bound dependent complex numbers with $|\gamma_{ij}| = 1$, also given in the Appendix D. The global exchange coupling parameters can be defined as a function of the local ones as follows:

$$\begin{pmatrix} J_1 \\ J_2 \\ J_3 \\ J_4 \end{pmatrix} = \frac{1}{3} \begin{pmatrix} -1 & 4 & 2 & 2\sqrt{2} \\ 1 & -4 & 4 & 4\sqrt{2} \\ -1 & -2 & -4 & 2\sqrt{2} \\ -1 & -2 & 2 & -\sqrt{2} \end{pmatrix} \cdot \begin{pmatrix} J_{zz} \\ J_{\pm} \\ J_{\pm\pm} \\ J_{z\pm} \end{pmatrix}. \tag{1.23}$$

The form of the local coupling matrix for the bound $\langle 01 \rangle$ will be

$$J_{01}^{local} = -2 \begin{pmatrix} J_{\pm} - J_{\pm\pm} & 0 & J_{z\pm} \\ 0 & J_{\pm} + J_{\pm\pm} & 0 \\ J_{z\pm} & 0 & -J_{zz}/2 \end{pmatrix}, \tag{1.24}$$

which can be immediately compared to (1.20).

1.3.2.1 The Hamiltonian of Ising spins with octupolar interactions

The local coordinate system is especially important when exchange interactions between Ising spins are being modelled. When the ground-state doublet symmetry constraints the magnetic moment to point along the local-z, it can be shown that the interaction matrix, in local coordinates, will not depend on the specific bound [23,34,35]. Hence, $\gamma_{ij} = -\zeta_{ij} = 1$ in Equation (1.22), and all bounds will share the same coupling coefficients matrix (1.24), which we rename as follows:

$$J_{ij}^{DO} = \begin{pmatrix} J_{xx} & 0 & J_{xz} \\ 0 & J_{yy} & 0 \\ J_{xz} & 0 & J_{zz} \end{pmatrix}. \tag{1.25}$$

The linearised Hamiltonian for dipolar-octupolar doublets is thus [35]

$$H_{Ex}^{DO} = \sum_{\langle ij \rangle} [J_{xx} S_i^x S_j^x + J_{yy} S_i^y S_j^y + J_{zz} S_i^z S_j^z + J_{xz}(S_i^x S_j^z + S_i^z S_j^x)]. \tag{1.26}$$

It is interesting to think about the physical origin of the non-diagonal coupling term J_{xz} in the matrix (1.25). To do that, we have to look back at Equation (1.10). If we express the Kramers ground-state doublet in the $|J, m_J\rangle$ basis, the eigenstates of Ising spins will have the form (see Chapter 4)

$$\begin{aligned} |\Gamma_0^{\pm}\rangle = \sum_J \sum_{m_J=-J}^{J} \alpha \left| J, m_J = \pm\frac{3}{2} \right\rangle \pm \beta \left| J, m_J = \mp\frac{3}{2} \right\rangle + \gamma \left| J, m_J = \pm\frac{9}{2} \right\rangle \pm \delta \left| J, m_J = \mp\frac{9}{2} \right\rangle \\ + \cdots + \nu \left| J, m_J = \pm J \right\rangle \pm \xi \left| J, m_J = \mp J \right\rangle. \end{aligned} \tag{1.27}$$

Note that, as a consequence of the three-fold rotation symmetry of the D_{3d} space group, the wave functions of each doublet will be composed by states with $|m_J\rangle$ separated in units of three. The operators $\boldsymbol{J} = (\boldsymbol{J}_x, \boldsymbol{J}_y, \boldsymbol{J}_z)$ projected onto the wave functions of Equation (1.27) return non-zero matrix elements only for $\boldsymbol{J}_z$. In the basis of the doublet ground-state, this matrix will be diagonal, proportional to $\tilde{\boldsymbol{S}}_z$.

Higher multipolar elements must therefore be considered if transverse coupling terms are to take part in the Ising pyrochlore exchange Hamiltonian. Quadrupolar operators, as for example $\boldsymbol{J}_x^2$, $\boldsymbol{J}_y^2$ and $\boldsymbol{J}_z^2$, are diagonal, proportional to the identity. The next most important contribution results then from the octupolar moments. The relevant operator, Equation (4.8) [29,36], will be discussed in more detail in Chapter 4. For now, it is interesting to mention that the transverse terms in the exchange Hamiltonian of Ising pyrochlores can be physically understood as a coupling between octupolar moments. This characteristic implies that multipolar interactions affect the magnetic excitations exhibited by pyrochlores and that neutron scattering techniques can be applied in order to investigate such states [29].

1.3.2.2 A note about the exchange Hamiltonian of pyrochlores

This is a short note, left here as a reminder to the reader, that the coupling matrices J_{ij} were initially derived purely on group theoretical grounds. For example, the J_4 in the work of Reference [24] was not identified as the components of the Dzyaloshinskii-Moriya vector, because, in principle, this consideration is not necessary [23]. Recently, however, the physical mechanism behind each one of the exchange coupling terms has been more deeply explored. In the preprints [37,38], Kitaev coupling given by $(J_2 - J_1)$ is invoked. Those considerations do not change the overall understanding and the derivation of the exchange coupling matrices shown here.

1.3.2.3 Spin waves and linear spin wave theory

Spin waves are collective excitations, characterised by a propagation vector $\boldsymbol{k}$, created out of a defined magnetic ground-state once a angular momentum deviation of $\hbar$ (spin flip) takes place in a system of N spins. Its quantisation unit is a boson called *magnon*. In a classical vector model, a spin wave can be represented by the precession of every localised spin at the lattice about a quantisation axis [39,40].

Once the exchange Hamiltonian is defined, the pertinent dispersion relations of the spin waves can be calculated. To do so, one starts by replacing the spin operators $\boldsymbol{S}_{i,j}^x, \boldsymbol{S}_{i,j}^y$ by the spin ladder operators defined as $\boldsymbol{S}_{i,j}^{\pm} = \boldsymbol{S}_{i,j}^x \pm i\boldsymbol{S}_{i,j}^y$ [4]. Additionally, Holstein and Primakoff [41] introduced a transformation in order to express $\boldsymbol{S}_i^z$ ($\boldsymbol{S}_j^z$) and $\boldsymbol{S}_i^{\pm}$ ($\boldsymbol{S}_j^{\pm}$) in terms of the magnon *creation* and *annihilation* operators $\boldsymbol{a}_i^+$ ($\boldsymbol{a}_j^+$) and $\boldsymbol{a}_i$ ($\boldsymbol{a}_j$), respectively, as [39]

$$\boldsymbol{S}_i^z = \hbar(S - \boldsymbol{a}_i^+ \boldsymbol{a}_i), \tag{1.28}$$

$$\boldsymbol{S}_i^+ = \hbar\sqrt{2S}\left(1 - \frac{\boldsymbol{a}_i^+ \boldsymbol{a}_i}{2S}\right)^{1/2} \boldsymbol{a}_i, \tag{1.29}$$

[4] Note that this procedure was already performed in Equation (1.22), where H_{ex} in the local coordinate system is defined.

and

$$S_i^- = \hbar\sqrt{2S}\,a_i^+\left(1-\frac{a_i^+ a_i}{2S}\right)^{1/2}, \tag{1.30}$$

where S is the total spin on a site i, j.

The approximation considered in *linear spin wave theory* (LSWT) is to truncate Equations (1.28)-(1.30) up to the first order in a_i or a_i^+, so that the resulting exchange Hamiltonian does not include quadratic terms of the annihilation/creation operators. This is an approximation justified when magnon-magnon interactions, i.e, processes involving creation and annihilation of two or three magnons, can be neglected. That this is indeed the case, one only discovers measuring the spin wave spectra of a compound at very low temperatures.

After performing the *Holstein-Primakoff transformation* and the LSWT approximation, the last step is to Fourier transform the operators (1.28)-(1.30) to obtain [40]

$$\begin{aligned} S_i^+ &= \hbar\sqrt{2S}\,a_i = \hbar\sqrt{\frac{2S}{N}}\sum_k e^{ik\cdot r_i}a_k, \\ S_i^- &= \hbar\sqrt{2S}\,a_i^+ = \hbar\sqrt{\frac{2S}{N}}\sum_k e^{-ik\cdot r_i}a_k^+, \end{aligned} \tag{1.31}$$

where r_i is the position of the magnetic atom i, N is the number of unit cells in the crystal and a_k^+ (a_k) are the creation (annihilation) operators of a magnon with wave vector k. Now the exchange Hamiltonian can be diagonalised, the diagonal elements of the resulting matrix being the dispersion relations $\omega(k)$ of the spin waves [42].

In this work, we use LSWT in order to compare its expected results with the excitations obtained from a powder sample of the pyrochlore $Yb_2Ti_2O_7$. The software SpinW, written by Sándor Tóth [43], is used to calculate the dispersion relations of the pyrochlore exchange Hamiltonian and their corresponding powder averaging.

1.3.3 Dipolar interaction

The interaction between two magnetic moments $\mu_i = g_J J^i \mu_B$ and $\mu_j = g_J J^j \mu_B$ separated by a distance $r_{ij}\hat{r}_{ij} = |r_i - r_j|$ is [44]

$$H_{Dip} = \left(\frac{\mu_0}{4\pi}\right)\frac{1}{2r_{nn}^3}\sum_{\langle ij\rangle}\frac{\mu_i\cdot\mu_j - 3(\mu_i\cdot\hat{r}_{ij})(\mu_j\cdot\hat{r}_{ij})}{(r_{ij}/r_{nn})^3}, \tag{1.32}$$

where g_J is the Landè g-factor [see Equation (B.3)], $\mu_0 = 4\pi\times10^{-7}$ T·m/A is the vacuum permeability and μ_B is the Bohr magneton. One complication in the theoretical treatment of the dipolar coupling in magnetic systems is that, as apparent in the Hamiltonian of Equation (1.32), the dipolar interaction is long-range, decaying slowly with r^3. It is also easy to see that the state of minimum energy of H_{Dip} is that for which $\mu_i \parallel \mu_j \parallel \hat{r}_{ij}$. This condition is only satisfied in an unidimensional system with collinear ferromagnetic spins. For any experimentally relevant material, predominant dipolar interactions lead, inevitably, to frustration [45].

Microscopic models of interatomic magnetism do not require the inclusion of the dipolar term in the Hamiltonian because, in general, it contributes only weakly to the Curie-Weiss temperature. On the other hand, for trivalent ions such as Gd^{3+}, Ho^{3+} and Dy^{3+}, which possess large localised magnetic moments, the magnetostatic energy scale demand the inclusion of H_{Dip} into the analysis. It is possible to fully incorporate the dipolar coupling between nearest

neighbours into the exchange matrix J_{ij} [10], a procedure that has been followed in several experimental works [11,29]. In the local coordinates system,

$$\begin{pmatrix} J_{zz}^{dip} \\ J_{\pm}^{dip} \\ J_{\pm\pm}^{dip} \\ J_{z\pm}^{dip} \end{pmatrix} = \frac{\mu_0 \mu_B^2}{12(4\pi)} \begin{pmatrix} 20g_z^2 \\ -g_{xy}^2 \\ 7g_{xy}^2 \\ -2\sqrt{2}g_{xy}g_z \end{pmatrix}, \tag{1.33}$$

where $g_z = 2g_J\langle\Gamma_0^{\pm}|J_z|\Gamma_0^{\pm}\rangle$ and $g_{xy} = g_J\langle\Gamma_0^{\pm}|J_{\pm}|\Gamma_0^{\mp}\rangle$.

In the spin wave work performed on $Yb_2Ti_2O_7$, dipolar interactions between the rare-earth ions were neglected, since the exchange coupling is largely dominant in the Hamiltonian [24]. However, this is not the rule. The most notorious frustrated ground-state resulting from the competition between exchange and dipolar interactions in Ising pyrochlores will be explored in the next section.

1.4 The genesis: the spin ice and the ice rules

The pyrochlores $Ho_2Ti_2O_7$ and $Dy_2Ti_2O_7$ are what can be called canonical *spin ice* materials. Looking superficially, the analogy between those systems and water ice can be slightly misinterpreted: pyrochlores are cubic systems, while water ice, in its most abundant I_h form, is a hexagonal crystal [46]. One has to look at the coordination of each H^+ proton, an exercise performed by Linus Pauling in 1935 [46], to understand what water ice and spin ices have in common.

As already known in 1935, the stability of liquid and solid water is guaranteed by the strong intermolecular hydrogen bounds. The question posed (and answered) by Pauling was the following: how is the intramolecular arrangement of atoms in H_2O? The oxygen arrangement was described based on x-ray measurements of ice. Each O^{2-} is tetrahedrally surrounded by other four oxygens, and the equilibration of the strong Coulomb repulsion between them is performed by the H^+, placed *somewhere* within the oxygen crystalline structure. The proposal of Pauling was that the *somewhere* was not in the barycentre of the bound between two O^{2-} ions, but that the hydrogen is way closer to one oxygen than to the other [46]. Moreover, each O^{2-} will be coordinated by two protons, one close and other far located from it. The assumption of Pauling is grounded on an entropic argument, which is fundamental in the discussion of spin ices as well. Since that, if the two protons are at unequal distances from the anion, a given water molecule can orient itself in six different ways and that each orientation has a probability $1/4$ of connection with an adjacent molecule, the total number of configurations for this structure is $\Omega = (\frac{6}{4})^N$, where N is the number of molecules. Considering that $S = k_B \ln \Omega$, the residual entropy of the frozen water at very low temperatures will be $R\ln(3/2)$ (or $\frac{R}{2}\ln(3/2)$ per H^+ ion).

Before Pauling's proposal, the experimental residual entropy of water ice had been determined to be ≈ 0.87 cal K/mol $\sim R\ln(3/2)$. The analogy was transferred to magnetic systems once Harris *et al.* [47] noticed that ferromagnetic coupled spins in the Ising pyrochlore possess a ground-state with a two-in-two-out arrangement, as shown in Figure 1.6. The calculation of the number of states is simple. Consider that N Ising spins may point only along two directions: up or down (actually, this is truth for any doublet ground-state). The total number of states is then $\Omega = 2^N$. However, only six out of 16 tetrahedra configurations obey the *ice rules*, with two spins pointing *in* and two pointing *out*. For a system with a number of tetrahedra $N_T = N/2$,

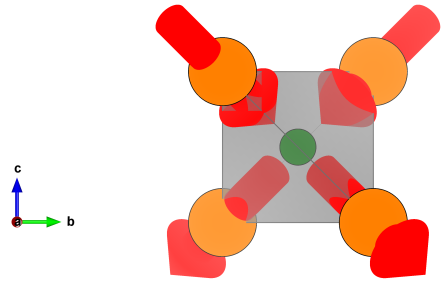

Figure 1.6: Top view (along the cubic $\langle 100 \rangle$ direction) of one of the spin arrangements of the spin ice manyfold. In total, six of them are possible for each tetrahedron.

the number of states is therefore $\Omega = 2^N (6/16)^{N_T}$. With this we recover an entropy *per spin* of $\frac{R}{2} \ln(3/2)$, equivalent to that deduced by Pauling for water ice.

The fact that the spin orientations in those pyrochlores can be directly mapped onto those of the proton positions in water ice motivated Harris *et al.* to name $Ho_2Ti_2O_7$ a *spin ice*. The empirical confirmation of the ground-state residual entropy in those materials came few years later, with heat capacity measurements performed on $Dy_2Ti_2O_7$. This experiment mimicked the measurement of the residual entropy in water ice [48]. It was not, however, immediately obvious *i.* why spin ices obey the ice rules and *ii.* why the calculation of the residual entropy, which disregards the geometrical structure of the pyrochlore lattice beyond any individual tetrahedron unit, gives such a good estimate of the experimental value [44].

Several studies try to answer those questions [5], but frustration is directly involved with the first one. Note that the spin ice is intrinsically different from the ordinary spin glass phase. Even though the low temperature state in spin ice is static and short-range ordered, the orientation of the spins is not random because of the constraints imposed by the ice rules. Moreover, structural disorder is not related to the development of the spin ice state, as it is for conventional spin glasses [50].

The frustration in spin ices is a direct consequence, primarily, of the crystal field anisotropy, and finally, of the ferromagnetic *effective* interactions. Both $Ho_2Ti_2O_7$ and $Dy_2Ti_2O_7$ have, hence, positive Curie-Weiss temperatures. The coupling is said "effective" because, in those materials, antiferromagnetic exchange and dipolar interactions compete [51]. The inclusion of the dipole-dipole correlations is, thus, fundamental to explain why spin ice obeys the ice rules [51]. The *dipolar spin ice model* was first proposed by Siddharthan *et al.* [52] shortly after the discovery of the spin ice state in $Ho_2Ti_2O_7$. Due to the long-range character of the dipolar interaction, the implementation of the calculation carried out to solve the model is far from trivial [44]. The results, nevertheless, lead to a good reproduction of neutron scattering measurements performed on spin ices, capturing the main features of the elastic pattern exhibited in the reciprocal space [51].

The spin correlations revealed by the magnetic diffuse scattering measured in spin ices hint even more. In 2008, Castelnovo *et al.* [53] proposed a model which supports the emergence of magnetic charge in spin ice compounds. In the *dumbbell model*, each dipole residing at the corners of the tetrahedra is replaced by a dumbbell of opposite charges separated by a distance $a_d = \sqrt{3/2} r_{nn}$. By construction, this model captures in essence the complete spin ice physics, including the minimum energy configurations satisfying the ice rules and the residual entropy. The simplest excitation is created out off the ground-state with a spin flip, which violates the

[5] See [49] and References therein.

ice rules. This move creates a magnetic charge at the centre of the "defective" tetrahedron. The biggest accomplishment of the dumbbell model is to demonstrate that the energy cost to propagate those defects is finite, and, therefore, the emergent monopoles created by a spin flip may be moved far apart by flipping a sequence of spins. As this is a thermally activated process, the monopole density in spin ices goes to zero as $T \to 0$.

When the density of induced monopoles is low enough (at low temperatures), the spin-spin correlation function displays the spatial anisotropy and the $1/r^3$ decay, which are characteristics of this so-called *Coulomb phase* [54]. The main experimental feature of spin ices are the consequent appearance, in elastic neutron scattering, of pinch-point singularities at particular lattice positions, the signature of dipolar correlations in spin space. The broadening of the line shapes of the pinch points with increasing temperature could be attributed to deviations from the ice rules stimulated by the creation of monopole/antimonopole pairs [55]. Other experiment described the measured neutron structure factor of $Dy_2Ti_2O_7$ in applied magnetic field as a pattern of crystallised positive and negative monopoles [56].

Spin ices are not the main subject of this thesis, but their discovery marks the beginning of intensive research of frustration in pyrochlore magnets.The nomenclature of the exotic states predicted to emerge in the ground-state of several pyrochlores is also based on the work on spin ices. Our concern in the next section is to describe conceptually a modified version of the spin ice Hamiltonian, the recipe to produce the *quantum spin ice*.

1.5 What is this thesis about: motivation and outline

Frustrated materials are interesting because, rationally thinking, they are the ones that present the best chances to display new, exotic phases of matter. Basically, one looks for the principles of quantum mechanics or quantum electrodynamics to be realised in condensed matter systems. This is not done so much to prove that the theory is right, as it is to show how much work is still needed in order to capture the experimental features challenging conventional physics.

When one refers specifically to frustrated magnetism in pyrochlores, this would mean in simple terms that we are trying to find the quantum analog of the spin ice. As exotic as emergent monopoles can be, spin ices are in reality classical materials. The Hamiltonian of $Ho_2Ti_2O_7$ and $Dy_2Ti_2O_7$ is composed of one single exchange term $J_{zz} > 0$ combined with dipolar interactions. An interesting theoretical exercise would be, thus, to include transverse interactions, or quantum fluctuations, in a ground-state exhibiting the well known, and very robust, spin ice behaviour.

Initially, the concept of *quantum spin ice* (QSI) was employed to describe the exotic phase of matter emerging in the limit $J_{zz} \gg J_{\pm}$ and $J_{\pm\pm} \gg J_{z\pm}$, as represented in Figure 1.7(a). This phase diagram has a special significance to this work, because it results from experiments performed on one of the materials studied in this thesis: the pyrochlore $Yb_2Ti_2O_7$. Ytterbium titanate was the first pyrochlore to have its exchange Hamiltonian, exactly the model of Equation (1.22), fitted to spin waves measured using inelastic neutron scattering [24]. At that moment, not long ago, the properties of $Yb_2Ti_2O_7$ were not known to be so sensitive to sample defects. The parameters reported in Reference [24] were largely consistent with those expected in an predominantly Ising system, weekly perturbed by the transverse *quantum* $J_{\pm}$, $J_{\pm\pm}$, $J_{z\pm}$ (see Table 7.1 in Chapter 7).

Reference [57] develops a theory, which has the advantage of not relying on perturbation theory, but on a method called by the authors of gauge mean field theory (gMFT). The gMFT supports the presence, when $J_{zz} > 0$ and $J_{\pm\pm} = 0$, of two exotic phases of matter sharing space with conventional ferromagnetic and antiferromagnetic states. These phases were denominated *Coulombic ferromagnet* (CFM) and *quantum spin liquid* (QSL), later renamed quantum spin ice [58].

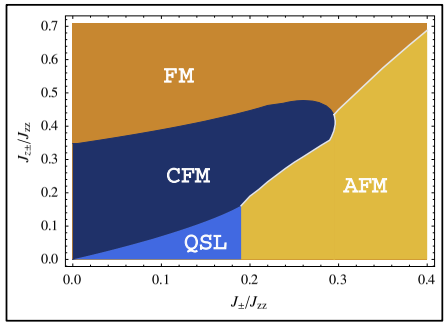

(a) Savary *et al.* Phys. Rev. Lett. **108**, 037202 (2012)

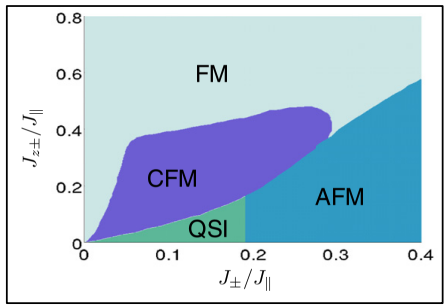

(b) Gingras *et al.* Rep. Prog. Phys. **77**, 056501 (2014)

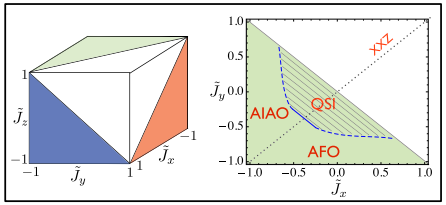

(c) Huang *et al.* Phys. Rev. Lett. **112**, 167203 (2014)

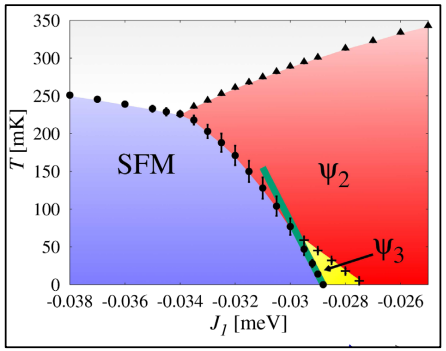

(d) Jaubert *et al.* Phys. Rev. Lett. **115**, 267208 (2015)

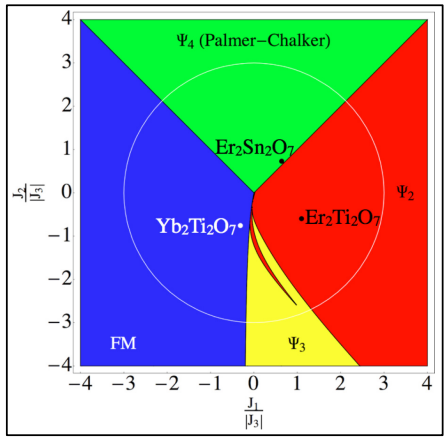

(e) Yan *et al.* Phys. Rev. B **95**, 094422 (2017)

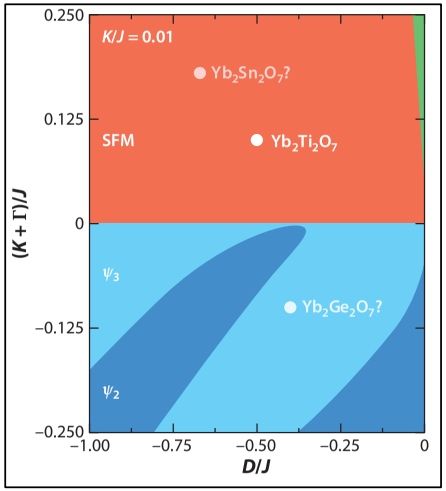

(f) Rau *et al.* Annu. Rev. Condens. Matter Phys. **10**, 357-86 (2019)

Figure 1.7: Phase diagrams, relevant to this work, spanning the research on pyrochlore magnets in the last years. (a) Gauge mean field theory phase diagram [57] of the Hamiltonian (1.22) for $J_{zz} > 0$ and $J_{\pm\pm} = 0$. Phases presented are "QSL" (*quantum spin liquid*), "CFM" (*Coulombic ferromagnet*), "FM" (*standard ferromagnet*) and "AFM" (*antiferromagnet*). (b) Slightly modified phase diagram, referent to (a), which takes into account the perturbative limit $J_{z\pm}/J_{zz} \ll 1$ [57,58]. Note that the nomenclature of the "QSL" phase was modified to "QSI", or *quantum spin ice* [58]. (c) The first diagram presenting the phases expected for dipole-octupole doublets in the pyrochlore lattice, using the model Hamiltonian (1.26). On the left hand side, unit cube of the XYZ model [34]. On the right hand side, the $\tilde{J}_z = 1$ surface of the cube, where the "dQSI" (*dipolar quantum spin ice*), "AIAO" (*all-in-all-out*) and "AFO" (*antiferro-octupolar*) phases are found [34]. (d)-(e) Classical ground-state phase diagrams, which make explicit the position of $Yb_2Ti_2O_7$ in the phase-space of long-range ordered pyrochlores [9,31,59]. All use the same model Hamiltonian (1.22). The Ψ_2 and Ψ_3 phases in (d), (e) and (f) correspond to each of the two basis vectors of the Γ_5 irreducible representation (see Table 2.1).

In the region where the perturbative limit applies ($J_{z\pm}/J_{zz} \to 0$), the phase diagram is most adequately sketched in Figure 1.7(b).

Believing that it had more to show, my thesis research started on the study of the intricate ground-state of $Yb_2Ti_2O_7$. It may seem unreasonable to study a system which has its Hamiltonian already determined based on inelastic neutron scattering experiment. As we are going to show in **Chapter 7**, the Hamiltonian fitted (and reviewed several times) by different groups using different samples seem to agree with the experiment only when sharp spin waves develop in the system in high applied magnetic fields. Under zero field, although some remnants of spin wave dynamics are indeed present in the pyrochlore, most of the excitations are of exotic origin and, to date, not completely understood. Recently, many works have focused on the effect that multiphase competition has in the ground-state of pyrochlores. This is illustrated in the classical phase diagrams of Figures 1.7(d)-(f), which demonstrate how close to phase boundaries Yb and also Er-based pyrochlores lie.

Another intriguing property of $Yb_2Ti_2O_7$ is that the compound displays long-range order in its ground-state, something which is totally absent in the QSI model [57]. This is a intentional spoiler of the results presented in **Chapter 6**, in which we detail the experimental findings about the static magnetism present on our $Yb_2Ti_2O_7$ sample.

As the $Yb_2Ti_2O_7$ results are the most complicated, they are left to the end. We initiate presenting the research which was chronologically performed later. Its main objective is to understand the magnetism of the Sm^{3+} ion in the frustrated pyrochlore lattice. Two materials, $Sm_2Ti_2O_7$ and $Sm_2Sn_2O_7$, with different B sites, for reasons that will be explored in **Chapter 3**, were studied. This work was proven very challenging from the experimental point of view, as many of those materials properties remained invisible to neutron scattering.

The research on Sm-based pyrochlores was initially conducted in order to identify the magnetic behaviour of compounds that, unlike spin ices, present vanishingly small dipolar interactions due to the weak magnetic moment of the samarium trivalent ion. This has an interesting effect on the Hamiltonian of Ising pyrochlores, class to which, as demonstrated in **Chapter 4**, the two Sm-based pyrochlores belong. This kind of doublet ground-state supports the *magnetic moment fragmentation* scenario, developed and discussed in the context of the experimental findings in the end of **Chapter 5**.

Ising pyrochlores may also develop QSI phases. In order to show that, the phase diagram for dipolar-octupolar doublets studied in Reference [34] is reproduced in Figure 1.7(c). The model Hamiltonian used in the construction of it is given in Equation (1.25), where the authors performed a pseudospin rotation to transform the four exchange coupling parameters into only three, which are referred in Figure 1.7(c) as $\tilde{J}_x, \tilde{J}_y, \tilde{J}_z$. The particular transformation is irrelevant to our work, although it must be taken into account once external magnetic field is included into the model [23]. Two versions of the QSI phases are present in the parameter space studied via gMFT, partially shown on the right hand side of Figure 1.7(c). Additionally, the conventional all-in-all-out (AIAO) phase and a new antiferro-octupolar order (AFO) may emerge. The AFO phase, as mentioned in Reference [34], does not present any on-site dipolar order.

Chapter 2

Experimental

2.1 General scattering theory of neutrons

Neutrons are chargeless, spin-1/2 particles with mass $m_n = 1838 m_e$, where $m_e = 9.109(3) \times 10^{-31}$ kg is the electron mass. They interact with matter mainly via the (very) short-range strong nuclear force or via dipole-dipole interactions with the atomic electron cloud [60]. For being chargeless, and, therefore, not being subject to Coulomb forces, neutrons can travel through matter and reach deeper regions in bulk materials [61]. Moreover, the dipole-dipole interaction render them especially sensitive to the sample magnetism. Those two important characteristics make neutrons to be considered the *golden standard* for the study of magnetic properties on condensed matter systems.

Apart from the sensibility to magnetism, there are also some other practical reasons for the suitability of neutron scattering techniques on the study performed in this thesis. Since we are working with oxide materials, the precise investigation of the structure of our samples requires the use of neutron diffraction. Unlike those of x-rays, to which light atoms as oxygen are transparent [62], the neutron cross-sections change in a quite erratically way along the periodic table. This is related to the intrinsic properties of the strong nuclear force and, consequently, the neutron cross-sections are not calculated, but measured [63]. Luckily enough, neutron experiments also allow the use of complex sample environment (as dilution cryostats) on an everyday basis. This is another reason for the necessity of employing neutron scattering in this work.

Before we get more into the particularities of neutron scattering, we examine some generalities of the physics surrounding neutrons. The maximum energy of the neutrons employed in scattering techniques is between $1 - 100$ eV, far from the relativistic regime [60, 61]. Those neutrons have an energy

$$E = \frac{m_n v^2}{2}, \tag{2.1}$$

where $m_n = 1.6749 \times 10^{-27}$ kg is the neutron mass and $\boldsymbol{v}$ is its velocity. SI units are not ideal in this situation, and from now on, neutrons are going to be defined either by their energy, in meV, or by their wavelength λ, given by the *de Broglie relation* [60, 61]

$$\lambda = \frac{h}{m_n \boldsymbol{v}}, \tag{2.2}$$

where h is the Planck constant. The neutron wave vector $\boldsymbol{k}$ has the direction of $\boldsymbol{v}$ and magnitude [60, 61]

$$\boldsymbol{k} = \frac{2\pi}{\lambda}. \tag{2.3}$$

In a scattering experiment, one is measuring the probability, within a solid angle $d\Omega$, that a neutron with incident $\boldsymbol{k}$ is scattered with a wave vector $\boldsymbol{k'}$. A schematic displaying the scattering

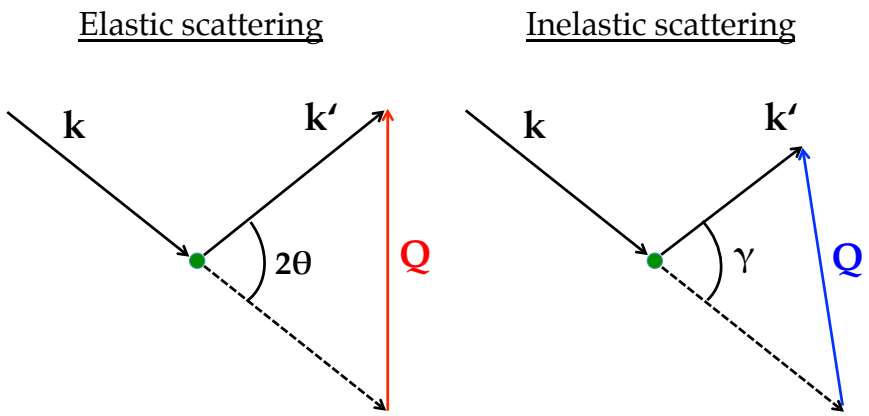

Figure 2.1: Schematic of a generic scattering process. $\boldsymbol{k}$ denotes the wave vector of the incident neutron scattered by a point nucleus. The wave vector of the scattered neutron is $\boldsymbol{k'}$.

process is shown in Figure 2.1. When a neutron "hits" an atom in the material, two processes may occur: either it is scattered with final energy equal to its incident energy ($k = k'$), or an energy transfer between neutron and system occurs. The first process is defined as *elastic scattering*, or *diffraction*, while the second is called *inelastic scattering*. In both situations, the *momentum transfer* $\boldsymbol{Q}$, or *scattering vector* is defined as [60,61]

$$\boldsymbol{Q} = \boldsymbol{k} - \boldsymbol{k'}. \tag{2.4}$$

The cosine rule yields, for the triangles of Figure 2.1,

$$Q^2 = k^2 + k'^2 - 2kk'cos(2\theta), \tag{2.5}$$

where 2θ can be replaced by γ, depending on the scattering process. Assuming the diffraction condition is satisfied and substituting Equations (2.3) and (2.4) in (2.5), we obtain

$$Q = \frac{4\pi}{\lambda}\sin(\theta). \tag{2.6}$$

Below, in parallel with some basic definitions of a crystallographic system and the conditions for elastic and inelastic scattering in condensed matter, we are going to develop briefly some fundamental principles of the neutron scattering theory.

2.2 Elementar scattering theory of neutrons

It was Léon van Hove that, in a work published in 1954, generalised the theory of scattering to be also applicable to neutrons [64]. He started by noting the two prerequisites for the validity of the Born-Oppenheimer approximation of the differential scattering cross-section:

(i) The initial state of the system is pure and not changed by the scattering process → in other words, this describes the elastic scattering.

(ii) The energy transfer occurring in the scattering process is negligible compared to the energy of the scattered probe → this is the so-called *static approximation* [60,61].

It is not difficult to see that, simply as stated above, the condition (ii) does not apply to inelastic neutron scattering. For a given wavelength, neutrons have energies comparable to the energy of elementary excitations of matter. This is, *inter alia*, one of the strengths of the technique.

The generalisation conceived by Van Hove, an the solution to the problem, was to extend the concept of *static pair-distribution function* $g(\boldsymbol{r})$, which describes the correlation between a particle of position $\boldsymbol{r'}+\boldsymbol{r}$ with a particle at the position $\boldsymbol{r'}$. The neutron cross-section should thus be expressible in terms of a *generalised pair-distribution function* $G(\boldsymbol{r},t)$, which now is also a function of time. Instead of describing only spatial correlations, $G(\boldsymbol{r},t)$ connects the particle at a position $\boldsymbol{r'}+\boldsymbol{r}$ at a time $t'+t$ with a particle at a position $\boldsymbol{r'}$ at a time t'. Note that this correlation is not determined only between pairs of particles, but also for single particles that, for example, moved a distance $\boldsymbol{r}$ in a time t (self-correlation).

The neutron scattering cross-section is defined as the number of neutrons scattered per second into a solid angle $d\Omega$ with energy transfer between $\hbar\omega$ and $\hbar(\omega+d\omega)$ [61, 65]. We imagine a system S in an initial state $|\lambda\rangle$ with energy E_λ and thermal population probability $\frac{1}{Z}\exp(-E_\lambda/k_\mathrm{B}T)$, where k_B is the Boltzmann constant, T is the temperature and Z is the partition function. Starting from the Fermi's golden rule, it can be shown that [61]

$$\frac{d^2\sigma}{d\Omega\, d\omega}=\left(\frac{m_n}{2\pi\hbar^2}\right)^2\frac{k'}{k}\sum_{\lambda',\boldsymbol{\sigma'}}\sum_{\lambda,\boldsymbol{\sigma}}p_\lambda p_\sigma|\langle\boldsymbol{k'},\boldsymbol{\sigma'},\lambda'|\boldsymbol{U}|\boldsymbol{k},\boldsymbol{\sigma},\lambda\rangle|^2\delta(\hbar\omega+E_\lambda-E_{\lambda'}). \tag{2.7}$$

After the scattering, the system is in a state $|\lambda'\rangle$ with energy $E_{\lambda'}$. The terms $\boldsymbol{\sigma}$ and $\boldsymbol{\sigma'}$ are the spin polarisability of the incoming and scattered neutrons and p_σ is the polarisation probability. $\boldsymbol{U}$ is the interaction operator, which depends on the specific scattering process. If we consider elastic scattering by a nuclei at a fixed position $\boldsymbol{r}_j$, the interaction operator takes the form of the *Fermi pseudopotential* [60, 61]

$$\boldsymbol{U}(\boldsymbol{r})=\frac{2\pi\hbar^2}{m_n}\sum_j b_j\delta(\boldsymbol{r}-\boldsymbol{r}_j), \tag{2.8}$$

where b_j is the scattering length of an isotope j. If one describes the incoming and outgoing neutron as plane waves, the matrix elements of $\boldsymbol{U}(\boldsymbol{r})$ are

$$\langle\boldsymbol{k'},\lambda'|\boldsymbol{U}(\boldsymbol{r})|\boldsymbol{k},\lambda\rangle=\left(\frac{2\pi\hbar^2}{m_n}\right)\langle\lambda'|\int d\boldsymbol{r}\, e^{-i\boldsymbol{k'}\cdot\boldsymbol{r}}\sum_j b_j\delta(\boldsymbol{r}-\boldsymbol{r}_j)\, e^{i\boldsymbol{k}\cdot\boldsymbol{r}}|\lambda\rangle, \tag{2.9}$$

which, after integration and substitution of $\boldsymbol{k}-\boldsymbol{k'}$ by $\boldsymbol{Q}$, becomes

$$\langle\boldsymbol{k'},\lambda'|\boldsymbol{U}(\boldsymbol{r})|\boldsymbol{k},\lambda\rangle=\left(\frac{2\pi\hbar^2}{m_n}\right)\langle\lambda'|\sum_j b_j\, e^{i\boldsymbol{Q}\cdot\boldsymbol{r}_j}|\lambda\rangle. \tag{2.10}$$

Inserting Equation (2.10) into Equation (2.7) and replacing the Schrödinger operator $e^{i\boldsymbol{Q}\cdot\boldsymbol{r}_j}$ by time dependent Heisenberg operators $e^{i\boldsymbol{Q}\cdot\boldsymbol{r}_j(t)}=e^{i\frac{\boldsymbol{H}t}{\hbar}}\,e^{i\boldsymbol{Q}\cdot\boldsymbol{r}_j}\,e^{-i\frac{\boldsymbol{H}t}{\hbar}}$, one finally obtains the cross-section,

$$\frac{d^2\sigma}{d\Omega\, d\omega}=\frac{1}{2\pi\hbar}\frac{k'}{k}\sum_{j,j'}b_j b_{j'}\int\langle e^{-i\boldsymbol{Q}\cdot\boldsymbol{r}_{j'}(0)}e^{i\boldsymbol{Q}\cdot\boldsymbol{r}_j(t)}\rangle e^{-i\omega t}\,dt. \tag{2.11}$$

Note that the operators $\boldsymbol{r}_j(0)$ and $\boldsymbol{r}_j(t)$ do not necessarily commute.

The integrand between brackets in Equation (2.11) is called *intermediate scattering pair-correlation function*

$$I(\boldsymbol{Q},t)=\frac{1}{N}\sum_{j,j'}\langle e^{i\boldsymbol{Q}\cdot\boldsymbol{r}_j(0)}e^{i\boldsymbol{Q}\cdot\boldsymbol{r}_j(t)}\rangle, \tag{2.12}$$

where N is the number of atoms in the system. The Fourier transform (in space) of Equation (2.12) returns the *space-time pair-correlation function* $G(\boldsymbol{r},t)$ as originally introduced by van Hove [64]. As the measurement occurs in the reciprocal space, most useful is the Fourier Transform of Equation (2.12) with respect to t, which yields

$$S(\boldsymbol{Q},\omega) = \frac{1}{2\pi\hbar}\int I(\boldsymbol{Q},t)e^{-i\omega t}\,dt. \tag{2.13}$$

This is the so-called neutron *dynamic structure factor*, which is directly related to Equation (2.11).

2.2.1 Coherent and incoherent scattering

Coming back to Equation (2.11), we have two cases to consider: $j = j'$ (self-correlation $G_s(\boldsymbol{r},t)$, see above) and $j \neq j'$ ($G_d(\boldsymbol{r},t)$). If

$$j = j', \qquad \langle b_j b_{j'}\rangle = \langle b_j b_j\rangle = \langle b^2\rangle. \tag{2.14}$$

On the other hand, if

$$j \neq j', \qquad \langle b_j b_{j'}\rangle = \langle b_j\rangle\langle b_{j'}\rangle = \langle b\rangle^2. \tag{2.15}$$

Equation (2.11) becomes then

$$\frac{d^2\sigma}{d\Omega\,d\omega} = N\frac{k'}{k}\int e^{-i\omega t}\,dt \int e^{i\boldsymbol{Q}\cdot\boldsymbol{r}}\,d\boldsymbol{r}\,(\langle b^2\rangle G_s(\boldsymbol{r},t) + \langle b\rangle^2 G_d(\boldsymbol{r},t)). \tag{2.16}$$

Assuming $G(\boldsymbol{r},t) = G_s(\boldsymbol{r},t) + G_d(\boldsymbol{r},t)$ and performing the Fourier transform in space, one can finally split the cross-section into two components:

$$\left(\frac{d^2\sigma}{d\Omega\,d\omega}\right)_{coh} = N\frac{k'}{k}\langle b\rangle^2 S_{coh}(\boldsymbol{Q},\omega), \tag{2.17}$$

and

$$\left(\frac{d^2\sigma}{d\Omega\,d\omega}\right)_{incoh} = N\frac{k'}{k}[\langle b^2\rangle - \langle b\rangle^2]S_{incoh}(\boldsymbol{Q},\omega). \tag{2.18}$$

Equations (2.17) and (2.18) show the origin of the coherent and incoherent scattering to which neutron techniques are sensitive. The incoherent cross-section

$$\sigma_{incoh} = 4\pi(\langle b^2\rangle - \langle b\rangle^2) \tag{2.19}$$

is a direct consequence of the disorder of scattering lengths in the sample.

Incoherent scattering can be separated into two types: nuclear and spin incoherent. The nuclear incoherent scattering results from the disordered distribution of scattering lengths from different isotopes [61]. The spin incoherent results from the presence of nuclear spins in the studied compound: once the nuclei also possess magnetic quantum number $I \neq 0$, the interacting system neutron + nucleus can be in a ortho (degeneracy $2I+2$) or a para (degeneracy $2I$) state, each having its own scattering length [61,65]. It is not difficult to see that, if a sample is composed mostly of one isotope with $I = 0$, as the isotopically enriched Sm-based pyrochlores, one expects that $\sigma_{incoh} \to 0$.

2.2.2 Elastic nuclear scattering

The elastic cross-section can be found by integrating Equation (2.11):

$$\frac{d\sigma}{d\Omega} = \int \frac{d^2\sigma}{d\Omega\, d\omega}\, d(\hbar\omega) = \sum_{j,j'} b_j b_{j'} \langle e^{-i\boldsymbol{Q}\cdot\boldsymbol{r}_{j'}} e^{i\boldsymbol{Q}\cdot\boldsymbol{r}_j} \rangle. \tag{2.20}$$

To simplify matters, we drop the operator formalism[1]. Considering again the conditions (2.14) and (2.15), we obtain [60, 61, 65]

$$\left(\frac{d\sigma}{d\Omega}\right)_{coh} = \langle b \rangle^2 \sum_{j,j'} e^{-i\boldsymbol{Q}\cdot(r_{j'} - r_j)} \tag{2.21}$$

and

$$\left(\frac{d\sigma}{d\Omega}\right)_{incoh} = N(\langle b^2 \rangle - \langle b \rangle^2) \tag{2.22}$$

The differential cross-section in Equation (2.21) caries a phase factor (the $e^{-i(\ldots)}$ term). Hence, coherent nuclear scattering carries with itself phase information and results from constructive interference of scattering from scattering pairs (correlations). The incoherent scattering, on the other hand, carries only information about scattering from single atoms and is proportional to N.

The Bragg's law, which is analogous to the Laue's diffraction condition, states that elastic scattering in a crystallographic lattice occurs whenever the momentum transfer vector $\boldsymbol{Q}$ is equal to one of the reciprocal lattice vectors $\boldsymbol{\tau}$ [62]. It is possible then to immediately identify the coherent elastic scattering as the Bragg scattering originating from the crystallographic lattice, which is a long-range ordered structure of atoms with translation symmetry, or, in other words, a *correlated* structure. The incoherent neutron scattering is present as an isotropic background underneath the Bragg peaks.

We focus on the Bragg scattering from now on. Assuming $\boldsymbol{r}_j = \boldsymbol{l}_j + \boldsymbol{d}_\alpha$, where $\boldsymbol{l}_j$ is the position vector of the j^{th} unit cell and $\boldsymbol{d}_\alpha$ is the position of the α^{th} atom belonging to the j^{th} unit cell, Equation (2.21) becomes

$$\left(\frac{d\sigma}{d\Omega}\right)_{coh} = N_0 \frac{(2\pi)^3}{\nu_0} \sum_{\tau} \sum_{\alpha,\alpha'} b_\alpha b_{\alpha'} e^{-i\boldsymbol{Q}\cdot(\boldsymbol{d}_{\alpha'} - \boldsymbol{d}_\alpha)} \delta(\boldsymbol{Q} - \boldsymbol{\tau}), \tag{2.23}$$

where N_0 is the number of unit cells, ν_0 is their volume and the Dirac delta expresses the Bragg condition.

There is a correction to be done in Equation (2.23), due to the assumption that $\boldsymbol{r}_j$ is not time dependent. An amplitude term equals to $e^{-2W_\alpha^{\alpha'}(Q)}$ has to be included in the cross-section is order to take into account the harmonic movement of the atoms around their equilibrium position. $e^{-2W_\alpha^{\alpha'}(Q)}$ is the momentum transfer dependent quantity called *Debye-Waller factor* [60, 61, 65]. Finally, we define the elastic coherent nuclear differential cross-section as

$$\left(\frac{d\sigma}{d\Omega}\right)_{coh} = N_0 \frac{(2\pi)^3}{\nu_0} \sum_{\tau} |S_\tau(\boldsymbol{Q})|^2 \delta(\boldsymbol{Q} - \boldsymbol{\tau}), \tag{2.24}$$

where $|S_\tau(\boldsymbol{Q})|^2 = \sum_{\alpha,\alpha'} b_\alpha b_{\alpha'} e^{-i\boldsymbol{Q}\cdot(\boldsymbol{d}_{\alpha'} - \boldsymbol{d}_\alpha)} e^{-2W_\alpha^{\alpha'}(Q)}$ is the lattice structure factor. Note that the incoherent cross-section in Equation (2.22) would also be dependent upon the Debye-Waller factor, once the formal calculation had been performed.

[1] The effect of the vibration of the atoms will be included below, without proof (see *Debye-Waller factor*).

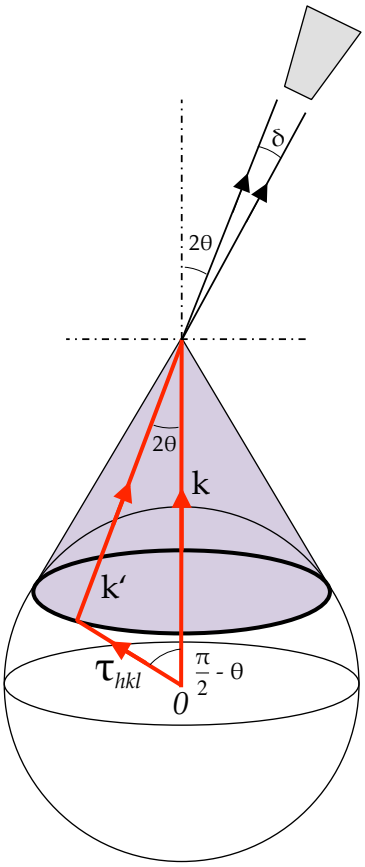

Figure 2.2: Experimental geometry of a powder diffraction experiment. The outer spherical shell represents the isotropic distribution of grains in a powder sample. For some fixed incident $\boldsymbol{k}$, some crystallites will be positioned so that the Bragg scattering condition is satisfied for a lattice vector $\boldsymbol{\tau}_{hkl}$. Instead of pointing in one direction, the scattering vectors $\boldsymbol{Q} = \boldsymbol{\tau}_{hkl}$ will draw a circumference in reciprocal space, the so-called Debye-Scherrer rings. The purple shaded area depicts the Debye-Scherrer cone spanned by the diffracted wave vectors $\boldsymbol{k'}$.

2.2.2.1 Structure determination: Rietveld refinemet

In an ideal powder sample, a large number of small crystallites are oriented randomly. This guarantees that, independently of the sample orientation, some crystallites will always satisfy the Bragg scattering condition for a fixed incident $\boldsymbol{k}$ [62]. This is represented in Figure 2.2, which shows the geometry of a powder diffraction experiment.

The distribution of grains in a powder sample is isotropic, and some of those have the correct orientation, relative to $\boldsymbol{k}$, to cause Bragg scattering. We suppose that, in this configuration, diffraction occurs for a particular scattering vector $\boldsymbol{Q} = \boldsymbol{\tau}_{hkl}$. Differently of what happens in a single crystal experiment, the scattering vector $\boldsymbol{Q}$ corresponding to the same $\boldsymbol{\tau}_{hkl}$ of all the crystallites does not point along one unique direction. Instead, every $\boldsymbol{Q}$ with terminating point lying on a ring of radius equal to $k'\sin(2\theta)$ satisfies the Bragg condition. This implies that, if, hypothetically, the detectors covered completely a two-dimensional area perpendicular to $\boldsymbol{k}$, the diffraction pattern would consist of *Debye-Scherrer rings*, each belonging to a reciprocal lattice plane of indexes h, k, l. Those rings define the base of cones (purple shaded area in Figure 2.2) spanned by all the wave vectors of modulus k'.

Clearly, in a real experiment the detector area is limited and, therefore, only a section of the Debye-Scherrer ring is accessed. This introduces an angular dependence on the measured intensities in the diffraction pattern. Moreover, one has to take into account the statistical distribution of crystallites, which causes a divergence in the scattered beam. This latter effect happens independently of the sample being single or polycrystalline, while the former occurs exclusively in powder diffraction. We start by defining mathematically the second one, which can be obtained by relaxing the Bragg condition in Equation (2.24) as follows:

$$\delta(\boldsymbol{Q}-\boldsymbol{\tau}) \rightarrow \int\int \delta(\boldsymbol{k}-\boldsymbol{k'}-\boldsymbol{\tau})d\boldsymbol{k'}d\theta = \frac{2}{k}\int \delta(Q^2-2kQ\sin\theta)d\theta. \tag{2.25}$$

Using the properties of the Dirac delta, one finds an angular dependence of the cross-section [62, 66]

$$\left(\frac{d\sigma}{d\Omega}\right)_{coh} \propto \frac{1}{\sin(2\theta)}. \tag{2.26}$$

There is still one correction left, which we consider now. The number of grains oriented to reflect in a given (h,k,l) position is proportional to the circumference of its respective Debye-Scherrer ring, which has, according to Figure 2.2, a radius $\boldsymbol{Q}_{hkl}\sin(\frac{\pi}{2}-\theta) \propto \cos(\theta)$. For each reflection with a different $\boldsymbol{Q}_{hkl}$, the detector sees ring sections of different lengths with a $\delta = constant$ angular coverage. The ring circumference is then $2\pi k'\sin(2\theta)$. Therefore the fraction of the Debye-Scherrer ring seen by the detector is $\delta/[2\pi k'\sin(2\theta)]$, which is proportional to $1/\sin(2\theta)$. Additionaly, for some crystal systems, different permutations of (h,k,l) may share the same ring, which adds a factor m_{hkl} in the cross-section of powder experiments, called *reflection multiplicity*. Including those corrections in Equation (2.26), derived before, we end up with [62]

$$\left(\frac{d\sigma}{d\Omega}\right)_{coh} \propto \frac{m_{hkl}\cos(\theta)}{\sin(2\theta)\sin(2\theta)} = \frac{m_{hkl}}{\sin(\theta)\sin(2\theta)}. \tag{2.27}$$

Equation (2.27) is known as *Lorentz factor*, which is a scattering angle dependent correction to the measured intensities in powder diffraction experiments.

The preceding analysis demonstrates that the information obtained from a powder experiment loses its three-dimensional character and, consequently, different directions in reciprocal space will have their contributions overlapped in the diffraction pattern. In addition to that, the data collected in an elastic scattering experiment are intrinsically limited. Since the only information accessed are intensities, the phase information contained in the structure factor [see Equation (2.24)] is lost. This is known as the *phase problem of crystallography* [67]. It is then said that a crystal structure cannot be determined, but rather estimated or refined, based on a guess or a previous knowledge of the characteristics of the compound. This process is called *structure refinement*.

The structure refinement of powder diffraction patterns has a special name after Hugo Rietveld, who created and first implemented the method in his work published in 1968 [68]. The aim of the method is to use the intensities of the entire profile to constrain or refine the parameters of a structural model. Initially, one assumes that the compound adopts one determinate structure, calculates its pattern and then compares it with the measured pattern. This process is repeated several times iteratively, while the model parameters are refined. The objective is to find the model that reproduces better the measured profile via a least squares fitting.

Usually, a structure refinement can be performed using computer softwares, like FullProf [69] or GSAS [70]. The parameters fitted in a Rietveld refinement can be many, and include instrumental dependent, as resolution/peak profile functions, and, the most important, sample

dependent parameters, like crystallographic lattice size and composition. More details about the fittings performed for each structure is given in the sessions where the data for our compounds is analysed.

2.2.3 Magnetic scattering

The calculation of the double differential cross-section [Equation (2.7)] for magnetic scattering is considerably more complicated than its nuclear counterpart. The neutron spin interacts with a magnetic field $\boldsymbol{H}$ associated with the magnetic moments of the unpaired electrons in the sample. The dipole-dipole interaction operator can be expressed as follows [65,71]:

$$\boldsymbol{U} = -\gamma\mu_N\boldsymbol{\sigma}\cdot\boldsymbol{H}, \tag{2.28}$$

where $\gamma = 1.91$ is the neutron gyromagnetic ratio, $\mu_\mathrm{N} = 5.05079\cdot10^{-27}$ J/T is the nuclear magneton, and $\boldsymbol{\sigma} = (\sigma_x, \sigma_y, \sigma_z)$ are the Pauli spin operators. The magnetic field associated with a single electron of spin $\boldsymbol{S}$ moving in an orbit with linear momentum $\boldsymbol{P}$ and located at a distance $\boldsymbol{R}$ from the neutron is [71]

$$\boldsymbol{H} = \boldsymbol{\nabla}\times\left(\frac{-2\mu_\mathrm{B}\boldsymbol{S}\times\boldsymbol{R}}{R^3}\right) - \frac{2\mu_\mathrm{B}\boldsymbol{P}\times\boldsymbol{R}}{\hbar R^3}. \tag{2.29}$$

The calculation of the matrix elements of Equation (2.28) is long and cumbersome and will not be reproduced here. Instead, we define the final form of the magnetic interaction operator as [65]

$$\boldsymbol{U} = \gamma\frac{e^2}{2m_e}\boldsymbol{\sigma}\cdot\boldsymbol{M}_\perp(\boldsymbol{Q}), \tag{2.30}$$

where e, m_e are the electron charge and mass, respectively. In Equation (2.30), $\boldsymbol{M}(\boldsymbol{Q})$ is the Fourier transform of the total magnetisation density of a magnetic ion. The subscript symbol $\perp$ means that the neutrons give access only to the perpendicular component of $\boldsymbol{M}(\boldsymbol{Q})$ relative to the scattering vector $\boldsymbol{Q}$. This property allows one to determine the directions of the magnetisation in the sample being measured.

Equation (2.30) is general and the form of $\boldsymbol{M}(\boldsymbol{Q})$ depends on the particular system being studied. For $4f$-electron compounds, which are subject to strong spin-orbit coupling, the right hand side of Equation (2.30) can be expressed as [65,71]

$$\boldsymbol{U} = -g_J f(\boldsymbol{Q})\boldsymbol{J}_\perp\cdot\boldsymbol{\sigma}, \tag{2.31}$$

where $\boldsymbol{J}_\perp$ is the *total* magnetic moment operator projected along the directions perpendicular to $\boldsymbol{Q}$. The term $f(\boldsymbol{Q})$ is the *magnetic form-factor* of the magnetic ion, which gives the Fourier transform of the normalised spin density at the magnetic site and, unlike the neutron scattering lengths, can be calculated rigorously [71,72]. The form-factor squared of most rare-earths is a function that decays with the increase in momentum transfer. The Sm^{3+} ion is an exception and its $f(\boldsymbol{Q})$ is going to be considered in Chapter 4.

Finally, the double differential magnetic cross-section can be shown to be [65]

$$\frac{d^2\sigma}{d\Omega\, d\omega} = \left(\frac{\gamma e^2}{m_e c^2}\right)^2\frac{k'}{k}e^{-2W(Q)}f^2(\boldsymbol{Q})\sum_{\alpha,\beta}\left(\delta_{\alpha,\beta} - \frac{Q_\alpha Q_\beta}{Q^2}\right)S^{\alpha\beta}(\boldsymbol{Q},\omega). \tag{2.32}$$

The *magnetic dynamic structure factor* $S^{\alpha\beta}(\boldsymbol{Q},\omega)$ is the quantity directly accessed by a neutron experiment. Instead of developing the operator formalism behind the explicit form of $S^{\alpha\beta}(\boldsymbol{Q},\omega)$,

it is more interesting to consider the relation between the dynamic structure factor and the generalised susceptibility $\chi^{\alpha\beta}(\boldsymbol{Q},\omega)$, given by the *fluctuation-dissipation* theorem [71,73,74]:

$$S^{\alpha\beta}(\boldsymbol{Q},\omega) = \frac{N\hbar}{\pi}\left(1 - e^{-\frac{\hbar\omega}{k_B T}}\right)^{-1} \mathrm{Im}\left[\chi^{\alpha\beta}(\boldsymbol{Q},\omega)\right], \tag{2.33}$$

where N is the number of magnetic atoms. Equation (2.33) indicates that the neutron can be understood as a microscopic magnetic probe which establishes a frequency and wave vector dependent magnetic field $H^{\beta}(\boldsymbol{Q},\omega)$ in the sample and measures a response $M^{\alpha}(\boldsymbol{Q},\omega)$ to it. The proportionality constant between the two is the generalised magnetic susceptibility tensor $\chi^{\alpha\beta}(\boldsymbol{Q},\omega)$. This property will be fundamental in the analysis performed in the inelastic data of the pyrochlore compound $Yb_2Ti_2O_7$, presented in Chapter 7.

2.2.3.1 Elastic magnetic scattering

The magnetic elastic cross-section can be expressed as [65]

$$\left(\frac{d\sigma}{d\Omega}\right)_{coh} = N_0\frac{(2\pi)^3}{v_0}\sum_{\tau}|\boldsymbol{S}_{M\perp}(\boldsymbol{Q})|^2\delta(\boldsymbol{Q}-\boldsymbol{\tau}) \tag{2.34}$$

where the magnetic structure factor $\boldsymbol{S}_{M\perp}(\boldsymbol{Q})$, differently from the nuclear $S_{\tau}(\boldsymbol{Q})$, has a vectorial character. In analogy with the nuclear elastic scattering, coherent magnetic neutron scattering will occur when the sample presents some kind of magnetic ordering, i.e. only when a system starts to develop magnetic correlations, usually at lower temperatures. Deep into the paramagnetic phase, the sample disordered magnetic moments will be another source of incoherent scattering.

Before defining $\boldsymbol{S}_{M\perp}(\boldsymbol{Q})$, we note that in Equation (2.34) it is assumed that the magnetic unit cell is identical to the crystallographic unit cell. However, this is in general not the case, and the magnetic unit cell may have a space group and a lattice parameter of its own. A small modification has thus to be introduced in Equation (2.34), which will become

$$\left(\frac{d\sigma}{d\Omega}\right)_{coh} = N_0\frac{(2\pi)^3}{v_0}\sum_{\tau}\sum_{k}|\boldsymbol{S}_{M\perp}(\boldsymbol{Q})|^2\delta(\boldsymbol{Q}-\boldsymbol{k}-\boldsymbol{\tau}), \tag{2.35}$$

where we define finally the magnetic structure factor as

$$\boldsymbol{S}_{M\perp}(\boldsymbol{Q}) = f(\boldsymbol{Q})\sum_{j}\boldsymbol{m}_{\boldsymbol{k},j}\, e^{i\boldsymbol{Q}\cdot\boldsymbol{r}_j}\, e^{-2W(\boldsymbol{Q})}. \tag{2.36}$$

In Equations (2.35) and (2.36), it is implicit that

$$\boldsymbol{m}_{l,j} = \sum_{\boldsymbol{k}}\boldsymbol{m}_{\boldsymbol{k},j}e^{-i\boldsymbol{k}\cdot\boldsymbol{R}_l}, \tag{2.37}$$

which represents the Fourier expansion of the magnetic moment distribution of an atom l located at a position $\boldsymbol{R}_l$ in the j^{th} unit cell with coefficients $\boldsymbol{m}_{\boldsymbol{k},j}$. In short, inside each Brillouin zone of the nuclear unit cell, there will be as many superlattice magnetic Bragg peaks as there are distinct wave vectors $\boldsymbol{k}$, each of those being located in a reciprocal point defined by $\boldsymbol{Q} = \boldsymbol{\tau} + \boldsymbol{k}$.

After neutron diffraction, one has to identify the magnetic structure of the sample from the measured magnetic Bragg peaks. It is important to note that a scattering experiment accesses only $\boldsymbol{m}_{\boldsymbol{k},j}$, and not the actual magnetic moment distribution $\boldsymbol{m}_{l,j}$. In this regard, the magnetic structure determination suffers from the same phase problem as the nuclear

structure determination, since the relative phase between the Fourier components cannot be measured. The absolute magnetic moments and their orientations have thus to be refined from a model magnetic structure. The most used method to choose the appropriate one is known as *representation analysis*. The representation analysis is extensively examined in the literature [75–77] and will be discussed here only in general lines in the next subsection.

The first step is to identify the so-called propagation vector $\boldsymbol{k}$ of the magnetic structure. This can be done by indexing the magnetic Bragg peaks present in the diffraction pattern. For example, when the magnetic and structural peaks coincide, the slightly modified Bragg condition of Equation (2.35) implies

$$\boldsymbol{Q} = \boldsymbol{\tau} + \boldsymbol{k} = \boldsymbol{\tau} \qquad \rightarrow \qquad \boldsymbol{k} = 0. \tag{2.38}$$

In many situations, the determination of the propagation vector is the most difficult step of the magnetic structure refinement, because the magnetic order developed in a compound may be described by more than one $\boldsymbol{k}$. Fortunately, all the pyrochlores studied in this work have a magnetic structure characterised by a single, commensurate propagation vector $\boldsymbol{k} = 0$.

After this step, group theoretical considerations can be used to find the symmetry allowed magnetic space groups for a given crystallographic group $\mathbf{G_0}$ [75,76,78]. The representation analysis method is based on the fact that *any* magnetic structure can be directly described by the basis vectors ψ_ν associated with the irreducible representation Γ_ν of a magnetic space group $\mathbf{G}_k$ [75]. Next, we explain what this means in practice.

2.2.3.2 Magnetic structure identification: representation analysis

A space group $\mathbf{G_0}$ is characterised by a set of symmetry elements. Those elements that, applied to $\boldsymbol{k}$, leave the propagation vector invariant, form a subgroup of $\mathbf{G_0}$, called the little group $\mathbf{G_k}$. The *representations* of $\mathbf{G_k}$ are a set of matrices that describe mathematically how the magnetic moments transform under the elements of the little group. The representations can be transformed in a set of ortogonal *irreducible representations* (IR), a procedure equivalent to the reduction of the representations into block-diagonal matrices.

We consider the effect of the elements of the $Fd\bar{3}m$ space group on the $\boldsymbol{k} = 0$ propagation vector. The magnetic site is the 16*d* Wyckoff position, and the unit cell contains in total four magnetic atoms. The decomposition of the representation $\Gamma(\mathbf{G_k})$ into irreducible representations Γ_ν can be shown to be [79]

$$\Gamma(\mathbf{G_k}) = 1\Gamma_3^{(1)} + 1\Gamma_5^{(2)} + 1\Gamma_7^{(3)} + 2\Gamma_9^{(3)} \tag{2.39}$$

The numeral in front of each term represents the number of times that an IR appears in the decomposition, while the superscripts indicate the IR dimension. Importantly, these quantities give explicitly one information: each irreducible representation will be composed of as many basis vectors as the product of times the IR appears in the decomposition multiplied by its dimension. Therefore, 1, 2, 3 and 6 ortogonal basis vectors should belong to $\Gamma_3, \Gamma_5, \Gamma_7$ and Γ_9, respectively.

The calculation of the basis vectors $\psi_{\nu,\alpha}$ for each Γ_ν is performed with the projector operator formula [78] and involves mostly linear algebra [76,78]. For this reason, the determination of $\mathbf{G_k}$ and their corresponding Γ_ν is performed using computer programs, like SARA*h* [77] or BASIREPS [80]. In Table 2.1 the possible IR's and their respective $\psi_{\nu,\alpha}$, calculated using the latter software for the $Fd\bar{3}m$ space group and the $\boldsymbol{k} = 0$ propagation vector, are shown. Some long-range ordered magnetic structures corresponding to the different Γ_ν are shown for one tetrahedron unit in Figure 2.3.

Γ_ν	$\psi_{\nu,\alpha}$	Atom 1			Atom 2			Atom 3			Atom 4		
		m_x	m_y	m_z	m_x	m_y	m_z	m_x	m_y	m_z	m_x	m_y	m_z
Γ_3	$\psi_{3,1}$	1	1	1	−1	−1	1	−1	1	−1	1	−1	−1
Γ_5	$\psi_{5,1}$	1	$-e^{i\frac{\pi}{3}}$	$e^{i\frac{2\pi}{3}}$	−1	$e^{i\frac{\pi}{3}}$	$e^{i\frac{2\pi}{3}}$	−1	$-e^{i\frac{\pi}{3}}$	$-e^{i\frac{2\pi}{3}}$	1	$e^{i\frac{\pi}{3}}$	$-e^{i\frac{2\pi}{3}}$
	$\psi_{5,2}$	$e^{i\frac{\pi}{3}}$	−1	$-e^{i\frac{2\pi}{3}}$	$-e^{i\frac{\pi}{3}}$	1	$-e^{i\frac{2\pi}{3}}$	$-e^{i\frac{\pi}{3}}$	−1	$e^{i\frac{2\pi}{3}}$	$e^{i\frac{\pi}{3}}$	1	$e^{i\frac{2\pi}{3}}$
Γ_7	$\psi_{7,1}$	1	−1	0	−1	1	0	1	1	0	−1	−1	0
	$\psi_{7,2}$	0	1	−1	0	1	1	0	−1	−1	0	−1	1
	$\psi_{7,3}$	−1	0	1	−1	0	−1	1	0	−1	1	0	1
Γ_9	$\psi_{9,1}$	1	1	0	−1	−1	0	1	−1	0	−1	1	0
	$\psi_{9,2}$	0	0	1	0	0	1	0	0	1	0	0	1
	$\psi_{9,3}$	0	1	1	0	1	−1	0	−1	1	0	−1	−1
	$\psi_{9,4}$	1	0	0	1	0	0	1	0	0	1	0	0
	$\psi_{9,5}$	1	0	1	1	0	−1	−1	0	−1	−1	0	1
	$\psi_{9,6}$	0	1	0	0	1	0	0	1	0	0	1	0

Table 2.1: Basis vectors $\psi_{\nu,\alpha}$ belonging to the four irreducible representations Γ_ν calculated by BASIREPS [80] using the symmetry elements of the $Fd\bar{3}m$ space group for a propagation vector $\boldsymbol{k} = 0$.

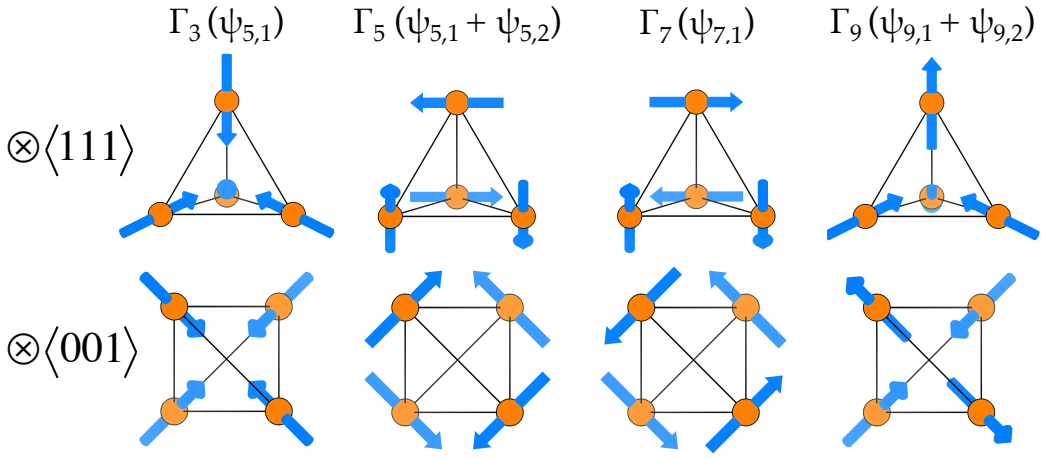

Figure 2.3: Most common magnetic structures adopted by pyrochlore compounds and their different irreducible representations. The structure represented by Γ_3 is the so called *all-in-all-out* arrangement. On the centre, two examples of XY structures. On the right, one example (*two-in-two-out* arrangement) of the lowest symmetry structures given by the basis vectors of Γ_9.

Finally, the coefficients of the Fourier expansion of Equation (2.37) can be expressed as a linear combinations of the basis vectors of a particular irreducible representation as follows:

$$\boldsymbol{m}_{\boldsymbol{k}=\boldsymbol{0}} = \boldsymbol{\Psi}_\nu = \sum_\alpha C_\alpha \psi_{\nu,\alpha}. \tag{2.40}$$

For simplicity, we drop the index j of the unit cell. The C_α denote the magnitude of the magnetic moment along the crystallographic axis x, y, z, and have their value refined based on the magnetic peak intensities. Since the structure factor is usually measured in arbitrary units,

the actual value of the coefficients C_α are scaled based on the nuclear structure factor. Therefore, without the measurement of the pure structural scattering, which can be accomplished in the paramagnetic state, the absolute values of the magnetic moment in powder samples cannot be determined.

2.2.4 Polarised neutrons

So far, we have neglected the initial σ and final σ' spin polarisability of the scattered neutrons in the calculation of the matrix elements in Equation (2.7). The complete form of the interaction potential is [61,65]

$$\boldsymbol{U} = \boldsymbol{b} + A\boldsymbol{I}\cdot\sigma + B\boldsymbol{M}\cdot\sigma, \tag{2.41}$$

where we introduced the interaction of the neutrons with the nuclear spins, given by $\boldsymbol{I}$. The coefficients A and B absorb the constant terms in front of the dot products [see Equation (2.30)] and $\boldsymbol{b}$ represents Equation (2.8).

Due to the orthogonality between momentum and spin states of the neutron, the matrix elements of the interaction potential can be factorised as

$$\langle \boldsymbol{k}', \sigma', \lambda' | \boldsymbol{U} | \boldsymbol{k}, \sigma, \lambda \rangle = \langle \boldsymbol{k}', \lambda' | \boldsymbol{U} | \boldsymbol{k}, \lambda \rangle \langle \sigma' | \boldsymbol{U} | \sigma \rangle. \tag{2.42}$$

We assume $|\sigma\rangle = |+\rangle, |-\rangle$. In this basis,

$$\langle \pm | \boldsymbol{U}_z | \pm \rangle = b \pm AI_z \pm BM_z, \quad \langle \pm | \boldsymbol{U}_z | \mp \rangle = 0, \tag{2.43}$$

and

$$\langle \pm | \boldsymbol{U}_\pm | \pm \rangle = 0, \quad \langle \pm | \boldsymbol{U}_\pm | \mp \rangle = AI_\pm + BM_\pm. \tag{2.44}$$

where, for a generic operator $\boldsymbol{O}$, $\langle \pm | \boldsymbol{O}_\pm \cdot \sigma | \pm \rangle = 0$, $\langle \pm | \boldsymbol{O}_\pm \cdot \sigma | \mp \rangle = O_\pm$ and $\langle \pm | \boldsymbol{O}_z \cdot \sigma | \pm \rangle = \pm O_z$.

The important information given by Equations (2.43) and (2.44) is that a spin-flip (change of the neutron polarisation from a state $|\pm\rangle$ to a state $|\mp\rangle$) only occurs when the direction of the magnetisation $\boldsymbol{M}$ is perpendicular to the neutron initial polarisation σ. This is the physical mechanism that allows one to determine the direction of the sample magnetisation measuring spin-flip and non-spin-flip scattering, as long as the initial neutron polarisation is known.

The cross-section depends upon the square of those matrix elements. Assuming scattering in the absence of electronic magnetism ($\langle \boldsymbol{M} \rangle = 0$) and disordered nuclear spins ($\langle \boldsymbol{I}_x \rangle = \langle \boldsymbol{I}_y \rangle = \langle \boldsymbol{I}_z \rangle = 0$), the coherent scattering will be proportional to

$$\langle + | \boldsymbol{U} | + \rangle = \langle - | \boldsymbol{U} | - \rangle = \langle b \rangle^2 \quad \text{and} \quad \langle + | \boldsymbol{U} | - \rangle = \langle - | \boldsymbol{U} | + \rangle = 0. \tag{2.45}$$

Equation (2.45) implies that nuclear coherent scattering does not involve a spin-flip. The estimation of the incoherent scattering involves the determination of the matrix elements

$$\begin{aligned} |\langle + | \boldsymbol{U}^2 | + \rangle| - |\langle + | \boldsymbol{U} | + \rangle^2| &= |\langle - | \boldsymbol{U}^2 | - \rangle| - |\langle - | \boldsymbol{U} | - \rangle^2| \\ &= \langle b^2 \rangle - \langle b \rangle^2 + \tfrac{1}{3} A^2 I(I+1), \\ |\langle - | \boldsymbol{U}^2 | + \rangle| - |\langle - | \boldsymbol{U} | + \rangle^2| &= |\langle + | \boldsymbol{U}^2 | - \rangle|^2 - |\langle + | \boldsymbol{U} | - \rangle^2| \\ &= \tfrac{2}{3} A^2 I(I+1), \end{aligned} \tag{2.46}$$

where we use $\langle \boldsymbol{I}_x^2 \rangle = \langle \boldsymbol{I}_y^2 \rangle = \langle \boldsymbol{I}_z^2 \rangle = \frac{1}{3} A^2 I(I+1)$. Equation (2.46) demonstrates that nuclear incoherent scattering does not involve spin-flip as well. Additionally, if the sample is composed of one single isotope $\langle b^2 \rangle = \langle b \rangle^2$, the intensity in the spin-flip channel is twice the intensity of the non-spin-flip channel.

2.3 Neutron scattering techniques

2.3.1 Sources

There are two ways to produce neutrons for research. The first one is using a version of a fission reactor that optimises neutron flux and power density. The second is hitting an accelerated beam of charged particles against a target. Both methods are briefly explained below. Subsections 2.3.1.1 and 2.3.1.2 have their text based on References [65, 81].

2.3.1.1 Research reactors: continuos sources

This method is based on the self-sustaining and continuos fission reaction. This is how neutrons are produced in FRM II, in Garching. Research reactors, differently from nuclear power plants, use few kg of $> 90\%$ enriched U^{235} fuel elements (93% enriched in FRM II). Those sources are optimised to generate the highest power within a small volume.

While the chain reaction is sustained, neutrons are produced at a steady rate. That is why research reactors are called *continuous* sources. Once the neutrons leave the core, they must be slowed down by a heavy water (D_2O) moderator, either to be used for scattering or to feed back the chain reaction. Depending on the neutron wavelength desired for experiments, the particles can be further thermalised by the so-called cold or hot sources. In FRM II, the cold source is filled with liquid deuterium kept at a temperature of about 20 K, while the hot source is a graphite block heated mainly by the gamma radiation of the core.

Finally, the moderated neutrons are conducted out of the sources to the instruments. The spectral distribution of those neutrons follow a Maxwellian curve with a maximum value at the source/moderator temperature. The instruments are mostly connected to the sources through neutron guides, which are tubes that conduct the particles via total internal reflection. The neutron guides can be as long as 100 m and their use decreases dramatically the flux loss.

2.3.1.2 Spallation sources

The term *spallation* describes the succession of events taking place when nuclei are bombarded by high energy ($\sim$ GeV) charged particles, which are accelerated in synchrotrons in short (< 1 μs) bursts. The collisions transfer high amounts of energy to the nuclides of the specific target atoms. This process has two main consequences: either some of the nuclides, among them neutrons, escape from the target, or the nuclei are left in a highly excited state. The subsequent decay of the nuclei involves evaporation of neutrons, with spectral distribution similar to that of neutrons produced by fission. The neutrons that escaped previously from the target, however, have a much broader energy spectrum, which extends to energies close to that of the incident particles.

The target is surrounded by moderators, which reduce the energy of the spallation neutrons in order to have them used for experiments. Although they have the same purpose as those of the reactor sources, the moderators are differently designed to slow down the neutrons quickly and let them leak out. As a consequence, the moderation of spallation neutrons is incomplete and the neutron flux curve is significantly different from a Maxwellian distribution at the short wavelength limit. The considerable flux of higher energy neutrons is one of the particular differences between spallation and reactor sources and allows diffraction measurements to be made up to way higher momentum transfers in reciprocal space.

The pulsed sources produce bursts of 1 to 50 μs duration separated 10 to 100 ms apart, depending on the energy. As the release of spallation neutrons happens within 10^{-15} s after the nuclei were hit, the time length of the neutron beam is determined by the time distribution of

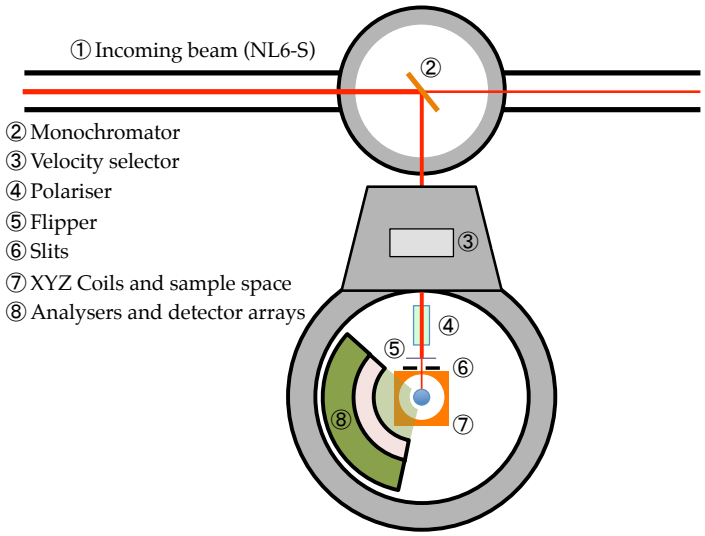

Figure 2.4: Schematic of DNS. Neutrons of incident $\lambda = 4.2$ Å are selected out from the cold source beam, and passes through a velocity selector, polariser and spin flipper before it interacts with the sample. The polarisation of the beam is kept constant by the XYZ-coils. After the scattering, only the neutrons with polarisation perpendicular to the scattering plane are detected.

the incident particles pulse. This has a second important implication: the experiments at pulsed neutron sources must be performed with time-of-flight (TOF) techniques.

2.3.2 DNS

Figure 2.4 shows a schematic draw of DNS. The instrument is the second at the neutron guide NL6-S of the research reactor FRM II. The neutrons come from the reactor cold source and the wavelength $\lambda = 4.2$ Å is selected by a pyrolytic graphite PG(002) monochromator. The velocity selector that follows the monochromator ensures that the incident beam is free from harmonics of the desired λ. After that, the beam passes by supermirror based polarisers, that select the incoming neutron polarisation perpendicular to the scattering plane, or z direction. In order to perform XYZ-polarisation analysis [82], the spin of the incident neutrons may be subject to a weak, perpendicular magnetic field generated by a π-flipper. This spin direction is kept constant by a guide-field generated by the XYZ-coils until immediately before the interaction with the sample. After the scattering, the neutron, in its way to the detector, passes though the spin analyser, which selects the neutron spin polarisation once more along the z axis [83].

DNS resolution and flux are optimised to measure diffuse scattering, i.e, elastic coherent scattering not necessarily in the form of Bragg peaks, using polarised neutrons. As DNS is an extremely versatile instrument, in this work it was mostly used to measure unpolarised neutron diffraction. Two reasons made us to opt for using unpolarised neutrons instead of performing the well known XYZ-polarisation analysis, technique which is one of the main motivations for the DNS design. In the Sm-based pyrochlores, the highest possible neutron flux was important in the magnetic structure determination (see Chapter 5). We verified that the use of the polariser represented a flux reduction of at least $2/3$ at the sample position. This amount of neutrons is indispensable for the measurement of extremely small magnetic moments. The other system studied, the pyrochlore $Yb_2Ti_2O_7$, presented in the last chapters, becomes ferromagnetic at $T_c = 280$ mK, while ferromagnetic correlations start to develop at

$T \sim 10T_C$. The net magnetisation in ferromagnetic materials depolarise the neutron beam and, in most cases, hinders the use of polarised neutrons in the analysis of their magnetic properties at temperatures close to and below the ordering transition.

2.3.3 Time-of-flight diffraction

In this work, we present diffraction data collected in both continuous and spallation sources. The information accessed is similar, but some differences in the experimental setup must be considered. The first of them is that in a time-of-flight experiment, the beam is not monochromatic, which is usually the *modus operandi* of a diffractometer at a continuos source (see DNS, for example). The second is the most obvious: in a TOF experiment the quantity being measured is the time t that the neutron takes to travel a given distance from the moderator until the sample and then from the sample until detector.

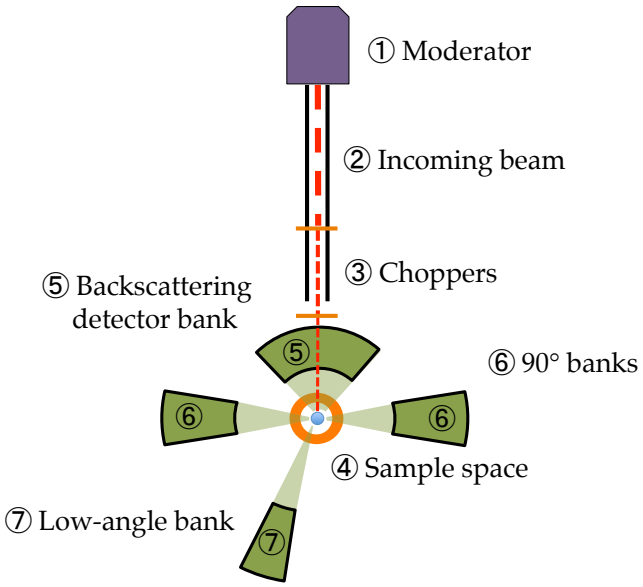

Figure 2.5: Schematic of the HRPD instrument. The neutron beam from the target passes by a moderator. In order to minimise the beam divergence, the neutron flight path from moderators until sample is $\sim$ 100 m. The frequency of the disc-choppers is selected in order to avoid overlapping between two different spallation bursts. The polychromatic beam reaches the sample and is detected at the highest resolution backscattering, intermediate resolution 90° and low resolution, low angle detector banks. The angular coverage of the detectors is exaggerated for clarity.

In Figure 2.5, we show a schematic of the HRPD instrument at ISIS. For a TOF experiment, the total flight path L of the neutron is precisely known. If the neutron has a velocity v before and after scattering, then [84]

$$L = vt. \tag{2.47}$$

The de Broglie relation (2.2) gives

$$m_n v = \frac{h}{\lambda}. \tag{2.48}$$

Combining Equations (2.47) and (2.48) with the Bragg formula (2.6), we obtain

$$t = L\frac{\lambda m_n}{h} = \frac{4\pi L m_n \sin(\theta)}{hQ}. \tag{2.49}$$

Making the substitution $Q = \frac{2\pi}{d}$, where d is the distance between successive lattice planes,

$$t[\mu s] = \frac{2m_n Ld\sin(\theta)}{h} \approx 505.56L[m]d[\text{Å}]\sin(\theta). \tag{2.50}$$

As a high resolution powder diffractometer, HRPD neutron guide is as long as it could be, around 100 m. Using Equation (2.49), we calculate that the time-of-flight of a neutron of wavelength 1 Å is of about 25 ms. At ISIS, the time between two bursts is of 20 ms [84]. Therefore, to avoid the overlap between two different pulses, two disc choppers (see Figure 2.5) are used to restrict the wavelength band. The time-of-flight window selected at HRPD runs between 30 and 130 μs.

The resolution in reciprocal space can be obtained by differentiating Equation (2.49),

$$\frac{\Delta d}{d} = \frac{\Delta t}{t} = \left[\left(\frac{\Delta L}{L}\right)^2 + (\Delta\theta)^2\cot^2(\theta)\right]^{\frac{1}{2}}. \tag{2.51}$$

Equation (2.51) demonstrates that the resolution depends on the angular divergence of the beam, which is mitigated by increasing the flight path of the neutron. Moreover, it is clear that the maximum resolution is obtained when the detector is positioned close to the backscattering position, for which $\theta = 180^\circ$. The highest resolution detector of HRPD is, therefore, the backscattering bank. The 90° banks have intermediate resolution but a broader momentum transfer coverage. The low angle bank has low resolution, but covers low momentum transfers, which are important mainly for observation of magnetic elastic scattering.

It is also evident that the resolution is independent of Q, a behaviour that contrasts with the continuous sources diffractometers [84]. Other differences are the characteristic peak shapes, which depend on the moderator neutron flux, and the Lorentz factor L, which should be recalculated for polychromatic beams [66]. For TOF diffraction,

$$L = d^4\sin(\theta). \tag{2.52}$$

The TOF diffractometer WISH, at ISIS, was also used by us. WISH was designed primarily for powder diffraction, and accesses a broader momentum transfer range with better resolution at low angles, comparing with HRPD. The instrument detector system consists of two arrays of detectors with an angular coverage of 10° to 170° and 190° to 350°, without gaps [85].

2.3.4 Time-of-flight spectroscopy

Most of the spectroscopic work in this thesis was performed at spallation sources. The schematic of an inelastic neutron scattering experiment is shown in Figure 2.6. Two configurations are possible, the direct and the indirect geometry. We detail the difference between both below.

In an inelastic scattering experiment, the energy transfer is given by

$$\Delta E = E_0 - E, \tag{2.53}$$

where E_0 and E are the neutron initial and final energies, respectively. In order to determine ΔE, the energy transfer has to be expressed as a function of time-of-flight. We split the total L in primary flight path L_1, from moderator to sample, and secondary flight path L_2, from sample until detector. According to Equations (2.1) and (2.47), the energy transfer is

$$\Delta E = \frac{1}{2}m_n\left[\left(\frac{L_1}{t-t_2}\right)^2 - \left(\frac{L_2}{t_2}\right)^2\right], \tag{2.54}$$

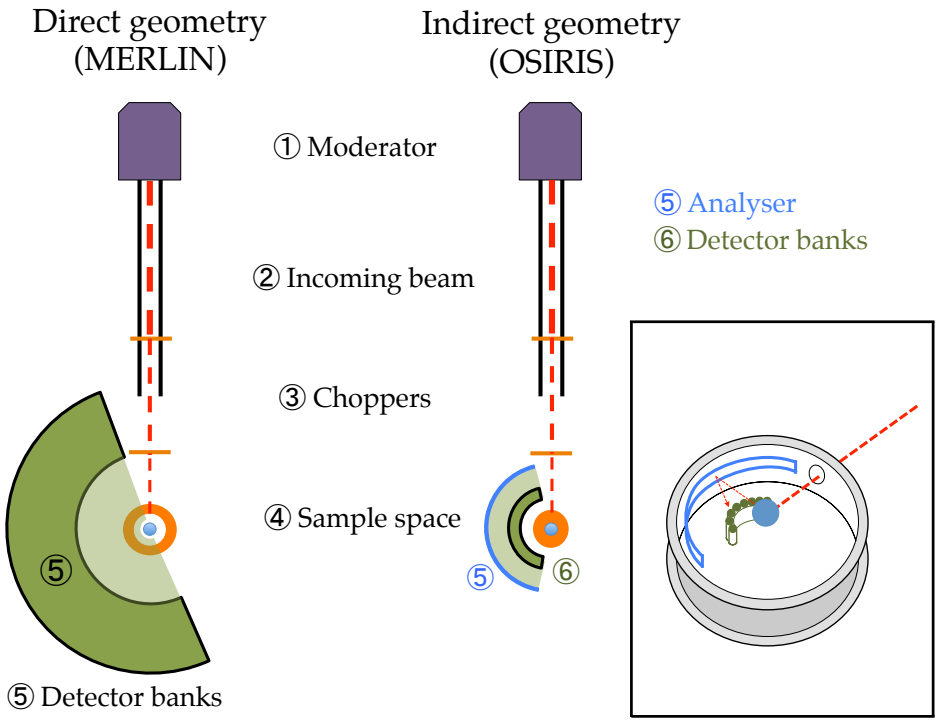

Figure 2.6: Schematic of the experimental configuration of direct and indirect geometry time-of-flight spectrometers used in this work. Note that the choppers in both instruments have different functions, which is detailed in the text. In a direct geometry instrument, a neutron beam with a single energy E_0 hits the sample and is scattered in the detectors direction. In the indirect geometry, a polychromatic beam is scattered by the sample in an array of analysers, that select an unique final energy E to be detected.

where we consider that the neutron travels a distance L_2 at a time t_2 and L_1 at a time $t - t_2$. Those times are the quantities measured and the distances are precisely known.

In a direct geometry spectrometer, as MERLIN [86], the incident energy is selected by a Fermi chopper prior to the scattering. The final energy is estimated based on the time-of-flight t_2 from sample to detector. In the indirect geometry instruments [87], on the other hand, the beam leaves the moderator, passes by the disk choppers, which have the function of avoiding frame overlap, and hits the sample. The scattered neutrons reach the single crystal analyser and only the neutrons with a specific final energy (1.845 meV in OSIRIS) are scattered back to the detectors positioned 175° below the horizontal plane. This experimental arrangement is illustrated in the inset of Figure 2.6.

Overall, MERLIN and OSIRIS are very different instruments. MERLIN is connected to a Gd poisoned water moderator. The best flux is reached for neutrons of incident energy $\sim$ 50 meV [86]. The instrument is therefore optimised to measure high energy processes, as phonons or crystal field excitations, offering an intermediate resolution. OSIRIS is a cold-neutrons instrument connected to a liquid H moderator cooled down to 25 K [88]. The energy resolution (FWHM) at the elastic line is of $\sim$ 25 μeV, which makes OSIRIS perfect for the studies of low energy excitations in condensed matter [88]. In the chapters that follow, more details about the use of the aforementioned instruments in the study of pyrochlore magnets will be given.

2.4 Muon spin relaxation (μSR)

Muon spin relaxation (rotation or resonance) is, unlike neutron scattering, an implantation technique. Positive charged muons, of energies ranging from 4 to 100 MeV are implanted into the material to be studied. From this moment on, those muons lose quickly, in about one picosecond, their energy via interactions (ionisation and scattering) mainly with the sample electrons [89,90]. Since the interactions are mostly of Coulombic origin, the initial spin direction of the muon is preserved with minimum depolarisation [89,90].

In its inertial reference frame, muons decay in one positron and two different neutrinos with a lifetime of 2.2 μs. The decay process violates parity: in simple words, the positron is emitted predominantly along the direction of the muon spin immediately before it decayed. This is the crucial characteristic that allows the application of muons in studies of magnetism in condensed matter systems. By monitoring the direction of the positron emission for sufficient long times, one can follow the muon spin precession at the particular site it has finally stopped [89,90].

We show a schematic of a μSR experiment in Figure 2.7. The apparatus contains the source, which is the very same proton synchrotron accelerator of spallation neutron sources, and two detectors, which we call L (left) and R (right). A muon with spin aligned antiparallel to its momentum, i.e., pointing along the direction from which the particle came, is implanted in the sample. When subject to a magnetic field $\boldsymbol{B}_{loc}$, as much as any other particle of spin different of zero, the muon spin precesses with a frequency $\omega_\mu = \gamma_\mu B_{loc}$, where $\gamma_\mu = 2\pi \times 0.01355\,\mathrm{MHz/G}$ is the muon gyromagnetic ratio. If the muon decays before it completes a $\pi/2$ rotation, within the detector arrangement we devised in Figure 2.7, the positron emerging from it will not be detected. Whenever the muon precesses $\pi/2$ or π before it decays, it will be detected by one of the two L or R detectors [91,92].

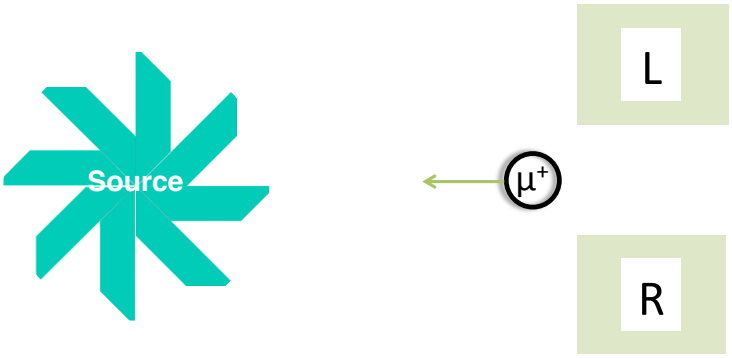

Figure 2.7: Schematic of a μSR experiment. The muons travel from the source with the spin pointing along the opposite direction of its momentum, to be detected by either the L or R detectors.

The local field $\boldsymbol{B}_{loc}$ experienced by the muon is not unique, but a vectorial sum of many different contributions. For insulators, it can be expressed as [91]

$$\boldsymbol{B}_{loc} = \boldsymbol{B}_{dip} + \boldsymbol{B}_{dem} + \boldsymbol{B}_{ext} + \boldsymbol{B}_{I}, \tag{2.55}$$

where $\boldsymbol{B}_{dip}$ is the dipolar field resulting from the interaction with the electronic spins, $\boldsymbol{B}_{dem}$ is the demagnetisation fields (important for single crystals) and $\boldsymbol{B}_{ext}$ is the external field applied

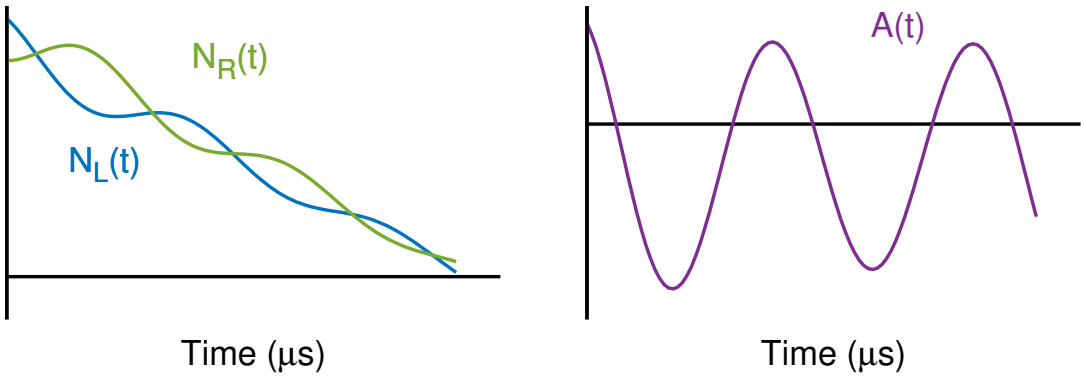

Figure 2.8: Expected asymmetry measured at high applied transverse fields. The positrons resulting from the muon decay are detected in one of the L and R detectors for a given time t, as shown in the left. Using Equation (5.1), one obtains the quantity of interest, the asymmetry $A(t)$ (right).

to the sample. The muon also interacts with the magnetic moment generated by the nuclear spins, which is taken into account in Equation (2.55) by the term $\boldsymbol{B}_I$.

One of the most important differences of the μSR in relation to other resonance techniques, like nuclear magnetic resonance (NMR) or electron paramagnetic resonance (EPR), is that the experiments can be conducted in zero applied magnetic fields. In this situation, the spin will precess around the internal field induced by a magnetic atom in the crystallographic site where the muon stopped. It is then said that muons are a real space, point-like probe to the magnetism of a sample. Moreover, muons are also an extremely sensitive probe to small magnetic fields, due to the muon large magnetic moment [91].

The quantity of interest in a μSR experiment is the time dependent asymmetry $A(t)$, which is defined as [89,90]

$$A(t) = \frac{N_L(t) - \alpha N_R(t)}{N_L(t) + \alpha N_R(t)}, \tag{2.56}$$

where N_L and N_R are the number of positrons detected in the left and right detector, respectively, as a function of time. α is an empirical parameter that accounts for the different efficiency of R and L. The intrinsic asymmetry of the weak-decay, equal to $1/3$, determines the maximum possible value of the initial asymmetry $A(0)$. The exact experimental value depends on α. In Figure 2.8 we show a representation of the expected asymmetry when a high transverse (in relation to the muon initial polarisation) magnetic field $\boldsymbol{B}_{ext}$ is applied to the sample. The muon spin is then expected to precess around the axis defined by $\boldsymbol{B}_{ext}$, and in the resulting measured asymmetry relaxation $A(t \neq 0)$ an oscillatory signal will be detected, as shown in the right hand side of Figure 2.8.

In ideal cases, and later we are going to show that the samples studied in this work do not behave ideally, the implanted muon will occupy one determined crystallographic site in the material. If the compound under study is an oxide, a simple electrostatic consideration indicates that the muon should stop close to an O^{2-} ion in an interstitial site. Regardless of the development of magnetic long-range order, usually the magnetic field $\boldsymbol{B}_{loc}$ experienced by the muon in the lattice is different of zero. $A(t \neq 0)$ is then determined by the width of the field distribution Δ at the muon site. More than that, the asymmetry relaxation reflects the dynamics of the spins in the material as "seen" by the muons, as it shows different features if the magnetic field distribution is static or if the field $\boldsymbol{B}_{loc}$ fluctuates at a rate ν. This makes μSR a suitable probe even if the magnetic order is short-range or random, as in spin-glasses [89,90,92].

In this work, μSR will be used to study the magnetism in the Sm-based pyrochlores. Complementary to our neutron scattering studies, we would like to ascertain the presence of long-range order, as well as dynamics, in the ground-states of those compounds. These results will be shown in Chapter 5.

Chapter 3

Sm-based pyrochlores: bulk properties

3.1 Overview and context

We initiate the results part of this thesis presenting our work on two relatively few studied Sm-based pyrochlores: the titanate $Sm_2Ti_2O_7$ and the stannate $Sm_2Sn_2O_7$. A couple of studies have been reported on the former compound [93–95], which is known for its photocatalytic [96], nuclear waste storage [97] and electronic applications [98]. For the stannate, reported work is limited to static magnetic susceptibility measurements [99].

In the research of frustration in pyrochlore magnets, both compounds are not only important for their novelty. Under standard solid state synthesis conditions, the pyrochlore phase formation, with few exceptions [7], obeys a strict rule. If the ionic radius ratio $R_{A^{3+}}/R_{B^{4+}}$ assumes values between 1.46 and 1.78, the cubic, ordered $A_2B_2O_7$ phase will form and remain stable at 1 atm pressure [6]. The stannates family is the only one that satisfies this condition for all the rare-earth ions, from Lu^{3+} to La^{3+}. The titanates family is more restricted, and the ratio $R_{Sm^{3+}}/R_{Ti^{4+}} = 1.78$ lies at the border of the stability-field diagram. It is interesting then to check the stability of the pyrochlore phase in samarium titanate, and that is one of the purposes of this chapter.

The direct consequence brought in by the change of the transition metal ion is the increase of the lattice parameter between titanate and stannate. It is then said that the effects of the non-magnetic ion substitution of the pyrochlore B site introduces a *chemical pressure* on the lattice. Our idea in synthesising those seemingly similar samples was to obtain consistent results, which could be further established by the comparison between the measured physical properties on both compounds. This is the proposition that is going to guide the work performed on the Sm pyrochlores.

The practical reason that inhibited more profound studies about frustrated magnetism on those samples using neutron scattering techniques is probably that, in its natural abundance, Sm is a high neutron absorber. More than that, Sm also has the smallest ordered magnetic moment of all the trivalent magnetic rare-earths. The challenges related with that research are then *i.* to circumvent the problem of the high absorption and *ii.* to measure the very week magnetism of the samarium ions.

In the course of this work, I was fortunate to be able to, as far as possible, overcome those problems. In this chapter, we deal specifically with structural analysis and bulk low temperature measurements, detailing the procedure that is going to, later, bring us to the solution of the problem *ii*.

3.2 Experimental details

The Sm-based pyrochlores studied in this work were prepared by the author of this thesis via the standard solid state process. Stoichiometric quantities of high purity ($>$ 99.99%) rare-earth and transition metal oxides were mixed according to the reactions

$$Sm_2O_3 + 2\,TiO_2 \xrightarrow{1200\,^\circ C} Sm_2Ti_2O_7$$

or

$$Sm_2O_3 + 2\,SnO_2 \xrightarrow{1300\,^\circ C} Sm_2Sn_2O_7.$$

In general, the full pyrochlore phase formation is not reached after a single sintering round. After each one, which lasted 36 hours, the resulting pellet is reground and pelletised again. Intermediate x-ray diffraction measurements were performed in order to check the evolution of the phase formation. After three sintering cycles the samples were considered to be composed of a single pyrochlore phase.

For the work with neutrons, isotopically enriched samples were synthesised. The rare-earth oxide raw material used was *nominally* composed of 98.5% of $^{154}Sm_2O_3$. However, samarium oxide is highly hygroscopic, and a diffraction pattern showed that the actual composition of the raw material was mostly $^{154}Sm_2(OH)_3$ ($P6_3/m$). The clean oxide phase was obtained by annealing the hydroxide in air, so that

$$2\,{}^{154}Sm(OH)_3 \xrightarrow{800\,^\circ C} {}^{154}Sm_2O_3 + 3\,H_2O.$$

After this procedure, the isotopically enriched samples were synthesised as explained above.

To check the sample quality, neutron diffraction was performed at the instrument HRPD at ISIS. Around 2 g of sample were loaded in 3 mm diameter, vanadium cylindrical sample cans. The samples were cooled in a liquid He cryostat down to 5 K and data were collected at 5, 20 and 100 K. Apart from those, room temperature diffraction patterns (labeled as 300 K below) were measured without the use of any sample environment. This procedure reduces considerably the non-sample related background.

Heat capacity at constant pressure (C_p) was measured at temperatures ranging from 100 mK up to 4 K using $\sim$ 0.3 mg sintered pellets of the $^{154}Sm_2Ti_2O_7$ and $Sm_2Sn_2O_7$ samples in a Quantum Design PPMS equipped with a dilution insert. Technical problems inhibited the measurement of C_p for $^{154}Sm_2Sn_2O_7$ at dilution temperatures.

3.3 Sample characterisation

In addition to the x-ray diffraction performed as a quick check of the sample phase and stoichiometry, neutron diffraction data were collected for the isotopically enriched samples. Simultaneous Rietveld refinements were performed on the data collected in the three different detector banks of HRPD using the software GSAS. The crystallographic model of the second origin choice is described in Table 3.1. In order to have a better quantitative estimation of the degree of enrichment in our sample, we opted for refining a double occupancy at the Wickoff 16*d* site. This position is chosen, initially, to be occupied by 98.5% ^{154}Sm ions, following the raw material fabricant specifications. The remaining 1.5% sites are filled with the other natural isotopes of the atom. The scattering length of those (-1.7 fm) is calculated using the individual scattering lengths, reproduced from Reference [63] in Table 3.2, normalised by their respective natural abundance.

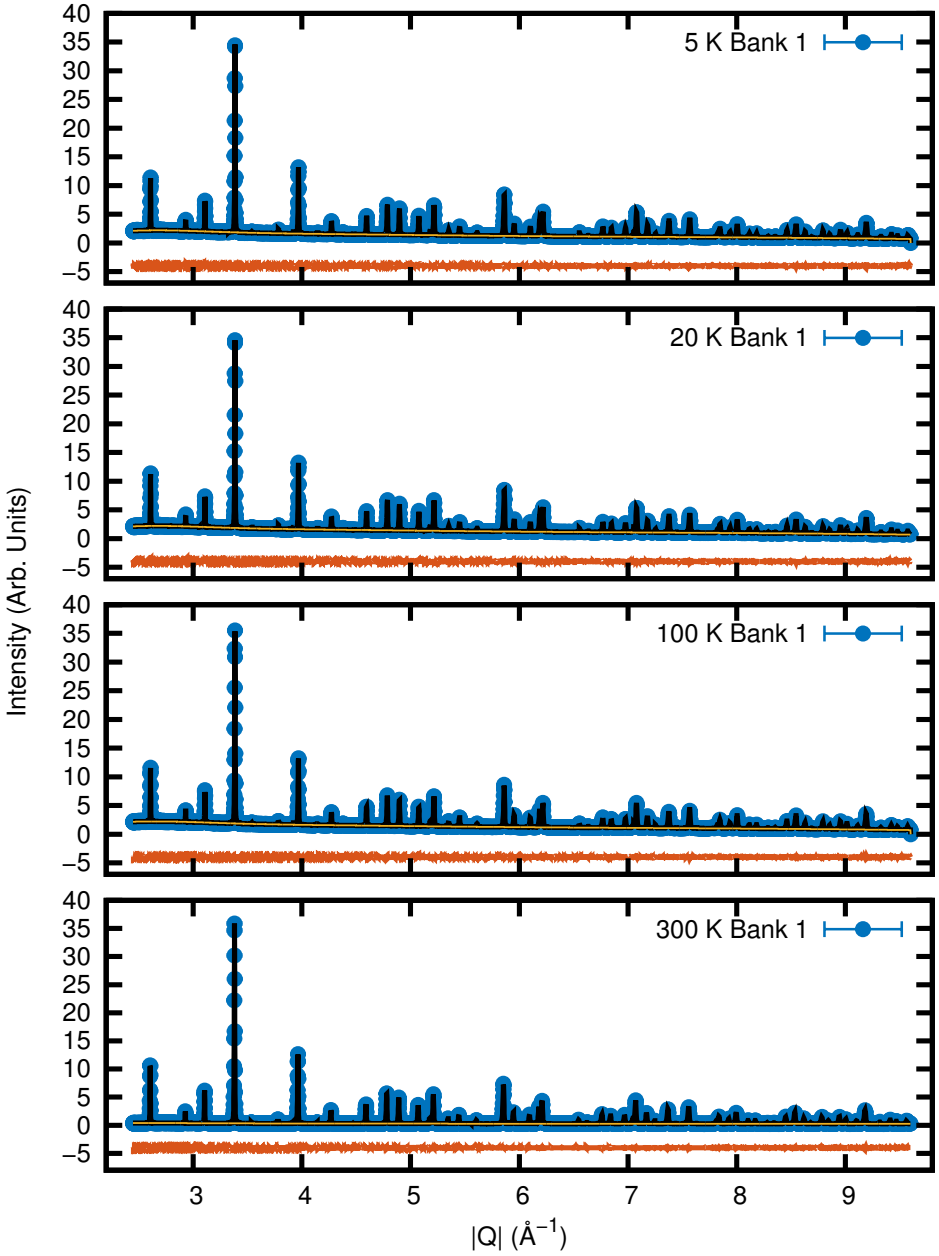

Figure 3.1: Data for the $^{154}Sm_2Sn_2O_7$ sample collected in the highest resolution backscattering detector bank of HRPD, or bank 1. Measurements were performed at 5 K, 20 K, 100 K and 300 K, as indicated in the figures labels. Note that the 300 K data set was measured in the absence of a sample environment (cryostat), what affects the measured background. The data (blue points) are plotted along with the calculated background (thin yellow lines), best refinement (black lines), and difference between refined and observed profiles (red line at the bottom of the plots).

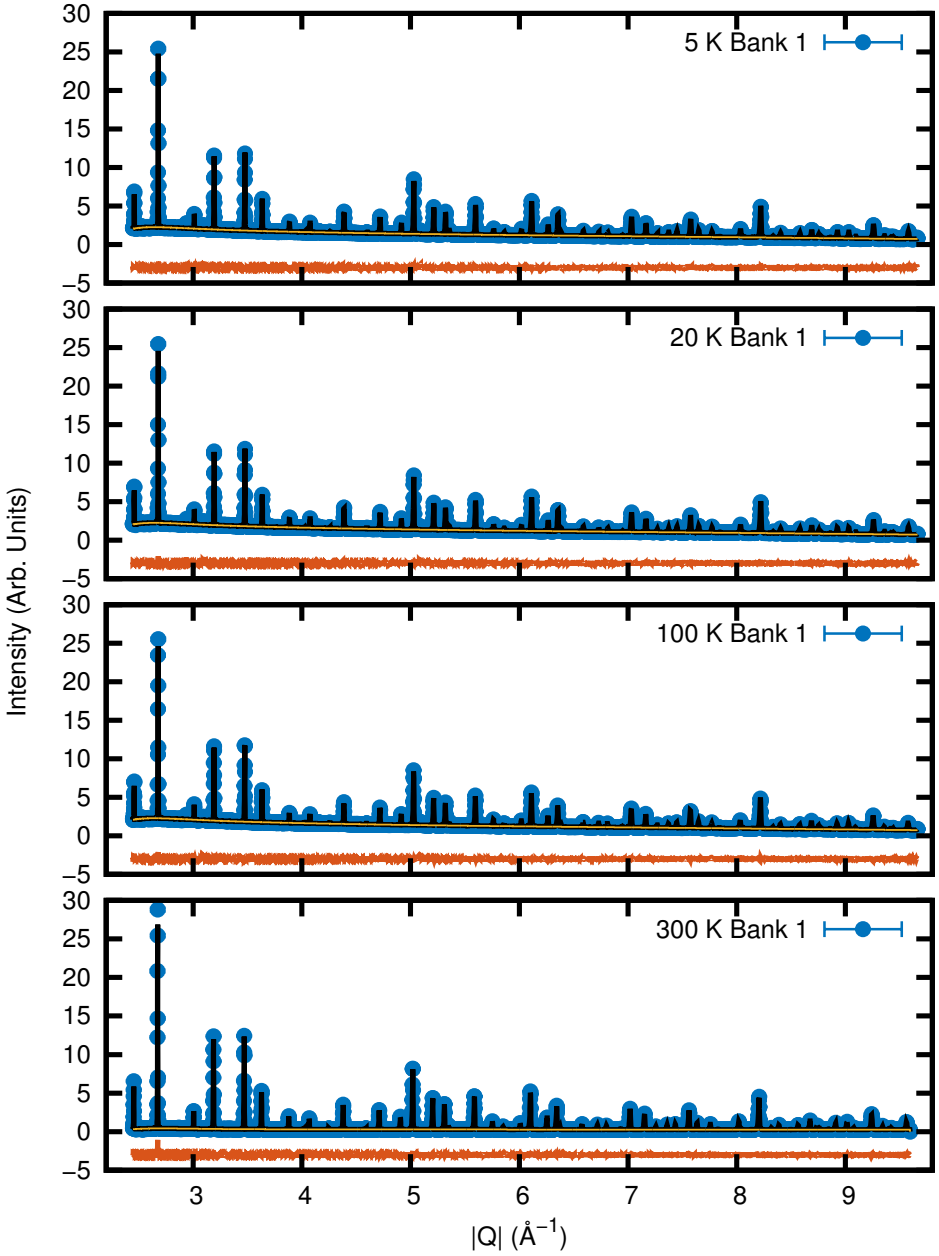

Figure 3.2: Data for the $^{154}Sm_2Ti_2O_7$ sample collected in bank 1. Measurements were performed at 5 K, 20 K, 100 K and 300 K, as indicated in the figures labels. Note that the 300 K data set was measured in the absence of a sample environment (cryostat), what affects the measured background. The data (blue points) are plotted along with the calculated background (thin yellow lines), best refinement (black lines), and difference between refined and observed profiles (red line at the bottom of the plots).

Atom	Site	X	Y	Z	Nominal Occupancy
^{154}Sm	16*d*	0.5	0.5	0.5	0.985
Sm	16*d*	0.5	0.5	0.5	0.015
Ti/Sn	16*c*	0	0	0	1.0
O^{8b}	8*b*	0.375	0.375	0.375	1.0
O^{48f}	48*f*	x	0.125	0.125	1.0

Table 3.1: Model (2^{nd} origin choice) used in the Rietveld refinement of the Sm-based pyrochlores presented in this work.

Isotope	I	Natural abundance	b_c (fm)
144	0	3.1	-3(4)
147	7/2	15.1	14(3)
148	0	11.3	3(4)
149	7/2	13.9	$-19.2(1) - 11.7(1)i$
150	0	7.4	14(3)
152	0	26.6	-5.0(6)
154	0	22.6	9.3(1.0)

Table 3.2: Sm isotopes scattering lengths reproduced from Reference [63].

We note that some uncertainty concerning the tabulated values of the scattering length of ^{154}Sm has been reported in the literature [100]. The precise knowledge of this value would be essential in the determination of occupancies and thermal displacement parameters. To systematically analyse and compare our data, we use in the refinements the tabulated values of Reference [63] (see Table 3.2), which is historically the main reference for neutron scattering lengths. Nevertheless, a cautionary note about the rigorous interpretation of the *absolute* values shown below is left here.

The refined profiles of $^{154}Sm_2Sn_2O_7$ are shown in Figures 3.1, E.1 and E.2, along with the full data set collected in HRPD. In Figures 3.2, F.1 and F.2 data and refinement of $^{154}Sm_2Ti_2O_7$ are displayed. As the samples were cooled in a He-flow cryostat, we note a pronounced background at low momentum transfers in the data measured up to 100 K. Clearly, the data set collected at room temperature displays little background, as expected for an almost *disorder free* sample. By disorder free, we mean not only the absence of (spin and nuclear) incoherent background, but also of structural disorder, that would contribute to a diffuse background underneath the Bragg peaks. This offers a previous visual indication of the sample quality.

Tables 3.3 and 3.4 contain the summary of the main refined parameters of stannate and titanate, respectively. For all the measured temperatures, the relative occupancy at the 16*d* position was allowed to vary from the nominal values given in Table 3.1. Invariably, the total occupancy of this site was constrained to be identical to one. Yet, the final values are consistent with each other and demonstrate that our samples are $\sim$ 98% enriched. The lattice parameters can be seen to show a very subtle increase from 5 K to 300 K. Interestingly, and especially for the stannate sample, the parameters shown in the first lines of the Tables 3.3 and 3.4 remain practically unaltered between 5 and 20 K.

Curiously, this behaviour is not repeated by the thermal parameters. Comparing the refined anisotropic displacement parameters (ADP's) of the transition metals (Sn/Ti) and O atoms in

Temperature (K)	Lattice Parameter (Å)	x	Occupancy of ^{154}Sm at the 16d site	R_{wp}
5	10.49775(2)	0.33379(4)	0.977(2)	0.0224
20	10.49779(5)	0.33378(4)	0.978(2)	0.0229
100	10.49924(1)	0.33371(4)	0.978(2)	0.0242
300	10.51140(4)	0.33351(3)	0.974(1)	0.0397
	Anisotropic displacement parameters $\times 100$ (Å^2)			
Atom	U_{11}	$U_{22} = U_{33}$	$U_{12} = U_{13}$	U_{23}
	5 K			
Sm	0.517(22)	0.517(22)	-0.048(13)	-0.048(13)
Sn	0.504(20)	0.504(20)	0.049(19)	0.049(19)
O^{8b}	0.810(32)	0.810(32)	0	0
O^{48f}	0.848(24)	0.638(19)	0	0.098(16)
	20 K			
Sm	0.518(18)	0.518(18)	-0.047(13)	-0.047(13)
Sn	0.481(14)	0.481(14)	0.047(19)	0.047(19)
O^{8b}	0.806(30)	0.806(30)	0	0
O^{48f}	0.833(19)	0.617(13)	0	0.096(16)
	100 K			
Sm	0.551(24)	0.551(24)	-0.076(14)	-0.076(14)
Sn	0.474(22)	0.474(22)	0.053(20)	0.053(20)
O^{8b}	0.785(35)	0.785(35)	0	0
O^{48f}	0.805(26)	0.620(21)	0	0.112(17)
	300 K			
Sm	0.762(19)	0.762(19)	-0.120(11)	-0.120(11)
Sn	0.633(18)	0.633(18)	0.025(16)	0.025(16)
O^{8b}	0.882(27)	0.882(27)	0	0
O^{48f}	1.020(21)	0.866(17)	0	0.250(15)

Table 3.3: Best refined parameters for $^{154}Sm_2Sn_2O_7$. The refined profiles are shown in Figs. 3.1, E.1 and E.2. All the parameters are obtained in the simultaneous fitting of data collected in the three detector banks of HRPD.

Tables 3.3 and 3.4, it can be seen that the ADP's anomalously *decrease* with *increasing* temperature. In the stannate this behaviour persists up to at least 100 K, while in the titanate the decrease is seen to happen between 5 and 20 K. The ADP's, in ideal cases, should quantify the effects of thermal/dynamic disorder in the sample. However, given the strong correlation between the parameters that govern the Bragg peak intensities, among them the background function, scattering lengths, site occupancies and the just mentioned ADP's, there is a probability that the decrease in the thermal parameters is a mere least-squares fitting artefact.

We test this hypothesis by investigating the presence, in our sample, of the most common defects (static disorder) in pyrochlore structures. The emergence of defects in the lattice is cumulative, in the sense that one defect somehow facilitate the appearance of other [101]. The cation anti-site disorder, more commonly referred as *stuffing*, was theoretically shown to be

Temperature (K)	Lattice Parameter (Å)	x	Occupancy of ^{154}Sm at the 16d site	R_{wp}
5	10.22182(4)	0.32637(5)	0.972(2)	0.0222
20	10.22224(5)	0.32640(5)	0.981(5)	0.0224
100	10.22645(5)	0.32634(5)	0.973(2)	0.0248
300	10.24148(4)	0.32611(4)	0.974(1)	0.0450
	Anisotropic displacement parameters $\times 100$ (Å^2)			
Atom	U_{11}	$U_{22} = U_{33}$	$U_{12} = U_{13}$	U_{23}
	5 K			
Sm	0.567(26)	0.567(26)	-0.005(16)	-0.005(16)
Ti	0.651(33)	0.651(33)	0.09(4)	0.09(4)
O^{8b}	0.786(30)	0.786(30)	0	0
O^{48f}	0.945(32)	0.735(27)	0	0.027(24)
	20 K			
Sm	0.563(25)	0.563(25)	-0.008(16)	-0.008(16)
Ti	0.610(33)	0.610(33)	0.09(4)	0.09(4)
O^{8b}	0.770(30)	0.770(30)	0	0
O^{48f}	0.948(33)	0.703(27)	0	0.027(24)
	100 K			
Sm	0.741(30)	0.741(30)	-0.049(19)	-0.049(19)
Ti	0.71(4)	0.71(4)	0.06(4)	0.06(4)
O^{8b}	0.853(34)	0.853(34)	0	0
O^{48f}	1.026(37)	0.778(30)	0	0.049(28)
	300 K			
Sm	0.993(24)	0.993(24)	-0.193(14)	-0.193(14)
Ti	0.850(29)	0.850(29)	-0.001(34)	-0.001(34)
O^{8b}	0.858(27)	0.858(27)	0	0
O^{48f}	1.092(28)	0.848(23)	0	0.138(20)

Table 3.4: Best refined parameters for $^{154}Sm_2Ti_2O_7$. The refined profiles are shown in Figs. 3.2, F.1 and F.2. All the parameters are obtained in the simultaneous fitting of data collected in the three detector banks of HRPD.

the lowest energy intrinsic disorder present in pyrochlores [101]. The defective structure has 16d positions occupied by transition metal ions, while the Sm atom would occupy the vacant 16c sites. This interchange is random and does not introduce a global symmetry breaking in the structure [6], i.e., those defects can be *a priori* quantified via the Rietveld refinements. We tried to introduce stuffing in our model but the obtained result returns a structure with an over-occupation of Ti^{4+}/Sn^{4+} in the 16c site. In any case, the result of this refinement would be arguable, given the uncertainty in the scattering length and isotopic occupancy at the rare-earth site.

The second most important defect is also an anti-site disorder, but this time occurring with the O^{2-} anions. The so-called *Frenkel pair* defects consist of a vacancy in the 48f site and a corresponding occupation of an otherwise empty 8a Wyckoff position [102, 103]. In our

Temperature (K)	x	Occupancy of ^{154}Sm at the 16d site	Occupancy of O at the 8b site	R_{wp}
5	0.33381(4)	0.976(2)	0.957(5)	0.0223
20	0.33381(4)	0.977(2)	0.957(5)	0.0228
100	0.33373(4)	0.977(2)	0.955(5)	0.0241
300	0.33351(3)	0.972(1)	0.973(4)	0.0395
	Anisotropic displacement parameters $\times 100$ (Å^2)			
Atom	U_{11}	$U_{22} = U_{33}$	$U_{12} = U_{13}$	U_{23}
	5 K			
Sm	0.523(22)	0.523(22)	-0.044(13)	-0.044(13)
Sn	0.523(20)	0.523(20)	0.033(19)	0.033(19)
O^{8b}	0.550(43)	0.550(43)	0	0
O^{48f}	0.844(24)	0.677(20)	0	0.098(16)
	20 K			
Sm	0.519(18)	0.519(18)	-0.043(13)	-0.043(13)
Sn	0.490(14)	0.490(14)	0.030(19)	0.030(19)
O^{8b}	0.546(42)	0.546(42)	0	0
O^{48f}	0.820(19)	0.646(13)	0	0.096(16)
	100 K			
Sm	0.558(24)	0.558(24)	-0.071(14)	-0.071(14)
Sn	0.493(22)	0.493(22)	0.037(20)	0.037(20)
O^{8b}	0.512(47)	0.512(47)	0	0
O^{48f}	0.801(26)	0.661(22)	0	0.111(17)
	300 K			
Sm	0.765(19)	0.765(19)	-0.117(11)	-0.117(11)
Sn	0.647(18)	0.647(18)	0.018(16)	0.018(16)
O^{8b}	0.703(36)	0.703(36)	0	0
O^{48f}	1.024(21)	0.896(18)	0	0.245(15)

Table 3.5: Parameters for $^{154}Sm_2Sn_2O_7$ after the inclusion of the 8b site occupancy in the refined model.

refinement, the included 8a oxygen occupancy is refined to zero for all temperatures, which indicates that the formation of Frenkel pairs is negligible.

Finally, the oxygen occupancy at the 8b sites is refined. Vacancies at those positions are a common defect in pyrochlores forming in the $Fd\bar{3}m$ structure, with a resulting off-stoichiometric $^{154}Sm_2B_2O_{7-\delta}$ chemical formula. Subramanian *et al.* [6] discusses the formation and stability of the pyrochlore phase for slight reductions in the oxygen content of the neutral structure. The new refined parameters are shown in Tables 3.5 and 3.6, respectively, for stannate and titanate.

For some temperatures, a small improvement in the error R_{wp} could be verified. This is most probably some marginal effect of the inclusion of one more parameter in the refinement. Observing the Tables 3.5 and 3.6, it is possible to see that the decrease in the occupancy at the 8b site, comparing oxygen-deficient and stoichiometric model, occurs at the expense of a reduction in the thermal parameters. In other words, this behaviour shows that those variables

Temperature (K)	x	Occupancy of ^{154}Sm at the 16d site	Occupancy of O at the 8b site	R_{wp}
5	0.32640(4)	0.971(2)	0.977(5)	0.0222
20	0.32643(5)	0.977(5)	0.974(5)	0.0223
100	0.32637(5)	0.972(2)	0.975(5)	0.0248
300	0.33611(4)	0.973(1)	0.985(4)	0.0449
	Anisotropic displacement parameters $\times 100$ (Å^2)			
Atom	U_{11}	$U_{22} = U_{33}$	$U_{12} = U_{13}$	U_{23}
	5 K			
Sm	0.577(26)	0.577(26)	-0.013(16)	-0.013(16)
Ti	0.675(34)	0.675(34)	0.08(4)	0.08(4)
O^{8b}	0.655(40)	0.655(40)	0	0
O^{48f}	0.977(33)	0.758(27)	0	0.024(24)
	20 K			
Sm	0.576(25)	0.576(25)	-0.016(16)	-0.016(16)
Ti	0.637(34)	0.637(34)	0.09(4)	0.09(4)
O^{8b}	0.623(40)	0.623(40)	0	0
O^{48f}	0.985(33)	0.729(27)	0	0.023(24)
	100 K			
Sm	0.752(30)	0.752(30)	-0.057(19)	-0.057(19)
Ti	0.74(4)	0.74(4)	0.06(4)	0.06(4)
O^{8b}	0.710(46)	0.710(46)	0	0
O^{48f}	1.06(4)	0.803(31)	0	0.046(28)
	300 K			
Sm	1.001(24)	1.001(24)	-0.198(14)	-0.198(14)
Ti	0.869(29)	0.869(29)	-0.003(34)	-0.003(34)
O^{8b}	0.775(35)	0.778(35)	0	0
O^{48f}	1.113(28)	0.868(24)	0	0.134(20)

Table 3.6: Parameters for $^{154}Sm_2Ti_2O_7$ after the inclusion of the 8b site occupancy in the refined model.

are correlated and cannot be disentangled in the refinement. Possibly, observation of a broader $|\mathbf{Q}|$-range with neutrons, considering that the Debye-Waller factor increases with the square of $|\mathbf{Q}|$, while vacancies would reduce the peak intensities uniformly along the probed momentum transfer, could produce more reliable results. In Tables 3.5 and 3.6, the refined oxygen deficiency is not only somewhat excessive, but also not consistent among all the measured temperatures. For the data measured below room temperatures, the O content at the 8b site is significantly lower than that refined for the 300 K data. Most probably, the refinement of the background plays a role in the quantification of the oxygen occupancy as well.

In what follows, we take aside the possibility that defects in the samples cause the strange behaviour in the thermal parameters. Since the quantification of those defects is not possible using exclusively Rietveld refinements, we turn to the direct observation of the differences in the measured profiles that are causing the decrease in the refined ADP's. If the parameters at

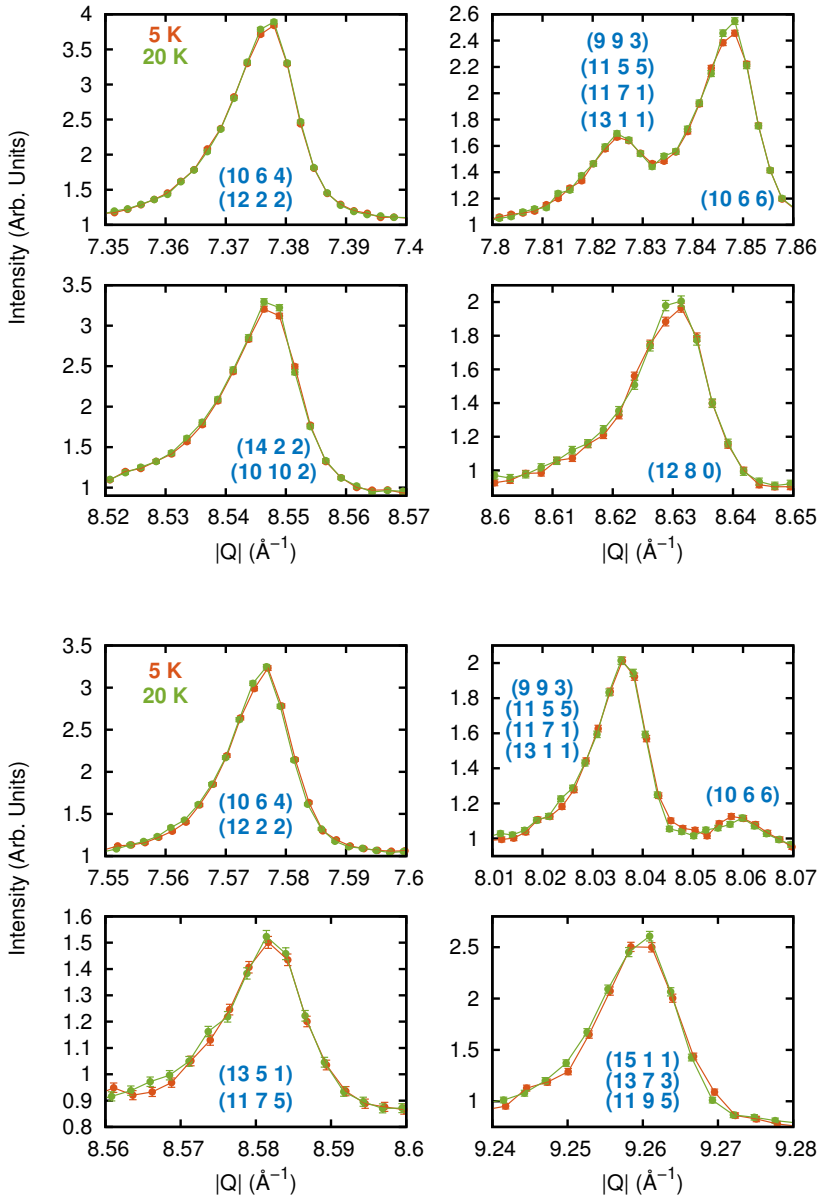

Figure 3.3: Some Bragg profiles of $^{154}Sm_2Sn_2O_7$ (top) and $^{154}Sm_2Ti_2O_7$ (bottom) collected in the bank 1 of HRPT at 5 and 20 K. The indexes of all the lattice planes that contribute to the Bragg peak intensity at a given $|\mathbf{Q}|$ are shown in blue.

20 K are effectively smaller than at 5 K, the peak intensities, specially in the higher $|\mathbf{Q}|$-region of the diffraction pattern, should *increase* when the temperature is *increased*. By plotting some high index Bragg peaks in Figure 3.3, we show that this is exactly the case. Especially for the stannate (top panel), which we have shown above to present the anomalous ADP's over a broader temperature range, it is clear that some intensities are indeed higher at 20 K, while the background and the lattice parameters do not seem to change considerably.

In the absence of complementary data, we can only speculate the reasons for this unusual intensity decrease. Inspired by some experimental findings on another rare-earth pyrochlore, $Tb_2Ti_2O_7$, which presents unusual crystallographic properties at low temperatures [104,105], we

investigate in the next chapter the possibility of magnetoelastic coupling between a phonon from the pyrochlore lattice and a crystalline electric field excitation. Recently, detailed investigations on classical spin ices [106] and the just mentioned quantum spin liquid candidate $Tb_2Ti_2O_7$ [107, 108] demonstrate the relevance of spin-lattice interactions as originators of spin-flips, also known as *Orbach processes*. The Orbach mechanism is responsible for the violation of the ice rules, the condition for the creation and propagation of the emergent monopoles in hot spin ice [106] (see Chapter 1).

If the overall features of $Tb_2Ti_2O_7$ are much less understood, they are definitely not less studied. Earlier research showed that a dynamic Jahn-Teller distortion most probably influences the development of long-range order at very low temperatures in the compound [109]. The establishment of a lattice distortion at temperatures as low as 400 mK is, from the experimental point of view, extremely challenging. More recently, however, it was experimentally demonstrated that the first excited CEF level in $Tb_2Ti_2O_7$ couples with an acoustic phonon to form a *vibronic bound state* [105]. Vibronic bound states carry characteristics of both phonons and single ion excitations, and are, therefore, not fully described by any of them. In Chapter 4, after the determination of the CEF levels in the Sm-based pyrochlores, we are going to return to this question, investigating more quantitively the possibility of magnetoelastic coupling in the compounds studied here.

3.4 Heat capacity and magnetic entropy

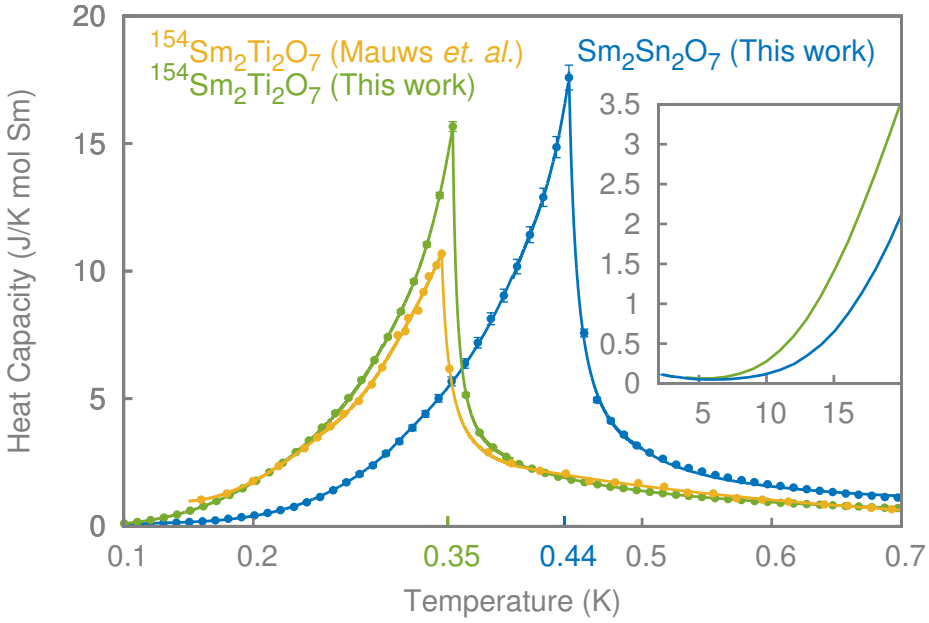

Figure 3.4: Low temperature heat capacity data measured for $^{154}Sm_2Ti_2O_7$ and $Sm_2Sn_2O_7$ (green and blue circles, respectively). For comparison, data of $^{154}Sm_2Ti_2O_7$ published in Reference [95] are also shown (yellow circles). The lines are guides to the eye. In the inset, heat capacity measured for the same samples at higher temperatures is shown. The error bars in this plot were omitted for clarity.

In Figure 3.4 the heat capacity at constant pressure (C_p) data collected using sintered pellets

of $^{154}Sm_2Ti_2O_7$ and $Sm_2Sn_2O_7$ are shown. The consistent presence of the phase transitions in both titanate samples, the isotopically enriched and the one with the natural isotopic abundance of the Sm atom, was checked. It is therefore expected that the phase transition is equally present in the stannate isotopic sample. Further neutron data, presented in Chapter 5 will show that this hypothesis is actually correct.

Along with data of this work, data published in Reference [95] are shown. The comparison of heat capacity anomalies displayed by different samples was already shown to be a reliable method to determine relative sample quality. In the last chapter of this thesis, we are going to present a famous example of the sensitiveness of heat capacity anomalies and phase transitions to slight variations in the sample stoichiometry: the quantum spin ice candidate pyrochlore $Yb_2Ti_2O_7$. Now, solely considering $^{154}Sm_2Ti_2O_7$, even though the anomaly of the sample of Mauws *et. al* has a smaller intensity than the anomaly of our sample, its position and sharpness are very similar. Thus, roughly speaking, we do not expect strong stoichiometry differences between the sample of Reference [95] and ours.

The anomaly of the stannate is very similar in shape and intensity to the one of the titanate, but takes place at higher temperature, around 440 mK. These similarities lead us to believe that both compounds may present very similar physical behaviour above and below phase transitions. It is also interesting to note that another Sm-based pyrochlore, the zirconate $Sm_2Zr_2O_7$, was shown to not present any sharp anomaly down to the lowest measured temperatures ($\sim$ 0.1 K) [110]. Instead, the zirconate shows a broad peak centred around 500 mK, which, in the work of Reference [110] was not attributed to the development of long-range order in the sample.

The magnetic entropy can be estimated from the heat capacity data using [48, 111]

$$\Delta S(T) = \int_{T_0}^{T} \frac{C_p(T')}{T'} \; dT', \tag{3.1}$$

where T is the sample temperature. Clearly, magnetism may not be the only contribution to the entropy of a sample at very low temperatures. Electron dynamics, in conductors, and hyperfine interactions in atoms that possess nuclear spin magnetic moment, are some examples of disorder that may increase the overall entropy displayed by the system. None of the previous applies to our Sm-based pyrochlores. The phonon contribution to the heat capacity is usually estimated by fitting a Debye $\propto T^3$ curve to low temperature data and extrapolating the result to temperatures below 10 K. However, there is some arbitrariness in the interval to which the Debye model can be fitted. We tried several for 10 K $< T <$ 20 K, but all returned an overestimated phonon contribution, producing heat capacities higher than the measured ones at lower temperatures. Therefore, we follow the procedure also adopted by Singh *et al.* [93] and neglect the phononic contribution to the heat capacity below 8 K. This approximation is probably valid considering our results of neutron diffraction, which do not show considerable structural differences or increase in the dynamical disorder between 5 and 20 K.

The entropy calculated using Equation (3.1) is shown in Figure 3.5. The $\Delta S(T)$ at low temperatures reaches asymptotically the value corresponding to $R\ln(2)$. Using the Boltzmann law, we recognise the ground-state of the system as a well isolated doublet, following the trend comum in almost all the other pyrochlores compounds (except Gd and Eu-pyrochlores) [7]. Since samarium is a Kramers ion, the doublet ground-state of the Sm-based pyrochlores is protected and its degeneracy cannot be lifted by any perturbation that does not break time reversal symmetry.

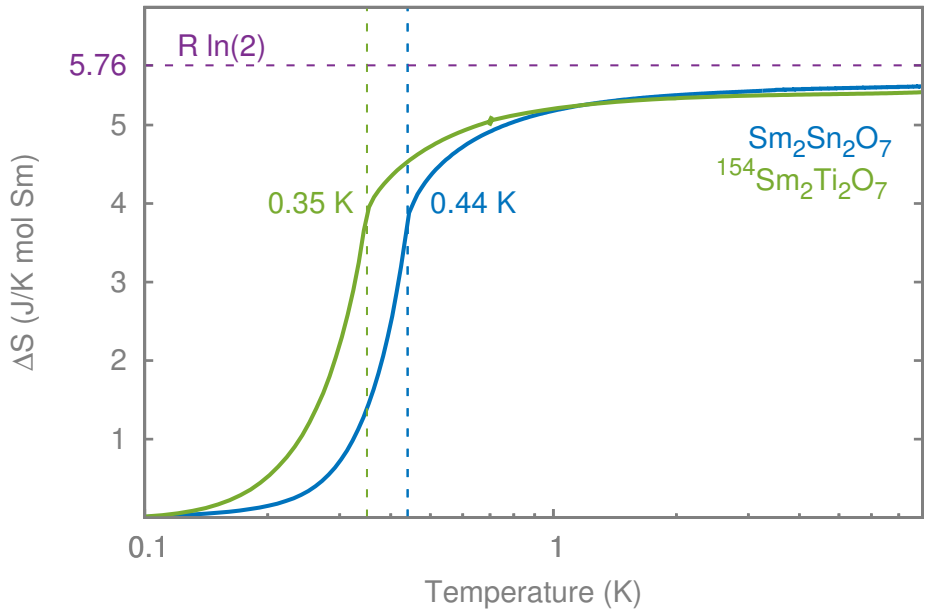

Figure 3.5: Estimated magnetic entropy for $T < 7$ K, calculated using Equation (3.1) and heat capacity data of Figure 3.4. The phonon contribution in the whole temperature range was neglected. The vertical dashed lines highlight the phase transition temperatures of both samples. The horizontal dashed line shows the value of $R\ln(2)$, the entropy expected for a doublet ground-state.

3.5 Summary of the results presented in this chapter

The focus of this chapter was on the precise structural characterisation of the synthesised compounds, especially because these results were never presented in the literature. Neutron diffraction was employed to show that both samples are formed by single pyrochlore phases. The most common defects present in stable pyrochlore compounds were investigated, and, finally, it was convincingly demonstrated that our samples are good exemplars of $^{154}Sm_2Ti_2O_7$ and $^{154}Sm_2Sn_2O_7$.

The structural analysis also revealed some unexpected results. The intensity of some high index Bragg peaks increase with increasing temperature. This effect is slightly more prominent in the stannate than in the titanate. In the next chapter, after the determination of the crystal electric field excitations in our samples, a possible explanation for this anomalous behaviour will be offered.

The low temperature heat capacity data show very strong and sharp anomalies for titanate and stannate at 350 mK and 440 mK, respectively. The estimation of the magnetic entropy suggests that the ground-state of the systems can be described as well isolated Kramers doublets. This considerations are going to be our starting point for the analysis presented in the next chapter.

Chapter 4

Sm-based pyrochlores: single ion properties and magnetic susceptibility

4.1 Overview and context

As we mentioned before, not much has been reported about the magnetic properties of Sm-based pyrochlores, apart from a handful of studies succinctly itemised below:

- Singh *et al.* [93] shows results of DC-susceptibility (χ_{DC}), C_{p} and Raman spectroscopy measurements conducted on a single crystal sample of $^{154}Sm_2Ti_2O_7$. The analysis of χ_{DC} and C_{p} demonstrated that the dipolar and exchange interactions in the titanate have smaller energy scales when compared to other members of the pyrochlore family. Down to 2 K, no signal of spin-freezing could be detected. A maximum in the susceptibility $\sim$ 140K was interpreted as a consequence of the single ion properties of the Sm^{3+} ion. Raman spectroscopy indicated the presence of four active low energy modes attributed to CEF excitations, while the ground-state $J = 5/2$ of Sm^{3+} is expected to split into a maximum of three doublets.

- Malkin *et al.* [94] reanalyses the susceptibility data measured by Singh *et al.* in order to estimate the CEF parameters of $^{154}Sm_2Ti_2O_7$. Despite the excellent agreement between experimental data and fitting, the CEF levels deduced in Malkin *et al.* depart strongly from the ones obtained in the Raman spectroscopy study of Reference [93].

- Mauws *et al.* [95] presented a more complete set of experiments on another single crystal sample of $^{154}Sm_2Ti_2O_7$, this time enriched with the isotope ^{154}Sm. It is shown that the titanate displays a heat capacity anomaly at $T_{\mathrm{N}}^{Ti} = 350$ mK, associated with the development of an antiferromagnetic all-in-all-out long-range order in the sample. Additionally, inelastic neutron scattering is employed to determine a third set of crystal electric field levels, which is partially inconsistent with both [93] and [94].

In this Chapter, we present new comprehensive inelastic neutron scattering measurements of the crystal electric field transitions between the ground-state doublet and the levels of the first excited multiplet of the Sm^{3+} ion. The energy and intensity of the measured levels are used as parameters of the fit conducted in order to solve the CEF scheme of the ion in the pyrochlore lattice. Our analyses demonstrate that the values of ground-state magnetic moment, when intermultiplet transitions are not neglected, are strongly suppressed from those predicted when considering uniquely the ground-state CEF splitting. We extend our investigation calculating the χ_{CEF} of the titanate and stannate and comparing it with the χ_{DC} measured in low applied magnetic fields. Following the determination of the eigenstates of the single ion Hamiltonian, possible multipolar and magnetoelastic coupling, as well as their implications, are discussed.

4.2 Experimental details

Inelastic neutron scattering measurements were performed at the time-of-flight (TOF) spectrometer MERLIN at ISIS [86]. Approximately 0.7 g of titanate and 1.4 g of stannate were packed in aluminium foil, subsequently curled up to form hollow cylinders of ~ 2 cm diameter and height. The samples were sealed in aluminium cans and cooled down to 5 K in a close cycle refrigerator (CCR) cryostat in He exchange gas.

Two experimental configurations were employed. Firstly, the instrument gadolinium chopper was operated in repetition-rate multiplication mode, which enables the simultaneous measurement of incident energies $E_i = 10, 19$ and, with higher flux, 50 meV for a rotation frequency of 250 Hz. With that setup, the spectra were measured at 5 and 150 K. For a frequency of 400 Hz, data were collected at 5 K for $E_i = 17,\ 28,\ 54$ and 150 meV. As we proceeded to data collection with higher neutron incident energies, the Gd chopper was substituted by a sloppy chopper and the spectra for a single $E_i = 300$ meV at 450 Hz were recorded at a temperature of 5 K. We note that, while the sloppy chopper was employed in measurements of the spectra of both samples, data with $E_i \leq 150$ meV were obtained *only* for the titanate.

Static susceptibility measurements were performed on our isotopically enriched samples down to 5 K in a Quantum Design MPMS SQUID magnetometer. Around 20 mg of each powder sample was pressed and loaded in a polymeric container. The diamagnetic signal of this container was subtracted from the raw SQUID voltage and a dipolar response function was fitted to the corrected data for each temperature point measured.

4.3 The Sm^{3+} form-factor

Experimentally, the observation of the ground-state ${}^6H_{5/2}$ multiplet splitting in Sm-based compounds using neutron scattering is particularly complicated. Even in low absorbing, isotopically enriched samples, phonon branches, stemming both from the pyrochlore and also from the aluminium can, are strongly present in the energy region probed. The biggest challenge is, however, imposed by the nature of the magnetic ion itself. As shown in Figure 4.1, instead of falling with increasing momentum transfer, the neutron form-factor squared $f^2(\mathbf{Q})$ curve for transitions ${}^6H_{5/2} \leftrightarrow {}^6H_{5/2}$ has a maximum at around 5 Å^{-1} [72]. The form-factor for transitions *within* the ground-state multiplet, thus, hinders a reliable separation of CEF and flat phonon branches in the experimentally accessed momentum transfer $|\mathbf{Q}| < 10$ Å^{-1} for neutrons of incident energy $E_i = 50$ meV. In order to identify modes belonging to the Hund's rules $J = 5/2$ ground-state multiplet splitting of the compound, we will have to rely on the temperature dependence of the data.

4.4 Inelastic neutron scattering results

The double differential neutron cross section [112]

$$\frac{d^2\sigma}{d\Omega dE} \propto \frac{k'}{k} f^2(\mathbf{Q}) e^{-2W(\mathbf{Q})} \sum_n p_n \sum_m |\langle m|\boldsymbol{M}_\perp(\mathbf{Q})|n\rangle|^2 \delta(E_m - E_n - E) \tag{4.1}$$

determines the CEF information accessed via neutron scattering. The terms k, k', $e^{-2W(\mathbf{Q})}$ and $f^2(\mathbf{Q})$ in Equation (4.1) were defined in Section 2.2.3. Moreover, $p_n = (1/Z)\sum_n e^{E_n/k_B T}$ is the population probability of the n^{th} CEF level and $|m\rangle$ and $|n\rangle$ are the final and initial states. In this work, we consider $W(\mathbf{Q}) = 0$. This is the common assumption made in the literature

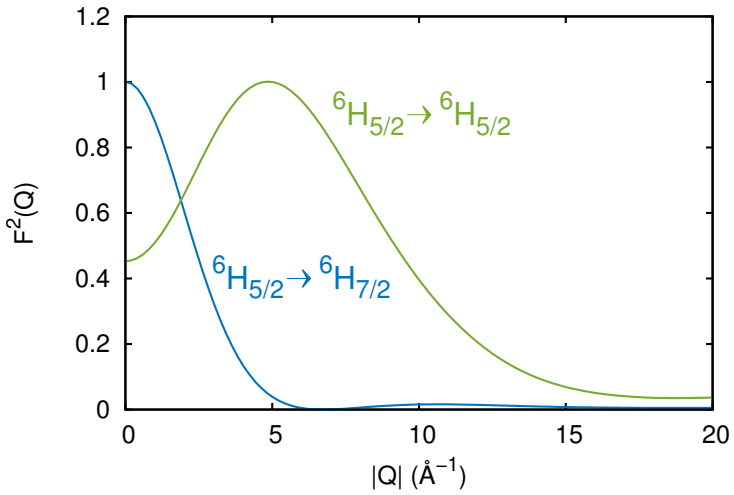

Figure 4.1: Calculated form-factors, in the dipole approximation, for transitions between the same ${}^6H_{5/2}$ multiplet (green) and from the ${}^6H_{5/2}$ to the ${}^6H_{7/2}$ multiplet (blue) of the Sm^{3+} ion. The maxima of both curves were normalised to be identically equal to one.

[22, 112], despite being rigorously correct only at $\mathbf{Q} = 0$. The component of the magnetisation perpendicular to the scattering vector $\mathbf{Q}$ is denoted by $\boldsymbol{M}_\perp(\mathbf{Q})$. When intermultiplet transitions are considered, $\langle \boldsymbol{M}_\perp(\mathbf{Q}) \rangle = -\frac{2}{3}\langle \boldsymbol{L}_\alpha + 2\boldsymbol{S}_\alpha \rangle$ [72], where $\boldsymbol{L}$ and $\boldsymbol{S}$ are the orbital and spin angular momentum operators and α is any of the orthogonal x, y, z axis. The factor $\frac{2}{3}$ appears due to the powder averaging of Equation (4.1) [113].

Data measured with neutrons of incident energy $E_i = 50$ meV are shown in Figure 4.2(a) and 4.2(b) for temperatures of 5 and 150 K, respectively. At 5 K, one weak, dispersionless mode can be observed around 16 meV in the interval $|\mathbf{Q}| = [1, 2]$ Å^{-1}. At 150 K, the mode intensity is surpassed by a general increase in the background, possibly consequence of the growing population of pyrochlore optical phonon levels at medium energies [114]. $|\mathbf{Q}|$-cuts showing the behaviour of this excitation with increasing temperature are shown in Figure 4.3(a).

Singh *et al.* [93] report, at energy transfers $\Delta E < 60$ meV, six expected Raman-active phonon modes and other four supposed CEF modes lying at energies around 11, 16, 20 and 33 meV. While we identify an excitation ~ 16 meV, our data measured with $E_i = 19$ meV neutrons (not shown) display no evidence of a CEF level at 11 meV. Similarly, the high density of phonon states around 20 and 33 meV does not allow us to directly identify, in the measured $S(|\mathbf{Q}|, \omega)$, those higher energy, supposed single ion excitations. Below, we are going to show that a mode at ~ 30 meV is predicted by our CEF analysis. The levels located at 11 and 20 meV were suggested, in an earlier Raman and IR spectroscopy work performed on $^{154}Sm_2Ti_2O_7$ and $^{154}Sm_2Sn_2O_7$ [115], to correspond to two IR-active phonon levels, which become also Raman-active due to a local symmetry lowering associated with crystal defects.

The inelastic neutron scattering data of Mauws *et al.* [95] indicate a CEF excitation taking place at ~ 16 meV and one additional at 70 meV. Indeed, we measure a flat excitation at 70 meV using neutrons of $E_i = 150$ meV, as shown in Figure 4.4. However, $|\mathbf{Q}|$-cuts performed for several momentum transfer intervals, displayed in Figure 4.3(b), reveal that this mode intensity increases with increasing $\langle \mathbf{Q} \rangle$ up to at least 10.5 Å^{-1}. Though, in our analysis, the contribution of the phononic background to this putative excitation is neglected, we note that its momentum transfer dependency contradicts that expected considering the form-factor for

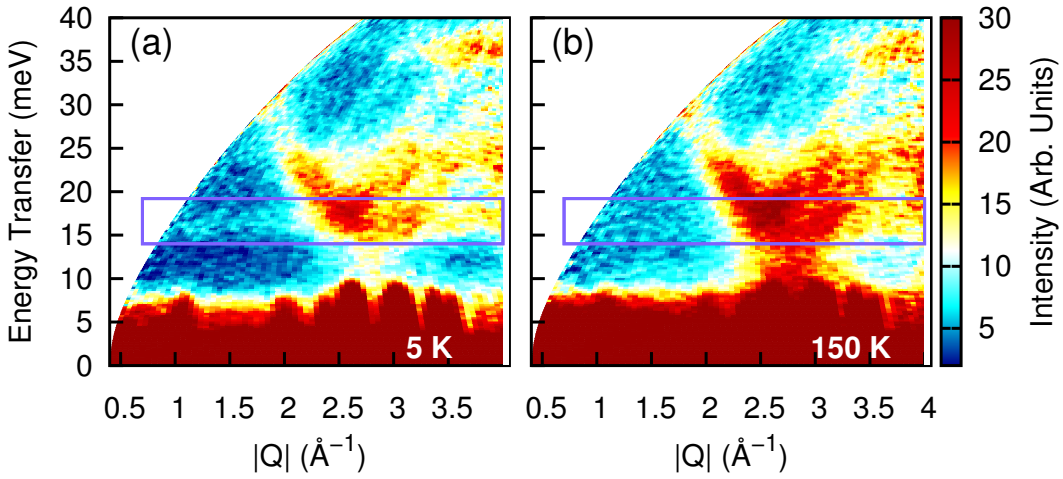

Figure 4.2: Contour color plots of $^{154}Sm_2Ti_2O_7$ data measured at MERLIN with a neutron initial energy $E_i = 50$ meV at (a) 5 K and (b) 150 K. The purple rectangles highlight the position of one possible CEF excitation at ~ 16 meV.

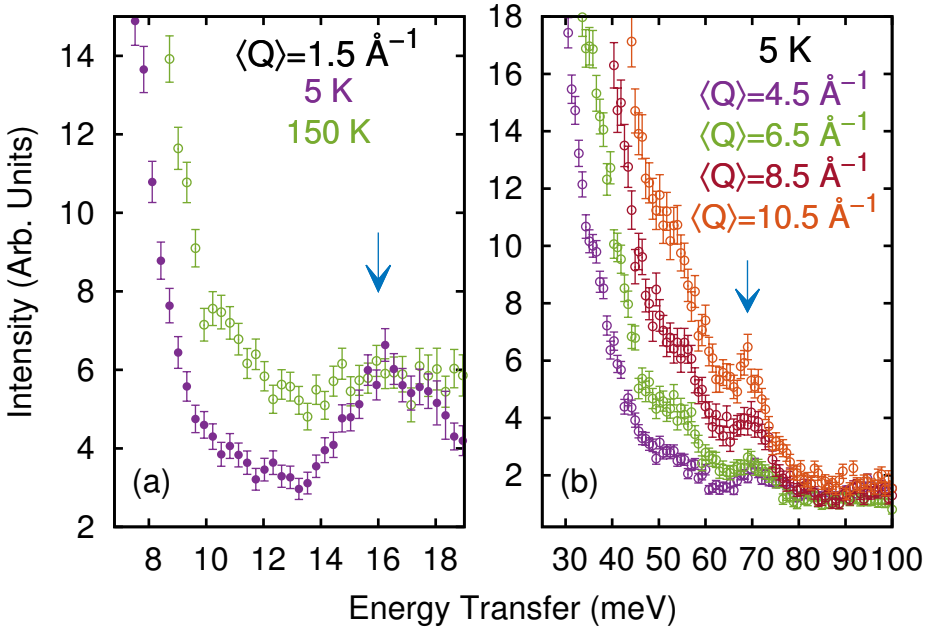

Figure 4.3: Momentum transfer cuts integrated over the interval $\langle \mathbf{Q} \rangle \pm 0.5$ Å^{-1}. (a) Temperature dependence of the mode observed at ~ 16 meV. (b) $|\mathbf{Q}|$-dependence of the flat excitation measured at 70 meV (corresponding to the contour plot shown in Figure 4.4). Note that the intensity of the excitation in (b) does not follow the form-factor calculated for transitions $^6H_{5/2} \leftrightarrow {}^6H_{5/2}$, shown in Figure 4.1.

transitions $^6H_{5/2} \leftrightarrow {}^6H_{5/2}$, as shown in Figure 4.1. We also note that this position in energy coincides with those of several Γ-point phonons in pyrochlores [114].

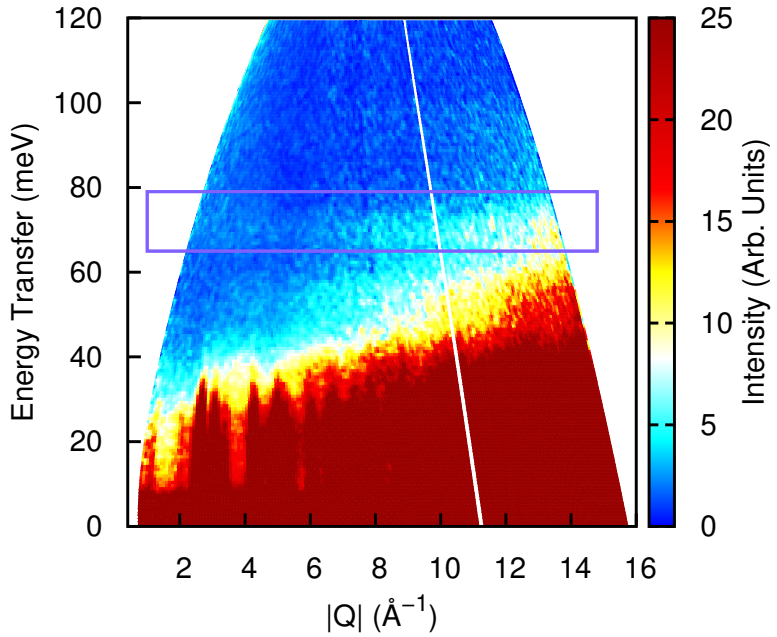

Figure 4.4: Spectra measured (uniquely) on the titanate sample at 5 K with neutrons of incident energy $E_i = 150$ meV. The purple rectangle ~ 70 meV emphasises the mode suggested in Reference [95] as being a CEF level.

As the observation of one (or two) CEF levels is not usually enough to perform a reliable calculation of the single ion Hamiltonian, we proceed our search for levels at higher energies. Following a trend common also in other light rare-earth compounds, the ground $^6H_{5/2}$ multiplet of Sm is relatively close in energy to the first excited $^6H_{7/2}$, and we expect to measure its splitting into four doublets at energies below 200 meV [116][1].

In Figures 4.5(a) and 4.5(b), the spectra measured at 5 K with $E_i = 300$ meV neutrons are shown for $^{154}Sm_2Ti_2O_7$ and $^{154}Sm_2Sn_2O_7$, respectively. Despite the weak signal, some low $|\mathbf{Q}|$ flat modes are present in both samples. We perform a $|\mathbf{Q}|$-cut integrated over the full interval where the form factor for transitions $^6H_{5/2} \leftrightarrow {}^6H_{7/2}$ is appreciably bigger than zero, i.e. where $|\mathbf{Q}| < 5$ Å^{-1}. Those cuts, shown in Figure 4.6, are fitted with Lorentzian distributions centred on the peak position and with a minimum FWHM limited by the instrumental resolution, estimated to be not smaller than 12 meV for the energy transfer range between 100 and 200 meV. In order to define the relative intensities of the modes, the FWHM of the excitations were assumed to be identical, which is a reasonable approximation for energies between 120 and 190 meV. For the background estimation (grey shaded area in Figure 4.6), we performed higher momentum transfer cuts with same width in $|\mathbf{Q}|$. The intensities of all of them were scaled ~ 100 meV, and, after subtraction, the data shown in Figure 4.7 (filled black circles) are obtained. Three distinct peaks can be distinguished at 127, 154 and 183 meV (green arrows). The presence of a fourth excitation between the latter two, at around 169 meV (pink arrow), can be inferred considering the overall width of this broad superposition of levels. The data extracted from those fittings are summarised in Table 4.1.

Next, we need to confirm that these modes really correspond to CEF levels resulting from the

[1]The measurement of the CEF modes explored from now on was possible due to the advice of Jianhui Xu and Bella Lake. The author of this thesis thanks them for their suggestions.

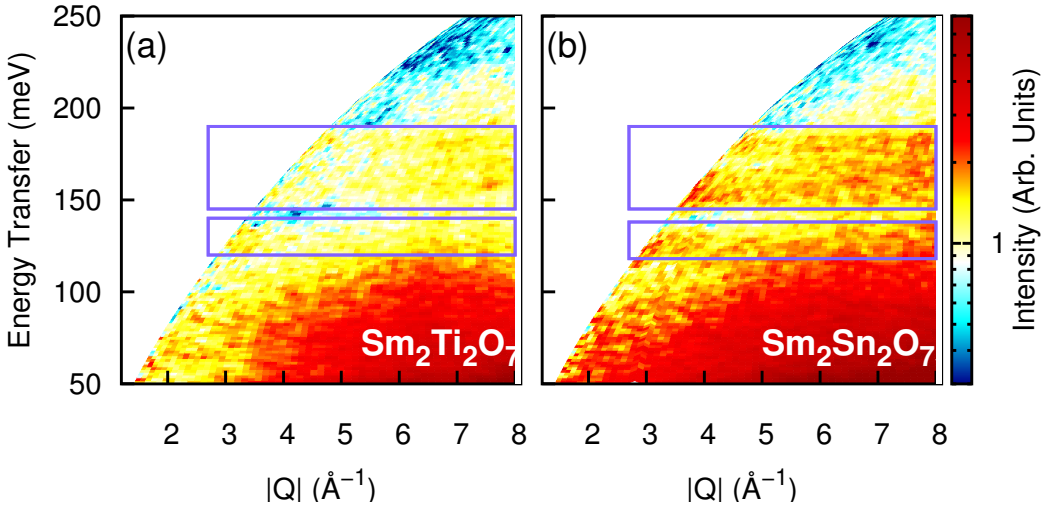

Figure 4.5: Possible CEF excitations, emphasised by purple rectangles, resulting from the splitting of the first excited $^6H_{7/2}$ multiplet on (a) titanate and (b) stannate samples. Data were collected at 5 K using neutrons of incident energy $E_i = 300$ meV.

free ion multiplet splitting of the Sm^{3+} in the pyrochlore lattice. In order to achieve that, we fit the single ion crystal field Hamiltonian of Equation (1.5) to the eigenenergies and intensity ratios obtained experimentally. Clearly, the inclusion of intermultiplet transitions in the model precludes the use of the Stevens' operator formalism in the fitting. The only approach left to treat the problem is then to use the tensor formalism with a substantial number of multiplets and diagonalise the resulting matrix. Luckily, that can be easily accomplished by the software SPECTRE [21][2]. As basis states, we made use of the 12 J values belonging to the two lowest multiplets in energy ^6H and ^6F of the Sm^{3+} ion [116]. Intermediate coupling, which is the mixing of levels with the same J but different L and S quantum numbers, was also taken into account. The values of the several spin-orbit parameters of the free ion Hamiltonian are taken from Reference [116] and are not fitted. The starting parameters, estimated via the fitting of the magnetic susceptibility of the material, were taken from Malkin *et al.* [94].

In the titanate data fitting, the energy of the mode at 16.1 meV, in addition to the other four levels from the second J multiplet splitting, was considered. Our trial to include the mode at 70 meV in a fitting comprising the full compound data set resulted unsuccessful. All the evidences, thus, rule out the possibility that this excitation really corresponds to a CEF level. The ground-state splitting of the stannate sample was not measured, but calculated based on the data fitting of the second multiplet splitting. The data after the background subtraction, along with the best CEF excitations fitting, are shown in Figure 4.7.

Our calculations predict that the second excited level of the ground multiplet of titanate and stannate should be present at ~ 30 meV. This is fully consistent with the Raman spectroscopy results of Reference [93]. The intensity of the transitions $|0\rangle \leftrightarrow |2\rangle$ calculated for both samples is the smallest in Table 4.1. That suggests another cause, besides the massive phonon density of states at intermediate energies, for the seemingly absence of this mode in the experimental $S(|\mathbf{Q}|, \omega)$. In the titanate, the transition $|1\rangle \leftrightarrow |2\rangle$, corresponding to an energy of ~ 14 meV, has a calculated intensity 30 times smaller than the intensity of the transition $|0\rangle \leftrightarrow |1\rangle$ at a

[2]I express my gratitude to Andrew Boothroyd for his extremely kind support in the use of his software, as well as discussions about the samarium particularities.

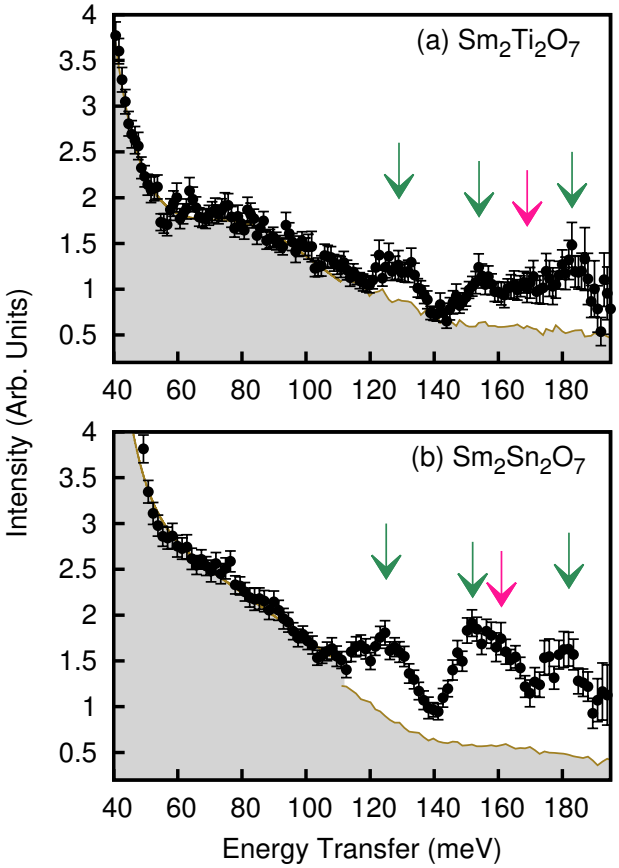

Figure 4.6: Momentum transfer cuts performed on the data of Figure 4.5 integrated over the interval $|\mathbf{Q}| = [0, 5]$ Å^{-1} for (a) titanate and (b) stanate samples. The arrows mark the position of possible excitations, which are also summarised in Table 4.1. The pink arrows indicate the position of an inferred, not perfectly resolved CEF mode.

temperature of 150 K, and is therefore not visible. The eigenvalues of H_{CEF} of stannate and titanate are very similar, with the strongest differences lying on the modes relative intensities. In the inelastic neutron scattering work performed in the zirconate [110], CEF levels were measured $\sim$ 130, 157, 168 and 183 meV, in close agreement with the samples analysed here.

Curiously, in one investigation made on another trivalent samarium compound, the high-T_c superconductor cuprate $SmBa_2Cu_3O_7$ [117], the intermultiplet transitions apear at energies 124, 154, 167 and 184 meV, i.e., very close to the ones measured in pyrochlores. The site symmetry of the rare-earth ion in $SmBa_2Cu_3O_7$ is, nevertheless, not the same. A similar result is found in another cuprate, Sm_2CuO_4, for which the point symmetry of the Sm^{3+} is C_{4v} [118]. Those works support not only the evidence that the single ion degeneracy liffting is only weekly sensitive to the local environment of the rare-earth ion [72], but also that the modes measured here really correspond to intermultiplet transitions occurring in Sm-based pyrochlores.

The calculated crystal field parameters are shown in Table 4.2. The values given in [95] were converted here to the Wybourne operator formalism using Equation (1.6), and are displayed for comparison in Table 4.2. As a consequence of the use of the Stevens' formalism, the non-diagonal elements in the Hamiltonian matrix obtained in Mauws *et al.* (with exception of B_3^4) are identically equal to zero.

We show the calculated doublet ground-states $|\pm 0\rangle$ in Table 4.3, which contains also the

$^{154}Sm_2Ti_2O_7$						
	Observed				Calculated	
Transition $\|LS\alpha\rangle \leftrightarrow \|L'S'\alpha'\rangle$	Energy (meV)	σ_E (meV)	Relative Intensity	σ_I	Energy (meV)	Relative Intensity
$\|0\rangle \leftrightarrow \|0\rangle$	0	0	-	-	0	0.05
$\|0\rangle \leftrightarrow \|1\rangle$	16.1*	0.2	-	-	16.0	0.15
$\|0\rangle \leftrightarrow \|2\rangle$	-	-	-	-	29.7	0.02
$\|0\rangle \leftrightarrow \|3\rangle$	126.7	0.5	1	-	127.2	1
$\|0\rangle \leftrightarrow \|4\rangle$	154.2	0.5	1.0	0.1	154.0	0.74
$\|0\rangle \leftrightarrow \|5\rangle$	169.3	0.9	0.8	0.1	169.6	0.92
$\|0\rangle \leftrightarrow \|6\rangle$	183.0	0.6	1.5	0.1	183.4	1.48
$^{154}Sm_2Sn_2O_7$						
	Observed				Calculated	
Transition $\|LS\alpha\rangle \leftrightarrow \|L'S'\alpha'\rangle$	Energy (meV)	σ_E (meV)	Relative Intensity	σ_I	Energy (meV)	Relative Intensity
$\|0\rangle \leftrightarrow \|0\rangle$	0	0	-	-	0	0.05
$\|0\rangle \leftrightarrow \|1\rangle$	-	-	-	-	13.0	0.18
$\|0\rangle \leftrightarrow \|2\rangle$	-	-	-	-	28.2	0.01
$\|0\rangle \leftrightarrow \|3\rangle$	125.2	0.4	1	-	125.2	1
$\|0\rangle \leftrightarrow \|4\rangle$	151.6	0.4	1.1	0.1	151.6	1.02
$\|0\rangle \leftrightarrow \|5\rangle$	161.4	0.5	0.9	0.1	161.4	1.04
$\|0\rangle \leftrightarrow \|6\rangle$	181.6	0.5	1.3	0.1	181.6	1.23

Table 4.1: Overview of the observed and calculated eigenstates and intensities of the CEF levels of $^{154}Sm_2Ti_2O_7$ and $^{154}Sm_2Sn_2O_7$. The position of the levels and their intensities (except for the level marked with *, which did not have its intensity used in the calculation) were obtained by fitting the data shown in Figures 4.3(a) and 4.6. The σ values are the standard deviation of the Lorentzian fittings. The intensities of the second multiplet splitting were all calculated relative to the transition $|0\rangle \leftrightarrow |3\rangle$. The $|n\rangle$ represents both degenerated wave functions of the n^{st} excited doublet.

	B_0^2	B_0^4	B_3^4	B_0^6	B_3^6	B_3^6
$^{154}Sm_2Ti_2O_7$	73.7	369.5	102.5	167.1	-123.0	141.8
$^{154}Sm_2Sn_2O_7$	83.1	319.7	111.8	133.4	-110.8	155.2
$^{154}Sm_2Ti_2O_7$ [94]	28.5	370.0	97.3	87.0	-78.0	124.0
$^{154}Sm_2Ti_2O_7$ [95]	164.6	393.4	0	0	0	0

Table 4.2: Crystal field parameters obtained in this work. The two last lines in the table show, for comparison, the set of crystal field parameters (in units of meV) published in the References [94, 95]. Note that the parameters of Reference [95] are estimated using the Stevens' operator formalism, with the immediate consequence that all B_q^6 parameters are identically equal to zero.

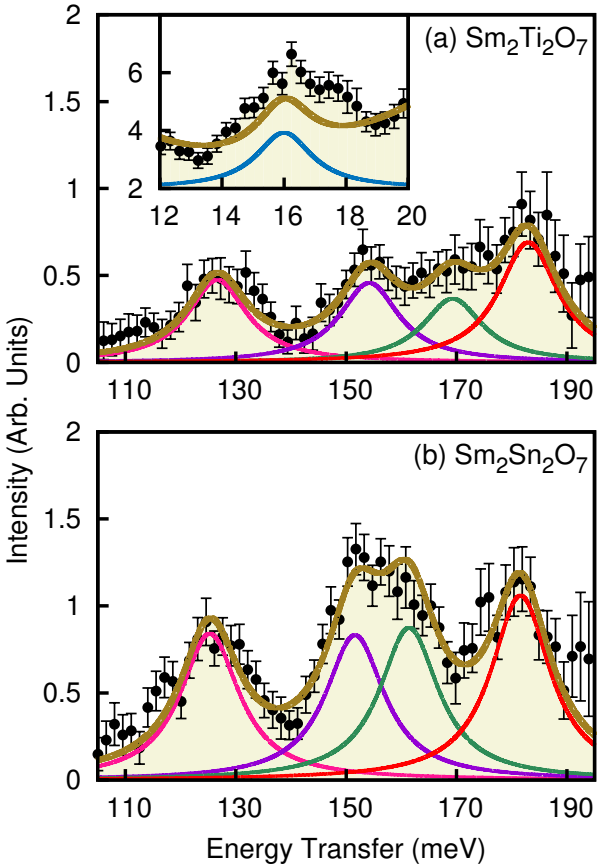

Figure 4.7: Background subtracted data of Figures 4.3 and 4.6 with superimposed calculated intensities obtained in our CEF analysis (see Table 4.2) for (a) titanate and (b) stannate. Note that the intensity of the level at 16 meV was neither used in the fitting or had a background estimated, nevertheless we show for completeness its calculated intensity in the inset of (a).

wave functions found based in the analyses presented in the References [94, 95]. All the wave functions displayed in Table 4.3 have ground-states composed mostly by the $|^6H_{5/2}, \mp\frac{3}{2}\rangle$ state, with contributions of higher angular momentum $J = 7/2$ and $J = 9/2$ states. The list of levels shown in the wave functions appear to be a slightly excessive, but in the next sections our option to show all of them will be justified.

The ground-state eigenstate determines the maximum ordered moment of the magnetic ion at $T = 0$, which is calculated as the expected value of the magnetic moment operator (see Appendix B)

$$\langle \boldsymbol{\mu}_\alpha^0 \rangle = |\langle \pm 0| - (\boldsymbol{L}_\alpha + 2\boldsymbol{S}_\alpha)\mu_B| \pm 0\rangle|, \tag{4.2}$$

where alpha indicates anyone of the spatial directions x, y, z. The only matrix element different of zero in Equation (4.2) is the expected value $\langle \boldsymbol{\mu}_z^0 \rangle$. The ground-state of the samarium pyrochlores has then an *Ising* character, and the crystal field constrains the magnetic moment to point along one of the $\langle 111 \rangle$ directions, defined here as the local-z axis.

The expected values of Equation (4.2) are presented in Table 4.4. The admixture of $^6H_{7/2}$ and $^6H_{9/2}$ terms in the ground-state doublet is very small, but its effect over the magnetic moment is surprisingly important: the value changes from the maximum $0.43\mu_B$ calculated in [95] to the $0.16\mu_B$ expected in our ground-state. We dedicate the following sections to explore other important consequences of the single ion effects in our samarium pyrochlores, applying, as far

$^{154}Sm_2Ti_2O_7$
$\|\pm0\rangle = \pm0.303\left\|^6H_{5/2},\mp\frac{3}{2}\right\rangle + 0.934\left\|^6H_{5/2},\pm\frac{3}{2}\right\rangle + 0.016\left\|^6H_{7/2},\mp\frac{3}{2}\right\rangle \mp 0.073\left\|^6H_{7/2},\pm\frac{3}{2}\right\rangle$
$\mp0.030\left\|^6H_{9/2},\mp\frac{3}{2}\right\rangle - 0.084\left\|^6H_{9/2},\pm\frac{3}{2}\right\rangle + 0.093\left\|^6H_{9/2},\mp\frac{9}{2}\right\rangle \mp 0.017\left\|^6H_{9/2},\pm\frac{9}{2}\right\rangle$
$^{154}Sm_2Sn_2O_7$
$\|\pm0\rangle = \pm0.084\left\|^6H_{5/2},\mp\frac{3}{2}\right\rangle + 0.981\left\|^6H_{5/2},\pm\frac{3}{2}\right\rangle + 0.005\left\|^6H_{7/2},\mp\frac{3}{2}\right\rangle \mp 0.058\left\|^6H_{7/2},\pm\frac{3}{2}\right\rangle$
$\mp0.012\left\|^6H_{9/2},\mp\frac{3}{2}\right\rangle - 0.076\left\|^6H_{9/2},\pm\frac{3}{2}\right\rangle + 0.093\left\|^6H_{9/2},\mp\frac{9}{2}\right\rangle \mp 0.039\left\|^6H_{9/2},\pm\frac{9}{2}\right\rangle$
$^{154}Sm_2Ti_2O_7$ [94]
$\|\pm0\rangle = \pm0.154\left\|^6H_{5/2},\mp\frac{3}{2}\right\rangle + 0.970\left\|^6H_{5/2},\pm\frac{3}{2}\right\rangle + 0.028\left\|^6H_{7/2},\mp\frac{3}{2}\right\rangle \mp 0.125\left\|^6H_{7/2},\pm\frac{3}{2}\right\rangle$
$^{154}Sm_2Ti_2O_7$ [95]
$\|\pm0\rangle = \left\|^6H_{5/2},\mp\frac{3}{2}\right\rangle$

Table 4.3: Ground-state wave functions of titanate and stannate. We use the spectroscopic notation $^{2S+1}L_J$ followed by the magnetic quantum number m_J to assign each basis functions $|L,S,J,m_J\rangle$. The bottom lines in the table show the values found in the analyses of References [94,95]. The wave function of Malkin *et al.* [94] was not reported in the original publication, so we recalculate it here based on the parameters obtained and reproduced in Table 4.2.

as possible, the results presented above in the analyses of several physical properties of those compounds.

	$\lvert\langle\boldsymbol{\mu}_\alpha^{\pm0}\rangle\rvert = \lvert\langle\boldsymbol{\mu}_z^{\pm0}\rangle\rvert$
$^{154}Sm_2Ti_2O_7$	0.16
$^{154}Sm_2Sn_2O_7$	0.27
$^{154}Sm_2Ti_2O_7$ [94]	0.11
$^{154}Sm_2Ti_2O_7$ [95]	0.43

Table 4.4: Ground-state CEF magnetic moments, in units of μ_B, calculated in this work. In the last two lines the values found by Malkin *et al.* [94] and Mauws *et al.* [95] are shown.

4.5 Magnetic susceptibility

4.5.1 Single ion susceptibility

We measure the static (DC) magnetic susceptibility χ_{DC} of our samples at several small applied fields. The data are shown in Figure 4.8. The χ_{DC} of $^{154}Sm_2Ti_2O_7$ is easily recognisable, for it shows a dip just below 50 K followed by a maximum at $\sim$ 120 K, after which it decreases monotonically up to room temperature. The susceptibility of $^{154}Sm_2Sn_2O_7$, on the other hand, displays no maximum up to 300 K. A blown up view of the susceptibility for temperatures $>$ 50 K is shown in the insets in Figure 4.8.

To perform the calculation of the single ion contribution to the magnetic susceptibility, we

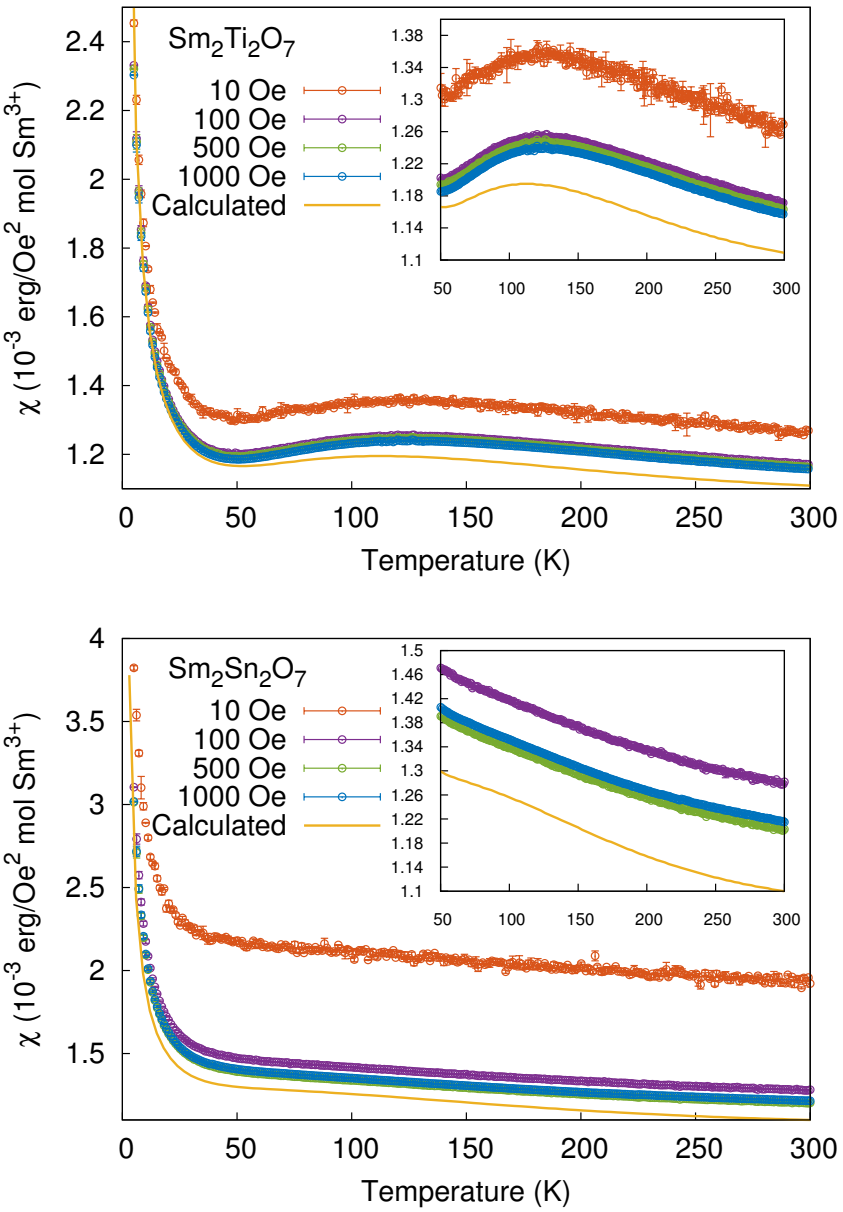

Figure 4.8: Static magnetic susceptibility χ_{DC} of $^{154}Sm_2Ti_2O_7$ (top) and $^{154}Sm_2Sn_2O_7$ (bottom). Data for four different small applied fields are presented. In the insets, the susceptibility at intermediate temperatures is emphasised. Clearly, the upturn present in the $^{154}Sm_2Ti_2O_7$ is absent in the stannate, which displays a linear behaviour at this temperature range. The yellow line shows the single ion contribution to χ_{DC}, calculated using Equations (4.3) and (4.4).

make use of the van Vleck equation [119]

$$\chi_{CEF,\alpha} = \frac{2N\beta}{Z}\left[\sum_n \frac{|\langle +n|\boldsymbol{\mu}_\alpha|+n\rangle|^2 + |\langle +n|\boldsymbol{\mu}_\alpha|-n\rangle|^2}{e^{\beta E_n}} + \frac{2}{\beta}\sum_{m>n}\frac{|\langle +m|\boldsymbol{\mu}_\alpha|+n\rangle|^2 + |\langle +m|\boldsymbol{\mu}_\alpha|-n\rangle|^2}{E_n - E_m}(e^{-\beta E_m} - e^{-\beta E_n})\right], \tag{4.3}$$

where N is the Avogadro's number, $Z = \sum_n e^{-\beta E_n}$ is the partition function and $\beta = 1/k_B T$. $E_{n,m}$ are the eigenvalues of the CEF Hamiltonian, which were presented in Table 4.1. The magnetic moment operator $\boldsymbol{\mu}_\alpha$ was defined in Equation (4.2). All the terms for which $m > n$ [second summation on the right hand side of Equation (4.3)] correspond to the so-called *van Vleck susceptibility*. Note that we neglect the sample own diamagnetic response. The powder susceptibility is found averaging Equation (4.3) over all spatial directions. As x and y are equivalent, it can be shown that [65]

$$\chi_{CEF,powder} = \frac{\chi_{CEF,z} + 2\chi_{CEF,x}}{3}. \tag{4.4}$$

The calculated $\chi_{CEF,powder}$ is shown along with the experimental results in Figure 4.8.

Our main objective with the single ion susceptibility calculation is to ratify our CEF analysis, particularly for the stannate, since the splitting of the Sm^{3+} ground-state multiplet was not observed. We note that the absolute values of the magnetic susceptibility are rather small, of the order of 10^{-3} erg/(Oe^2 mol Sm^{3+}). Consequently, our measurements appear to be extremely sensitive to magnetic impurities and to the perturbation induced by small applied magnetic fields. In both samples and for all fields, the experimental χ_{DC} is shifted upwards when compared to the calculated $\chi_{CEF,powder}$, being higher the differences between 10 and 100 Oe than between 100 and 1000 Oe. Even so, the theoretical single ion susceptibility reproduces extremely well the peculiar shape of the curves, and confirms that the non-Currie behaviour of the van Vleck susceptibility is related to crystal field effects.

In order to demonstrate the effect, over χ_{DC}, of the increased population of excited CEF levels as the temperature increases, the titanate is taken as example. We split term by term the summations in Equation (4.3) and show explicitly some of them in Figure 4.9 as a function of temperature. The panel (a) displays the allowed transitions for a field applied along the local-z, or parallel $\|$, axis (i.e. transitions for which $\langle \boldsymbol{\mu}_z \rangle \neq 0$). The component of the magnetic susceptibility perpendicular to the local-z direction, which we denote by $\chi_\perp$, is given in Figure 4.9(b).

The view of the individual contributions emphasises the striking relative magnitude of the van Vleck susceptibility associated with intermultiplet transitions (note, for example, the $|0\rangle \rightarrow |5\rangle$ along the local-z axis). Furthermore, because $\chi_\|$ is minimum where the $\chi_\perp$ is maximum, around 80 K, Figure 4.9 additionally offers the explanation for the upturn detected in the experimental powder averaged χ_{DC} of the titanate.

To close this small discussion about the titanate sample, we compare our results with the susceptibility measured by Singh *et al.* [93] and fitted by Malkin *et al.* [94]. In Figure 4.10 we plot the data and calculation obtained here along with data obtained in Reference [93]. The calculation performed in Reference [94] was reproduced by us using the crystal field parameters of Table 4.2. In the work of Singh *et al.*, the magnetic susceptibility was measured in a single crystal sample and no special orientation of it with applied magnetic field is chosen (at least no one is mentioned). There is some discrepancy between the measured values for both samples, especially at low temperatures. That can be consequence, as we already noted, of the presence of a small amount of magnetic impurities in our sample. Another reason can be simply that, because of the compound strong anisotropy, the susceptibility reported in Singh *et al.* does not correspond to a perfectly powder averaged χ_{DC} and, unlike the procedure followed by Malkin *et al.*, should not be modelled as such. This second hypothesis would, moreover, explain the slightly better agreement between the experimental values at higher temperatures, when more CEF levels are populated and the system, consequently, is more isotropic.

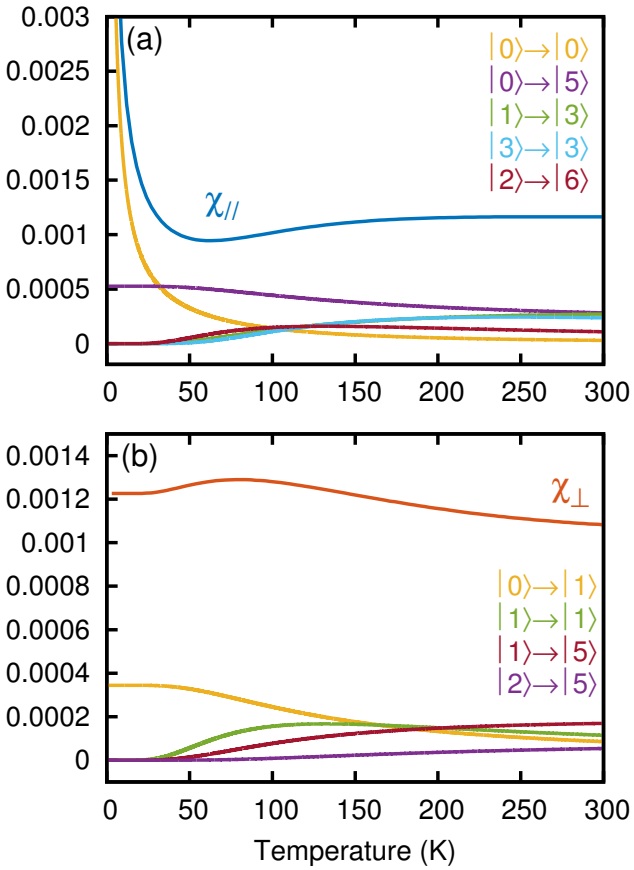

Figure 4.9: Powder susceptibility calculated for $^{154}Sm_2Ti_2O_7$, separated in parallel ($\chi_{\parallel}$) and perpendicular ($\chi_{\perp}$) components. Each transition $|n\rangle \rightarrow |m\rangle$ represents one term in the summation of Equation (4.3). Note that the transitions allowed for magnetic fields applied along the z direction can only occur between levels of same symmetry (see Appendix A).

4.5.2 Magnetic interactions: Curie-Weiss fitting

Beyond the single ion suceptibility, we analyse χ_{DC} at low temperatures to obtain informations about the interactions between the magnetic atoms [3]. The inclusion of exchange interactions into the Hamiltonian of a magnetic system causes a shift θ_{CW} in the point where the reciprocal susceptibility intercepts the temperature axis [120]. This is modelled by the Curie-Weiss model

$$\chi_{ex} = \frac{N\mu_{eff}^2}{k_B(T - \theta_{CW})} + \chi_{vv}, \tag{4.5}$$

where χ_{vV} is the van Vleck susceptibility and μ_{eff}^2 is the ground-state magnetic moment, or *effective* moment, both already defined. The parameter θ_{CW} is the *Curie-Weiss temperature*. This quantity, in theory, defines the development of long-range order in the system and is proportional to the strength of the interactions between the magnetic atoms. In frustrated magnets, nevertheless, θ_{CW} adquires a much more elusive character, since the value of θ_{CW} seems to *not* correlate with the existence (or not) of phase transitions in the material and an ultimate magnetically ordered ground-state [7]. The reason behind that is one of the main

[3] In the absence of strong dipolar interactions caused by large magnetic moments, the exchange interaction is the dominant term in the Hamiltonian of pyrochlores [7].

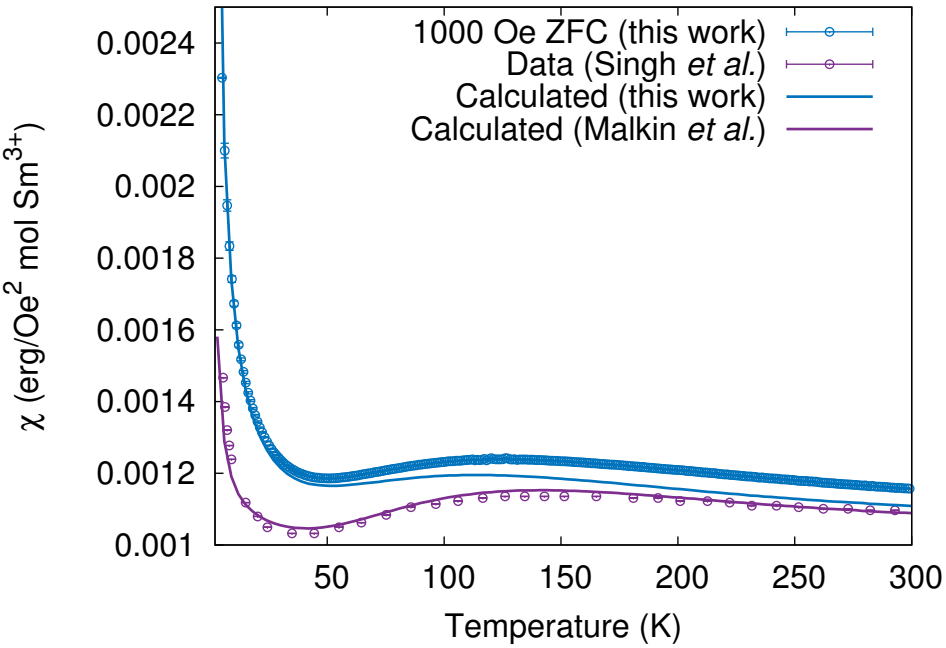

Figure 4.10: Powder susceptibility of $^{154}Sm_2Ti_2O_7$ measured in an 1000 Oe magnetic field (blue circles) and calculated in this work (blue line). The purple empty circles and lines show the susceptibility measured in a single crystal by Singh *et al.* [93] and modelled in the work of Malkin *et al.* [94]

motivations for the study of frustrated magnets: how far can go the competition between interactions in order to suppress long-range order completely?

Equation (4.5) is fitted to the 1000 Oe susceptibility data. At temperatures $T \ll E_{|\pm1\rangle}/k_B \sim 150$ K, where $E_{|\pm1\rangle}$ is the energy of the first excited CEF doublet in the stannate or titanate, $\chi_{vV} \sim 10^{-3}$ erg/(Oe^2 mol Sm^{3+}) is expected to be constant[4]. Similarly, it could be assumed that, at low temperatures, $\mu_{eff} = \langle \boldsymbol{\mu}_z^0 \rangle$, as given in Table 4.4. However, since the calculated χ_{CEF} does not reproduce optimally the measured susceptibility, μ_{eff} and χ_{vV}, together with the θ_{CW}, are kept as fitting parameters. Thus we open the possibility that both quantities acquire values that depart from those calculated in Section 4.4.

	$^{154}Sm_2Ti_2O_7$		$^{154}Sm_2Sn_2O_7$	
Fitting inteval (K)	[5, 30]	[5, 20]	[5, 30]	[5, 20]
μ_{eff} (μ_B)	0.23(2)	0.24(3)	0.27(3)	0.29(4)
θ_{CW} (K)	-0.26(4)	-0.43(8)	0.11(6)	-0.44(7)
χ_{vV} ($\times 10^{-4}$)	10.10(2)	9.98(6)	11.81(4)	11.22(7)

Table 4.5: Parameters obtained from the fitting of Equation (4.5) to the 1000 Oe field susceptibility data for titanate and stannate. The van Vleck χ_{vV} contribution to the susceptibility is given in units of erg Oe^{-2} mol^{-1}. The best fittings in the interval from 5 to 30 K are shown in Figure 4.11.

[4]The van Vleck susceptibility χ_{vV} was calculated for both compounds using Equation (4.3)

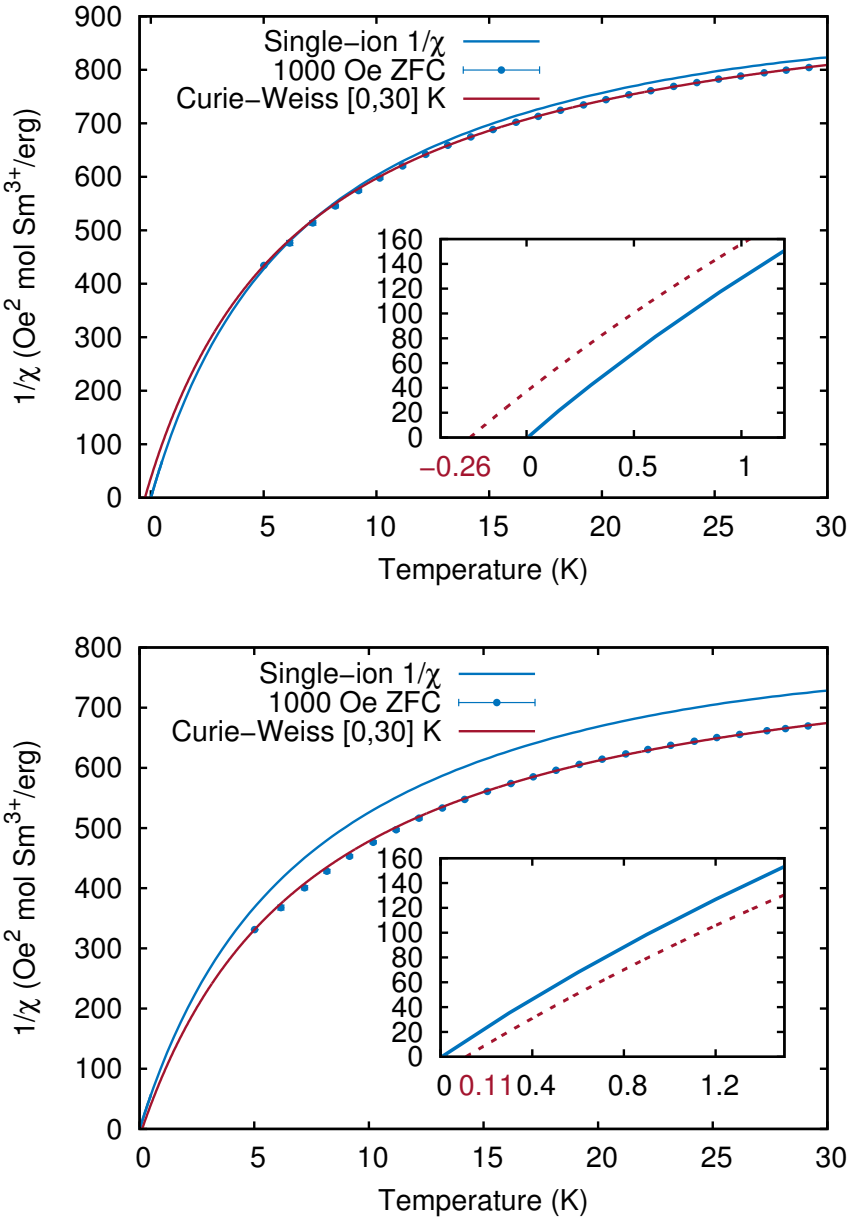

Figure 4.11: Curie-Weiss fitting to the low temperature susceptibility of $^{154}Sm_2Ti_2O_7$ (top) and $^{154}Sm_2Sn_2O_7$ (bottom) . Data (blue filled circles) were collected in an 1000 Oe applied magnetic field. The fit shown here (dark red line) is performed in the temperature interval $[0, 30]$ K. The blue line corresponds to the single ion inverse susceptibility, calculated using Equation (4.3) and presented previously in the plots of Figure 4.8. In the insets, a zoomed in view of the intercept of the curves with the temperature axis is shown.

The results of the Curie-Weiss fittings are gathered in Table 4.5. They were performed between two different intervals for which only the ground-state would be significantly populated: between 5 and 20 K and between 5 and 30 K[5].The best fittings for the broader temperature

[5]This is done because, in line with what was mentioned before, the significance of the Curie-Weiss fitting results in frustrated pyrochlores is arguable. Many times, it has been shown that θ_{CW} depends strongly on the temperature fitting interval [121, 122].

interval are shown in Figure 4.11. Overall, for both intervals the parameters are in agreement with the titanate values reported by Singh *et al.* [93], and the stannate values reported by Bondah-Jagalu *et al.* [99]. Nevertheless, the Curie-Weiss temperature of the stannate appears to be more sensitive to the increase of the upper limit of the temperature fitting interval. Paradoxically, θ_{CW} changes from $0.11(6)$ K, signalising effective ferromagnetism, to $-0.44(7)$ K, signalising predominantly antiferromagnetic interactions. In Bondah-Jagalu *et al.* [99], which performed the fittings within the interval $[5, 20]$ K, a higher, ferromagnetic $\theta_{\mathrm{CW}} = 1.36(21)$ K is reported. In the next Chapter, neutron diffraction results are going to demonstrate that the stannate effectively develops a long-range antiferromagnetic order. Clearly, however, we cannot conclude which interactions are predominant in those compounds considering only the Curie-Weiss fitting.

4.6 Quadrupolar and magnetoelastic coupling

The lattice normal vibrations distort slightly the crystalline electric field surrounding the magnetic atom. The interaction between phonons and the electrons of the $4f$ shell is known as *magnetoelastic coupling* [123, 124]. Our interest in investigating a possible magnetoelastic coupling in the Sm-based pyrochlores is to find an explanation to the unusual decrease of the anisotropic displacement parameters of some atoms in the lattice with the increase in temperature, as discussed in the end of Section 3.3.

The manifestations of the magnetoelastic coupling in the experimental neutron structure factor are manyfold, and include the complete hybridisation of the CEF excitations and phonon dispersions [124,125] as well as the formation of vibronic bound states [105,126,127]. A vibronic bound state is a hybridised mode that shares similarities with single ion and phonon excitations. In the presence of coupling, vibronic modes appear close to pure CEF states in the $S(|\mathbf{Q}|, \omega)$. The energy of the latter is nevertheless shifted, so that the mean energy of the CEF and vibronic state, as well as their combined intensity, can be regarded as the original values of the crystal field excitation in the absence of coupling [126, 128].

In the structure factor shown earlier in this Chapter, neither hybridisations or bound states could be directly identified. On the other hand, phonons and CEF excitations appear at similar energies, as the measured $S(|\mathbf{Q}|, \omega)$ presented in Figures 4.2 and 4.4 demonstrate. Hence, the foremost prerequisite for the occurrence of this interaction is satisfied by the Sm-based pyrochlores. In what follows, we briefly discuss the possibility of existence of a magnetoelastic coupling between the single ion excitations and the pyrochlore phonons.

The deformations around the 16*d* Wyckoff positions caused by lattice vibrations can be described in first approximation by quadrupolar operators [128]. Those can be treated as operator equivalents of the quadratic forms of the rare-earth point group (D_{3d}), and are determined using an ordinary character table [129]. It is easy to show that the relevant operators for pyrochlores, grouped by symmetry, are

$$\begin{aligned} \boldsymbol{O_1}(A_1) &= 3J_z^2 - J(J+1), \\ \boldsymbol{O_{2,3}}(E) &= J_x^2 - J_y^2, \quad J_xJ_y + J_yJ_x, \\ \boldsymbol{O_{4,5}}(E) &= J_xJ_z + J_zJ_x, \quad J_yJ_z + J_zJ_y, \end{aligned} \tag{4.6}$$

where we intentionally keep the notation of Reference [114]. The selection rules for interactions determine that quadrupolar coupling can only occur when the symmetry of the operator is identical to the symmetry of the phonon mode [128]. Inspection of Table III of Reference [114] indicates that pyrochlore optical phonon modes with energy similar to CEF excitations of both stannate and titanate, and symmetry E, cross the Brillouin zone center at ~ 14 meV and

$^{154}Sm_2Ti_2O_7$
$\|\pm1\rangle = 0.943 \left\|{}^6H_{5/2}, \mp\frac{1}{2}\right\rangle \mp 0.131 \left\|{}^6H_{5/2}, \pm\frac{5}{2}\right\rangle$
$\|\pm2\rangle = -0.026 \left\|{}^6H_{5/2}, \pm\frac{1}{2}\right\rangle \pm 0.072 \left\|{}^6H_{5/2}, \mp\frac{1}{2}\right\rangle \pm 0.302 \left\|{}^6H_{5/2}, \mp\frac{5}{2}\right\rangle + 0.851 \left\|{}^6H_{5/2}, \pm\frac{5}{2}\right\rangle$
$^{154}Sm_2Sn_2O_7$
$\|\pm1\rangle = \pm0.177 \left\|{}^6H_{5/2}, \mp\frac{1}{2}\right\rangle + 0.937 \left\|{}^6H_{5/2}, \pm\frac{1}{2}\right\rangle \pm 0.168 \left\|{}^6H_{5/2}, \mp\frac{5}{2}\right\rangle - 0.032 \left\|{}^6H_{5/2}, \pm\frac{5}{2}\right\rangle$
$\|\pm2\rangle = \mp0.122 \left\|{}^6H_{5/2}, \pm\frac{1}{2}\right\rangle + 0.014 \left\|{}^6H_{5/2}, \mp\frac{1}{2}\right\rangle \pm 0.099 \left\|{}^6H_{5/2}, \pm\frac{5}{2}\right\rangle + 0.893 \left\|{}^6H_{5/2}, \mp\frac{5}{2}\right\rangle$

Table 4.6: Eigenstates $|\pm n\rangle$ of the n^{th} excited CEF levels. These functions are used in the calculation of the quadrupolar matrix elements shown in Table 4.7.

$\sim$ 28 meV. Even though Ruminy *et al.* [114] report first principles calculations of three other pyrochlores, namely the spin ices $Ho(Dy)_2Ti_2O_7$ and $Tb_2Ti_2O_7$, the position of the phonon branches will vary only slightly as a consequence of mass and lattice parameters differences between the compounds reported here and there. The variations in zone centre phonon energies with the change of rare-earth atoms can be observed in the earlier work of Vandenborre *et al.* [115].

The modes at 14 and 28 meV correspond to the motion of the rare-earth with respect to the oxygen cage (bending of the $O^{48f}-Sm-O^{8b}$ and $O^{48f}-Sm-O^{48f}$ bonds and stretching of the $Sm-O^{8b}$ bond) and, in the stannate, the highest energy mode has a strong contribution of $O^{48f}-Sn-O^{48f}$ stretching [115]. We arrive thus to an explanation about why the anomalous anisotropic displacement parameters of different atoms are to a greater or lesser extent affected by the magnetoelastic coupling. The temperature scale at which this anomalous behaviour is observed also supports the occurrence of interaction, since, once the lowest energy CEF levels are depopulated, the coupling breaks down and the ADP's assume the more natural tendency to increase with increasing temperatures.

In the *dispersionless model*, the Hamiltonian of the magnetoelastic interaction is given by [124, 130]

$$H_{mec} = \sum_n E_n(|n\rangle \langle n|) + \hbar\omega_0 \sum_\mu (\boldsymbol{a}_\mu^\dagger \boldsymbol{a}_\mu + 1/2) - g_0 \sum_\mu (\boldsymbol{a}_\mu + \boldsymbol{a}_\mu^\dagger)\boldsymbol{O}_\mu, \tag{4.7}$$

where $|n\rangle$ represents $|+n\rangle$ and $|-n\rangle$, the eigenstates of the n^{th} excited CEF level. The $\boldsymbol{a}_\mu$ and $\boldsymbol{a}_\mu^\dagger$ are the annihilation and creator operators of a phonon with displacement μ and energy $\hbar\omega_0$. The parameter g_0 is an empirical quantity giving the strength of the magnetoelastic interaction. Once a vibronic state resulting from the coupling between a phonon and a CEF level is detected in the spectra, g_0 can be determined via a least-squares refinement in order to find the values that diagonalise H_{mec} [126, 128].

As the value of g_0 must be determined from experiment, and this is an information our results did not deliver, we restrict ourselves to obtaining the absolute value squared of the quadrupolar matrix elements, the other terms that affect the relative strength of coupling in Equation (4.7). The procedure is to calculate $|\langle \boldsymbol{O}_\mu \rangle|^2$ for transitions from the ground-state to the first or second excited-state (or vice-versa), i.e. $|\langle +0| \boldsymbol{O}_\mu |+1(+2)\rangle|^2 = |\langle -0| \boldsymbol{O}_\mu |-1(-2)\rangle|^2$ and $|\langle +0| \boldsymbol{O}_\mu |-1(-2)\rangle|^2 = |\langle -0| \boldsymbol{O}_\mu |+1(+2)\rangle|^2$. The only operators with matrix elements different of zero are $\boldsymbol{O}_{4,5}$. We then use the wave functions of Table 4.6, together with those of the ground-state given in Table 4.3, to find the values presented in Table 4.7.

The face values in Table 4.7 are meaningless without a ground for comparison between $^{154}Sm_2Ti_2O_7$ and $^{154}Sm_2Sn_2O_7$ and other members of the pyrochlore family. Fortunately, some

	$^{154}Sm_2Ti_2O_7$	$^{154}Sm_2Sn_2O_7$
$\lvert\langle +0\rvert \boldsymbol{O}_{4,5} \lvert +1\rangle\rvert^2$	1.84	5.47
$\lvert\langle +0\rvert \boldsymbol{O}_{4,5} \lvert -1\rangle\rvert^2$	5.35	2.06
$\lvert\langle +0\rvert \boldsymbol{O}_{4,5} \lvert +2\rangle\rvert^2$	28.43	0.11
$\lvert\langle +0\rvert \boldsymbol{O}_{4,5} \lvert -2\rangle\rvert^2$	6.90	15.79

Table 4.7: Finite matrix elements of the quadrupolar operators of Equation (4.6) for transitions from the ground-state to the first and second excited doublets.

recent works shed light on the interaction between phononic and magnetic degrees of freedom in those materials, especially after study conducted by Fennell *et al.* [105]. This group worked intensively, firstly on first principle calculations of the phonon modes propagating over a large extent of the Brillouin zone [114] and, later, on the influence of the magnetoelastic coupling on the magnetic behaviour of some of the most well studied pyrochlores [105,106]. Reference [106], in particular, studies the mechanisms of spin-flipping in the "hot spin ice". Ruminy *et al.* [106] also present the expected values of the quadrupolar operators for, *inter alia*, $Ho_2Ti_2O_7$. The $|\langle \boldsymbol{O}_\mu \rangle|^2$ calculated here are overall of the same order of magnitude than those of the spin ice. More recently, Gaudet *et al.* [125] showed that a so far undetected vibronic bond state exists in Ho^{3+} pyrochlores, demonstrating its presence close to a CEF level for which the $\sum_\mu |\langle \boldsymbol{O}_\mu \rangle|^2$ is one order of magnitude higher than the values calculated for the Sm-based pyrochlores.

4.7 Comment on the possible octupolar coupling

Continuing our discussion about multipolar terms in the pyrochlore Hamiltonian, we comment now on one particularity that $^{154}Sm_2Ti_2O_7$ and $^{154}Sm_2Sn_2O_7$ share with some of their sister compounds. The ground-state of the easy-axis Kramers doublets that contain the terms $\left|^{2S+1}L_J, \pm\frac{3}{2}\right\rangle$, $\left|^{2S+1}L_J, \pm\frac{9}{2}\right\rangle$ and $\left|^{2S+1}L_J, \pm\frac{15}{2}\right\rangle$ have the special denomination of dipole-octupole doublets [34, 113]. The reason is simple: those terms in the doublets are connected by an octupolar operator. The relevant operator was shown in References [29,34,36] to be

$$\boldsymbol{\tau} = i(\boldsymbol{J}_+^3 + \boldsymbol{J}_-^3). \tag{4.8}$$

Recently, octupolar coupling was invoked to explain exotic excitations measured in $Nd_2Zr_2O_7$. $Nd_2Zr_2O_7$ is a light rare-earth pyrochlore, which develops an all-in-all-out order below $T_N = 285$ mK [36] or $T_N \approx 0.4$ mK [122]. The ordered magnetic moment of $(0.8 \pm 0.05)\mu_B/(1.26 \pm 0.02)\mu_B$ is strongly reduced from the expected $2.3\mu_B/2.65\mu_B$ calculated from the CEF analysis of the References [36,122].

The curious result provided by inelastic neutron scattering performed in $Nd_2Zr_2O_7$ is that the observed dynamics, manifested in the form of sharp spin waves, cannot be recovered using a model Hamiltonian including only Ising interactions. Also curious is the flat band of excitations that exhibit pinch-point patterns in reciprocal space [29, 110]. Unlike the classical spin ices, though, the flat band is gapped from the elastic line, appearing at an energy of about 70 μeV [29]. Two different models were proposed to explain this strange spin dynamics in $Nd_2Zr_2O_7$ [29,35], both relying on the dipolar-octupolar nature of the Kramers doublet of the Nd^{3+} ion in the pyrochlore lattice.

The agreement between the two models lies in the concept of fragmentation, which had its classical version introduced by Brooks-Barlett *et al.* [131]. The theory results organically from

the dumbbell model of spin ices. The magnetic moment density $\boldsymbol{M}$ in one tetrahedron can be decomposed in two components as

$$\boldsymbol{M} = \boldsymbol{M}_m + \boldsymbol{M}_d = \nabla\psi(r) + \nabla \times \boldsymbol{Q}, \tag{4.9}$$

i.e., into a divergence-free density $\boldsymbol{M_d}$ related to a dipolar field, and a divergence-full $\boldsymbol{M_m}$ related to the emergent monopole density (see Section 1.4). When the compound obeys strictly the ice rules (spin ice at very low temperatures), $\boldsymbol{M_m} = 0$. The work of Brooks-Barlett *et al.*, however, emphasises that the conversion of density between $\boldsymbol{M_d}$ and $\boldsymbol{M_m}$ is gradual, and, in the most general situation, magnetic "charge" can coexist with an emergent Coloumb phase, which exhibits long-range order. Following this approach, it is inferred and later, proved, that a structure of crystallised doubly charged monopoles, which satisfies the condition $\boldsymbol{M_d} = 0$ everywhere, corresponds to the all-in-all-out order. As the charge density $\boldsymbol{M}$ is shared between the two contributions, the materials in their fractionalised state present all-in-all-out long-range structure concomitantly with the most famous spin ice characteristic: the pinch-point pattern.

This theory suffered adaptations in order to describe the experimental findings on $Nd_2Zr_2O_7$, including transverse Hamiltonian terms determined by the octupole-octupole interaction [29,34] or introduced as a natural consequence of the special symmetry of the doublet [34,35]. Even though it is outside of the scope of this work to compare or comment on theories, it is worth to note that the XYZ model of Benton [35] seems to capture better the experimental details of the $Nd_2Zr_2O_7$ spectra.

4.8 Summary of the results presented in this chapter

This Chapter presented results of inelastic neutron scattering measurements conducted in order to investigate the crystal electric field excitations present in Sm-based pyrochlores. The aim of this analysis was to find the single ion, ground and excited-state wave functions that closely describe macroscopic bulk quantities, such as static magnetic susceptibility and its unusual non-linear van Vleck contribution.

An issue raised in Chapter 3, about why the ADP's of the Rietveld refinements present an unusual decrease with increasing temperature, is discussed. The answer to this question is connected to the calculation of the first multipolar matrix elements relevant to pyrochlores. It was shown that magnetoelastic interactions are likely to happen in those compounds, although the definitive experimental evidence, which would be the measurement of a vibronic bounding state, is left to future experiments.

Independently of the dipolar static magnetism, another conclusion from the CEF analyses is that Sm-based pyrochlores belong to the class of materials that possess dipolar-octupolar doublet ground-states [36,95]. In addition to the dipolar matrix elements connecting the $|\pm 0\rangle$ states, which would result in the ordered magnetic moment calculated using Equation (4.2), the next most important contribution to the total magnetic moment results from the matrix elements of the octupolar operator [36] connecting the states $\left|{}^6H_{3n/2}, \pm\frac{3n}{2}\right\rangle$. An interesting question to be addressed is whether the ground-state associated octupolar moments order or remain dynamic at low temperatures. It is possible that the system undergoes an octupolar ordering, as predicted by the XYZ model of Reference [34]. Similarly to the dipolar case, the octupolar ordering gives rise to a symmetry breaking resulting in a phase transition in heat capacity. Another possibility, already mentioned in Reference [95], is that octupolar-octupolar coupling induces the magnetic moment fragmentation, in a similar fashion to the studied in the pyrochlore $Nd_2Zr_2O_7$ [29,36]. Neutron diffraction probes directly only dipolar ordering, while octupolar interactions can be indirectly inferred from the magnetic excitations present in

the material [29,36] (see also Subsection 1.3.2.1). Considering that fragmentation indeed occurs in Sm-based pyrochlores, it would be interesting to find out whether it could be measured with neutron scattering employing small quantities of powder samples. In the next chapter we examine further this question.

Chapter 5

Sm-based pyrochlores: magnetic long-range order and ground-state dynamics

5.1 Overview and context

Chapter 4 ended with a question: can the Sm-based pyrochlores present fractionalised excitations? The answer is obviously *yes*, since, in first analysis, $Sm_2Ti_2O_7$ and $Sm_2Sn_2O_7$ display the essential theoretical requirements for fragmentation. The present chapter will focus on the search of experimental signatures that could prove this statement.

We have seen in Chapter 3 that $^{154}Sm_2Ti_2O_7$ and $^{154}Sm_2Sn_2O_7$ present sharp anomalies in their low temperature heat capacities, at temperatures $T_N^{Ti} = 350$ mK and $T_N^{Sn} = 440$ mK, respectively. Now, we perform neutron diffraction measurements at low temperatures to investigate if this anomaly is indeed caused by a phase transition to a long-range ordered magnetic state. In addition to the neutron data, more sensitive μSR measurements are employed in order to detect spontaneous oscillations caused by very small magnetic moments, which would in principle be unmeasurable using neutron scattering.

As the peculiar ground-state dynamics are one of the signatures of the fragmentation physics, inelastic neutron scattering is also performed on the powder samples. Finally, we point out some of the experimental difficulties related to those measurements and the interpretation of the results.

5.2 Experimental details

Unpolarised neutron diffraction measurements were carried out at very low temperatures at the instruments DNS at MLZ, and WISH at ISIS [85]. Only $^{154}Sm_2Ti_2O_7$ was measured at WISH. The powder was loaded in a copper cylinder can sealed in He atmosphere. Subkelvin temperatures were achieved with help of an Oxford dilution insert placed in an Oxford cryostat. Measurements were performed at 50 mK, 700 mK and 10 K for approximately 6 hours at each temperature.

At DNS, diffraction data were collected for both $^{154}Sm_2Ti_2O_7$ and $^{154}Sm_2Sn_2O_7$ using a FRM II standard cryogen-free dilution cryostat. The powders were loaded in an annular cooper cylinder can and sealed in He atmosphere. To speed up the cooling process, $\sim$ 0.1 ml of deuterated ethanol was added to the samples. This procedure was already used by us before and resulted in the successful cooling of powders in the dilution temperature regime. For the stannate, data were collected for 12 hours at 75 and 600 mK and for the titanate for at least 18 hours at 170 and 600 mK.

μSR data were recorded in the transverse field (TF) geometry at several temperatures using the instrument HAL-9500 at PSI. Few grams of the isotopically enriched powder samples were loaded, pressed and wrapped in a 10 μm thick silver foil, which was subsequently attached to a

high purity silver plate with GE-varnish. The silver plate was connected to the cold-finger of a dilution cryostat built exclusively for the instrument.

Inelastic neutron scattering experiments conducted on the stannate sample were performed at the instrument OSIRIS, at ISIS, while backscattering data was collected for the titanate at SPHERES, at MLZ. The sample mounting procedures were the same performed for the measurements at DNS, as described above. The spectra were recorded upon cooling for several hours at each temperature, until sufficiently good statistics could be achieved.

5.3 Long-range order

Figure 5.1(a) displays $^{154}Sm_2Ti_2O_7$ data collected at the highest resolution detector bank of WISH (average $2\theta \sim 152°$) at 700 mK. The diffraction pattern shown is interrupted around the peaks belonging to either the sample can (Cu) or to the dilution insert (Al) Bragg peaks. Only the momentum transfer range relevant to the observation of magnetism in Sm, based on the $f^2(\mathbf{Q})$ of Figure 4.1, is displayed.

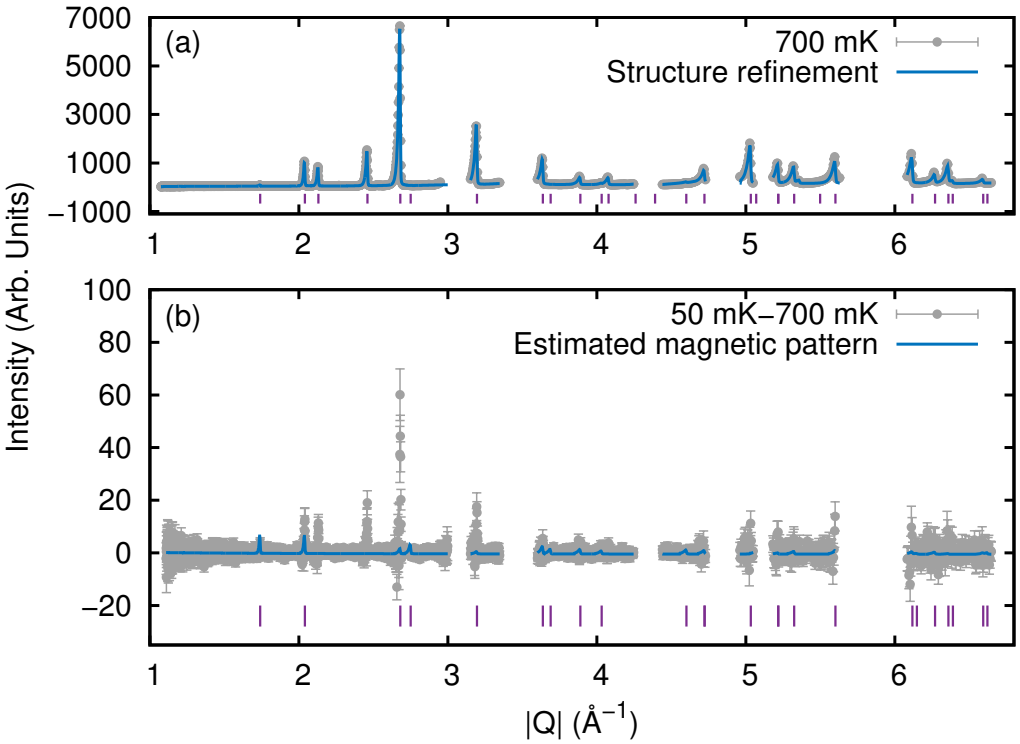

Figure 5.1: Diffraction patterns of the $^{154}Sm_2Ti_2O_7$ sample measured at WISH. (a) Data collected at a temperature of 700 mK is displayed. The regions containing Bragg peaks from the copper sample can or from the cryostat aluminium are omitted. (b) Subtraction of data collected at 700 mK from data collected at 50 mK. The strongest differences in panel (b) correlate with the intensity of the structural Bragg peaks shown in (a). The tick marks in (a) highlight the position of structural reflections, while in (b) they mark the position of expected magnetic Bragg peaks for a structure corresponding to the irreducible representation Γ_3.

We remind the reader that, in the titanate, the anomaly in heat capacity takes place at $T_N^{Ti} = 350$ mK (see Figure 3.4). In order to investigate the presence of magnetic ordering in the sample below this temperature, the data collected at 700 mK was subtracted from data

measured at 50 mK. The resulting difference is shown in Figure 5.1(b). The relevant differences, measured above the background level, appear all at structural Bragg peak positions. Moreover, the intensity of the peaks in Figure 5.1(b) correlates strongly with the intensity of the nuclear reflections in 5.1(a).

Initially, given the limited experimental time, we suspected that the actual sample temperature had not reached the nominal 50 mK, which would be the cause behind the lack of magnetic reflections in the pattern of Figure 5.1(b). The sample was then reloaded in a copper annular cylinder and sealed in He atmosphere. At DNS, using unpolarised neutrons to maximise the neutron flux at sample position, new diffraction patterns were collected at 170 mK and 600 mK. Figure 5.2(a) shows the diffraction pattern measured above the phase transition temperature, while Figure 5.2(b) shows the difference between low and high temperature diffraction patterns, exactly as in Figure 5.1(b). The correlation between measured peak intensities in 5.2(a) and 5.2(b) is less obvious, since the weaker (220) and (331) reflections (red thicks) have a magnitude comparable with the stronger (111) and (400) structural Bragg peaks. Even so, analogously to the WISH data, the DNS measurement does not offer a clear-cut signal of sample magnetism.

In Mauws *et al.* [95], polarised and unpolarised neutron diffraction results suggested the presence of an all-in-all-out long-range order in a single crystal sample of $^{154}Sm_2Ti_2O_7$. In their work, the intensity of the (220) Bragg reflection shows a drop at T_N^{Ti} upon warming from the base temperature. The ordered magnetic moment reported in Reference [95] is of $0.44(7)\mu_B$, which is in agreement with the ground-state magnetic moment calculated with their crystal field analysis (see Table 4.4).

Comparing the nominal experimental conditions between our DNS data and the measurements of Reference [95], it is possible that the temperature of 170 mK is not low enough for our sample magnetisation to reach full saturation. Nevertheless, in the sample of Mauws *et al.*, as far as we can visually determine from the published data, the (220) peak intensity already reaches $\sim 90\%$ of its maximum just below 200 mK. We believe that it is unlikely that the temperature of our powder did not go across T_N^{Ti} in any of the two experiments at WISH and DNS. Given that, again based on the (220) intensity data of Reference [95], the onset of the ordered phase is very sharp, we expect that small temperature differences from T_N^{Ti} would produce visual effects on the measured diffraction pattern.

Site	X	Y	Z	$m^a(\mu_B)$	$m^b(\mu_B)$	$m^c(\mu_B)$
1	$\frac{1}{2}$	$\frac{1}{2}$	$\frac{1}{2}$	0.14(1)	0.14(1)	0.14(1)
2	$\frac{1}{4}$	$\frac{1}{4}$	$\frac{1}{2}$	-0.14(1)	-0.14(1)	0.14(1)
3	$\frac{1}{2}$	$\frac{1}{4}$	$\frac{1}{4}$	0.14(1)	-0.14(1)	-0.14(1)
4	$\frac{1}{4}$	$\frac{1}{2}$	$\frac{1}{4}$	-0.14(1)	0.14(1)	-0.14(1)

Table 5.1: Magnetic moments obtained in the refinement of $^{154}Sm_2Sn_2O_7$ data of Figure 5.2(d). m^a, m^b and m^c are the magnetic moment components along the global-x, y and z axis, respectively.

As we have predicted, the study of one Sm-based pyrochlore would greatly support the analysis performed on the other. The data obtained at DNS for the stannate sample at 600 mK is shown in Figure 5.2(c), while the subtraction between low (75 mK) and high temperature is shown in 5.2(d). Unlike the titanate, the diffraction pattern of $^{154}Sm_2Sn_2O_7$ does display clear Bragg peaks in the difference plot. Only two of them are observed within the DNS momentum transfer window, corresponding to the also structural (220) and (311) positions. Representation

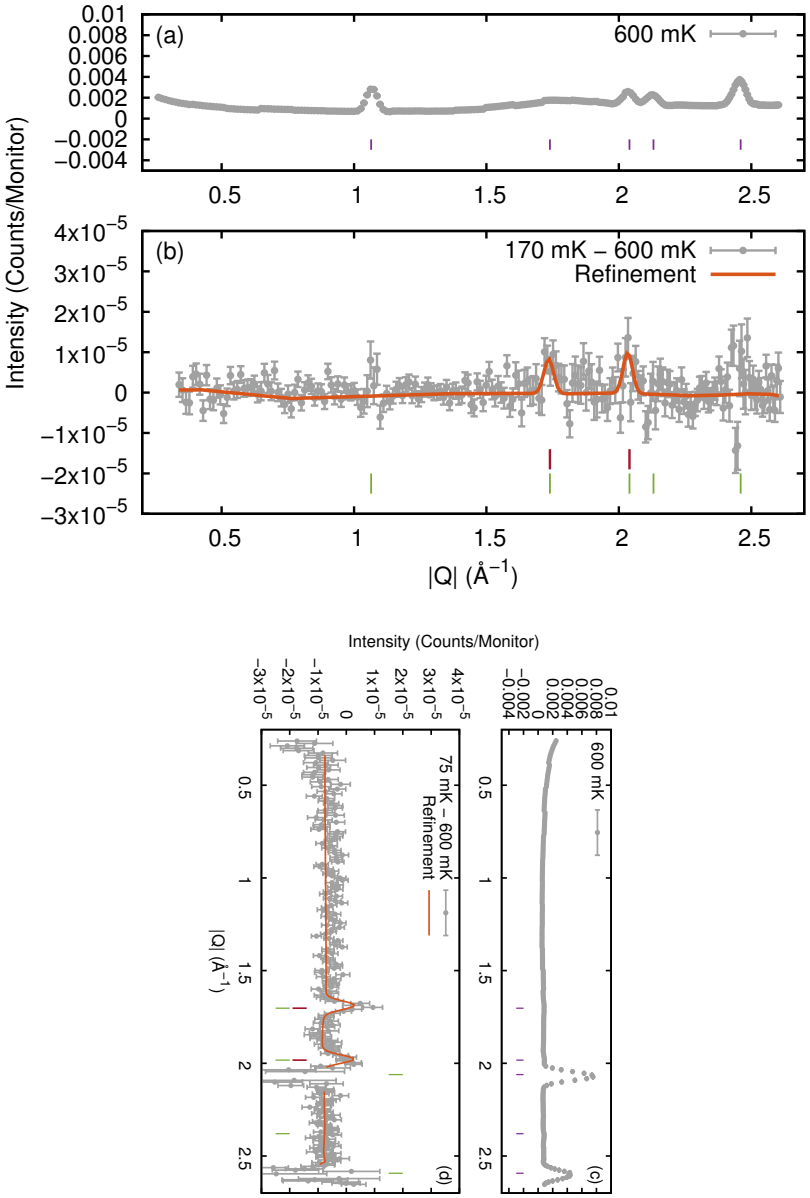

Figure 5.2: Diffraction patterns of $^{154}Sm_2Ti_2O_7$ (a) and $^{154}Sm_2Sn_2O_7$ (c) measured at DNS. (a) and (c): data collected at a temperature of 600 mK is displayed. (b) and (d): subtraction of low and high temperature data, as indicated in the labels. The tick marks in (a) and (c) highlight the position of structural reflections, while in (b) and (d) they mark the position of expected magnetic Bragg peaks for a structure corresponding to the irreducible representation Γ_3.

analysis performed in the $Fd\bar{3}m$ space group shows that the propagation vector $\boldsymbol{k} = 0$ magnetic structure which displays uniquely those reflections is the all-in-all-out arrangement, with irreducible representation Γ_3. The refined profile is shown along with the magnetic scattering data in Figure 5.2(d). The refined magnetic moment, $\mu_{ref} = 0.25(2)\mu_B$, is in remarkable agreement with the one predicted in the crystal field analysis, namely, $\langle \boldsymbol{\mu}_z^0 \rangle = 0.27\mu_B$. The individual components of the magnetic moment along each one of the global crystallographic axis is shown in Table 5.1, for one tetrahedron unit.

With the results for the stannate in hands, we return to the problem of the $^{154}Sm_2Ti_2O_7$. The unambiguous long-range order cannot be shown, but a maximum value of ordered magnetic moment from WISH and DNS data, limited by background and noise level, can be definitely estimated. We repeat the representation analysis carried out on the stannate and determine a maximum $\mu_{\rm ref} \sim 0.17\mu_{\rm B}$ from both datasets collected for the titanate. Those final fittings are superposed to the measured patterns in Figures 5.1(b) and 5.2(b).

5.4 μSR results

The low temperature *zero field* μSR asymmetry of $^{154}Sm_2Ti_2O_7$, collected at HAL-9500, are shown in the top panel of Figure 5.3. In the ordered state, if the muon occupies only magnetic equivalent sites subject to a local field $\boldsymbol{B_{loc}}$, one expects to measure spontaneous oscillations in the asymmetry in response to the perpendicular component of $\boldsymbol{B_{loc}}$, or $B_{loc}^{\perp}$. Nevertheless, the titanate asymmetry displays no oscillations, and even no temperature dependence in the measured temperature range.

Before describing the model we used to extract quantitative information from the measured asymmetry, the data recorded for $^{154}Sm_2Sn_2O_7$ is shown in the bottom panel of Figure 5.3. The temperature interval covered in the stannate experiment is relatively broader and the highest temperature accessed was of 10 K, well above $T_{\rm N}^{Sn} = 440$ mK. Similarly to the titanate, very few, if any, temperature dependence can be perceived in $A(t)$ uniquely from the plots.

In transverse field geometry, the muon depolarisation can be shown to obey the function [91]

$$A(t) = A(0)\exp\left(-\frac{\Delta^2 t^2}{2\gamma_\mu^2}\right)\cos(\omega_\mu t), \tag{5.1}$$

where $\omega_\mu = \gamma_\mu B_{loc}^{\perp}$. The quantity Δ/γ_μ is the variance (rms width) of the internal field distribution along the applied field. Equation (5.1) describes an oscillatory cosine function involved in a gaussian envelope.

Generally speaking, three main hypothesis can be speculated as causes for the absence of oscillations in the muon asymmetry when the material is in its long-range ordered phase. The first is that $B_{loc}^{\perp} = 0$. In the all-in-all-out magnetic structure, the geometric centre of the rare-earth tetrahedra is the single point where the local field is identically equal to zero [110]. As this position is expected to host an oxygen atom in ideal pyrochlore samples (i.e. most sites should not be vacant), this hypothesis can be ruled out. The occupation, by the muon, of many magnetically inequivalent sites is a second probable cause. That would result in a broad internal field distribution, or conversely a broad Δ. Once, in Equation (5.1), $\frac{\Delta}{\gamma_\mu} \gg \omega_\mu$, a strong depolarisation should be detected at early times [91], similarly to what happens in spin ice systems [132]. However, no evidence suggesting a sharp asymmetry loss close to $t = 0$ is visible in our muon data.

The third and last explanation, usually considered more plausible in frustrated pyrochlore studies that report μSR results, is that the internal field is not necessarily static in the muon resolved time window [133–138]. A fast fluctuation rate of $B_{loc}^{\perp}$ may cause a strong damping of the muon oscillations in the ordered state. When dynamics are involved, an approximation to the asymmetry function is the Abragam formula [91]

$$A(t) = A(0)\exp\left\{-\frac{\Delta^2}{\gamma_\mu^2\nu^2}\left[\exp(-\nu t) - 1 + \nu t\right]\right\}\cos(\omega_\mu t), \tag{5.2}$$

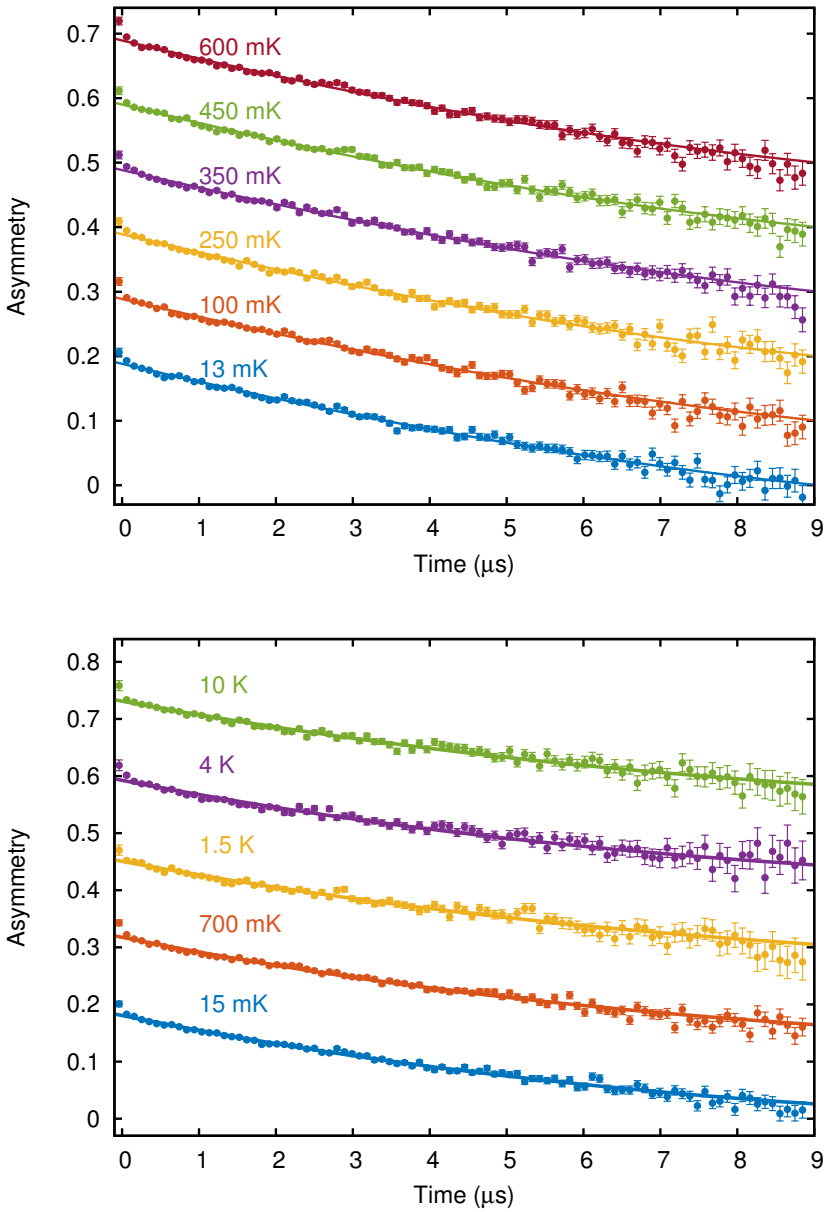

Figure 5.3: Asymmetry $A(t)$ measured at several temperatures for $^{154}Sm_2Ti_2O_7$ (top) and $^{154}Sm_2Sn_2O_7$ (bottom). For clarity, each next temperature was dislocated by steps of 0.1 in asymmetry. The continuous lines are fittings of Equation (5.3) for a small residual applied transverse field of ~ 2 G. The fitting parameters are shown in Figure 5.4(a) and 5.4(b).

where ν is the local field fluctuation rate. We do not use explicitly Equation (5.2) here, but it is useful for determining the shape of $A(t)$ in the fast fluctuation limit, or *motional narrowing limit*. If $\nu \gg \Delta$, Equation (5.2) reduces to

$$A(t) = A(0) \exp\left(-\frac{\Delta^2}{\gamma_\mu^2 \nu} t\right) \cos(\omega_\mu t). \tag{5.3}$$

For simplicity, we assume $\frac{\Delta^2}{\gamma_\mu^2 \nu} = \lambda$, which is going to be called *relaxation rate* from now on. Equation (5.3) was fitted to the experimental $A(t)$, and the best fittings are shown as

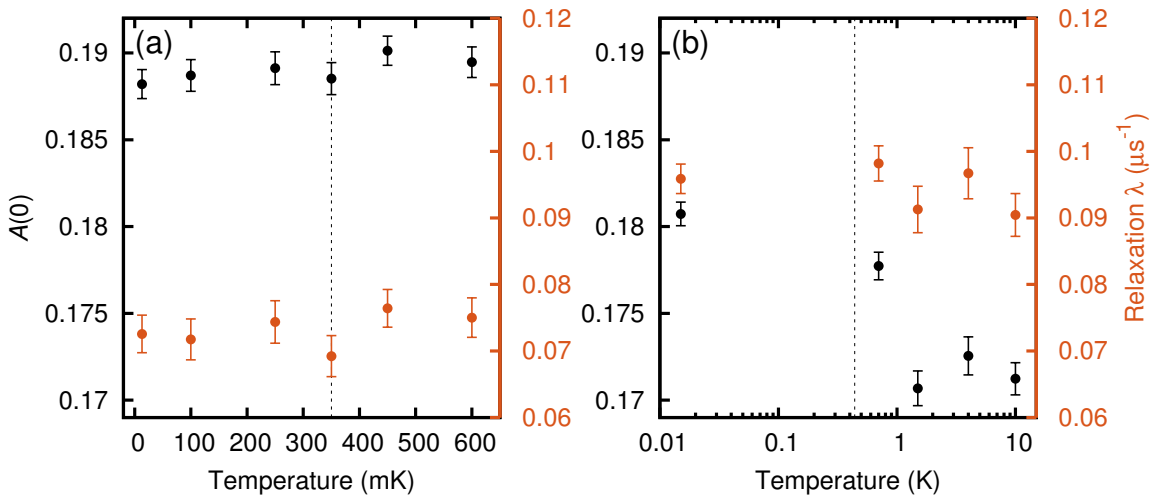

Figure 5.4: Initial asymmetry $A(0)$ and relaxation rate λ obtained from the fitting of Equation (5.3) to the data measured at several temperatures for (a)$^{154}Sm_2Ti_2O_7$ and (b)$^{154}Sm_2Sn_2O_7$. Note that the horizontal axis of the panel (b) is in log scale, due to the broader temperature range at which data were collected. The vertical dashed lines highlight the phase transition temperature of both compounds.

continuous lines along with the data in Figure 5.3. We note that the argument of the cosine function is necessarily different of zero, because the experiment was performed with a small residual transverse field of ~ 2 G. Despite being small, this field causes a slower recovery of the asymmetry at longer times ($> 7\ \mu s$).

In Figure 5.4, the temperature dependence of λ can be observed. As it could be anticipated from Figure 5.3, no considerable variation in the relaxation is observed over the temperature range measured for both samples. The initial asymmetry loss is stronger in the stannate, and this is the first noticeable difference between the compounds. Moreover, the relaxation of $^{154}Sm_2Sn_2O_7$ is also faster, as the higher values of λ in Figure 5.4(b) demonstrate. In Figure 5.5, the asymmetry of both samples measured at the dilution base temperature is directly compared.

The initial asymmetry does not change considerably with temperature in $^{154}Sm_2Ti_2O_7$. However, a weak drop in $A(t)$ is detected upon warming in the stannate. Since the decrease is stronger between 700 mK and 1.5 K, it is not clear that a relationship between relaxation and phase transition at T_N^{Sn} indeed exists. A decrease in $A(0)$ associated with an increase in λ signalises an overall slowing down of the dynamics of the system [132, 139], and indicates that most of the muon depolarisation is taking place outside the muon time resolved window. Therefore, it is strange that the drop in $A(0)$ is being detected upon an increase in the temperature, while the most intuitive behaviour would be that the dynamics slow down when the temperature decreases.

A final interesting feature in the measured $A(t)$ is the fast initial asymmetry loss. To illustrate that, we show in the inset of Figure 5.5 the measured early time relaxation along with the fitting carried out using Equation (5.3). The drop in asymmetry indicates the presence of a second, faster relaxation component at early times, a behaviour that, though contra-intuitive, has been observed in systems shown to develop long-range order at a critical temperature T_c [133, 134, 139]. However, the additional λ in those compounds becomes gradually more important upon cooling, as the temperature reaches values closer to T_c, subsequently decreasing

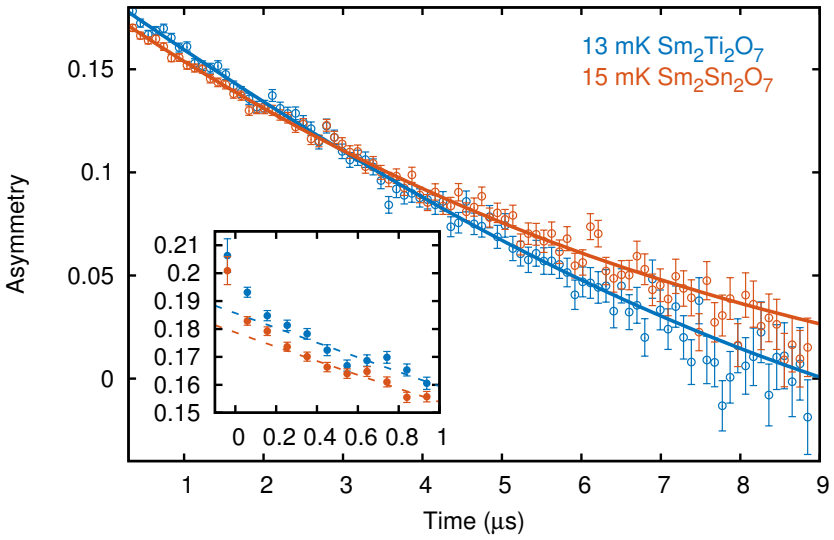

Figure 5.5: $A(t)$ measured at base temperature (circles with error bars) and best fittings of Equation (5.3) (continuous lines in the main plot, dashed lines in the inset) for $^{154}Sm_2Ti_2O_7$ and $^{154}Sm_2Ti_2O_7$. In the inset, the initial asymmetry loss is highlighted.

down to a plateau. The lack of temperature dependence in $A(t)$ and the constant relaxation rate measured above and below T_N in both compounds is therefore intriguing.

A high enough applied transverse field ($B_T \gg 5\Delta/\gamma_\mu$ [91]) transforms Equation (5.2) back into (5.1) [140], which is independent of ν. That is a method to probe the internal field distribution Δ along the direction of B_T at the muon site. Transverse field measurements are also useful to obtain information that can be related to the macroscopic sample properties. In the paramagnetic state, under an applied B_T, the muon spin will precess with a frequency $\gamma_\mu(B_T - B_{loc}^{\perp})$. Consequently, a shift in the oscillation frequency, the so-called *Knight shift*, will be detected [132]. This frequency shift is proportional to the field independent paramagnetic susceptibility χ of the compound.

Initially, we performed transverse field measurements on $^{154}Sm_2Ti_2O_7$ in order to measure a possible Knight shift in the precession frequency of the muon. In Figure 5.6, we show the fast Fourier transform of field data measured at two different temperatures. In the ω-space, both the muon precession frequencies and the field distribution Δ can be directly observed, since the Fourier transform of Equation (5.1) is simply given by

$$A(t) = C \exp\left(-\frac{(\omega - \omega_\mu)^2}{2\Delta^2}\right), \tag{5.4}$$

where C is a normalisation factor.

From Figure 5.6, it is clear that no frequency shift is measured. The muon spin frequency ω_μ is almost precisely equal to B_T for temperatures above (600 mK) and below (15 mK) T_N^{Ti}. Under fields equal to 5000 Oe and 20000 Oe, shown in the middle panels of Figure 5.6, some slight difference between the two temperatures can be observed in the Fourier transform. However, as those differences do not appear systematically for all the magnetic fields probed, either smaller or higher, we disregard this as a significant result.

Also in Figure 5.6, the internal field distribution Δ can be seen to increase with increasing

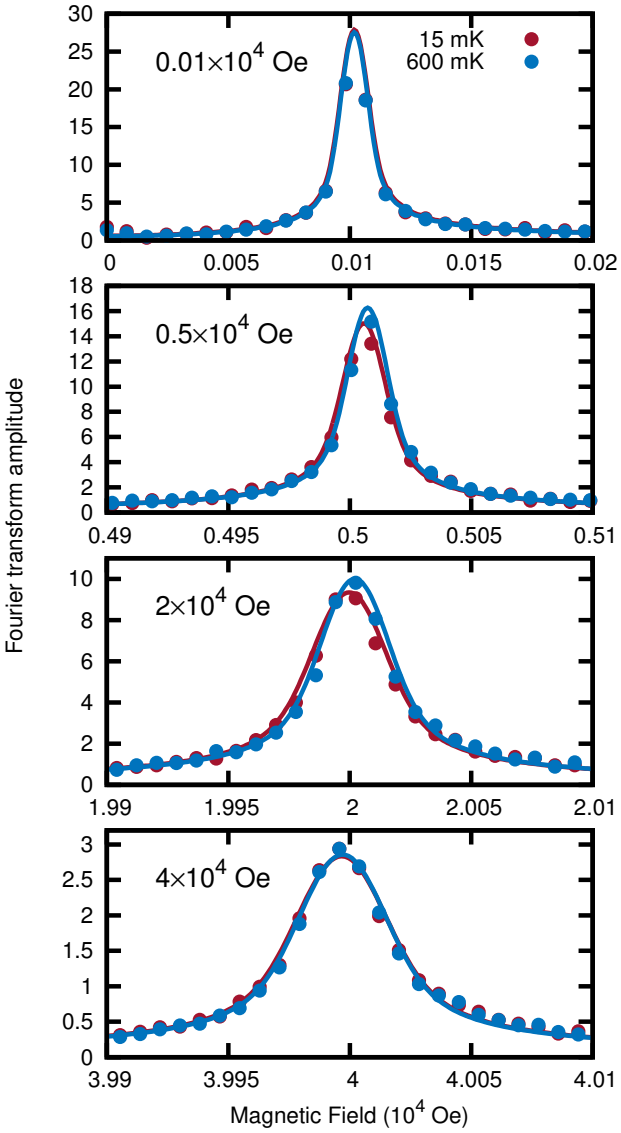

Figure 5.6: Fast Fourier transform of the $A(t)$ of $^{154}Sm_2Ti_2O_7$ measured at 16 and 600 mK under several applied magnetic fields.

magnetic field. Rather than being an intrinsic magnetic characteristic of the compound, this effect is analogous to the *powder line broadening* observed in polycrystalline samples also in other spin resonance techniques, as NMR [113, 141, 142]. Since the system is strongly anisotropic and given the powder averaging of the $\boldsymbol{B}_{loc}$ relative to the external field, a measurement of the intrinsic field distribution at the muon site is unaccessible.

As it is not clear how much the applied magnetic field disturbes the magnetic moments of the Sm^{3+} ion, on the stannate sample, we studied the effects of smaller applied fields at the time dependent asymmetry. The data for a $B_T = 10$ Oe collected at several temperatures are shown in Figure 5.7. As before, no temperature dependence in the oscillations induced by the external field is observed.

Nothing is surprising when one refers to muon results in frustrated systems, especially in pyrochlore magnets. A large body of work has presented muon results which can be consistent [143–145] or inconsistent [132–139, 146–149] with other probes, as neutron scattering

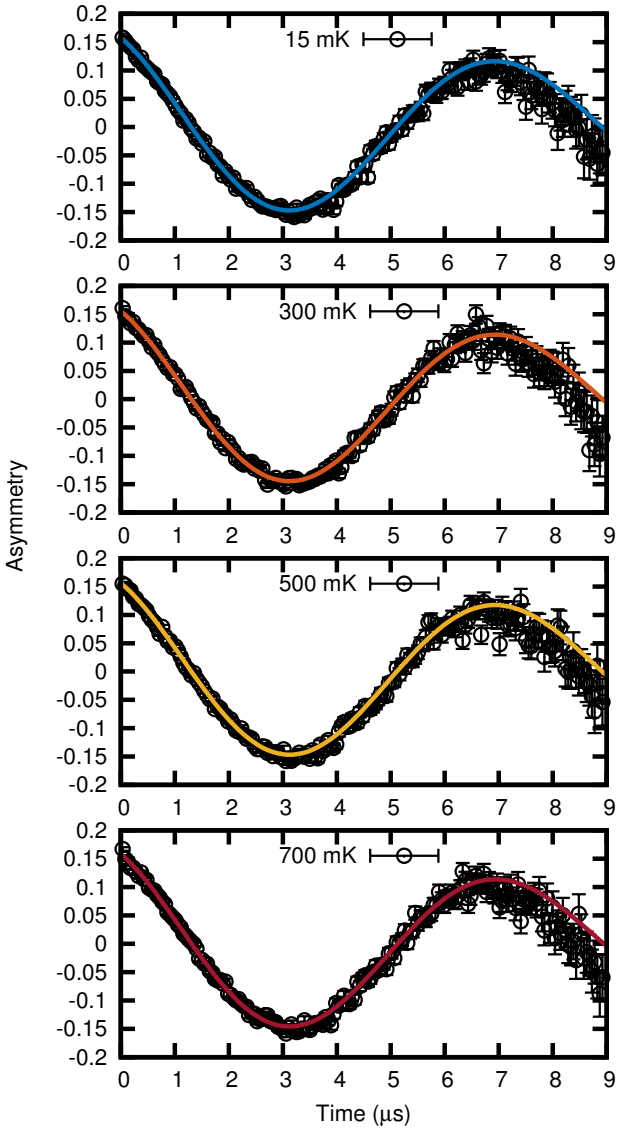

Figure 5.7: Stannate $A(t)$ measured under an applied magnetic field $B_T = 10$ Oe for several temperatures above and below T_N^{Sn}.

or susceptibility measurements. All those studies have in common the application of μSR techniques to probe the ground-state of pyrochlore magnets. Most of them are, as determined by neutron diffraction, long-range ordered. Nevertheless, from all the works cited above, only two systems shown to be ordered at low temperatures, $Nd_2Sn_2O_7$ and $Gd_2Ti_2O_7$, present oscillations in the muon asymmetry spectra [134, 147]. It does not mean, however, that the asymmetry is consistent with that expected for a conventional ordered system. In coexistence with the spontaneous oscillations, References [134, 147] present an exponential relaxation, believed to be caused by a non-vanishing dynamic component of the system of spins.

A possible explanation to this inconsistency is that μSR and neutron scattering probe different time scales. In other words, what appears to be static to neutrons may be far too dynamic in the muon time resolved window. That motivates the authors of References [147, 150] to attribute the exponential relaxation occurring in the ordered state to the so-called *persistent spin dynamics*. This conclusion points to the existence of a spin component that never orders

down to the lowest measurable temperatures, the foremost indication that the systems are, indeed, frustrated. In fact, the latter works performed on pyrochlore magnets hugely benefitted from that conclusion, as most studies following Reference [147] find an exponential relaxation attributed to persistent spin dynamics in the ground-states of those compounds.

In the work of Reference [95], a Gaussian, temperature dependent asymmetry decay and, importantly, no oscillations, are measured in a $^{154}Sm_2Ti_2O_7$ single crystal sample. It is necessary then to address the contrasting behaviour, which is not rare in pyrochlore studies, between our sample and theirs. For example, the pyrochlore titanate $Yb_2Ti_2O_7$, the object of study of the next chapters of this thesis, has presented qualitatively different μSR results for different samples [139, 146]. However, this compound seems to present a sample dependence in most of its magnetic properties, including a very sensitive heat capacity phase transition. In Chapter 3, we showed that the phase transition of the sample of Reference [95] is almost identical to the one in our sample, what is an indication that the quality of the samples is similar.

Other two explanations for our results cannot be completely ruled out. The most appealing one is that our experiment is flawed, i.e., that the muons are *i.* stopping in the sample surroundings, like in the silver foil which covers the sample, for example, or *ii.* that both samples did not cool down. In the former case, however, at very low temperatures, the expected relaxation would reflect a static, random field distribution, or a Kubo-Toyabe asymmetry decay [89, 92], what is absolutely different from what we observed. The other doubt, concerning the temperature, can never be eliminated.

5.5 Inelastic neutron scattering results

We start this section presenting our trial to identify excitations in the $^{154}Sm_2Sn_2O_7$ spectrum. In Figure 5.8 three momentum transfer cuts performed on data collected at OSIRIS are displayed. The sample was measured at three temperatures: one (25 mK) way below $T_N^{Sn} = 450$ mK, another closer to the phase transition (400 mK) and one above (600 mK). The experimental $|\boldsymbol{Q}|$-range accessed in the experiments belongs to the interval $[0.3, 1.8]$ Å^{-1}, with an interruption between $[0.8, 1.0]$ Å^{-1} due to some defective detectors. The observation of weak ground-state dynamics, if existent, would be specially favoured in the stannate sample, due to the absence of strong structural Bragg peaks in the momentum transfer window of OSIRIS [see for exemple Figure 5.2(a) (bottom)].

Even so, the relevant information present in Figure 5.8 is the lack of temperature dependence in the data of $^{154}Sm_2Sn_2O_7$. This is emphasised by the simultaneous plot of the instrumental resolution function of OSIRIS determined from vanadium calibration scans. Clearly, quasielastic scattering or inelastic modes are absent in the spectra of the stannate for all the temperatures observed. Elastic incoherent scattering concentrates basically all the spectral weight, except in the high $|\boldsymbol{Q}|$ region, which contains the strong structural (400) Bragg peak.

Although the absence of excitations in the 25 mK spectrum of the stannate may not be surprising, one would expect to observe quasielastic scattering signalising paramagnetic fluctuations above T_N^{Sn}. They should be apparent at 600 mK, just above the ordering temperature. Once the long-range order is developed, the quasielastic spectral weight becomes elastic, signalising a static ground-state in the time window probed by neutrons. The failure in detecting the paramagnetic scattering brings about two possibilities: either the dynamics are too slow to be detectable considering the instrumental resolution of ~ 25 μeV of OSIRIS (or even too slow to be detectable, hypothetically, in the neutron dynamic range of the highest resolution spectrometer) or too weak to carry enough spectral weight measurable with the current experimental statistics.

To try to overcome the resolution problem, we performed backscattering spectroscopy at the

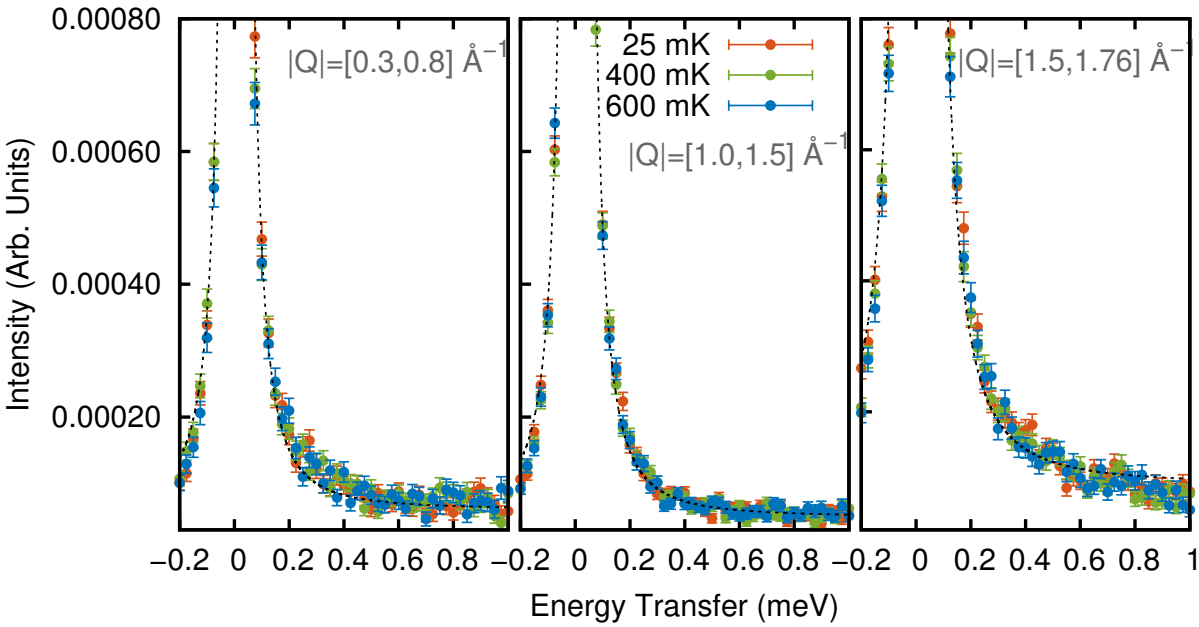

Figure 5.8: $|\boldsymbol{Q}|$-cuts performed on the spectra of $^{154}Sm_2Sn_2O_7$ measured at OSIRIS at 25, 400 and 600 mK. The momentum transfer intervals covered in each cut are indicated in the Figure labels. The black dashed lines represent the resolution function estimated from vanadium scans. No temperature dependence indicative of evolution in the inelastic pattern is observed.

instrument SPHERES, at MLZ [151]. Now the intrinsic instrumental resolution is of ~ 0.6 μeV, which allows us to identify dynamic processes in a $\Delta t = \hbar/\Delta E =$ time scale. The instrument in Garching offers the exact complimentary data to the experimental information obtained before, with a dynamical range of ~ 28 μeV, a bit larger than the OSIRIS elastic line width. In order to obtain some insights about the spectra of the titanate sample, at SPHERES we collected data for $^{154}Sm_2Ti_2O_7$.

The spectra, shown in Figure 5.9, are measured at four different temperatures. This time, data were collected up to 3 K, so that the possibility of the system being already frozen at temperatures $T \gg T_N^{Ti} = 350$ mK could be excluded. Unfortunately, the information given by the backscattering experiment is not more than that obtained before. As Figure 5.9 shows, fluctuations in the ground-state, as well as paramagnetic scattering above $T_N^{Ti} = 350$ mK, are absent also in the titanate.

5.6 Summary of the results presented in this chapter

This is the last Chapter presenting results of the Sm-based pyrochlores. Its main objectives were to probe the magnetic properties of $^{154}Sm_2Ti_2O_7$ and $^{154}Sm_2Sn_2O_7$ at very low temperatures.

Based on heat capacity measurements shown in Chapter 3, neutron diffraction was employed to ascertain the presence of magnetic long-range order in the ground-state of both samples.

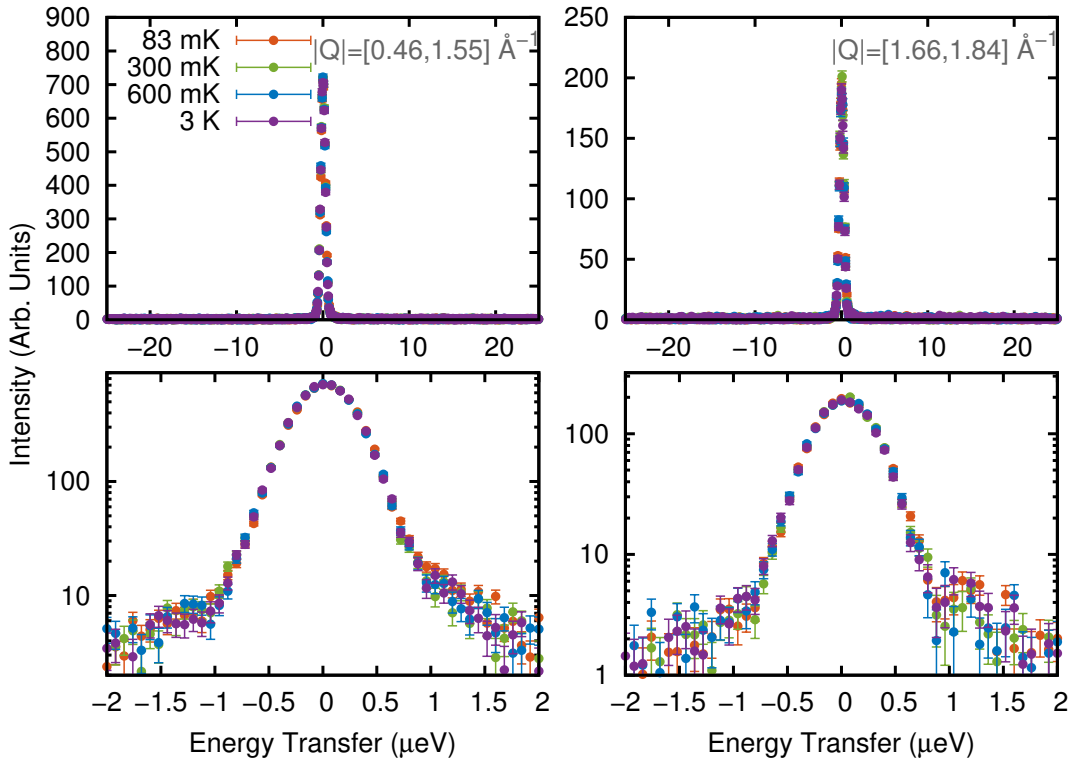

Figure 5.9: Top: data, grouped by detector, of $^{154}Sm_2Ti_2O_7$ measured at SPHERES. The $|\boldsymbol{Q}|$-range comprised by each curve is indicated in the Figure labels. Data were collected at 83, 300, 600 mK and, finally, 3 K. Bottom: blown up view of the data of the top panels. Note that the intensity axis is now in log scale. As for the stannate, no temperature dependence is observed in the spectra. The width of the curves is verified to be strictly given by the resolution (0.65 μeV), with a slight, instrumental asymmetry at the tails.

While one is clearly identified in the DNS elastic data of $^{154}Sm_2Sn_2O_7$, in the titanate, if existent, no order could not be accessed in our experiments at WISH and DNS.

As for the muon experiment, it is not clear whether it can definitely point to the existence of either order or disorder in frustrated pyrochlores. Because we cannot assure that the powder samples were, indeed, at the nominal mixing chamber temperatures, the absence of spontaneous muon spin precession in our μSR studies, or even the measured asymmetry, cannot be used to draw definitive conclusions.

The information obtained employing inelastic neutron scattering in the measurement of excitations was shown to be strongly limited, especially considering the observation time necessary to gather statistically significant information about the magnetic scattering. Nevertheless, the trial by itself was definitely required: the presence of dynamic magnetic moment is the *sine qua non* indication of the quantum spin ice behaviour.

If we were not fortunate to obtain this signature for the Sm-based pyrochlores, that is certainly not true for the compound presented next. The results of Chapters 6 and 7 represent a considerable advance in the understanding of how, at least empirically, frustration may affect the spin dynamics of the enigmatic $Yb_2Ti_2O_7$.

Chapter 6

The ground-sate of $Yb_2Ti_2O_7$ I: magnetic long-range order

6.1 Overview and context

Our work on the pyrochlore $Yb_2Ti_2O_7$ was left to the end, and these last two chapters will be dedicated to a complete analysis performed on a powder sample of this compound. Ytterbium titanate was my first research topic, and the sample was not synthesised by me. The study started unpretentious: the published work on the compound, although interesting, was demonstrated to be of validity somewhat limited to the particular samples reported. Moreover, the intrinsic physics displayed in the ground-states of pristine samples, as became clear after some particular works [152,153], including my own [79], is not, in the present moment, close to be understood.

It is almost impossible to initiate this chapter without an overview of the $Yb_2Ti_2O_7$ literature. The history of the compound is long, and the first work (results of its infamous heat capacity anomaly) was presented exactly 50 years ago by Blöte *et al.* [154]. Deeper investigations started in the end of the last century and beginning of the 2000's, following the discovery of the spin ices. Unlike those on its famous sisters, the studies on ytterbium titanate did not report so straightforwardly the nature of the phase transition measured decades before. The rest is history, and the single general consensus seems to be that $Yb_2Ti_2O_7$ is unique in its own way. It is the purpose of the next chapters to show why.

The work on $Yb_2Ti_2O_7$ is presented in the chronological order in which the experiments where performed. For clarity, we separate the results in two: the *static* part in this chapter and the *dynamics* in the next. The evidences are summed up in the end of Chapter 7, where a complete discussion about the results takes place.

6.2 State of the science

$Yb_2Ti_2O_7$ has attracted intense research in recent years [24,152,155,156] as a possible quantum spin ice candidate [58]. The crystal field acting on the lowest energy $^2F_{7/2}$ multiplet of the Yb^{3+} lifts the ground-state degeneracy of the rare-earth into four Kramers doublets. The 700 K gap between the predominantly $m_J = \pm 1/2$ ground-sate and the first excited level [157,158] is the largest within the whole titanate family [22]. This property renders $Yb_2Ti_2O_7$ a very robust effective spin-1/2 system, particularly suited for theoretical investigations on the QSI physics based on an anisotropic spin Hamiltonian model [24,152,153,155].

Particularly noteworthy is the strong sample dependence of the magnetic behaviour of $Yb_2Ti_2O_7$ at low temperatures. One suggestion for the discrepant results presented by different samples is the so-called *stuffing*, in this sense meaning that the Yb^{3+} ions expected to occupy the A lattice site are randomly distributed on the B site, which in principle should host only Ti^{4+} ions. This substitution was shown to occur on 2.3% of the B sites in the sample reported in

the studies presented in References [159,160], a rather small amount of site disorder that can suppress a phase transition at $T_c \sim 280$ mK [161].

Another, more recent, examples of sample dependent behaviour were reported by two works performed on nominally stoichiometric powder samples [160,162], which show distinct long-range magnetic orders evolving at low temperatures. Reference [160] proposes an ice-like splayed ferromagnetic ground-state, in which the magnetic moments are canted $(14 \pm 5)^\circ$ from the cubic $\langle 100 \rangle$ axis, in a two-in-two-out arrangement. The neutron diffraction data of Reference [162] seem to be consistent with the development of an all-in-all-out ferromagnetic structure below T_c, considering that the representation analysis within the $Fd\bar{3}m$ structural space group fails in reproducing the adopted magnetic structure.

In this chapter we present experiments carried out in order to characterise in detail a powder sample of $Yb_2Ti_2O_7$. Rietveld refinements performed on high-resolution neutron powder diffraction data are used to determine precisely our sample stoichiometry. Heat capacity at constant pressure displays a sharp phase transition at $T_c = 280$ mK. In addition to this anomaly, a second, higher temperature broad hump is also observed centred at $\sim$ 2.5 K. Neutron diffraction confirms the development of a *quasicollinear* ferromagnetic long-range order below T_c with a strongly reduced ordered moment of the Yb^{3+} ions.

6.3 Experimental details

The powder sample was prepared by the group of M. R. Lees at the University of Warwick using the standard solid state reaction method. Stoichiometric quantities of Yb_2O_3 and TiO_2 oxides were mixed, pressed into pellets and sintered at 1300 °C for several days with intermediate grindings [163].

High resolution neutron powder diffraction was performed at the HRPT diffractometer at the Paul Scherer Institute (PSI) [164], Switzerland, at 2 and 150 K. The powder was loaded in a vanadium cylindrical sample can and cooled in a liquid He cryostat. A neutron wavelength of 1.155 Å was chosen in order to have an optimal combination of intensity and resolution.

The molar heat capacity at constant pressure (C_p) of our $Yb_2Ti_2O_7$ powder was measured using our in-house Physical Property Measurement System (PPMS) from Quantum Design. After the addenda measurement, a pressed powder sample was mounted on a dilution refrigerator insert. The size and shape of the sample were chosen in order to optimize the thermal coupling between sample and puck, which was maintained at more than 70% for all temperature points measured above 100 mK.

Polarised and unpolarised neutron diffraction measurements were carried out at DNS. Approximately 6 g of powder were packed in an annular cylinder sample holder made with oxygen-free copper and sealed in a He atmosphere. Measurements were taken in the temperature range from 100 mK up to 600 mK in a dilution insert installed in a top-loading CCR cryostat. Particular attention was paid to the thermalisation of powders in the mK temperature regime. Typical neutron polarisation rate at the chosen neutron wavelength ($\lambda = 4.2$ Å) is of about 96%. The standard procedures such as flipping-ratio correction and normalisation of detector efficiency have been applied for data analysis. Additional diffraction data were also collected at OSIRIS for approximately 2 hours. These data offer a considerably better ($\Delta d/d \sim 10^{-3}$) resolution than our DNS data.

6.4 Sample stoichiometry

Rietveld refinements were performed on the powder diffraction patterns collected at 2 and 150 K using FullProf [69]. The model employed in the refinement is presented in Table 6.1. Initially, the perfect stoichiometric model, with $\alpha = 0$, is considered, and the patterns were fitted together in order to obtain the best set of instrument dependent parameters. After that, lattice constants, $48f$ oxygen free-position and isotropic displacement parameters (IDP) were refined for each temperature separately. Given the oxygen environment surrounding the Yb^{3+} site, it is expected that the displacement parameters are actually anisotropic [6]. The results obtained for the Sm-based pyrochlores in Chapter 3, however, support our assumption that the displacement anisotropy at temperatures $T < 100$ K is negligible. Moreover, as the quality of the fitting, in the present case, does not respond in a sensible way to the refinement of the anisotropic displacement parameters, we opted to carry out the refinement of the IDP's and analyse their behaviour with the stuffing level as discussed in the text below. The calculated patterns are plotted along with the measured ones in Figure 6.1. The refined set of parameters are summarised in Tables 6.2 and 6.3.

Atom	Site	X	Y	Z	Nominal Occupancy
Yb	16*d*	0.5	0.5	0.5	1.0
Ti	16*c*	0	0	0	1.0-α
Yb	16*c*	0.5	0.5	0.5	α
O^{8b}	8*b*	0.375	0.375	0.375	1.0-$\alpha/2$
O^{48f}	$48f$	x	0.125	0.125	1.0

Table 6.1: Model used in the Rietveld refinement of $Yb_2Ti_2O_7$. The parameter α denotes the sample *stuffing level*.

Temperature (K)	Lattice Parameter (Å)	x	Occupancy of Yb^{3+} at 16c site	R_{wp}
Stoichiometric model				
2	10.01275(2)	0.33140(5)	-	0.0671
150	10.02061(2)	0.33105(6)	-	0.0787
1.5 (Yaouanc *et al.*)	10.0220(5)	0.332(1)	-	-
150 (Ross *et al.*)	10.01111(3)	0.33122(3)	-	0.0414
Stuffed model				
2	10.01273(2)	0.33126(5)	0.0009(1)	0.0670
150	10.02059(2)	0.33095(6)	0.0010(1)	0.0785
150 (Ross *et al.*)	10.01111(3)	0.33121(3)	0.002(1)	0.0415

Table 6.2: Refined lattice parameters and x coordinates for the stoichiometric and stuffed models. For comparison, results from the *sintered powder* of Ross *et al.* [159] and Yaouanc *et al.* [162] are shown.

As reported in several studies [6,7,165,166] and noted in Chapter 3, pyrochlores are prone to oxygen deficiencies, especially at the Wickoff 8*b* site. A safe estimate of oxygen vacancies

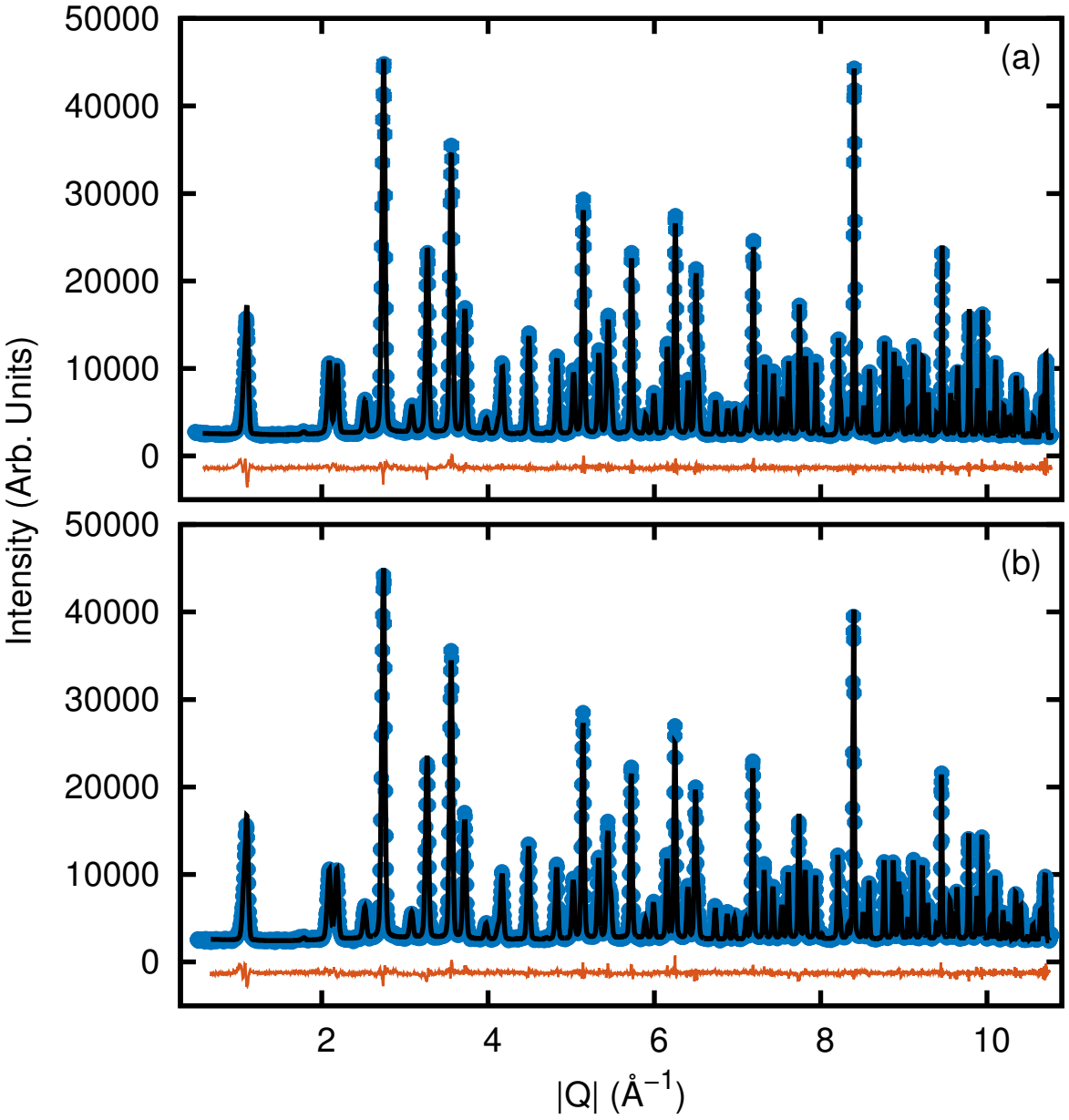

Figure 6.1: High resolution neutron diffraction data (blue circles) and best refinement (black lines) for data collected at (a) 150 K and (b) 2 K. The difference between the calculated and the measured intensities is given by the orange line below each pattern.

Ion	IDP at 2 K (Å^2)	IDP at 150 K (Å^2)
Stoichiometric Model		
Yb	0.124(4)	0.347(5)
Ti	0.21(1)	0.31(1)
O^{8b}	0.309(5)	0.396(6)
O^{48f}	0.21(1)	0.26(1)
Stuffed Model		
Yb	0.147(4)	0.37(5)
Ti / Yb	0.12(2)	0.21(2)
O^{8b}	0.267(6)	0.348(7)
O^{48f}	0.21(1)	0.26(1)

Table 6.3: Isotropic displacement parameters refined at 2 and 150 K for both models considered in this work. The refined profiles are shown in Figure 6.1.

is possible because the reflection conditions for the pyrochlore structure allow the Rietveld refinement of the oxygen content unambiguously: those Bragg peaks for which $h+k+l=4n$ and that, additionally, do not match the conditions $h,k,l=4n$ or $h,k,l=4n+2$ [examples are (220), (422), (620), etc.] contain scattering contributions exclusively from O^{2-} ions. The refinement of the occupancy of the $8b$ position supports a 0.6% reduced oxygen content in our sample, without an overall change in the other parameters obtained for the stoichiometric model, already shown in Tables 6.2 and 6.3.

Possible stuffing ($\alpha \neq 0$) was also considered and a model with Yb^{3+} at the Ti^{4+} site was refined. The fit parameters are displayed in Tables 6.2 and 6.3. Our results for the stuffed model are compared with the results of Ross *et al.* [159] at 150 K. While refined separately for each temperature, the α, which we call *stuffing level*, shows almost the same value given uncertainties. The lattice parameter and x values also do not change significantly from one model to the other. As already widely discussed in Reference [159], the thermal displacement parameters have been shown to be sensitive, in particular at the $16c$ site, to stuffing.

In order to investigate the behaviour of the IDP's quantitatively, we considered two different scenarios. In the first, we fixed all the parameters obtained in the stoichiometric model. By changing the stuffing level on the $16c$ Wyckoff position and the oxygen occupancy, which we should modify in order to keep the charge neutrality of the material, we analysed the variation in the fitting χ^2. It can be seen in the main panel of Figure 6.2, in which the results of this analysis are shown, that the minimum of the χ^2 is located between 0 and 1%.

In the second scenario, we allow the IDP of the $16c$ site to vary freely while manually changing the stuffing level and analysing the behaviour of the χ^2. All the other parameters were kept fix. The results are displayed in the inset of Figure 6.2, where it can be clearly seen that IDP and stuffing level are inversely correlated parameters. This can be understood if we note that *i.* the symmetry and reflection conditions for Yb and Ti sites are the same and *ii.* both thermal displacement and ionic substitution may reduce, although with a different $|\boldsymbol{Q}|$ dependence, the measured peak intensities. Consequently, the discrepancy between the fitted IDP values presented in Table 6.3 for stuffed and stoichiometric models is in a great extent dependent on the differences in scattering cross-sections of Yb (23.4 barns) and Ti (4.35 barns). As the displacement parameters are constrained to the atomic site, it is natural that the calculated IDP's are smaller in the model in which one puts Yb in the place of the less scattering Ti. When

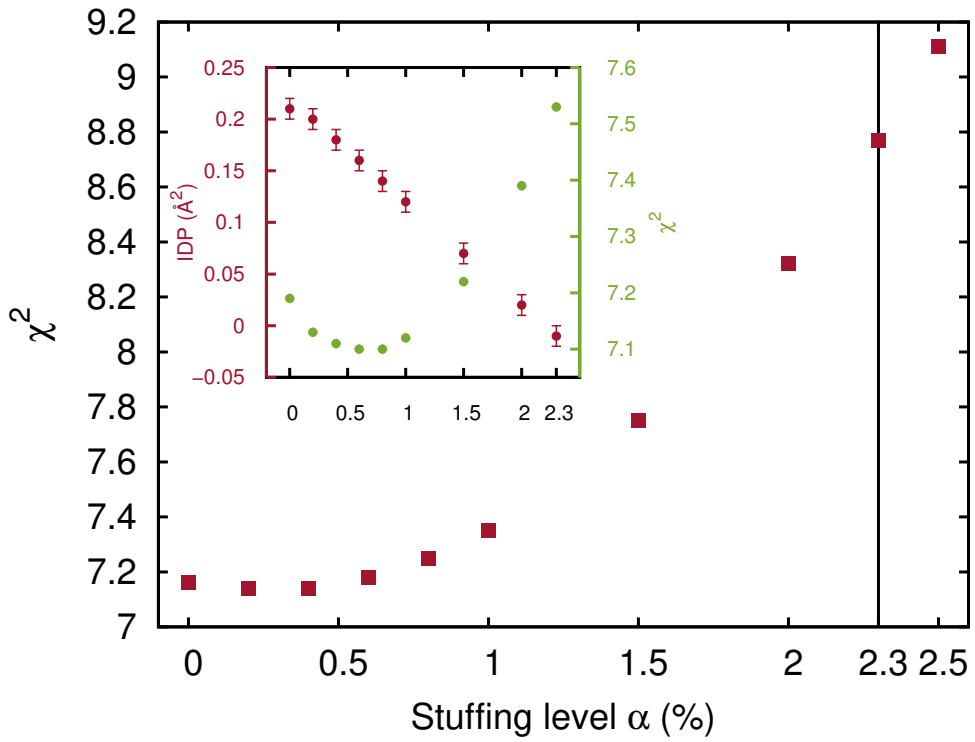

Figure 6.2: Refinement χ^2 plotted versus the stuffing level at 2 K. The minimum values of the uncertainty parameter remain below 1% stuffing. The solid black line highlights the χ^2 when the 2.3% stuffing level is reached. The inset shows the IDP and χ^2 versus the stuffing level calculated using FullProf. There is a clear linear correlation between the parameters. As the number of Yb^{3+} ions in the 16c site increases, the IDP value decreases, becoming negative for 2.3%.

the 2.3% stuffing level is reached, the fit values for IDP become negative, which is unphysical for a quadratic parameter.

This analysis demonstrates the difficulties in discerning small stuffing from other general disorder that may be present in a polycrystalline sample using only Rietveld refinement of neutron diffraction data. Hence, given the refinement uncertainties and the minimum in the error parameters, we can only establish an upper limit of 1% to the stuffing level of the $Yb_2Ti_2O_7$ sample studied here.

6.5 Phase transition

Figure 6.3 shows the sharp heat capacity anomaly exhibited in our sample at $T_c = 280$ mK. The literature reporting on $Yb_2Ti_2O_7$ demonstrates that the temperature and amplitude of the λ-shaped peak are strongly sample dependent. For those single crystals in which an sharp anomaly is observed [152, 156, 161], the critical temperature ranges from 160 to 270 mK. For powders, this spread is smaller and temperatures from 210 mK [154] to the 280 mK, measured in our sample, are reported.

Additionally in Figure 6.3, the behaviour of the low temperature anomaly under small applied magnetic fields is shown. These measurements were performed with the objective to find evidences about the nature of both transition and compound's ground-state. The peak

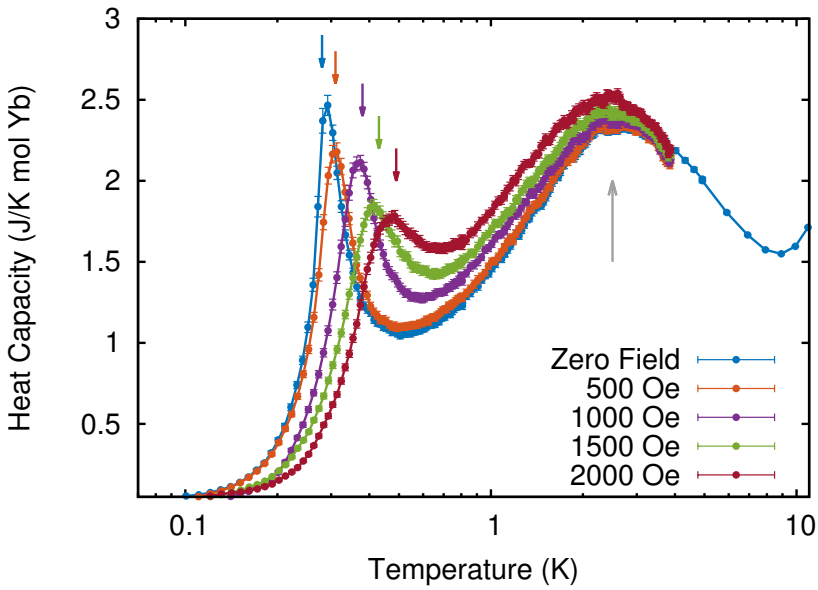

Figure 6.3: Heat capacity anomaly of $Yb_2Ti_2O_7$ powder under zero and several small applied magnetic fields. The arrows highlight the position of the sharp anomaly related to each field, excepting for the grey arrow pointing upwards, which marks the position of the broad anomaly, ~ 2.5 K.

sharpness presents a strong field dependence and its position shifts to higher temperatures as the field increases. The changes in the anomaly shape seem to indicate that the low temperature phase transition would be fully suppressed by the application of a critical magnetic field, as other recent studies on $Yb_2Ti_2O_7$ also suggest [152,167]. The field applied heat capacity anomaly was the first indication obtained in this work of the ferromagnetic nature of our powder sample's ground-state.

The C_p in Figure 6.3 also displays a second, broader hump centred at 2.5 K (gray arrow). Unlike the λ-shaped anomaly, this peak shows little, if any, field dependence. Indeed, if the sharp anomaly is not reproducible in different samples, the same does not apply to the broad one. This is recognised to be an almost universal feature in $Yb_2Ti_2O_7$ [166,168], regardless the presence or not of a phase transition at low temperatures. In the next chapter, the onset of the broad anomaly hump below 10 K will be shown to correlate strongly with the appearance and development of a *continuum of excitations* in the spectra of the compound.

6.6 Magnetic structure

A measurement of the spin-flipping ratio f of the scattered neutrons in the vicinity of the critical temperature is plotted along with the measured heat capacity in Figure 6.4. This quantity is defined as

$$f = \frac{N_\uparrow - N_{\uparrow bkg}}{N_\downarrow - N_{\downarrow bkg}}, \tag{6.1}$$

where $N_\uparrow$ and $N_\downarrow$ are the counts in the non-spin-flip and spin-flip channels, respectively, and the index bkg indicates background counts. The f of our sample was measured at the position of the (111) structural (and magnetic) reflection using the highest count-rate channel, in this case the x.

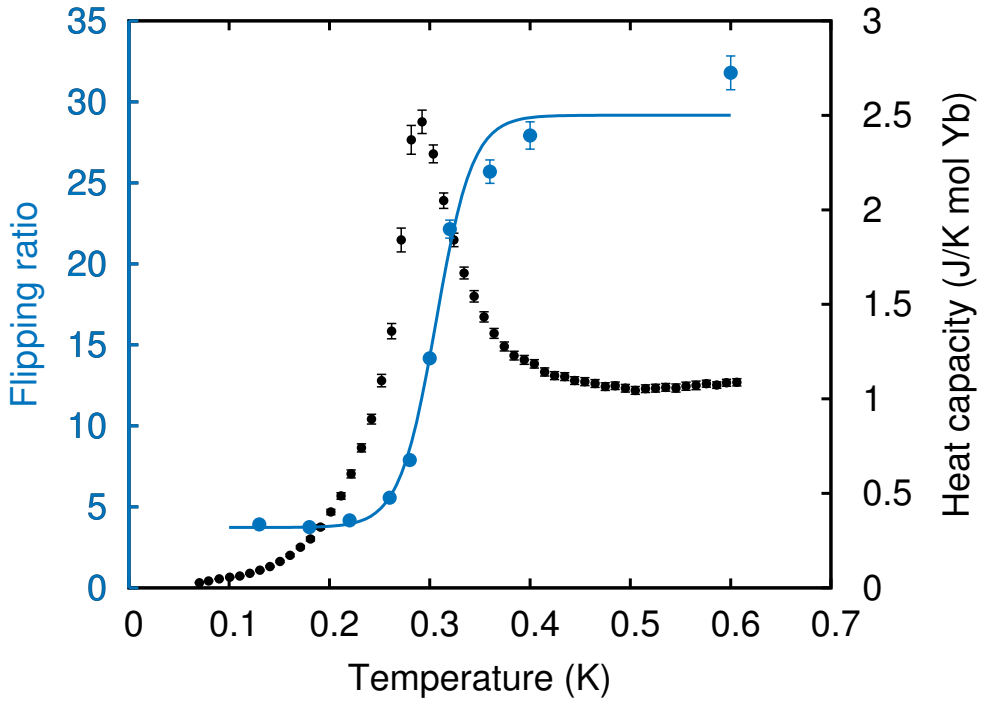

Figure 6.4: The flipping ratio measured at the (111) Bragg position (blue). The line is a guide to the eye. The zero field phase transition in heat capacity (black) is plotted for immediate comparison between depolarisation and phase transition temperatures.

A drop in the flipping ratio immediately allows one to correlate the heat capacity anomaly with a change in the magnetic structure of the sample. The beam depolarisation suggests the development of ferromagnetic domains below T_c. To conclusively prove that hypothesis, diffraction data were collected using unpolarised neutrons also at DNS. As expected, magnetic Bragg peaks corresponding to a propagation vector $\boldsymbol{k} = 0$ structure are observed below the phase transition temperature. In Figure 6.5(a)-(c), the changes in the intensities of the (111), (222) and (400) Brillouin zone centres around T_c are shown. This is a clear evidence that the phase transition does correspond to a spontaneous symmetry breaking, in disagreement with what has been reported for other powder samples [160, 169, 170].

The diffraction pattern obtained by subtracting the DNS data measured at 300 mK from the data measured at 100 mK is displayed in Figure 6.6(a). The representation analysis performed in this work was described in Chapter 2 and is analogous to that of Gaudet *et al.* [160]. The irreducible representation better describing the structure is the $\Gamma_9^{(3)}$. We point out a crucial difference between our data from that of Reference [160]: our result does not allow us to affirm that the canting angle relative to the $\langle 100 \rangle$ cubic axis is different of zero to within error ($\pm 1^\circ$). The (200) and (220) magnetic Bragg peaks, which are apparent in the case of the structure being an ice-like splayed ferromagnet, i.e., having an antiferromagnetic component, are not visible in our data, which indicates that our $Yb_2Ti_2O_7$ sample develops a *quasicollinear* ferromagnetic structure below the phase transition. The refined magnetic moment along each one of the crystallographic axis within one tetrahedron unit is presented in Table 6.4. The total value of $0.87(2)\mu_B$ is in agreement with that reported in [160], but strongly reduced from the $\approx 1.8\mu_B$ expected from high field magnetisation measurements [163]. No evidence supporting the

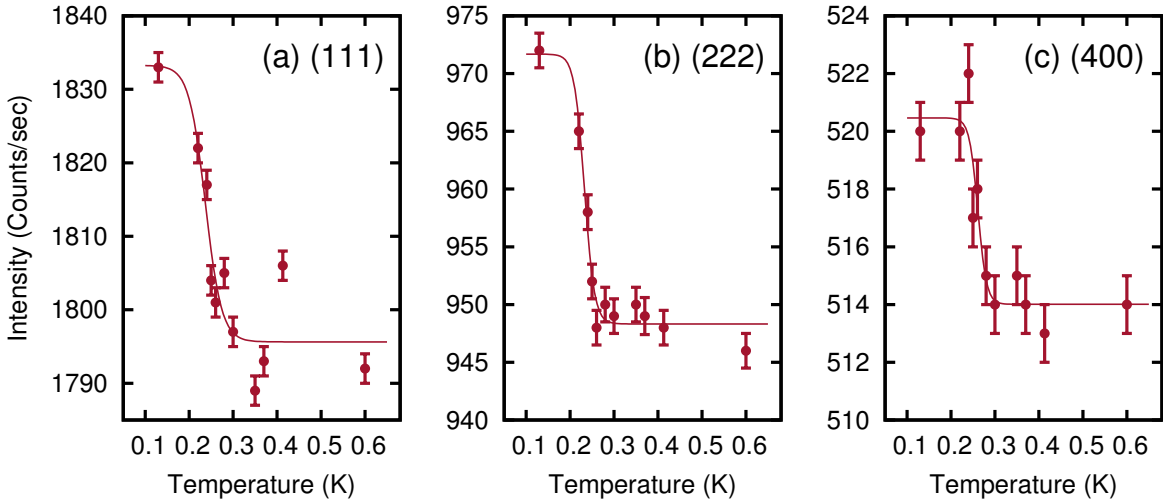

Figure 6.5: Changes in the intensity of the (111), (222) and (400) reflections around T_c, measured at DNS. The full profile difference is shown in Figure 6.6(a).

Site	X	Y	Z	$m^a(\mu_B)$	$m^b(\mu_B)$	$m^c(\mu_B)$
1	$\frac{1}{2}$	$\frac{1}{2}$	$\frac{1}{2}$	0.00(2)	0.00(2)	0.87(1)
2	$\frac{1}{4}$	$\frac{1}{4}$	$\frac{1}{2}$	-0.00(2)	-0.00(2)	0.87(1)
3	$\frac{1}{2}$	$\frac{1}{4}$	$\frac{1}{4}$	-0.00(2)	0.00(2)	0.87(1)
4	$\frac{1}{4}$	$\frac{1}{2}$	$\frac{1}{4}$	0.00(2)	-0.00(2)	0.87(1)

Table 6.4: Magnetic moments obtained in the refinement shown in Figure 6.6(a). m^a, m^b and m^c are the magnetic moment components along the global-x, y and z axis, respectively.

structure observed by Yaounanc *et al.* [162] is found, particularly the strong (220) magnetic Bragg peak reported at their sample ground-state.

In Figure 6.6(b), the difference between the high resolution diffraction data collected at 50 and 300 mK at OSIRIS is displayed. No refinement was performed on these data, but the results are fully consistent with those obtained from the unpolarised neutron diffraction data collected at DNS. The average peak width (FWHM) in the measured $|\boldsymbol{Q}|$-range, obtained by the fitting of a Lorentzian line shape to the reflections in the profile, is of about 0.008 $Å^{-1}$. This would correspond to a magnetic order with a correlation length of at least 780 Å, a number that sets down the long-range character of the ferromagnetic order of $Yb_2Ti_2O_7$.

Sample dependence clearly complicates the overall understanding of $Yb_2Ti_2O_7$ ground-state. Once believed to not order down to the lowest temperatures [169, 171], for many years the sharp anomaly displayed in $Yb_2Ti_2O_7$ heat capacity could not be attributed to any spontaneous symmetry breaking taking place in the material. Until recently, only the single crystal of References [156, 172] was shown to display the magnetic Bragg peaks of a ferromagnet below T_c. In the work of Yasui *et al.*, a simple collinear structure with ordered moment of $(1.1 \pm 0.1)\mu_B$ is reported.

Later work on powders established the long-range ordered nature ground-sate, even though the magnetic structure is still disputed, as pointed out above. The powder of Reference [160]

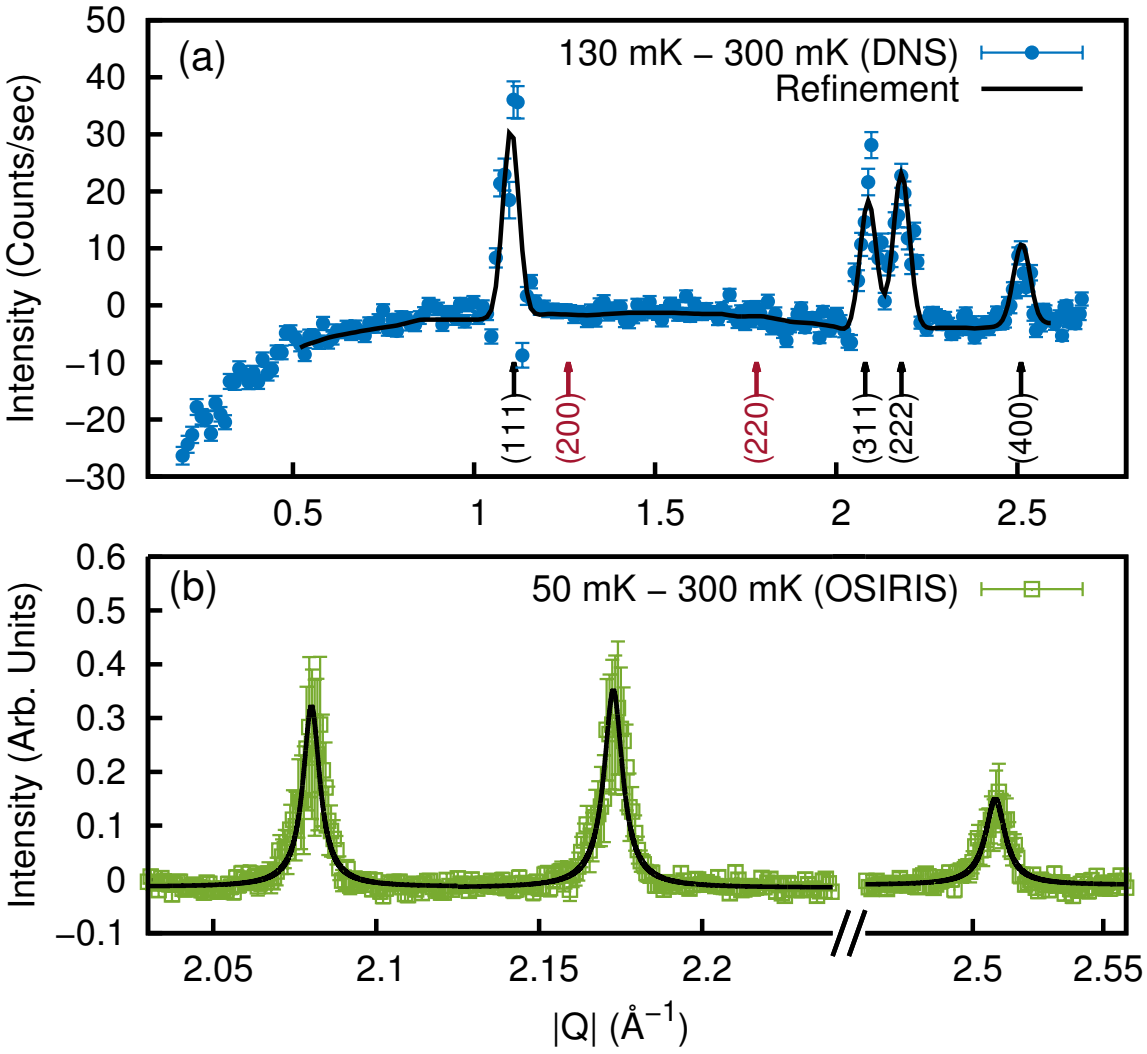

Figure 6.6: (a) Difference between the DNS unpolarised neutron diffraction data collected at 130 and 300 mK (blue circles with error bars), interpreted as pure magnetic scattering, along with the refined magnetic structure (black line). The positions of the (200) and (220) magnetic Bragg peaks, present in a splayed ice-like ferromagnet and not apparent in our data, are highlighted by red arrows. (b) Difference between the OSIRIS diffraction data obtained at 50 and 300 mK. The Lorentzian fits (black line) are used to estimate a minimum correlation length of 780 Å to the ground-state ferromagnetic order.

displays a very sharp phase transition in C_p at $T = 260$ mK. Neutron diffraction measurements show that the Bragg (111) intensity in their sample is approximately constant while warming from 100 mK to $\sim$350 mK. Reference [162] does not report detailed temperature dependence of the measured intensities, but it is supposed that it is only below the phase transition that the sample develops the all-in-all-out ferromagnetic order. Recent work [167] on single crystal reports results in close resemblance to ours. Notwithstanding being performed using the intensities of only three Bragg peaks, the magnetic structure refinement also supports that $Yb_2Ti_2O_7$ is a canted two-in-two-out ferromagnet with ordered moment of $0.90(3)\mu_B$ and a canting angle of $8(6)^\circ$.

6.7 Summary of the results presented in this chapter

This chapter presented an introductory analysis of the magnetic frustration manifested in the pyrochlore $Yb_2Ti_2O_7$. Along with an introduction detailing the problematics surrounding the science published before our work, we added new results which are going to guide us through the interpretation of the spectra shown and analised in Chapter 7.

The precise characterisation of the sample was demonstrated to be an important requisite in works reporting on the magnetic properties of $Yb_2Ti_2O_7$, especially because the reproducibility of those results is strongly dependent on the sample stoichiometry and crystallinity. The Rietveld refinements are, therefore, presented at first in this chapter and form the basis which this work was built on.

The heat capacity measurements, performed before any neutron scattering experiment, provide possibly the strongest evidence of the ferromagnetic nature of the compound's ground-state. The neutron beam depolarisation detected in our diffraction experiment definitely establishes that conclusion, which contradicts the literature reporting that, in $Yb_2Ti_2O_7$, no long-range order is developed below the sharp phase transition at $T_c = 280$ mK. The difference pattern obtained from the subtraction of data collected above and below T_c is used to estimate an ordered magnetic moment of $0.87(2)\mu_B$, a value close to the reported in previous works. However, the structure and the possible canting angle relative to the crystallographic $\langle 100 \rangle$ and equivalent axis still presents some variability between samples.

Chapter 7

The ground-state of $Yb_2Ti_2O_7$ II: magnetic excitations

7.1 Overview and context

Not only the static ground-state of ytterbium titanate produces inconsistent results depending on the sample analysed. Controversies also exist in the reported spin dynamics of the material at low temperatures. Linear spin wave theory could successfully reproduce the high field propagating spin waves detected at temperatures below T_c [24, 152]. On the other hand, to date, the predicted gapped magnetic excitations in zero field, consequence of the exchange anisotropy in the Hamiltonian, have not been confirmed experimentally. The reported spin dynamics displays little or no change while increasing the temperature from 50 mK to at least 2 K in both single crystal and powder samples [160, 173].

The applicability of linear spin wave theory is possibly limited by the quantum fluctuations exhibited by the compound at low fields. The mechanism giving rise to these fluctuations is still debated. It has been suggested that the proximity of $Yb_2Ti_2O_7$ to a phase boundary between two competing magnetic ground-states is a possible cause for the dynamical character of the ground-state [31, 59]. Reference [59] proposes that an order-by-disorder mechanism may drive the system to a XY Ψ_2/Ψ_3 magnetic phase before it eventually adopts an energetically favourable splayed ferromagnetic state, in a *double phase transition* process. Indeed, a new set of exchange parameters place the compound very close to the boundary between the Ψ_3 and the splayed ferromagnetic phases in a calculated semiclassical phase diagram [reproduced in Figure 1.7(d)]. The proximity to a critical point would in principle explain the sensitivity of $Yb_2Ti_2O_7$ to weak disorder, as is the case in stuffed samples.

In this chapter, we present the high resolution neutron spectroscopy measurements carried out in order to investigate the dynamics exhibited deep in the ordered state of ytterbium titanate. The work shown here is complimentary to data analysed in Chapter 6. Our results, the most accurate to date displaying the intrinsic magnetic behaviour of $Yb_2Ti_2O_7$ at low temperatures, reveal the multitude of excitations that can be observed yet in powder samples. Finally, we comment, taking into consideration not only the experimental evidences provided by our work, but also that taken from a vast literature, how the true ground-state of this pyrochlore most likely looks like.

7.2 Experimental details

The results of the next sections were obtained in the course of two beam times carried out at ISIS. High resolution inelastic neutron scattering was performed at the backscattering inverted geometry time-of-flight spectrometer OSIRIS with a fixed neutron final energy $E_f = 1.845$ meV selected by a pyrolytic graphite PG(002) analyser. For this experiment, 2 g of the same sample used in the other experiments performed on $Yb_2Ti_2O_7$ were loaded in a copper annular can and

sealed in He atmosphere. One day before the first measurement at base temperature, the sample was mounted in a Kelvinox Oxford Instruments dilution insert and cooled down to 50 mK. Data were collected upon warming for at least 12 hours at different temperatures in several runs of approximately two hours each. After individual checks, datasets of the same temperature were combined. The mean energy resolution provided by OSIRIS, as high as 25 μeV, can be seen to not change considerably within the experimental dynamic range from -0.2 to 1.2 meV [88].

7.3 Inelastic neutron scattering results

The contour plots in Figure 7.1 display the response of the measured spectra to the changes in temperature. At 10 K [panel (a)], nothing more than a typical paramagnetic behaviour is exhibited. At 2.5 K [panel (b)], the appearance of weak quasielastic scattering at low $|\boldsymbol{Q}|$ signals the development of dynamical ferromagnetic correlations in the sample. Concomitantly, as will be clearly shown later, a weak diffuse *continuum* of scattering forms at energy transfers higher than 0.4 meV. Down to 500 mK [panel (c)], both features become stronger and at 50 mK, an energy gap opens at the low momentum transfer region, showing clear features in the spectra at temperatures below T_c.

In Figures 7.2 and 7.3, some representative cuts made along the energy axis are shown. To model the observed line shapes, we note that the measured neutron scattering intensity $I(|\boldsymbol{Q}|,\omega)$ is proportional to the dynamic structure factor $S(|\boldsymbol{Q}|,\omega)$[1]. According to the *fluctuation-dissipation* theorem, $S(|\boldsymbol{Q}|,\omega)$ can be obtained assuming a, here, damped harmonic oscillator model for the imaginary part of the generalised magnetic susceptibility $\chi^{\alpha,\beta}(|\boldsymbol{Q}|,\omega)$ [60, 73]. The following equation for the paramagnetic scattering is then obtained:

$$I(\hbar\omega) = \frac{A}{\pi}\,\frac{\hbar\omega}{1-\exp(-\beta\hbar\omega)}\,\frac{\Gamma_Q}{(\hbar\omega)^2+\Gamma_Q^2}, \tag{7.1}$$

where Γ_Q is the half width of the quasielastic component, $\hbar\omega$ is the neutron energy transfer, $\beta = (k_B T)^{-1}$, and T is the sample temperature. The inelastic (gapped) excitations were fitted with a standard Lorentzian convolved with the instrumental resolution function determined from the vanadium scans.

The evolution of the ferromagnetic correlations, manifested as quasielastic scattering at low $|\boldsymbol{Q}|$, can be seen in Figure 7.2(a)-(c), which displays cuts binned in the range $|\boldsymbol{Q}| = [0.3, 0.6]$ Å^{-1} for different temperatures above T_c. The line shape is broad (green shaded area for all the plots) and its tails extend over a wide energy range. At lower temperatures, this component narrows and displays an increase in magnitude around zero energy transfer, signalling overall slower spin dynamics. At 500 mK [Figure 7.2(c)], closer to the phase transition temperature, this contribution is sharp and asymmetrically broadened at the base of the elastic line, as the *detailed balance* theorem establishes [61]. Quantitatively, those behaviours are captured in the fitting parameters A and Γ_Q of Equation (7.1), which are shown as a function of temperature in Figure 7.4.

In Figure 7.3(a)-(c), cuts of the spectrum measured at 50 mK binned in the ranges $|\boldsymbol{Q}| = [0.3, 0.6]$ Å^{-1}, $|\boldsymbol{Q}| = [0.9, 1.2]$ Å^{-1} and $|\boldsymbol{Q}| = [1.5, 1.8]$ Å^{-1}, respectively, are shown. The gapped sharp excitation feature, clearly observed for $|\boldsymbol{Q}| < 0.6$ Å^{-1} in the contour plot of Figure 7.1(d), can be seen in all three cuts at $\hbar\omega \sim 0.17$ meV. This flat-band-like excitation mode seems slightly dispersive, and its intensity is stronger at the magnetic zone centre regions around (000) and (111). Despite being outside the measured momentum transfer range, the tail of the dispersions

[1] See Section 2.2.3 in Chapter 2, where the powder-averaged $|\boldsymbol{Q}|$ was replaced by $\boldsymbol{Q}$.

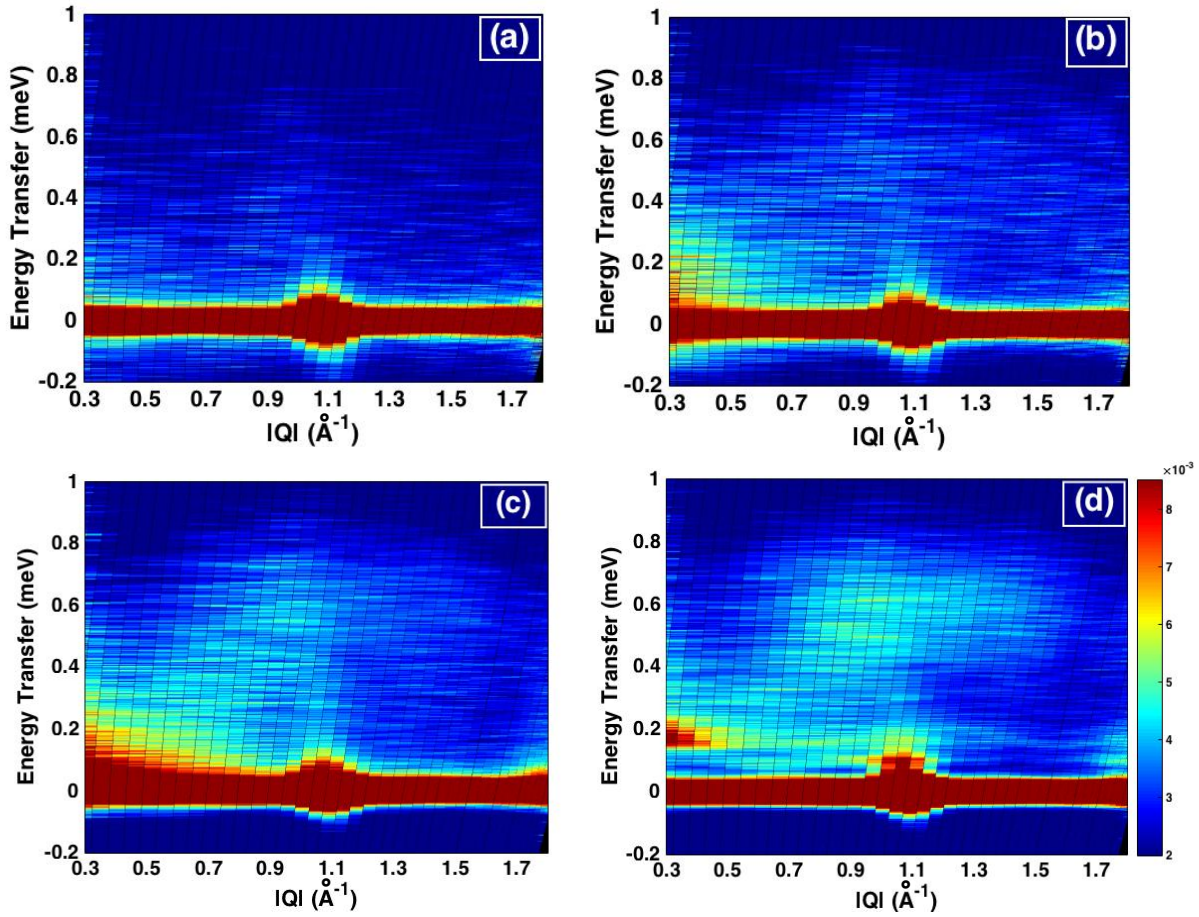

Figure 7.1: Inelastic neutron scattering spectra measured at OSIRIS at (a) 10 K, (b) 2.5 K, (c) 500 mK and (d) 50 mK. A nominal experimental interval of $|Q| = [0.2, 1.8]$ Å^{-1} is accessed at $\hbar\omega = 0$. For our purposes, however, scattering from the lowest momentum transfer detectors is avoided in the analysis.

stemming from the (311) and (222) positions are also present in the contour plots and cuts of Figure 7.3. Its intrinsic width is estimated to be around 70 μeV based on the fitting shown in Figure 7.3(a). Furthermore, in Figure 7.3(b)-(c), an additional resolution limited sharp excitation is visible at $\hbar\omega \sim 0.1$ meV, with the strongest intensity observed near the (111) Bragg position.

Despite the long-range magnetic order and the gapped magnetic excitation modes evident at both 0.17 and 0.1 meV at 50 mK, a broad quasielastic scattering component extending up to at least 1 meV is observed to persist in the whole measured momentum transfer range. This behaviour was reported, in single crystal samples, to manifest in the form of rods of scattering along the $\langle 111 \rangle$ reciprocal lattice directions [156, 171, 173, 174]. In Reference [174], the scattering intensity in the rods grows on approaching T_c and, at 30 mK, shows reduced spectral weight (which the authors of that work call *depletion*) below 0.2 meV in comparison with 500 mK data. In Reference [173], the spectral weight of the rods is little affected when the temperature is increased up to 850 mK. In our case, even though no information about directions in reciprocal space can be obtained, the strong shift of the quasielastic contribution to positive energies ultimately causes the suppression of the scattering magnitude at the energy gap region, explaining thus the depletion observed in Reference [174].

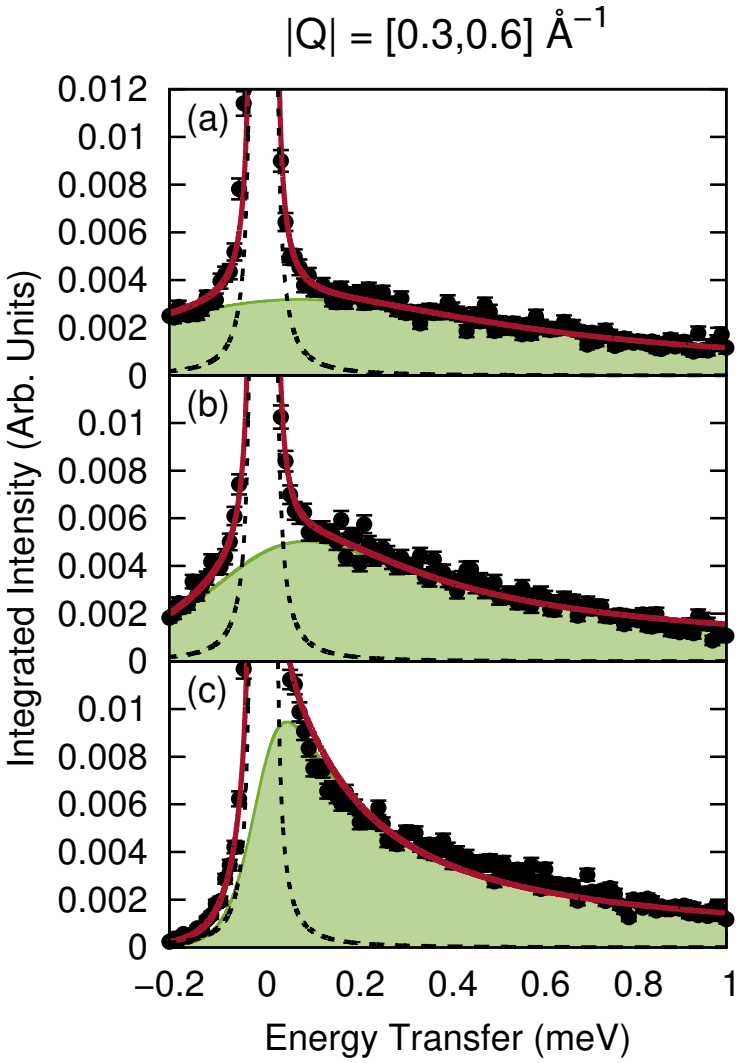

Figure 7.2: Cuts along the energy axis binned in the interval $|Q| = [0.3, 0.6]$ Å^{-1} for (a) 10 K, (b) 2.5 K and (c) 500 mK. The red lines show the sum of all the fitted components (see main text) to the measured curves (black points with error bars). The black dashed line is the estimated contribution of the elastic incoherent scattering to the profiles. The green shaded area corresponds to the fitted quasielastic scattering according to Equation (7.1).

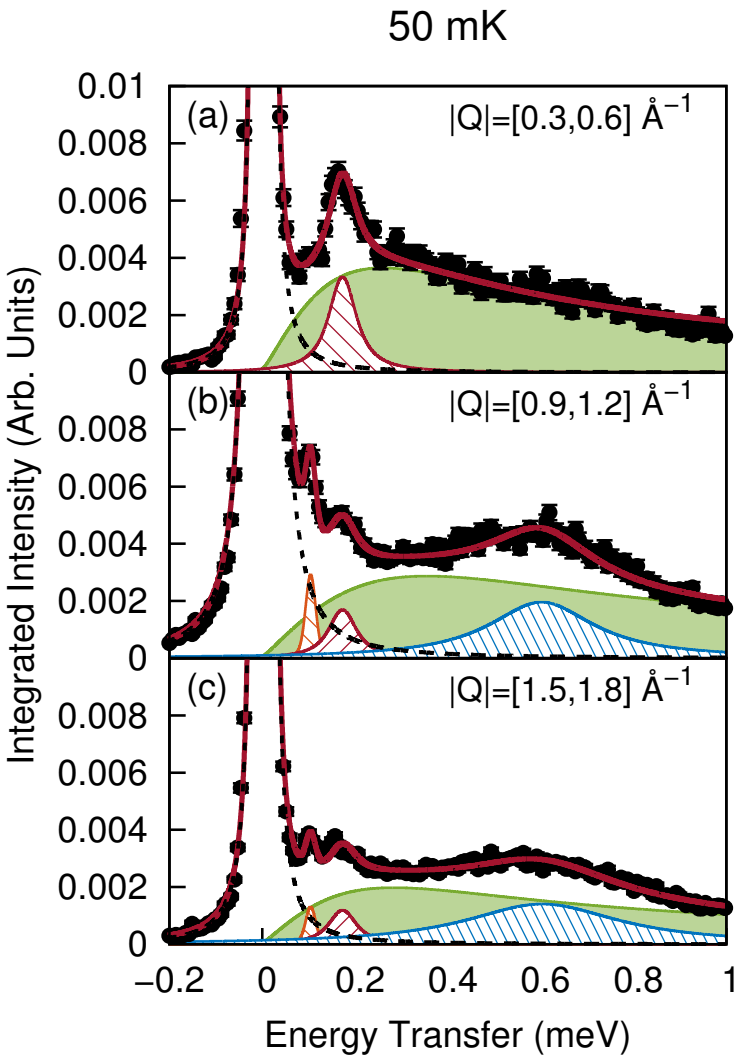

Figure 7.3: Three different cuts performed on 50 mK data for (a) $|Q| = [0.3, 0.6]$ Å^{-1}, (b) $|Q| = [0.9, 1.2]$ Å^{-1} and (c) $|Q| = [1.5, 1.8]$ Å^{-1}. Note that the (111) Bragg peak is contained in the $|Q|$-range of panel (b) and that it causes the observed broadening of the elastic line. In addition to the estimated quasielastic scattering (green), two sharp magnetic excitations (orange and red dashed areas, respectively) at $\hbar\omega = 0.10$ meV (FWHM = 25 μeV) and at $\hbar\omega = 0.17$ meV (FWHM = 70 μeV) and estimated inelastic continuum (blue dashed area) contribute to the observed line shape.

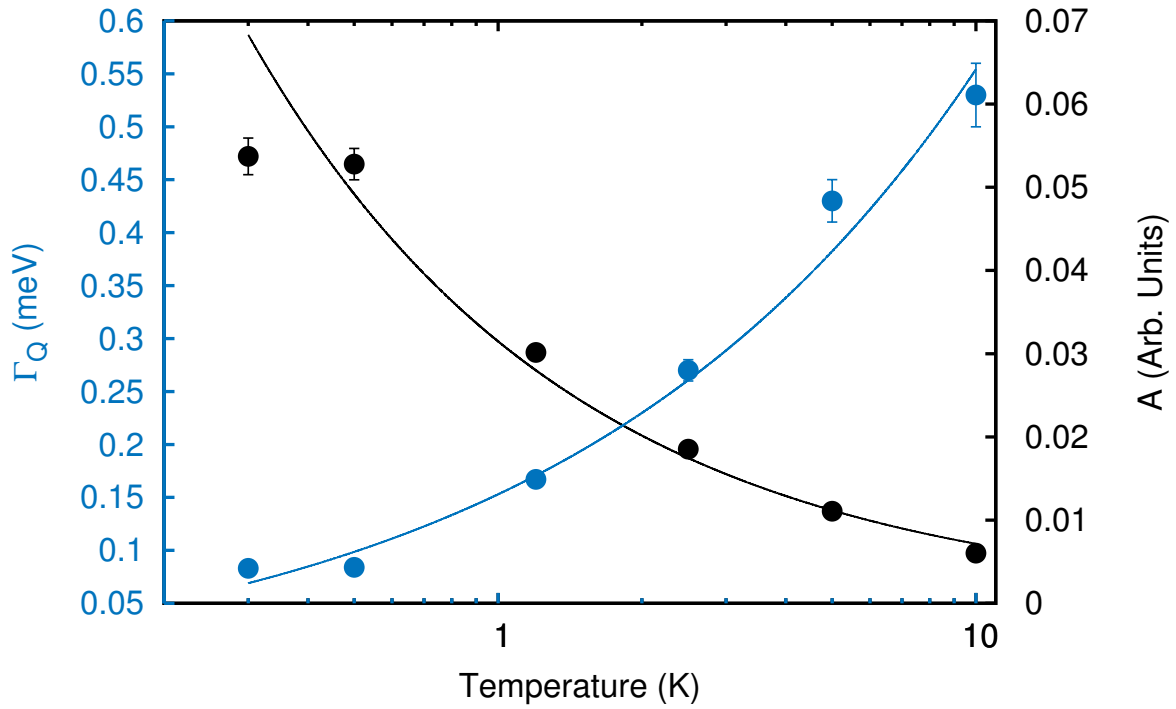

Figure 7.4: Temperature evolution of the two fitting parameters Γ_Q and A for temperatures measured above T_c. The solid lines are guides to the eye.

A third characteristic feature of the magnetic excitations spectra of $Yb_2Ti_2O_7$ is the continuum-like inelastic scattering component around 0.6 meV. In Figure 7.5, where we plot the temperature dependence of the intensity of a $|\boldsymbol{Q}|$-cut integrated over a broad momentum transfer range, the scattering spectral weight within the continuum region of the spectra can be seen to increase steadily relative to 10 K. At 2.5 K the intensity at the tail of the elastic line is approximately constant up to the maximum $\sim$ 0.6 meV (purple arrow in Figure 7.5), after which it starts to decrease. Upon further cooling, this component sharpens to form at 50 mK the prominent peak in the $|\boldsymbol{Q}| > 0.9$ Å^{-1} region, already displayed in the panels of Figure 7.3.

In Figure 7.6, an energy cut integrated over $\hbar\omega = [0.4, 0.8]$ meV is plotted as a function of momentum transfer. The integrated intensity at 10 K was subtracted from the data at each temperature shown and the result was then divided by the magnetic form-factor of the Yb^{3+} ions. This excitation appears approximately featureless at 5 and 2.5 K , with a slightly increased magnitude for the latter temperature. At 500 mK, a maximum in the dispersion arises $\sim$ 0.9 Å^{-1}, which is accompanied at 50 mK by another maximum taking place $\sim$ 1.4 Å^{-1}. Apart from this subtle change at higher $|\boldsymbol{Q}|$ and unlike the lower energy sharp excitations, the continuum seems to be little affected by the phase transition to the magnetic ordered phase.

All the reports of gapped magnetic excitations in $Yb_2Ti_2O_7$ contain solely data collected in applied magnetic fields [24, 152]. In single crystals, regardless of sample stoichiometry issues, the field induced order displays clear sharp spin wave branches, which are modelled using linear spin wave theory. Robert *et al.* [173] further constrains the parameter space using Monte Carlo and spin dynamics simulations in order to reproduce some of the diffuse elastic

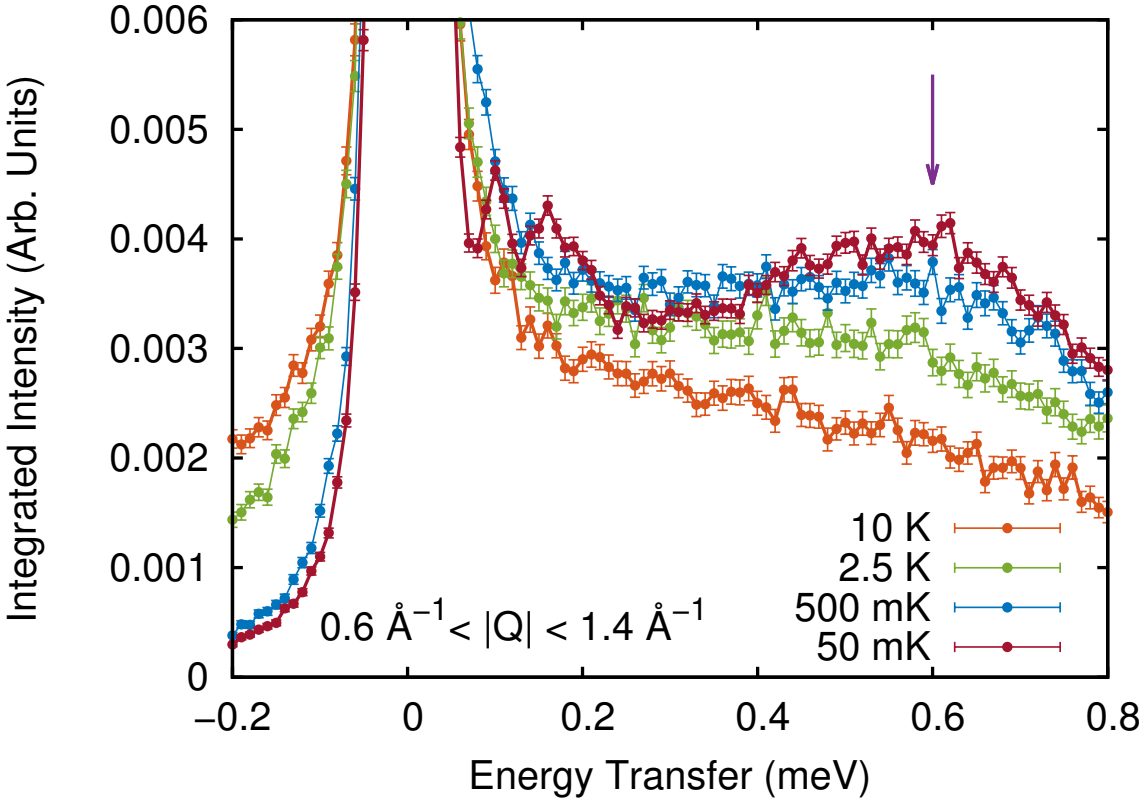

Figure 7.5: Broad $|Q|$-cut corresponding to the integrated intensity over the interval $|Q| = [0.6, 1.4]$ Å^{-1}. The purple arrow highlights the position of the maximum of the $Yb_2Ti_2O_7$ continuum at 50 mK.

scattering features appearing in zero applied magnetic field. We use the software SPINW [43] and the sets of exchange parameters determined in References [24, 173] and, more recently, in Reference [152], to calculate the powder-averaged, resolution convolved magnetic excitations expected to emerge in zero field below T_c. The results are shown in Figure 7.7. Since the model of Ross *et al.* [24] was already discussed for powders in Reference [160], we do not reproduce the respective contour plot here. For a quick comparison, the parameters, in local and global coordinates (see Section 1.3.2 in Chapter 1), reported in these three works are given in Table 7.1.

Despite the successful reproducibility of the high field regime of the magnetic excitation spectra, the fitted exchange parameters do not give an accurate account of the excitations measured in our sample. The closest resemblance is seen at low $|Q|$, where a strong dispersive gapped mode is predicted to be visible in the powder spectra. However, the branch observed in our experiment is almost flat and the measured gap of 0.17 meV appears overestimated in all models, but closer to the calculation based on the exchange parameters of Thompson *et al.* No sharp excitation mode $\sim$ 0.1 meV can be reproduced in the spin wave calculations based on the exchange parameters of Table 7.1, as demonstrated by the cuts performed in the calculated spectra displayed in Figure 7.7(c). Given that this mode, of energy of around 1 K, is clearly absent above T_c, we conclude that its emergence can only be associated with the ground-state magnetic order.

Even thought the four distinct calculated spin wave modes are expected to be discernible at higher momentum transfers for an instrumental resolution of 25 μeV [see Figure 7.7(c)], the

	J_{zz}	$J_{\pm}$	$J_{\pm\pm}$	$J_{z\pm}$	J_1	J_2	J_3	J_4	g_{xy}	g_z
Ross *et al.* [24]	0.17	0.05	0.05	-0.14	-0.09	-0.22	-0.29	0.01	4.32	1.80
Thompson *et al.* [152]	0.026	0.074	0.048	-0.159	-0.028	-0.326	-0.272	0.049	4.17	2.14
Robert *et al.* [173]	0.07	0.085	0.04	-0.15	-0.03	-0.32	-0.28	0.02	4.09	2.06

Table 7.1: Exchange parameters determined in References [24, 152, 173] in both local (J_{zz}, $J_{\pm}$, $J_{\pm\pm}$, $J_{z\pm}$) and global (J_{α}) coordinates, with the corresponding calculated g-factors g_{xy} and g_z (see Equation (1.33) for a definition). All the values for the exchange parameters are given in units of meV.

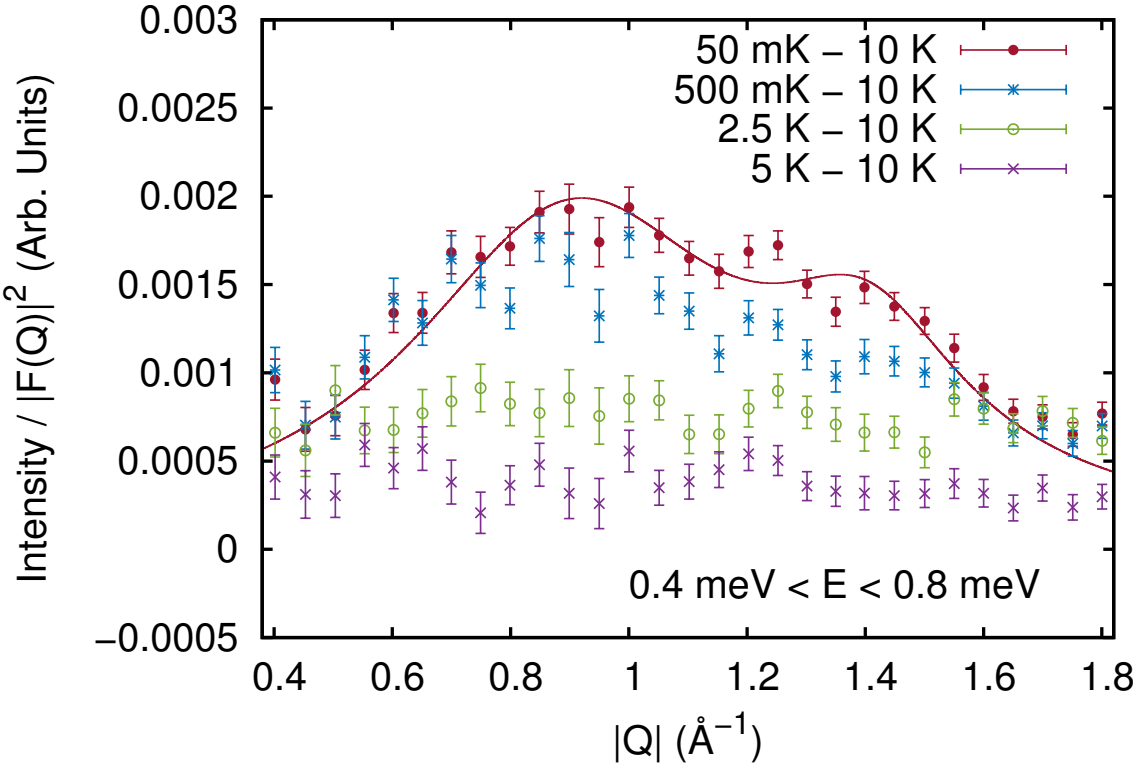

Figure 7.6: Energy binned in the range $\hbar\omega = [0.4, 0.8]$ meV displaying the $|Q|$ dependence of the continuum. The dispersion is double-peaked at 0.9 and 1.4 Å^{-1}. The red line is a guide to the eye.

continuum at higher energies may tentatively be interpreted as a result of the superposition caused by powder-averaging of the excitation branches. A similar observation in single crystals, however, weakens this hypothesis [152, 173]. We interpret this excitation as a strong evidence that above the sharp phase transition temperature this compound is not in a conventional paramagnetic state up to at least 2.5 K. In fact, the temperature evolution of the continuum may well be related to the broad hump in heat capacity shown in the Figure 6.3 of Chapter 6. The broad anomaly has an onset at 10 K and a maximum around 2.5 K, temperature below which the heat capacity experiences a smooth decrease down to the sharp phase transition at T_c.

Recently, an alternative explanation to the continuum of scattering emerging in the $Yb_2Ti_2O_7$ ground-state was suggested. Analyses of the predicted spin waves calculated based on data of terahertz spectroscopy [175] and inelastic neutron scattering [152] suggest that at low and zero magnetic fields the single and multiple-magnon branches in the compound may overlap. This provides a decay route for the one-magnon excitation and, consequently, suppresses the development of conventional spin waves in the ordered phase. This effect, which has been invoked in a broader context lately [176], is known as *quasiparticle breakdown*, and it is usually reported in low-dimensional quantum spin systems [177, 178]. We point out, however, that the continuum observed here displays significant spectral weight already at 2.5 K $\sim 10T_c$, much above the effective formation of single-magnon modes and, consequently, above the temperature at which magnon decays can occur.

Lastly, we comment on the striking similarities of the low temperature behaviour observed

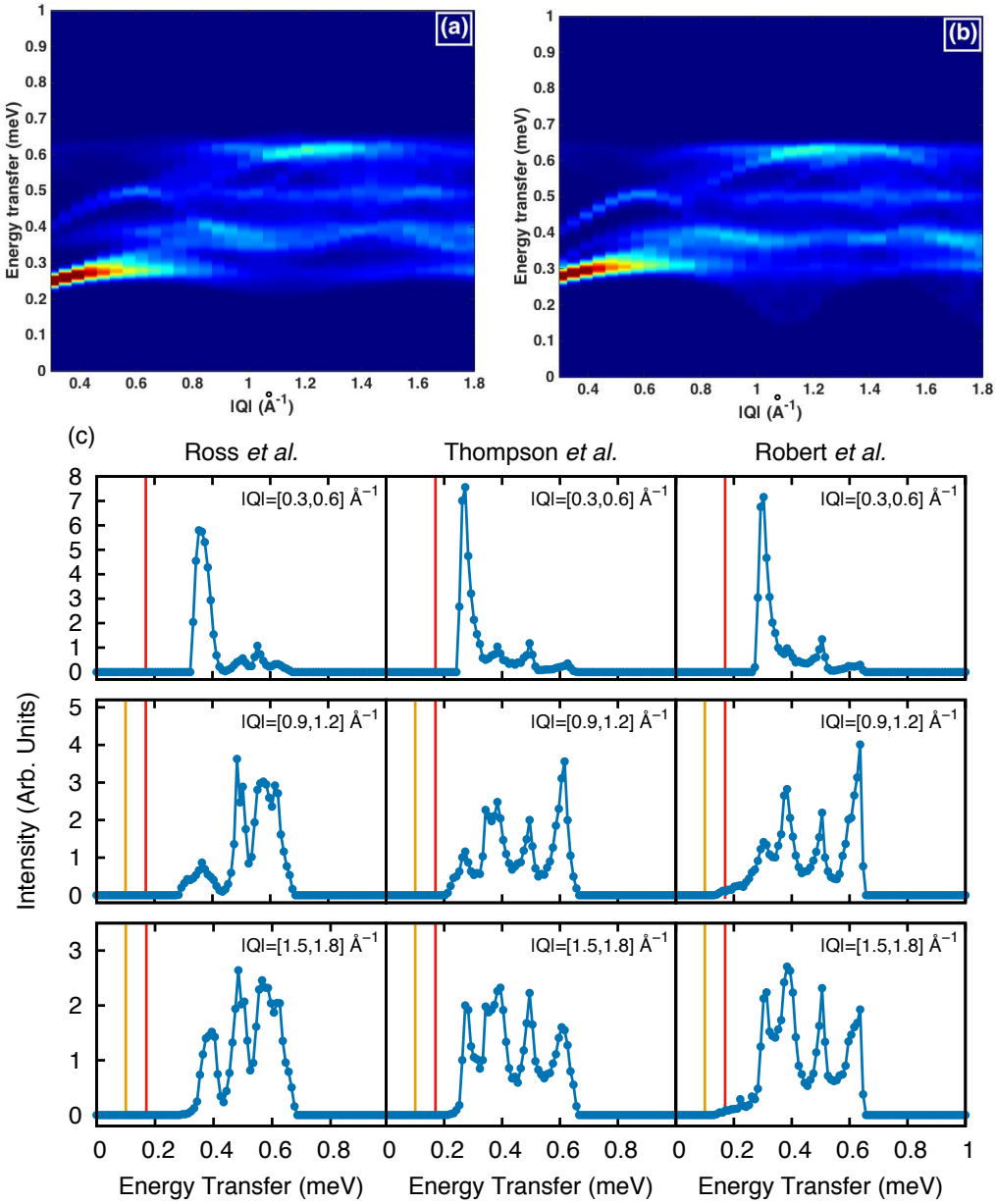

Figure 7.7: Resolution convolved (25 μeV) expected spin wave spectra calculated using the exchange parameters determined in (a) Reference [152] and (b) Reference [173]. (c) Cuts along the energy axes in the same $|Q|$-ranges shown in Figure 7.3, including now the model of Reference [24]. The yellow and red lines mark the position of the two sharp excitations measured in our sample.

in the isomorphous compound $Yb_2Sn_2O_7$ and the one presented in our $Yb_2Ti_2O_7$ sample. The heat capacity of $Yb_2Sn_2O_7$ displays a sharp anomaly at $T_c = 0.15$ K followed by a broad hump ~ 2 K [137]. In the stannate, the neutron diffraction supports the development of an ice-like splayed ferromagnetic structure below T_c with an ordered moment of $1.05(2)\mu_B$. Nevertheless, μSR measurements show evidence of persistent spin dynamics in the compound's ground-state [137]. Inelastic neutron scattering measurements performed on a different powder sample confirm this scenario. As it can be seen in the contour plots of Reference [179], the inelastic continuum is prominent already at 3 K and evolves down to 50 mK, showing weak dispersion and stronger intensity at $|\boldsymbol{Q}| = 0.9$ Å^{-1}. No gapped modes are reported in Reference [179], something that may be a consequence of insufficient instrumental energy resolution (0.1 meV in their experiment). These works show strong evidence that $Yb_2Sn_2O_7$ may mimic the behaviour reported here for $Yb_2Ti_2O_7$, in spite of the chemical pressure arising from the different occupation of the B site.

7.4 Final remarks

Generically, below a phase transition, the quasielastic scattering is expected to split its spectral weight into elastic (static) contribution and inelastic dynamical scattering in form of coherent spin wave modes. Instead, we observe that at 50 mK inelastic excitations coexist with a quasielastic contribution, which signals that spin fluctuations remain important in the compound's ground-state. From these observations, several important questions arise and we discuss some of them below, one by one:

i. Are the fluctuations caused by poor thermalisation of the sample at low temperatures? That is always possible, especially if we consider that the thermalisation in powders is inherently poor. However, evidences in our data show that this an improbable possibility. First, the neutron scattering spectra show clear temperature dependence. Second, the diffraction data collected just after the inelastic scattering measurements above and below the phase transition temperature at OSIRIS (see Figure 6.6(b) in Chapter 6) display the Bragg peaks of a long-range ferromagnetic order. In other words, if some small amount of sample remains at temperatures above T_c, it is unlikely that it would be the single cause for the significant fluctuating component we observe to persist in $Yb_2Ti_2O_7$ down to 50 mK.

ii. Are the fluctuations caused by sample inhomogeneities? Arguing against this suggestion, it should be enough to say that the sample displays the phase transition and develops long-range ferromagnetic order, which has been shown to be suppressed in non-stoichiometric samples. We also point out that *all* the inelastic neutron scattering data for $Yb_2Ti_2O_7$ samples reported to date have shown dynamics in the zero applied magnetic field ground-state. So, to suggest that the fluctuations are due to sample inhomogeneities would be equivalent to saying that *all* the samples of $Yb_2Ti_2O_7$ are affected by disorder and do not show the *real* behaviour of the compound.

iii. Are the fluctuations caused by an intrinsic dynamical ground-state surviving in the long-range ordered regime? This possibility is the most promising and, given the large body of work showing the eccentricities of the magnetism displayed by $Yb_2Ti_2O_7$, it is natural to link our results with the models developed for the QSI. Indeed, the ground-state excitations we observe are exotic, but a key experimental fact places the compound away from the theoretical QSI phases: the ground-state static long-range ferromagnetic structure not (totally) disrupted by quantum fluctuations (see, for example, the discussions in Reference [180] and the recent reviews in References [58, 181]). A good *qualitative* description of our observations seems to be achieved when we compare our experimental results with those predicted by the gMFT theory developed

in Reference [57]. The so-called Coulombic Ferromagnet (CFM) phase, whose elementary excitations are an inelastic continuum of *spinons*, instead of conventional spin waves, displays magnetic order and supports the existence of a gapless photon mode. The settling of $Yb_2Ti_2O_7$ in a CFM phase would, however, require a drastic revision of the J_α reported for the material, since the exchange parameters pertinent to $Yb_2Ti_2O_7$ seem to place the compound far away from this new state of matter.

If $Yb_2Ti_2O_7$ is a real QSI, more investigations on the spin liquid phase above T_c may provide important evidence. Possible monopole dynamics at temperatures $\sim$ 1.5 K were recently reported [182, 183]. Furthermore, the broad anomaly in heat capacity, which we associate here with the inelastic continuum developing at low temperatures, seems to configure an important turning point in the magnetic dynamics of the compound without any obvious consequences in the elastic scattering. We stress that more work, both theoretical and experimental, preferably carried out on well characterised single crystals, is necessary to clarify the blurred physical picture that was built for $Yb_2Ti_2O_7$ throughout the years.

7.5 Summary of the results presented in this chapter

In this final chapter, we complement our diffraction data, presented in Chapter 6, with high resolution inelastic neutron scattering measurements. Powder spherical averaging hides information about directions in reciprocal space, which would be fundamental in order to perform a robust quantitative analysis on the $Yb_2Ti_2O_7$ spectra. Nevertheless, we show that sharp excitation modes clearly exist and that they loosely correspond to what is predicted from high magnetic field data. No other sample of $Yb_2Ti_2O_7$, powder or single crystal, has been reported so far to display gapped magnetic excitations in the long-range ordered state, even though these are expected given the strong exchange anisotropy of the Hamiltonian.

In the ferromagnetic phase, importantly, spin fluctuations translated into a persistent quasielastic scattering are still present down to at least 50 mK. At temperatures well above T_c a broad continuum of excitations develops upon cooling. It is difficult to say whether this pyrochlore can be placed in one of the many exotic phases that are theoretically expected to be present in frustrated magnets. We believe that our measurements reveal important information on the ground-state of $Yb_2Ti_2O_7$ and pave the way for a better understanding of the nature of this frustrated magnet.

Chapter 8

Conclusions and outlook

This chapter summarises the main information contained in this PhD thesis.

The theoretical literature surrounding the research on the exchange Hamiltonian of pyrochlores can be impressively unclear from the experimental, and practical, point of view. One of the tasks performed in Chapter 1 was to "translate" some concepts that can be rather elusive and abstract using simpler definitions, accessible in textbooks of Quantum Mechanics. This was meant to facilitate my own understanding of the physics exhibited by those compounds, and also to guide me through the evaluation of what, in those theories, and within the context of the frustrated pyrochlores research, in fact sound.

It is impossible to talk about frustration in pyrochlores without mentioning the physics and the concepts developed for spin ices. As stated in the introductory chapter, spin ices represent the *genesis* of the research on pyrochlore magnets, even if the low temperature magnetism of the compounds presented here do *not* resemble that presented in $Dy_2Ti_2O_7$ and $Ho_2Ti_2O_7$. It is also based on them that the research on the quantum spin ice candidates reached the levels of one of the most promising in condensed matter physics.

The technique of choice of this thesis, although I have used many, is neutron scattering. In Chapter 2 its theory was examined in detail. This chapter also included schematic representations of the instruments where I had the opportunity to measure my samples' properties. The account is certainly incomplete, for neutron scattering instrumentation is content for a full PhD thesis. The necessary information for the interpretation of the data collected and presented in the following chapters was, however, contained there. The μSR technique, which is developed in detail in Chapter 5, was introduced just after the neutron instrumental section.

The main results part started in Chapter 3 with the basic characterisation performed on the Sm-based pyrochlores $^{154}Sm_2Ti_2O_7$ and $^{154}Sm_2Sn_2O_7$. Rietveld refinements were used to probe the stoichiometry of our samples. The heat capacity data measured at very low temperatures display a sharp anomaly associated with a phase transition taking place at $T_N^{Ti} = 350$ mK and $T_N^{Sn} = 440$ mK. It was then shown that most of the magnetic entropy associated with the ground-state Kramers doublet of the Sm^{3+} is recovered with this phase transition. Whereas some small difference from the estimated asymptotic $R\ln(2)$ is verified in Figure 3.5, hardly any significance can be attributed to it, given the complete disregard of other contributions, beyond electronic magnetism, to the heat capacity below 10 K.

The crystal field scheme of the Sm^{3+} ion in the pyrochlore lattice is solved in Chapter 4. Those analyses were performed not only in order to estimate the dipolar magnetic moment of our samples, which would be the most directly accessible quantity using neutron scattering techniques, but also the relative weight that multipolar moments have in the ground-state wave function. Only after those estimations, possible quadrupolar coupling with phonons and octupolar-octupolar interactions in the exchange Hamiltonian can be quantitatively accessed.

Eventually, magnetoelastic interactions are indeed possible in $^{154}Sm_2Ti_2O_7$ and $^{154}Sm_2Sn_2O_7$. We believe that the anomalous behaviour of the anisotropic displacement parameters of the powder samples is an evidence pointing towards a coupling between magnetic and structural

degrees of freedom, which would be slightly stronger in the stannate than in the titanate. The highest matrix elements presented in Table 4.7 are those that connect the transitions from the ground-state to the second excited CEF state, with a small preponderance of the magnitudes calculated for the titanate. The final answer about the effective strength of a possible coupling is then left to the determination of the magnitude of g_0, which is ~ 0.04 for $Ho_2Ti_2O_7$ [125].

The low temperature investigations on the Sm-based pyrochlores were treated in Chapter 5. There, the first neutron data set collected for the samples, measured on $^{154}Sm_2Ti_2O_7$ at WISH, was shown. Due to the very small effective magnetic moment of the samarium ion, by that time it was unclear whether some magnetism could be effectively detected in the Sm-based pyrochlores by means of neutron diffraction. Nevertheless, based on the strong phase transition in heat capacity, it was decided that an investigation with neutrons at low temperatures was necessary. The experiment with the titanate was repeated at DNS, but no clear sign of long-range order could be identified. On the stannate, on the other hand, magnetic Bragg peaks could be clearly measured. The magnitude of the ordered moment was estimated to be $\mu_{ref} = 0.25(2)\mu_B$, very close to the $\langle \mu_z^0 \rangle = 0.27\mu_B$ calculated in the crystal field analysis.

Our μSR results do not reveal any novelty about the magnetism in the ground-state of $^{154}Sm_2Ti_2O_7$ and $^{154}Sm_2Sn_2O_7$. Some of the possible reasons for that were explored already in Chapter 5. Now, as this is also an outlook section, we mention the last thing to be examined: the influence of the probe on the object being studied. Rarely this effect has been considered in the literature. Nevertheless, it should be expected that a fast particle like a muon would leave behind a raster of defects as it runs through the crystallographic lattice. Reference [184] demonstrates that the muon changes significantly the local symmetry of the rare-earth ion, which alters the CEF scheme and lifts the degeneracy of the rare-earth doublet ground-state. The atom studied was Pr^{3+}, which is a non-Kramers ion and therefore has the ground-state degeneracy not protected from perturbations that do not break time reversal symmetry. In the fashion conceived in Reference [184], therefore, the ground-state of the Sm-based pyrochlores would be unaffected by the muon. Nevertheless, the transformations induced into a system with a less robust ground-state, or even when the time reversal symmetry is broken below T_N, could be apparent in the measured $A(t)$. How? That is an interesting question we leave for further works.

It is difficult to indicate one single cause for the vast emptiness in the Sm-based pyrochlores neutron spectra. If we consider that the moments remain dynamic in the muon time window for all temperatures, as our results in Section 5.4 seem to suggest, hardly these dynamics would not be detected by neutrons. At this point, it is difficult to not be somehow negative about the last results of the Sm-based pyrochlores presented in this work. Seemingly, at least with the amount of (powder) sample available, or even in the current neutron sources, an experiment to detect the tiny fluctuating magnetic moment of samarium in the pyrochlore lattice is unfeasible. We have thus encountered intrinsic limitations of neutron scattering as a technique. This work, which is far from being complete, serves as encouragement to the development of neutron scattering instruments, beamlines and sources capable to offer solutions to those fundamental problems presented generically by frustrated magnets.

In Chapter 6, we switched our focus to another compound. $Yb_2Ti_2O_7$ is well known for the strong sample dependence of its magnetic ground-state. The first thing to be analysed is the possibility of a long-range ordered magnetic phase to be emerging below the sharp phase transition anomaly at $T_c = 280$ mK. As a response to the sample ferromagnetism, the DNS neutron beam shows a strong depolarisation taking place already above T_c. Magnetic Bragg peaks confirm a structure with an ordered moment of $\mu = 0.87(2)\mu_B$. As the resolution of the DNS data does not allow us to affirm that the order in $Yb_2Ti_2O_7$ is truly long-range, we

performed diffraction measurements also at OSIRIS, and endorsed the long-range character of the ferromagnetism in ytterbium titanate.

High resolution neutron spectroscopy displayed the evolution, upon cooling, of the magnetic correlations in the system. From about 2.5 K, the onset of ferromagnetic correlations is suggested by a broad quasielastic scattering prominent at low $|\boldsymbol{Q}|$. Additionally, an inelastic continuum of scattering develops at energy transfers around 0.6 meV. These features exhibit progressively stronger magnitude when the temperature is decreased down to 500 mK. At 50 mK, an energy gap of 0.17 meV opens to form a flat mode in the spectra. An additional sharp feature is visible at 0.1 meV. The significant amount of quasielastic scattering at this temperature once again shows that, despite the long-range order, the magnetic moment of the Yb^{3+} fluctuates down to temperatures as low as 50 mK. Using three different sets of exchange parameters, reported in [24], [152] and [173], we calculated the powder averaged spectra of the spin wave excitations expected to emerge in the ground-state and performed a qualitative comparison between the predictions and our experimental results in $Yb_2Ti_2O_7$.

Clearly, no theoretical account captured the main features of the compound's spectra. Since the publication of our results [79], some attempts have been made to understand better the role of neglected terms in the exchange Hamiltonian. Particularly, how the extension of linear spin wave theory to include magnon interactions would explain the coexistence of long-range order and continuum of excitations. In the context of the quasiparticle breakdown invoked in Reference [152], the two or three-magnon coupling may be the immediate cause for the appearance of the ytterbium titanate continuum. A recent preprint by Rau *et al.* [38] presents non-linear spin wave theory calculations and directly compares the results with our zero field data and also those from Reference [152]. The conclusion is that, at least in low fields, the renormalisation of the one-magnon spectrum cannot capture quantitatively many aspects of the experimental spectra. What the theoretical works performed recently on ytterbium titanate are unanimous in reaffirming, however, is the proximity of the pyrochlore with a phase boundary between two different long-range ordered states. It is still to be explained, thus, how this affects the magnetic excitations of the material.

Appendix A

Symmetry analysis of the D_{3d} ($\bar{3}m$) point group

In Chapters 1 and 4, we made indirect use of group theoretical results in order to deduce the splitting scheme of each J multiplet caused by crystal electric field effects. This appendix details shortly these calculations.

The number of times n_s that a given irreducible representation Γ_s is contained into a reducible representation is given by

$$n_s = \frac{1}{h}\sum_P \chi_s(P)\chi_\omega(P), \tag{A.1}$$

where P is any symmetry operation belonging to the D_{3d} point group and $h = 24$ is its order (number of symmetry operations). The character table for the double group of D_{3d} is reproduced in Table A.1. The notation is chosen to follow that of Reference [185].

The parameter $\chi_s(P)$ in Equation (A.1) is the character (trace) of the irreducible representation γ_s, while $\gamma_\omega(P)$ is the character of the classes of D_{3d}. Those values can be calculated algebraically [13] and are given here in Table A.2.

With Tables A.1 and A.2 in hands, we can calculate n_s, i.e., we can determine the number of levels in which each of the J multiplets will split once the point symmetry of the magnetic atom

	E	$\bar{E}$	$2C_3$	$2\bar{C}_3$	$3C_2'$	$3\bar{C}_2'$	I	$\bar{I}$	$2S_6$	$2\bar{S}_6$	$3\sigma_d$	$3\bar{\sigma}_d$
Γ_1^+	1	1	1	1	1	1	1	1	1	1	1	1
Γ_2^+	1	1	1	1	-1	-1	1	1	1	1	-1	-1
Γ_3^+	2	2	-1	-1	0	0	2	2	-1	-1	0	0
Γ_1^-	1	1	1	1	1	1	-1	-1	-1	-1	-1	-1
Γ_2^-	1	1	1	1	-1	-1	-1	-1	-1	-1	1	1
Γ_3^-	2	2	-1	-1	0	0	-2	-2	1	1	0	0
Γ_4^+	2	-2	1	-1	0	0	2	-2	1	-1	0	0
Γ_5^+	1	-1	-1	1	i	-i	1	-1	-1	1	i	-i
Γ_6^+	1	-1	-1	1	-i	i	1	-1	-1	1	-i	i
Γ_4^-	2	-2	1	-1	0	0	-2	2	-1	1	0	0
Γ_5^-	1	-1	-1	1	i	-i	-1	1	1	-1	-i	i
Γ_6^-	1	-1	-1	1	-i	i	-1	1	1	-1	i	-i

Table A.1: Character table for the double group of D_{3d}.

J	E	C_3	C_2	I	S_6	σ
5/2	6	0	0	± 6	0	0
7/2	8	1	0	± 8	± 1	0
9/2	10	-1	0	± 10	∓ 1	0

Table A.2: Characters of the classes of D_{3d} contained in the reducible representations of the full rotation group.

is D_{3d}. Explicitly, for $J = \frac{5}{2}$,

$$\begin{aligned} n_s(\Gamma_4^+) &= \frac{1}{24}[(2\times 6)+(-2\times -6)+(2\times 6)+(-2\times -6)=6\times 4] = \frac{12\times 4}{24} = 2, \\ n_s(\Gamma_5^+) &= \frac{1}{24}[(1\times 6)-(1\times -6)+(1\times 6)-(1\times -6)] = \frac{6\times 4}{24} = 1, \\ n_s(\Gamma_6^+) &= \frac{1}{24}[(1\times 6)-(1\times -6)+(1\times 6)-(1\times -6)] = \frac{6\times 4}{24} = 1, \end{aligned} \tag{A.2}$$

The n_s for the other irreducible representations is trivially zero. It can be seen from (A.2) that the $J = \frac{5}{2}$ multiplet splits into three levels: two with an irreducible representation Γ_4^+ and one with symmetry $\Gamma_5^+ + \Gamma_6^+$ (also referred as $\Gamma_{5,6}$ [23, 110]). After the analyses carried out in Chapter 4, we conclude that the ground-state doublet has the $\Gamma_5^+ + \Gamma_6^+$ symmetry and the two excited doublets have the Γ_4^+ symmetry. Physically speaking, $\Gamma_5^+ + \Gamma_6^+$ doublets have the pyrochlore Ising anisotropy, while Γ_4^+ states have a XY character.

Appendix B

Matrix elements of the magnetic moment operator

In this appendix, we define all the matrix elements necessary to perform the analysis presented in Chapter 4. The magnetic moment operator is

$$\boldsymbol{\mu}_\alpha = -(g_L \boldsymbol{L}_\alpha + g_S \boldsymbol{S}_\alpha)\mu_B, \tag{B.1}$$

where $g_L = 1$ and $g_S \approx 2$ are the g-factors of the orbital and spin angular momentum, respectively. In the presence of spin-orbit coupling, L and S may not be good quantum numbers, but J is. If we want to represent the magnetic moment operator as

$$\boldsymbol{\mu}_\alpha = \mu_B g_J \boldsymbol{J}_\alpha, \tag{B.2}$$

which is appropriate only when transitions occur within a J multiplet, one identifies

$$g_J = \frac{3}{2} + \frac{S(S+1) - L(L+1)}{2J(J+1)}, \tag{B.3}$$

a term referred as *Landè* g-factor. It is useful to split the the magnetic moment operator (B.2) into three ortogonal components $\boldsymbol{\mu}_x, \boldsymbol{\mu}_y, \boldsymbol{\mu}_z$, where $\boldsymbol{\mu}_x = \frac{1}{2}\mu_B g_J(\boldsymbol{J}_+ + \boldsymbol{J}_-)$ and $\boldsymbol{\mu}_y = -\frac{i}{2}\mu_B g_J(\boldsymbol{J}_+ - \boldsymbol{J}_-)$ and $\boldsymbol{\mu}_z = \mu_B g_J \boldsymbol{J}_z$. The $\boldsymbol{J}_+$ and $\boldsymbol{J}_-$ are called *ladder operators*, and have matrix elements

$$\langle S, L, J, m_J \pm 1 | \, \boldsymbol{J}_\pm \, | S, L, J, m_J \rangle = \sqrt{J(J+1) - m_J(m_J \pm 1)}, \tag{B.4}$$

while

$$\langle S, L, J, m_J | \, \boldsymbol{J}_z \, | S, L, J, m_J \rangle = m_J. \tag{B.5}$$

Note that the expected values $\langle \boldsymbol{J} \rangle$ vanish when transitions occur between levels with different total angular momentum quantum numbers J [72], i.e.

$$\langle J', m_J' | \, \boldsymbol{J} \, | J, m_J \rangle = \delta_{J,J'} \tag{B.6}$$

As considerable part of our work deals with intermultiplet transitions, more generic relations to the matrix elements of the magnetic moment operator (B.1) have to be defined. The derivation of the $\langle \boldsymbol{\mu} \rangle$ when $J' \neq J$ involves Racah algebra [12], and is not reproduced here. Instead, we limit ourselves to the dipole approximation, within which only transitions for $J' = J \pm 1$ are allowed, and state below, without proof:

$$\langle S, L, J, m_J | \, \boldsymbol{L}_z + 2\boldsymbol{S}_z \, | S, L, J-1, m_J \rangle = (J^2 - m_J^2)^{\frac{1}{2}} \langle S, L, J || \boldsymbol{\Lambda} || S, L, J-1 \rangle, \tag{B.7}$$

and

$$\langle S, L, J, m_J | \, \boldsymbol{L}_x + 2\boldsymbol{S}_x \, | S, L, J-1, m_J \pm 1 \rangle = \pm \frac{1}{2} [J(J+1) - m_J(m_J \pm 1)]^{\frac{1}{2}} \langle S, L, J || \boldsymbol{\Lambda} || S, L, J-1 \rangle, \tag{B.8}$$

where the *double matrix element*

$$\langle S, L, J||\mathbf{\Lambda}||S, L, J-1\rangle = \left[\frac{(S+L+J+1)(S+L-J+1)(J+L-S)(J-L+S)}{4J^2(2J+1)(2J-1)}\right]^{\frac{1}{2}}. \quad \text{(B.9)}$$

The matrix element of the component of the magnetic moment projected along y can be deduced from the component along x using

$$\langle S, L, J, m_J|\, \boldsymbol{L_y} + 2\boldsymbol{S_y}\, |S, L, J-1, m_J \pm 1\rangle = \mp i \langle S, L, J, m_J|\, \boldsymbol{L_x} + 2\boldsymbol{S_x}\, |S, L, J-1, m_J \pm 1\rangle\,. \quad \text{(B.10)}$$

Appendix C

Matrix representations of the symmetry operations for axial vectors

The way that each symmetry operation acts on the components of a pseudovector can be represented by 3×3 matrices. Those which are relevant in the determination of the exchange Hamiltonian presented in Chapter 1 are given below. The nomenclature of the symmetry operations follow the Schoenflies notation, according to Appendix A.

$$C_3^{[111]} = \begin{pmatrix} 0 & 0 & 1 \\ 1 & 0 & 0 \\ 0 & 1 & 0 \end{pmatrix}, \tag{C.1}$$

$$S_4^x = \begin{pmatrix} 1 & 0 & 0 \\ 0 & 0 & -1 \\ 0 & 1 & 0 \end{pmatrix}, \tag{C.2}$$

$$S_4^y = \begin{pmatrix} 0 & 0 & 1 \\ 0 & 1 & 0 \\ -1 & 0 & 0 \end{pmatrix}, \tag{C.3}$$

$$S_4^z = \begin{pmatrix} 0 & -1 & 0 \\ 1 & 0 & 0 \\ 0 & 0 & 1 \end{pmatrix}, \tag{C.4}$$

$$C_2^x = \begin{pmatrix} 1 & 0 & 0 \\ 0 & -1 & 0 \\ 0 & 0 & -1 \end{pmatrix}, \tag{C.5}$$

$$\sigma^{[011]} = \begin{pmatrix} -1 & 0 & 0 \\ 0 & 0 & 1 \\ 0 & 1 & 0 \end{pmatrix}. \tag{C.6}$$

Appendix D

Local coordinate system

The matrices below are used in the transformation of the coordinate system from local to global (or *vice-versa*). They can be found by stacking side-by-side the coordinates of the local x, y, z axis and transposing the resulting matrix. As the transformation is unitary, $R_\alpha^T R_\alpha = R_\alpha R_\alpha^T = \mathbb{1}$.

$$R_0 = \frac{1}{\sqrt{6}} \begin{pmatrix} -2 & 1 & 1 \\ 0 & -\sqrt{3} & \sqrt{3} \\ \sqrt{2} & \sqrt{2} & \sqrt{2} \end{pmatrix}, \tag{D.1}$$

$$R_1 = \frac{1}{\sqrt{6}} \begin{pmatrix} -2 & -1 & -1 \\ 0 & \sqrt{3} & -\sqrt{3} \\ \sqrt{2} & -\sqrt{2} & -\sqrt{2} \end{pmatrix}, \tag{D.2}$$

$$R_2 = \frac{1}{\sqrt{6}} \begin{pmatrix} 2 & 1 & -1 \\ 0 & -\sqrt{3} & -\sqrt{3} \\ -\sqrt{2} & \sqrt{2} & -\sqrt{2} \end{pmatrix}, \tag{D.3}$$

$$R_3 = \frac{1}{\sqrt{6}} \begin{pmatrix} 2 & -1 & 1 \\ 0 & \sqrt{3} & \sqrt{3} \\ -\sqrt{2} & -\sqrt{2} & \sqrt{2} \end{pmatrix}. \tag{D.4}$$

With the coordinates transformation, some complex coefficients appear in the linearised form of the Hamiltonian [see Equation (1.22)]. Those terms are presented in a matricial form as follows:

$$\zeta = -\gamma^* \begin{pmatrix} 0 & -1 & e^{i\pi/3} & e^{-i\pi/3} \\ -1 & 0 & e^{-i\pi/3} & e^{i\pi/3} \\ e^{i\pi/3} & e^{-i\pi/3} & 0 & -1 \\ e^{-i\pi/3} & e^{i\pi/3} & -1 & 0 \end{pmatrix}. \tag{D.5}$$

Appendix E

Refined profiles of $^{154}Sm_2Sn_2O_7$

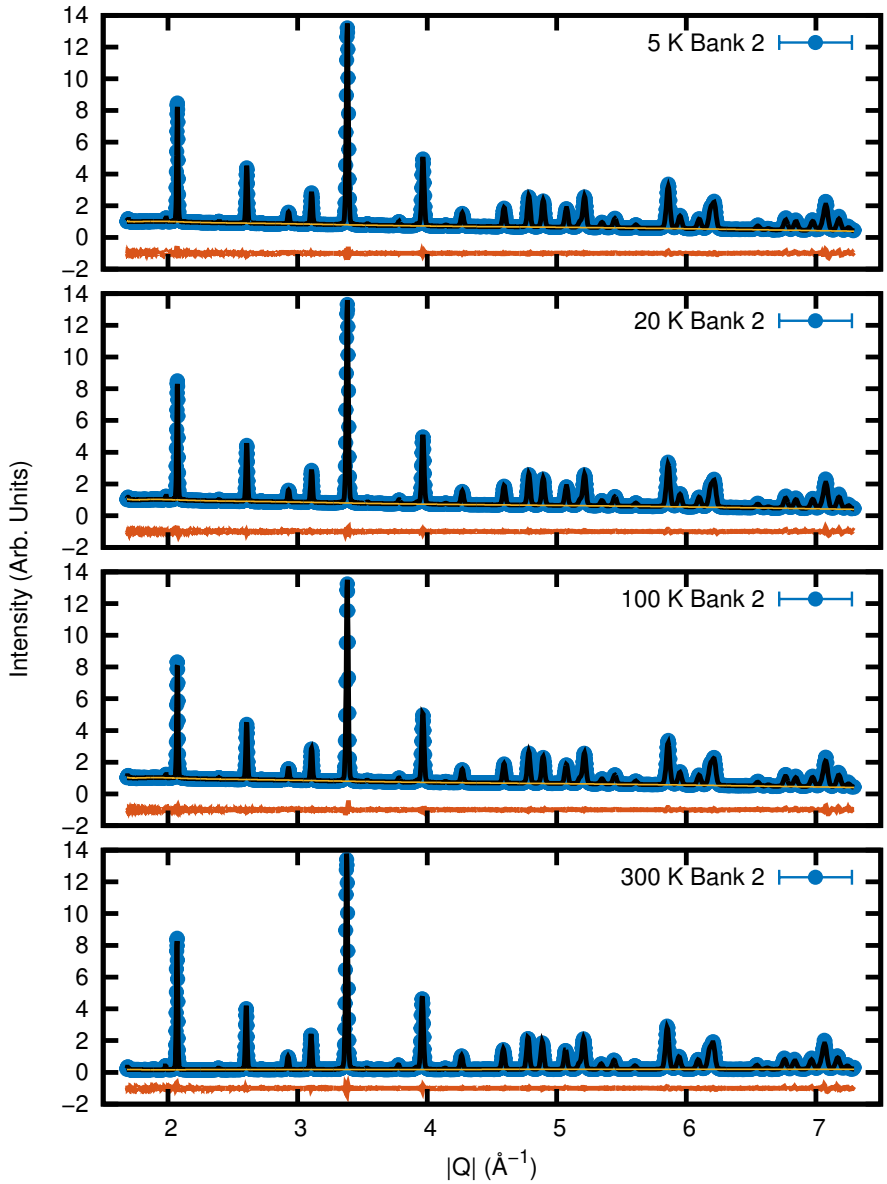

Figure E.1: Data for the $^{154}Sm_2Sn_2O_7$ sample collected in the intermediate resolution detector bank of HRPD, or bank 2. Measurements were performed at 5 K, 20 K, 100 K and 300 K, as indicated in the figures labels. The colour code follows the specified in the caption of Figure 3.1.

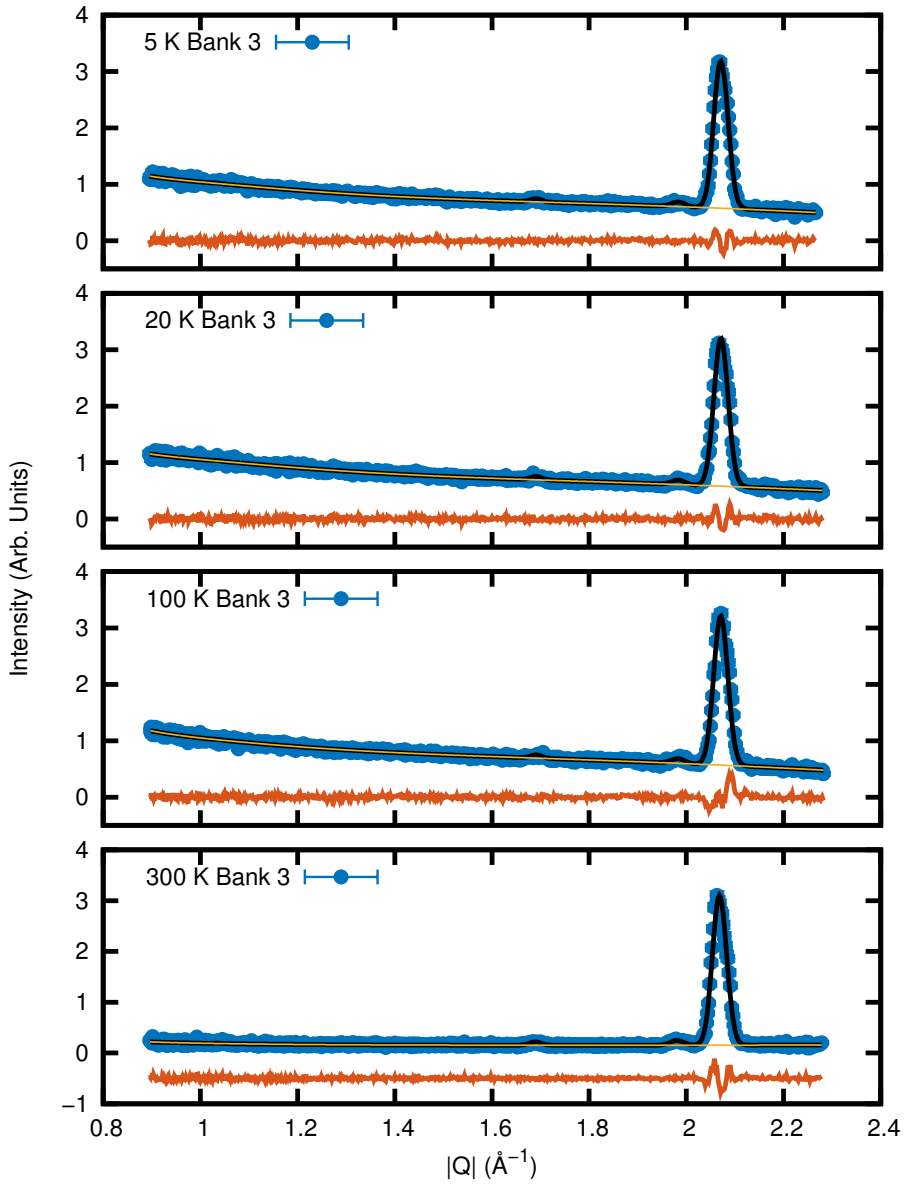

Figure E.2: Data for the $^{154}Sm_2Sn_2O_7$ sample collected in the low resolution, low momentum transfer detector bank of HRPD, or bank 3. Measurements were performed at 5 K, 20 K, 100 K and 300 K, as indicated in the figures labels. The colour code follows the specified in the caption of Figure 3.1.

Appendix F

Refined profiles of $^{154}Sm_2Ti_2O_7$

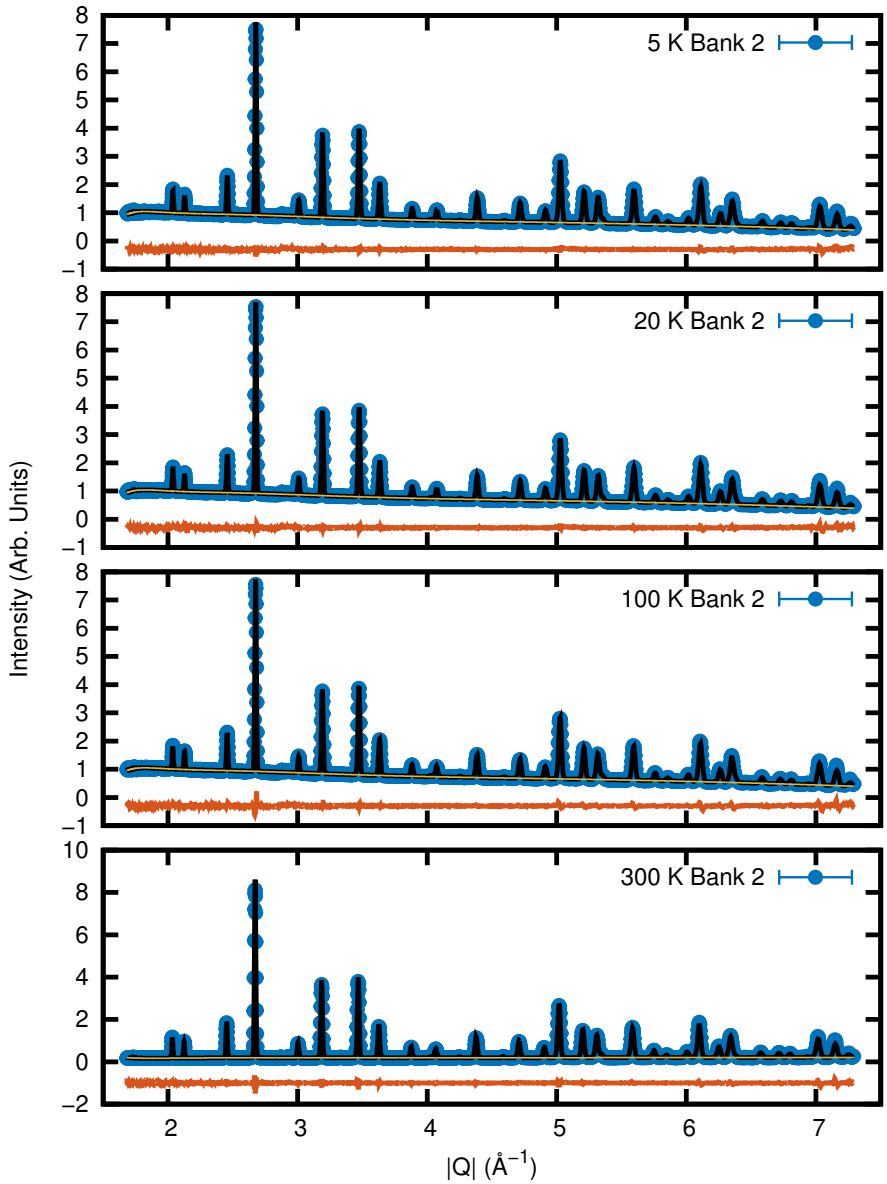

Figure F.1: Data for the $^{154}Sm_2Ti_2O_7$ sample collected in bank 2. Measurements were performed at 5 K, 20 K, 100 K and 300 K, as indicated in the figures labels. The colour code follows the specified in the caption of Figure 3.2.

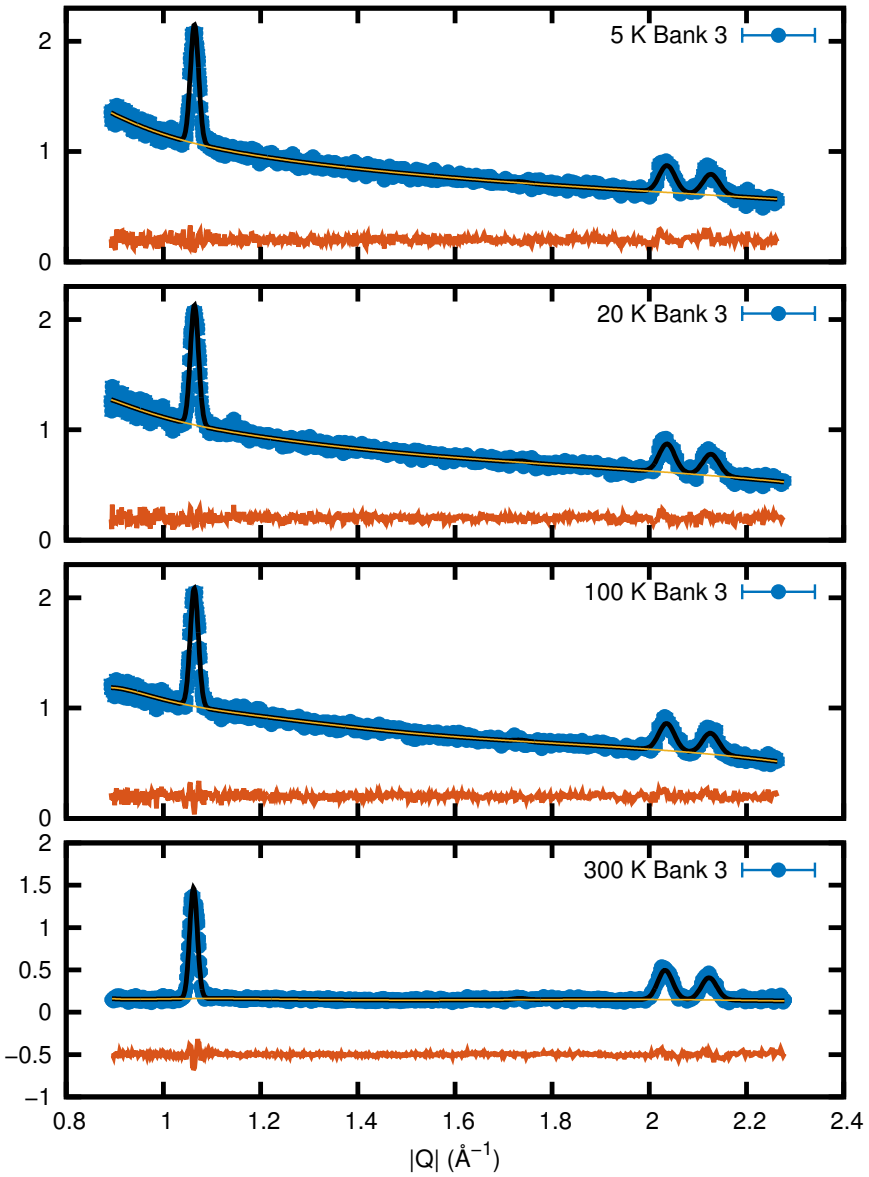

Figure F.2: Data for the $^{154}Sm_2Ti_2O_7$ sample collected in bank 3. Measurements were performed at 5 K, 20 K, 100 K and 300 K, as indicated in the figures labels. The colour code follows the specified in the caption of Figure 3.2.

Bibliography

[1] P. W. Anderson, "The concept of frustration in spin glasses," *Journal of the Less Common Metals*, vol. 62, pp. 291–294, 1978.

[2] J. A. Mydosh, "Spin glasses: redux: an updated experimental/materials survey," *Reports on Progress in Physics*, vol. 78, no. 5, p. 052501, 2015.

[3] J. E. Greedan, M. Sato, X. Yan, and F. S. Razavi, "Spin-glass-like behavior in $Y_2Mo_2O_7$, a concentrated, crystalline system with negligible apparent disorder," *Solid State Communications*, vol. 59, no. 12, pp. 895–897, 1986.

[4] H. J. Silverstein, K. Fritsch, F. Flicker, A. M. Hallas, J. S. Gardner, Y. Qiu, G. Ehlers, A. T. Savici, Z. Yamani, K. A. Ross, B. D. Gaulin, M. J. P. Gingras, J. A. M. Paddison, K. Foyevtsova, R. Valenti, F. Hawthorne, C. R. Wiebe, and H. D. Zhou, "Liquidlike correlations in single-crystalline $Y_2Mo_2O_7$: An unconventional spin glass," *Physical Review B*, vol. 89, p. 054433, 2014.

[5] G. H. Wannier, "Antiferromagnetism. The Triangular Ising Net," *Physical Review*, vol. 79, pp. 357–364, 1950.

[6] M. A. Subramanian, G. Aravamudan, and G. V. Subba Rao, "Oxide pyrochlores — A review," *Progress in Solid State Chemistry*, vol. 15, no. 2, pp. 55–143, 1983.

[7] J. S. Gardner, M. J. P. Gingras, and J. E. Greedan, "Magnetic pyrochlore oxides," *Reviews of Modern Physics*, vol. 82, pp. 53–107, 2010.

[8] J. E. Greedan, "Frustrated rare earth magnetism: Spin glasses, spin liquids and spin ices in pyrochlore oxides," *Journal of Alloys and Compounds*, vol. 408–412, pp. 444–455, 2006. Proceedings of Rare Earths'04 in Nara, Japan.

[9] J. G. Rau and M. J. P. Gingras, "Frustrated Quantum Rare-Earth Pyrochlores," *Annual Review of Condensed Matter Physics*, vol. 10, no. 1, pp. 357–386, 2019.

[10] A. W. C. Wong, Z. Hao, and M. J. P. Gingras, "Ground state phase diagram of generic XY pyrochlore magnets with quantum fluctuations," *Physical Review B*, vol. 88, p. 144402, 2013.

[11] L. Savary, K. A. Ross, B. D. Gaulin, J. P. C. Ruff, and L. Balents, "Order by Quantum Disorder in $Er_2Ti_2O_7$," *Physical Review Letters*, vol. 109, p. 167201, 2012.

[12] M. T. Hutchings, "Point-Charge Calculations of Energy Levels of Magnetic Ions in Crystalline Electric Fields," in *Solid State Physics*, vol. 16, pp. 227–273, New York: Academic Press, 1964.

[13] B. G. Wybourne, *Spectroscopic Properties Of Rare Earths*. New York: John Wiley and Sons, Inc., 1965.

[14] H. A. Buckmaster and R. Chatterjee, "The Analysis of EPR Spectra Using Tesseral Tensor Angular Momentum Operators," *physica status solidi (b)*, vol. 209, no. 2, pp. 433–441, 1998.

[15] H. A. Buckmaster, R. Chatterjee, and J. A. Tuszynski, "The derivation of a symmetry-adapted generalized spin Hamiltonian," *The Journal of Chemical Physics*, vol. 83, no. 8, pp. 4001–4004, 1985.

[16] A. J. Freeman and J. P. Desclaux, "Dirac-Fock studies of some electronic properties of rare-earth ions," *Journal of Magnetism and Magnetic Materials*, vol. 12, no. 1, pp. 11–21, 1979.

[17] J. A. Tuszynski, H. A. Buckmaster, R. Chatterjee, and J. M. Boteler, "Point-group discrimination using the *c*-axis angular variation of the EPR fine-structure spectra for *S*-state ions," *Journal of Magnetic Resonance (1969)*, vol. 63, no. 2, pp. 241–254, 1985.

[18] S. Rosenkranz, A. P. Ramirez, A. Hayashi, R. J. Cava, R. Siddharthan, and B. S. Shastry, "Crystal-field interaction in the pyrochlore magnet $Ho_2Ti_2O_7$," *Journal of Applied Physics*, vol. 87, no. 9, pp. 5914–5916, 2000.

[19] K. W. H. Stevens, "Matrix Elements and Operator Equivalents Connected with the Magnetic Properties of Rare Earth Ions," *Proceedings of the Physical Society. Section A*, vol. 65, no. 3, pp. 209–215, 1952.

[20] B. Bleaney and K. W. H. Stevens, "Paramagnetic resonance," *Reports on Progress in Physics*, vol. 16, no. 1, pp. 108–159, 1953.

[21] A. T. Boothroyd, SPECTRE – *a program for calculating spectroscopic properties of rare earth ions in crystals*, 1990-2014.

[22] A. Bertin, Y. Chapuis, P. D. de Réotier, and A. Yaouanc, "Crystal electric field in the $R_2Ti_2O_7$ pyrochlore compounds," *Journal of Physics: Condensed Matter*, vol. 24, no. 25, p. 256003, 2012.

[23] S. H. Curnoe, "Exchange interactions in two-state systems: rare earth pyrochlores," *Journal of Physics: Condensed Matter*, vol. 30, no. 23, p. 235803, 2018.

[24] K. A. Ross, L. Savary, B. D. Gaulin, and L. Balents, "Quantum Excitations in Quantum Spin Ice," *Physical Review X*, vol. 1, p. 021002, 2011.

[25] J. N. Reimers, A. J. Berlinsky, and A.-C. Shi, "Mean-field approach to magnetic ordering in highly frustrated pyrochlores," *Physical Review B*, vol. 43, pp. 865–878, 1991.

[26] D. Tsuneishi, M. Ioki, and H. Kawamura, "Novel ordering of the pyrochlore Heisenberg antiferromagnet with the ferromagnetic next-nearest-neighbour interaction," *Journal of Physics: Condensed Matter*, vol. 19, no. 14, p. 145273, 2007.

[27] Y. Iqbal, T. Müller, P. Ghosh, M. J. P. Gingras, H. O. Jeschke, S. Rachel, J. Reuther, and R. Thomale, "Quantum and Classical Phases of the Pyrochlore Heisenberg Model with Competing Interactions," *Physical Review X*, vol. 9, p. 011005, 2019.

[28] J. G. Rau and M. J. P. Gingras, "Spin slush in an extended spin ice model," *Nature Communications*, vol. 7, p. 12234, 2016.

[29] S. Petit, E. Lhotel, B. Canals, M. Ciomaga Hatnean, J. Ollivier, H. Mutka, E. Ressouche, A. R. Wildes, M. R. Lees, and G. Balakrishnan, "Observation of magnetic fragmentation in spin ice," *Nature Physics*, vol. 12, pp. 746–750, 04 2016.

[30] Z. L. Dun, J. Ma, H. B. Cao, Y. Qiu, J. R. D. Copley, T. Hong, M. Matsuda, J. G. Cheng, M. Lee, E. S. Choi, S. Johnston, and H. D. Zhou, "Competition between the inter- and intra-sublattice interactions in $Yb_2V_2O_7$," *Physical Review B*, vol. 91, p. 064425, 2015.

[31] H. Yan, O. Benton, L. Jaubert, and N. Shannon, "Theory of multiple-phase competition in pyrochlore magnets with anisotropic exchange with application to $Yb_2Ti_2O_7$, $Er_2Ti_2O_7$, and $Er_2Sn_2O_7$," *Physical Review B*, vol. 95, p. 094422, 2017.

[32] T. Moriya, "Anisotropic Superexchange Interaction and Weak Ferromagnetism," *Physical Review*, vol. 120, pp. 91–98, 1960.

[33] M. Elhajal, B. Canals, R. Sunyer, and C. Lacroix, "Ordering in the pyrochlore antiferromagnet due to Dzyaloshinsky-Moriya interactions," *Physical Review B*, vol. 71, p. 094420, 2005.

[34] Y.-P. Huang, G. Chen, and M. Hermele, "Quantum Spin Ices and Topological Phases from Dipolar-Octupolar Doublets on the Pyrochlore Lattice," *Physical Review Letters*, vol. 112, p. 167203, 2014.

[35] O. Benton, "Quantum origins of moment fragmentation in $Nd_2Zr_2O_7$," *Physical Review B*, vol. 94, p. 104430, 2016.

[36] E. Lhotel, S. Petit, S. Guitteny, O. Florea, M. Ciomaga Hatnean, C. Colin, E. Ressouche, M. R. Lees, and G. Balakrishnan, "Fluctuations and All-In–All-Out Ordering in Dipole-Octupole $Nd_2Zr_2O_7$," *Physical Review Letters*, vol. 115, p. 197202, 2015.

[37] L. E. Chern and Y. B. Kim, "Magnetic Order with Fractionalized Excitations: Applications to $Yb_2Ti_2O_7$." Preprint, 2018.

[38] J. G. Rau, R. Moessner, and P. A. McClarty, "Magnon interactions in the frustrated pyrochlore ferromagnet $Yb_2Ti_2O_7$." Preprint, 2019.

[39] W. Nolting and A. Ramakanth, "Heisenberg Model," in *Quantum Theory of Magnetism*, pp. 273–386, Berlin, Heidelberg: Springer, 2009.

[40] D. D. Stancil and A. Prabhakar, "Quantum Theory of Spin Waves," in *Spin Waves: Theory and Applications*, pp. 33–66, Boston, MA: Springer US, 2009.

[41] T. Holstein and H. Primakoff, "Field Dependence of the Intrinsic Domain Magnetization of a Ferromagnet," *Physical Review*, vol. 58, pp. 1098–1113, Dec 1940.

[42] R. M. White, M. Sparks, and I. Ortenburger, "Diagonalization of the Antiferromagnetic Magnon-Phonon Interaction," *Physical Review*, vol. 139, pp. A450–A454, Jul 1965.

[43] S. Toth and B. Lake, "Linear spin wave theory for single-Q incommensurate magnetic structures," *Journal of Physics: Condensed Matter*, vol. 27, no. 16, p. 166002, 2015.

[44] M. J. P. Gingras, "Spin Ice," in *Introduction to Frustrated Magnetism: Materials, Experiments, Theory* (C. Lacroix, P. Mendels, and F. Mila, eds.), vol. 164, pp. 293–329, Berlin, Heidelberg: Springer, 2011.

[45] L. R. Corruccini and S. J. White, "Dipolar antiferromagnetism in the spin-wave approximation," *Physical Review B*, vol. 47, pp. 773–777, 1993.

[46] L. Pauling, "The Structure and Entropy of Ice and of Other Crystals with Some Randomness of Atomic Arrangement," *Journal of the American Chemical Society*, vol. 57, no. 12, pp. 2680–2684, 1935.

[47] M. J. Harris, S. T. Bramwell, D. F. McMorrow, T. Zeiske, and K. W. Godfrey, "Geometrical Frustration in the Ferromagnetic Pyrochlore $Ho_2Ti_2O_7$," *Physical Review Letters*, vol. 79, pp. 2554–2557, 1997.

[48] A. P. Ramirez, A. Hayashi, R. J. Cava, R. Siddharthan, and B. S. Shastry, "Zero-point entropy in 'spin ice'," *Nature*, vol. 399, pp. 333–335, 1999.

[49] S. V. Isakov, R. Moessner, and S. L. Sondhi, "Why Spin Ice Obeys the Ice Rules," *Physical Review Letters*, vol. 95, p. 217201, 2005.

[50] S. T. Bramwell, "A spin on cool complexity," *Nature Physics*, vol. 2, p. 219, 2006.

[51] S. T. Bramwell, M. J. Harris, B. C. den Hertog, M. J. P. Gingras, J. S. Gardner, D. F. McMorrow, A. R. Wildes, A. L. Cornelius, J. D. M. Champion, R. G. Melko, and T. Fennell, "Spin Correlations in $Ho_2Ti_2O_7$: A Dipolar Spin Ice System," *Physical Review Letters*, vol. 87, p. 047205, 2001.

[52] R. Siddharthan, B. S. Shastry, A. P. Ramirez, A. Hayashi, R. J. Cava, and S. Rosenkranz, "Ising Pyrochlore Magnets: Low-Temperature Properties, 'Ice Rules,' and Beyond," *Physical Review Letters*, vol. 83, pp. 1854–1857, 1999.

[53] C. Castelnovo, R. Moessner, and S. L. Sondhi, "Magnetic monopoles in spin ice," *Nature*, vol. 451, pp. 42–45, 01 2008.

[54] M. J. P. Gingras, "Observing Monopoles in a Magnetic Analog of Ice," *Science*, vol. 326, no. 5951, pp. 375–376, 2009.

[55] T. Fennell, P. P. Deen, A. R. Wildes, K. Schmalzl, D. Prabhakaran, A. T. Boothroyd, R. J. Aldus, D. F. McMorrow, and S. T. Bramwell, "Magnetic Coulomb Phase in the Spin Ice $Ho_2Ti_2O_7$," *Science*, vol. 326, no. 5951, pp. 415–417, 2009.

[56] D. J. P. Morris, D. A. Tennant, S. A. Grigera, B. Klemke, C. Castelnovo, R. Moessner, C. Czternasty, M. Meissner, K. C. Rule, J.-U. Hoffmann, K. Kiefer, S. Gerischer, D. Slobinsky, and R. S. Perry, "Dirac Strings and Magnetic Monopoles in the Spin Ice $Dy_2Ti_2O_7$," *Science*, vol. 326, no. 5951, pp. 411–414, 2009.

[57] L. Savary and L. Balents, "Coulombic Quantum Liquids in Spin-1/2 Pyrochlores," *Physical Revew Letters*, vol. 108, p. 037202, 2012.

[58] M. J. P. Gingras and P. A. McClarty, "Quantum spin ice: a search for gapless quantum spin liquids in pyrochlore magnets," *Reports on Progress in Physics*, vol. 77, no. 5, p. 056501, 2014.

[59] L. D. C. Jaubert, O. Benton, J. G. Rau, J. Oitmaa, R. R. P. Singh, N. Shannon, and M. J. P. Gingras, "Are Multiphase Competition and Order by Disorder the Keys to Understanding $Yb_2Ti_2O_7$?," *Physical Review Letters*, vol. 115, p. 267208, 2015.

[60] S. W. Lovesey, *Theory of neutron scattering from condensed matter*, vol. I. United Kingdom: Clarendon Press, 1984.

[61] G. L. Squires, *Introduction to the Theory of Thermal Neutron Scattering*. United Kingdom: Cambridge University Press, 3 ed., 2012.

[62] J. Als-Nielsen and D. McMorrow, *Elements of Modern X-ray Physics*. United Kingdom: John Wiley and Sons, Inc., 2011.

[63] V. F. Sears, "Neutron scattering lengths and cross sections," *Neutron News*, vol. 3, no. 3, pp. 26–37, 1992.

[64] L. Van Hove, "Correlations in Space and Time and Born Approximation Scattering in Systems of Interacting Particles," *Physical Review*, vol. 95, pp. 249–262, 1954.

[65] A. Furrer, J. Mesot, and T. Strässle, *Neutron Scattering in Condensed Matter Physics*. WORLD SCIENTIFIC, 2009.

[66] B. Buras and L. Gerward, "Relations between integrated intensities in crystal diffraction methods for X-rays and neutrons," *Acta Crystallographica Section A*, vol. 31, no. 3, pp. 372–374, 1975.

[67] R. W. Harrison, "Phase problem in crystallography," *Journal of the Optical Society of America A*, vol. 10, no. 5, pp. 1046–1055, 1993.

[68] H. M. Rietveld, "A profile refinement method for nuclear and magnetic structures," *Journal of Applied Crystallography*, vol. 2, no. 2, pp. 65–71, 1969.

[69] J. Rodríguez-Carvajal, "Recent advances in magnetic structure determination by neutron powder diffraction," *Physica B: Condensed Matter*, vol. 192, no. 1-2, pp. 55–69, 1993.

[70] A. C. Larson and R. B. von Dreele, *General Structure Analysis System* (GSAS), 2004.

[71] S. W. Lovesey, *Theory of neutron scattering from condensed matter*, vol. II. United Kingdom: Clarendon Press, 1984.

[72] R. Osborn, S. Lovesey, A. Taylor, and E. Balcar, "Intermultiplet transitions using neutron spectroscopy," in *Handbook on the Physics and Chemistry of Rare Earths*, vol. 14, pp. 1–61, Amsterdan: Elsevier, 1991.

[73] H. B. Callen and T. A. Welton, "Irreversibility and Generalized Noise," *Physical Review*, vol. 83, pp. 34–40, 1951.

[74] W. Marshall and R. D. Lowde, "Magnetic correlations and neutron scattering," *Reports on Progress in Physics*, vol. 31, no. 2, pp. 705–775, 1968.

[75] J. Rossat-Mignod, "Magnetic Structures," in *Neutron Scattering* (K. Sköld and D. L. Price, eds.), vol. 23 of *Methods in Experimental Physics*, pp. 69–157, Academic Press, 1987.

[76] J. Rodríguez-Carvajal and F. Bourée, "Symmetry and magnetic structures," *EPJ Web of Conferences*, vol. 22, p. 00010, 2012.

[77] A. Wills, "A new protocol for the determination of magnetic structures using simulated annealing and representational analysis (SARA*h*)," *Physica B: Condensed Matter*, vol. 276-278, pp. 680–681, 2000.

[78] A. Wills, "Magnetic structures and their determination using group theory," *Journal de Physique IV*, vol. 11, no. 9, pp. Pr9–133–Pr9–158, 2001.

[79] V. Peçanha-Antonio, E. Feng, Y. Su, V. Pomjakushin, F. Demmel, L.-J. Chang, R. J. Aldus, Y. Xiao, M. R. Lees, and T. Brückel, "Magnetic excitations in the ground state of $Yb_2Ti_2O_7$," *Physical Review B*, vol. 96, p. 214415, 2017.

[80] J. Rodríguez-Carvajal, "BASIREPS: a program for calculating irreducible representations of space groups and basis functions for axial and polar vector properties." Unpublished.

[81] I. S. Anderson, P. J. Brown, J. M. Carpenter, G. Lander, R. Pynn, J. M. Rowe, O. Schärpf, V. F. Sears, and B. T. M. Willis, "Neutron techniques," in *International Tables for Crystallography (2006).*, vol. C, ch. 4.4, pp. 430–487, Dordrecht: Springer Netherlands, 2004.

[82] O. Schärpf and H. Capellmann, "The XYZ-Difference Method with Polarized Neutrons and the Separation of Coherent, Spin Incoherent, and Magnetic Scattering Cross Sections in a Multidetector," *physica status solidi (a)*, vol. 135, no. 2, pp. 359–379, 1993.

[83] Heinz Maier-Leibnitz Zentrum *et al.*, "DNS: Diffuse scattering neutron time-of-flight spectrometer," *Journal of large scale facilities*, vol. 1, p. A27, 2015.

[84] B. T. M. Willis, "Crystallography with a pulsed neutron source," *Zeitschrift für Kristallographie*, vol. 209, no. 5, pp. 385–389, 1994.

[85] L. C. Chapon, P. Manuel, P. G. Radaelli, C. Benson, L. Perrott, S. Ansell, N. J. Rhodes, D. Raspino, D. Duxbury, E. Spill, and J. Norris, "Wish: The New Powder and Single Crystal Magnetic Diffractometer on the Second Target Station," *Neutron News*, vol. 22, no. 2, pp. 22–25, 2011.

[86] R. I. Bewley, R. S. Eccleston, K. A. McEwen, S. M. Hayden, M. T. Dove, S. M. Bennington, J. R. Treadgold, and R. L. S. Coleman, "MERLIN, a new high count rate spectrometer at ISIS," *Physica B: Condensed Matter*, vol. 385-386, Part 2, pp. 1029–1031, 2006.

[87] C. J. Carlile and M. A. Adams, "The design of the IRIS inelastic neutron spectrometer and improvements to its analysers," *Physica B: Condensed Matter*, vol. 182, no. 4, pp. 431–440, 1992.

[88] F. Demmel and K. Pokhilchuk, "The resolution of the tof-backscattering spectrometer OSIRIS: Monte Carlo simulations and analytical calculations," *Nuclear Instruments and Methods in Physics Research Section A: Accelerators, Spectrometers, Detectors and Associated Equipment*, vol. 767, pp. 426–432, 2014.

[89] Y. J. Uemura, "μSR relaxation functions in magnetic materials," in *Muon Science: Muons in Physics, Chemistry and Materials* (S. L. Lee, S. H. Kilcoyne, and R. Cywinski, eds.), New York: Taylor and Francis Group, 1999.

[90] S. J. Blundell, "Spin-polarized muons in condensed matter physics," *Contemporary Physics*, vol. 40, no. 3, pp. 175–192, 1999.

[91] P. D. de Réotier and A. Yaouanc, "Muon spin rotation and relaxation in magnetic materials," *Journal of Physics: Condensed Matter*, vol. 9, no. 43, pp. 9113–9166, 1997.

[92] A. Yaouanc and P. D. de Réotier, *Muon Spin Rotation, Relaxation, and Resonance*. Oxford: Oxford University Press, 2011.

[93] S. Singh, S. Saha, S. K. Dhar, R. Suryanarayanan, A. K. Sood, and A. Revcolevschi, "Manifestation of geometric frustration on magnetic and thermodynamic properties of the pyrochlores $Sm_2X_2O_7$ (X = Ti, Zr)," *Physical Review B*, vol. 77, p. 054408, 2008.

[94] B. Z. Malkin, T. T. A. Lummen, P. H. M. van Loosdrecht, G. Dhalenne, and A. R. Zakirov, "Static magnetic susceptibility, crystal field and exchange interactions in rare earth titanate pyrochlores," *Journal of Physics: Condensed Matter*, vol. 22, no. 27, p. 276003, 2010.

[95] C. Mauws, A. M. Hallas, G. Sala, A. A. Aczel, P. M. Sarte, J. Gaudet, D. Ziat, J. A. Quilliam, J. A. Lussier, M. Bieringer, H. D. Zhou, A. Wildes, M. B. Stone, D. Abernathy, G. M. Luke, B. D. Gaulin, and C. R. Wiebe, "Dipolar-octupolar Ising antiferromagnetism in $Sm_2Ti_2O_7$: A moment fragmentation candidate," *Physical Review B*, vol. 98, p. 100401, 2018.

[96] W. Zhang, Z. Ma, L. Du, and H. Li, "Role of PEG4000 in sol-gel synthesis of $Sm_2Ti_2O_7$ photocatalyst for enhanced activity," *Journal of Alloys and Compounds*, vol. 704, pp. 26–31, 2017.

[97] M. Jafar, P. Sengupta, S. N. Achary, and A. K. Tyagi, "Phase evolution and microstructural studies in $CaZrTi_2O_7$ (zirconolite)–$Sm_2Ti_2O_7$ (pyrochlore) system," *Journal of the European Ceramic Society*, vol. 34, no. 16, pp. 4373–4381, 2014.

[98] M. E. Rabanal, A. Várez, U. Amador, E. Arroyo y Dompablo, and F. García-Alvarado, "Structure and reaction with lithium of tetragonal pyrochlore-like compound $Sm_2Ti_2O_7$," *Journal of Materials Processing Technology*, vol. 92-93, pp. 529–533, 1999.

[99] V. Bondah-Jagalu and S. T. Bramwell, "Magnetic susceptibility study of the heavy rare-earth stannate pyrochlores," *Canadian Journal of Physics*, vol. 79, no. 11-12, pp. 1381–1385, 2001.

[100] B. J. Kennedy and M. Avdeev, "The structure of *B*-type Sm_2O_3. A powder neutron diffraction study using enriched ^{154}Sm," *Solid State Sciences*, vol. 13, no. 9, pp. 1701–1703, 2011.

[101] L. Minervini, R. W. Grimes, and K. E. Sickafus, "Disorder in Pyrochlore Oxides," *Journal of the American Ceramic Society*, vol. 83, no. 8, pp. 1873–1878, 2004.

[102] Y. Li, P. M. Kowalski, G. Beridze, A. R. Birnie, S. Finkeldei, and D. Bosbach, "Defect formation energies in $A_2B_2O_7$ pyrochlores," *Scripta Materialia*, vol. 107, pp. 18–21, 2015.

[103] R. Sibille, E. Lhotel, M. Ciomaga Hatnean, G. J. Nilsen, G. Ehlers, A. Cervellino, E. Ressouche, M. Frontzek, O. Zaharko, V. Pomjakushin, U. Stuhr, H. C. Walker, D. T. Adroja, H. Luetkens, C. Baines, A. Amato, G. Balakrishnan, T. Fennell, and M. Kenzelmann, "Coulomb spin liquid in anion-disordered pyrochlore $Tb_2Hf_2O_7$," *Nature Communications*, vol. 8, no. 1, p. 892, 2017.

[104] J. P. C. Ruff, B. D. Gaulin, J. P. Castellan, K. C. Rule, J. P. Clancy, J. Rodriguez, and H. A. Dabkowska, "Structural Fluctuations in the Spin-Liquid State of $Tb_2Ti_2O_7$," *Physical Review Letters*, vol. 99, p. 237202, 2007.

[105] T. Fennell, M. Kenzelmann, B. Roessli, H. Mutka, J. Ollivier, M. Ruminy, U. Stuhr, O. Zaharko, L. Bovo, A. Cervellino, M. K. Haas, and R. J. Cava, "Magnetoelastic Excitations in the Pyrochlore Spin Liquid $Tb_2Ti_2O_7$," *Physical Review Letters*, vol. 112, p. 017203, 2014.

[106] M. Ruminy, S. Chi, S. Calder, and T. Fennell, "Phonon-mediated spin-flipping mechanism in the spin ices $Dy_2Ti_2O_7$ and $Ho_2Ti_2O_7$," *Physical Review B*, vol. 95, p. 060414, 2017.

[107] M. Ruminy, L. Bovo, E. Pomjakushina, M. K. Haas, U. Stuhr, A. Cervellino, R. J. Cava, M. Kenzelmann, and T. Fennell, "Sample independence of magnetoelastic excitations in the rare-earth pyrochlore $Tb_2Ti_2O_7$," *Physical Review B*, vol. 93, p. 144407, 2016.

[108] M. Ruminy, F. Groitl, T. Keller, and T. Fennell, "Neutron Larmor diffraction investigation of the rare-earth pyrochlores $R_2Ti_2O_7$ (R = Tb, Dy, Ho)," *Physical Review B*, vol. 94, p. 174406, 2016.

[109] A. P. Sazonov, A. Gukasov, H. B. Cao, P. Bonville, E. Ressouche, C. Decorse, and I. Mirebeau, "Magnetic structure in the spin liquid $Tb_2Ti_2O_7$ induced by a [111] magnetic field: Search for a magnetization plateau," *Physical Review B*, vol. 88, p. 184428, 2013.

[110] J. Xu, *Magnetic properties of rare earth zirconate pyrochlores*. PhD thesis, Technische Universität Berlin, 2017.

[111] S. T. Bramwell and M. J. P. Gingras, "Spin Ice State in Frustrated Magnetic Pyrochlore Materials," *Science*, vol. 294, no. 5546, pp. 1495–1501, 2001.

[112] A. J. Princep, H. C. Walker, D. T. Adroja, D. Prabhakaran, and A. T. Boothroyd, "Crystal field states of Tb^{3+} in the pyrochlore spin liquid $Tb_2Ti_2O_7$ from neutron spectroscopy," *Physical Review B*, vol. 91, p. 224430, 2015.

[113] A. Abragam and B. Bleaney, *Electron paramagnetic resonance of transition ions*. Oxford Classic Texts in the Physical Sciences, United Kingdom: Oxford: Clarendon press, 1970.

[114] M. Ruminy, M. Núñez Valdez, B. Wehinger, A. Bosak, D. T. Adroja, U. Stuhr, K. Iida, K. Kamazawa, E. Pomjakushina, D. Prabakharan, M. K. Haas, L. Bovo, D. Sheptyakov, A. Cervellino, R. J. Cava, M. Kenzelmann, N. A. Spaldin, and T. Fennell, "First-principles calculation and experimental investigation of lattice dynamics in the rare-earth pyrochlores $R_2Ti_2O_7$ (R = Tb, Dy, Ho)," *Physical Review B*, vol. 93, p. 214308, 2016.

[115] M. T. Vandenborre, E. Husson, J. P. Chatry, and D. Michel, "Rare-earth Titanates and Stannates of Pyrochlore Structure; Vibrational Spectra and Force Fields," *Journal of Raman Spectroscopy*, vol. 14, no. 2, pp. 63–71, 1983.

[116] W. T. Carnall, G. L. Goodman, K. Rajnak, and R. S. Rana, "A systematic analysis of the spectra of the lanthanides doped into single crystal LaF_3," *The Journal of Chemical Physics*, vol. 90, no. 7, pp. 3443–3457, 1989.

[117] M. Guillaume, W. Henggeler, A. Furrer, R. S. Eccleston, and V. Trounov, "Intermultiplet Crystal-Field Transitions in $SmBa_2Cu_3O_7$," *Physical Review Letters*, vol. 74, pp. 3423–3426, 1995.

[118] T. Strach, T. Ruf, M. Cardona, C. T. Lin, S. Jandl, V. Nekvasil, D. I. Zhigunov, S. N. Barilo, and S. V. Shiryaev, "Raman study of intermultiplet crystal-field transitions in Sm_2CuO_4," *Physical Review B*, vol. 54, pp. 4276–4282, 1996.

[119] J. H. van Vleck, *The Theory of Electric and Magnetic Susceptibilities*. United Kingdom: Oxford University Press, 1932.

[120] S. J. Blundell, *Magnetism in Condensed Matter*. United Kingdom: Oxford University Press, 2001.

[121] S. T. Bramwell, M. N. Field, M. J. Harris, and I. P. Parkin, "Bulk magnetization of the heavy rare earth titanate pyrochlores - a series of model frustrated magnets," *Journal of Physics: Condensed Matter*, vol. 12, no. 4, pp. 483–495, 2000.

[122] J. Xu, V. K. Anand, A. K. Bera, M. Frontzek, D. L. Abernathy, N. Casati, K. Siemensmeyer, and B. Lake, "Magnetic structure and crystal-field states of the pyrochlore antiferromagnet $Nd_2Zr_2O_7$," *Physical Review B*, vol. 92, p. 224430, 2015.

[123] P. Thalmeier and P. Fulde, "Rare Earth systems in a magnetic field: Coupling of elastic and magnetic properties," *Zeitschrift für Physik B Condensed Matter*, vol. 22, no. 4, pp. 359–366, 1975.

[124] P. Thalmeier, "Theory of the bound state between phonons and a CEF excitation in $CeAl_2$," *Journal of Physics C: Solid State Physics*, vol. 17, no. 23, pp. 4153–4177, 1984.

[125] B.-Q. Liu, P. Čermák, C. Franz, C. Pfleiderer, and A. Schneidewind, "Lattice dynamics and coupled quadrupole-phonon excitations in $CeAuAl_3$," *Physical Review B*, vol. 98, p. 174306, 2018.

[126] J. Gaudet, A. M. Hallas, C. R. C. Buhariwalla, G. Sala, M. B. Stone, M. Tachibana, K. Baroudi, R. J. Cava, and B. D. Gaulin, "Magnetoelastically induced vibronic bound state in the spin-ice pyrochlore $Ho_2Ti_2O_7$," *Physical Review B*, vol. 98, p. 014419, 2018.

[127] S. Guitteny, J. Robert, P. Bonville, J. Ollivier, C. Decorse, P. Steffens, M. Boehm, H. Mutka, I. Mirebeau, and S. Petit, "Anisotropic Propagating Excitations and Quadrupolar Effects in $Tb_2Ti_2O_7$," *Physical Review Letters*, vol. 111, p. 087201, 2013.

[128] S. W. Lovesey and U. Staub, "Magnetoelastic model for the relaxation of lanthanide ions in $YBa_2Cu_3O_{7-\delta}$ observed by neutron scattering," *Physical Review B*, vol. 61, pp. 9130–9139, 2000.

[129] A. Gelessus, W. Thiel, and W. Weber, "Multipoles and Symmetry," *Journal of Chemical Education*, vol. 72, no. 6, p. 505, 1995.

[130] P. Thalmeier and P. Fulde, "Bound State between a Crystal-Field Excitation and a Phonon in $CeAl_2$," *Physical Review Letters*, vol. 49, pp. 1588–1591, 1982.

[131] M. E. Brooks-Bartlett, S. T. Banks, L. D. C. Jaubert, A. Harman-Clarke, and P. C. W. Holdsworth, "Magnetic-Moment Fragmentation and Monopole Crystallization," *Physical Review X*, vol. 4, p. 011007, 2014.

[132] J. Lago, S. J. Blundell, and C. Baines, "μSR investigation of spin dynamics in the spin-ice material $Dy_2Ti_2O_7$," *Journal of Physics: Condensed Matter*, vol. 19, no. 32, p. 326210, 2007.

[133] V. K. Anand, D. L. Abernathy, D. T. Adroja, A. D. Hillier, P. K. Biswas, and B. Lake, "Muon spin relaxation and inelastic neutron scattering investigations of the all-in/all-out antiferromagnet $Nd_2Hf_2O_7$," *Physical Review B*, vol. 95, p. 224420, 2017.

[134] A. Bertin, P. Dalmas de Réotier, B. Fåk, C. Marin, A. Yaouanc, A. Forget, D. Sheptyakov, B. Frick, C. Ritter, A. Amato, C. Baines, and P. J. C. King, "$Nd_2Sn_2O_7$: An all-in–all-out pyrochlore magnet with no divergence-free field and anomalously slow paramagnetic spin dynamics," *Physical Review B*, vol. 92, p. 144423, 2015.

[135] P. Dalmas de Réotier, A. Yaouanc, L. Keller, A. Cervellino, B. Roessli, C. Baines, A. Forget, C. Vaju, P. C. M. Gubbens, A. Amato, and P. J. C. King, "Spin Dynamics and Magnetic Order in Magnetically Frustrated $Tb_2Sn_2O_7$," *Physical Review Letters*, vol. 96, p. 127202, 2006.

[136] F. Bert, P. Mendels, A. Olariu, N. Blanchard, G. Collin, A. Amato, C. Baines, and A. D. Hillier, "Direct Evidence for a Dynamical Ground State in the Highly Frustrated $Tb_2Sn_2O_7$ Pyrochlore," *Physical Review Letters*, vol. 97, p. 117203, 2006.

[137] A. Yaouanc, P. Dalmas de Réotier, P. Bonville, J. A. Hodges, V. Glazkov, L. Keller, V. Sikolenko, M. Bartkowiak, A. Amato, C. Baines, P. J. C. King, P. C. M. Gubbens, and A. Forget, "Dynamical Splayed Ferromagnetic Ground State in the Quantum Spin Ice $Yb_2Sn_2O_7$," *Physical Review Letters*, vol. 110, p. 127207, 2013.

[138] J. Xu, C. Balz, C. Baines, H. Luetkens, and B. Lake, "Spin dynamics of the ordered dipolar-octupolar pseudospin-$\frac{1}{2}$ pyrochlore $Nd_2Zr_2O_7$ probed by muon spin relaxation," *Physical Review B*, vol. 94, p. 064425, 2016.

[139] L.-J. Chang, M. R. Lees, I. Watanabe, A. D. Hillier, Y. Yasui, and S. Onoda, "Static magnetic moments revealed by muon spin relaxation and thermodynamic measurements in the quantum spin ice $Yb_2Ti_2O_7$," *Physical Review B*, vol. 89, p. 184416, 2014.

[140] S. R. Dunsiger, A. A. Aczel, C. Arguello, H. Dabkowska, A. Dabkowski, M.-H. Du, T. Goko, B. Javanparast, T. Lin, F. L. Ning, H. M. L. Noad, D. J. Singh, T. J. Williams, Y. J. Uemura, M. J. P. Gingras, and G. M. Luke, "Spin Ice: Magnetic Excitations without Monopole Signatures Using Muon Spin Rotation," *Physical Review Letters*, vol. 107, p. 207207, 2011.

[141] J. Higinbotham and I. Marshall, "NMR lineshapes and lineshape fitting procedures," in *Annual Reports on NMR Spectroscopy*, vol. 43, pp. 59–120, Academic Press, 2001.

[142] F. L. Pratt, "Field dependence of μSR signals in a polycrystalline magnet," *Journal of Physics: Condensed Matter*, vol. 19, no. 45, p. 456207, 2007.

[143] M. J. Graf, S. M. Disseler, C. Dhital, T. Hogan, M. Bojko, A. Amato, H. Luetkens, C. Baines, D. Margineda, S. R. Giblin, M. Jura, and S. D. Wilson, "Magnetism and magnetic order in the pyrochlore iridates in the insulator-to-metal crossover region," *Journal of Physics: Conference Series*, vol. 551, no. 1, p. 012020, 2014.

[144] R. Sibille, E. Lhotel, V. Pomjakushin, C. Baines, T. Fennell, and M. Kenzelmann, "Candidate Quantum Spin Liquid in the Ce^{3+} Pyrochlore Stannate $Ce_2Sn_2O_7$," *Physical Review Letters*, vol. 115, p. 097202, 2015.

[145] R. Asih, N. Adam, S. S. Mohd-Tajudin, D. P. Sari, K. Matsuhira, H. Guo, M. Wakeshima, Y. Hinatsu, T. Nakano, Y. Nozue, S. Sulaiman, M. I. Mohamed-Ibrahim, P. K. Biswas, and I. Watanabe, "Magnetic Moments and Ordered States in Pyrochlore Iridates $Nd_2Ir_2O_7$ and $Sm_2Ir_2O_7$ Studied by Muon-Spin Relaxation," *Journal of the Physical Society of Japan*, vol. 86, no. 2, p. 024705, 2017.

[146] R. M. D'Ortenzio, H. A. Dabkowska, S. R. Dunsiger, B. D. Gaulin, M. J. P. Gingras, T. Goko, J. B. Kycia, L. Liu, T. Medina, T. J. Munsie, D. Pomaranski, K. A. Ross, Y. J. Uemura, T. J. Williams, and G. M. Luke, "Unconventional magnetic ground state in $Yb_2Ti_2O_7$," *Physical Review B*, vol. 88, p. 134428, 2013.

[147] A. Yaouanc, P. D. de Réotier, V. Glazkov, C. Marin, P. Bonville, J. A. Hodges, P. C. M. Gubbens, S. Sakarya, and C. Baines, "Magnetic Density of States at Low Energy in Geometrically Frustrated Systems," *Physical Review Letters*, vol. 95, p. 047203, 2005.

[148] P. D. de Réotier, A. Yaouanc, A. Bertin, C. Marin, S. Vanishri, D. Sheptyakov, A. Cervellino, B. Roessli, and C. Baines, "Low temperature crystal structure and local magnetometry for the geometrically frustrated pyrochlore $Tb_2Ti_2O_7$," *Journal of Physics: Conference Series*, vol. 551, no. 1, p. 012021, 2014.

[149] J. Lago, T. Lancaster, S. J. Blundell, S. T. Bramwell, F. L. Pratt, M. Shirai, and C. Baines, "Magnetic ordering and dynamics in the *XY* pyrochlore antiferromagnet: a muon-spin relaxation study of $Er_2Ti_2O_7$ and $Er_2Sn_2O_7$," *Journal of Physics: Condensed Matter*, vol. 17, no. 6, pp. 979–988, 2005.

[150] A. Yaouanc, P. Dalmas de Réotier, A. Bertin, C. Marin, E. Lhotel, A. Amato, and C. Baines, "Evidence for unidimensional low-energy excitations as the origin of persistent spin dynamics in geometrically frustrated magnets," *Physical Review B*, vol. 91, p. 104427, 2015.

[151] Heinz Maier-Leibnitz Zentrum *et al.*, "SPHERES: Backscattering spectrometer," *Journal of large scale facilities*, vol. 1, p. A30, 2015.

[152] J. D. Thompson, P. A. McClarty, D. Prabhakaran, I. Cabrera, T. Guidi, and R. Coldea, "Quasiparticle Breakdown and Spin Hamiltonian of the Frustrated Quantum Pyrochlore $Yb_2Ti_2O_7$ in a Magnetic Field," *Physical Review Letters*, vol. 119, p. 057203, 2017.

[153] R. Applegate, N. R. Hayre, R. R. P. Singh, T. Lin, A. G. R. Day, and M. J. P. Gingras, "Vindication of $Yb_2Ti_2O_7$ as a Model Exchange Quantum Spin Ice," *Physical Review Letters*, vol. 109, p. 097205, 2012.

[154] H. W. J. Blöte, R. F. Wielinga, and W. J. Huiskamp, "Heat-capacity measurements on rare-earth double oxides $R_2M_2O_7$," *Physica*, vol. 43, no. 4, pp. 549–568, 1969.

[155] J. D. Thompson, P. A. McClarty, H. M. Rønnow, L. P. Regnault, A. Sorge, and M. J. P. Gingras, "Rods of Neutron Scattering Intensity in $Yb_2Ti_2O_7$: Compelling Evidence for Significant Anisotropic Exchange in a Magnetic Pyrochlore Oxide," *Physical Review Letters*, vol. 106, p. 187202, 2011.

[156] L.-J. Chang, S. Onoda, Y. Su, Y.-J. Kao, K.-D. Tsuei, Y. Yasui, K. Kakurai, and M. R. Lees, "Higgs transition from a magnetic Coulomb liquid to a ferromagnet in $Yb_2Ti_2O_7$," *Nature Communications*, vol. 3, p. 992, 2012.

[157] J. A. Hodges, P. Bonville, A. Forget, M. Rams, K. Królas, and G. Dhalenne, "The crystal field and exchange interactions in $Yb_2Ti_2O_7$," *Journal of Physics: Condensed Matter*, vol. 13, no. 41, pp. 9301–9310, 2001.

[158] J. Gaudet, D. D. Maharaj, G. Sala, E. Kermarrec, K. A. Ross, H. A. Dabkowska, A. I. Kolesnikov, G. E. Granroth, and B. D. Gaulin, "Neutron spectroscopic study of crystalline electric field excitations in stoichiometric and lightly stuffed $Yb_2Ti_2O_7$," *Physical Review B*, vol. 92, p. 134420, 2015.

[159] K. A. Ross, T. Proffen, H. A. Dabkowska, J. A. Quilliam, L. R. Yaraskavitch, J. B. Kycia, and B. D. Gaulin, "Lightly stuffed pyrochlore structure of single-crystalline $Yb_2Ti_2O_7$ grown by the optical floating zone technique," *Physical Review B*, vol. 86, p. 174424, 2012.

[160] J. Gaudet, K. A. Ross, E. Kermarrec, N. P. Butch, G. Ehlers, H. A. Dabkowska, and B. D. Gaulin, "Gapless quantum excitations from an icelike splayed ferromagnetic ground state in stoichiometric $Yb_2Ti_2O_7$," *Physical Review B*, vol. 93, p. 064406, 2016.

[161] K. E. Arpino, B. A. Trump, A. O. Scheie, T. M. McQueen, and S. M. Koohpayeh, "Impact of stoichiometry of $Yb_2Ti_2O_7$ on its physical properties," *Physical Review B*, vol. 95, p. 094407, 2017.

[162] A. Yaouanc, P. D. de Réotier, L. Keller, B. Roessli, and A. Forget, "A novel type of splayed ferromagnetic order observed in $Yb_2Ti_2O_7$," *Journal of Physics: Condensed Matter*, vol. 28, no. 42, p. 426002, 2016.

[163] E. Lhotel, S. R. Giblin, M. R. Lees, G. Balakrishnan, L. J. Chang, and Y. Yasui, "First-order magnetic transition in $Yb_2Ti_2O_7$," *Physical Review B*, vol. 89, p. 224419, 2014.

[164] P. Fischer, G. Frey, M. Koch, M. Könnecke, V. Pomjakushin, J. Schefer, R. Thut, N. Schlumpf, R. Bürge, U. Greuter, S. Bondt, and E. Berruyer, "High-resolution powder diffractometer HRPT for thermal neutrons at SINQ," *Physica B: Condensed Matter*, vol. 276-278, pp. 146–147, 2000.

[165] G. Sala, M. J. Gutmann, D. Prabhakaran, D. Pomaranski, C. Mitchelitis, J. B. Kycia, D. G. Porter, C. Castelnovo, and J. P. Goff, "Vacancy defects and monopole dynamics in oxygen-deficient pyrochlores," *Nature Materials*, vol. 13, no. 5, pp. 488–493, 2014.

[166] A. Mostaed, G. Balakrishnan, M. R. Lees, Y. Yasui, L.-J. Chang, and R. Beanland, "Atomic structure study of the pyrochlore $Yb_2Ti_2O_7$ and its relationship with low-temperature magnetic order," *Physical Review B*, vol. 95, p. 094431, 2017.

[167] A. Scheie, J. Kindervater, S. Säubert, C. Duvinage, C. Pfleiderer, H. J. Changlani, S. Zhang, L. Harriger, K. Arpino, S. M. Koohpayeh, O. Tchernyshyov, and C. Broholm, "Reentrant Phase Diagram of $Yb_2Ti_2O_7$ in a $\langle 111 \rangle$ Magnetic Field," *Physical Review Letters*, vol. 119, p. 127201, 2017.

[168] A. M. Hallas, J. Gaudet, N. P. Butch, M. Tachibana, R. S. Freitas, G. M. Luke, C. R. Wiebe, and B. D. Gaulin, "Universal dynamic magnetism in Yb pyrochlores with disparate ground states," *Physical Review B*, vol. 93, p. 100403, 2016.

[169] J. A. Hodges, P. Bonville, A. Forget, A. Yaouanc, P. Dalmas de Réotier, G. André, M. Rams, K. Królas, C. Ritter, P. C. M. Gubbens, C. T. Kaiser, P. J. C. King, and C. Baines, "First-Order Transition in the Spin Dynamics of Geometrically Frustrated $Yb_2Ti_2O_7$," *Physical Review Letters*, vol. 88, p. 077204, 2002.

[170] J. S. Gardner, G. Ehlers, N. Rosov, R. W. Erwin, and C. Petrovic, "Spin-spin correlations in $Yb_2Ti_2O_7$: A polarized neutron scattering study," *Physical Review B*, vol. 70, p. 180404, 2004.

[171] K. A. Ross, J. P. C. Ruff, C. P. Adams, J. S. Gardner, H. A. Dabkowska, Y. Qiu, J. R. D. Copley, and B. D. Gaulin, "Two-Dimensional Kagome Correlations and Field Induced Order in the Ferromagnetic XY Pyrochlore $Yb_2Ti_2O_7$," *Physical Review Letters*, vol. 103, p. 227202, 2009.

[172] Y. Yasui, M. Soda, S. Iikubo, M. Ito, M. Sato, N. Hamaguchi, T. Matsushita, N. Wada, T. Takeuchi, N. Aso, and K. Kakurai, "Ferromagnetic Transition of Pyrochlore Compound $Yb_2Ti_2O_7$," *Journal of the Physical Society of Japan*, vol. 72, no. 11, pp. 3014–3015, 2003.

[173] J. Robert, E. Lhotel, G. Remenyi, S. Sahling, I. Mirebeau, C. Decorse, B. Canals, and S. Petit, "Spin dynamics in the presence of competing ferromagnetic and antiferromagnetic correlations in $Yb_2Ti_2O_7$," *Physical Review B*, vol. 92, p. 064425, 2015.

[174] K. A. Ross, L. R. Yaraskavitch, M. Laver, J. S. Gardner, J. A. Quilliam, S. Meng, J. B. Kycia, D. K. Singh, T. Proffen, H. A. Dabkowska, and B. D. Gaulin, "Dimensional evolution of spin correlations in the magnetic pyrochlore $Yb_2Ti_2O_7$," *Physical Review B*, vol. 84, p. 174442, 2011.

[175] L. Pan, S. K. Kim, A. Ghosh, C. M. Morris, K. A. Ross, E. Kermarrec, B. D. Gaulin, S. M. Koohpayeh, O. Tchernyshyov, and N. P. Armitage, "Low-energy electrodynamics of novel spin excitations in the quantum spin ice $Yb_2Ti_2O_7$," *Nature Communications*, vol. 5, p. 4970, 2014.

[176] A. M. Hallas, J. Gaudet, N. P. Butch, G. Xu, M. Tachibana, C. R. Wiebe, G. M. Luke, and B. D. Gaulin, "Phase Competition in the Palmer-Chalker XY Pyrochlore $Er_2Pt_2O_7$," *Physical Review Letters*, vol. 119, p. 187201, 2017.

[177] T. Hong, Y. Qiu, M. Matsumoto, D. A. Tennant, K. Coester, K. P. Schmidt, F. F. Awwadi, M. M. Turnbull, H. Agrawal, and A. L. Chernyshev, "Field induced spontaneous quasiparticle decay and renormalization of quasiparticle dispersion in a quantum antiferromagnet," *Nature Communications*, vol. 8, p. 15148, 2017.

[178] M. B. Stone, I. A. Zaliznyak, T. Hong, C. L. Broholm, and D. H. Reich, "Quasiparticle breakdown in a quantum spin liquid," *Nature*, vol. 440, no. 7081, pp. 187–190, 2006.

[179] Z. L. Dun, E. S. Choi, H. D. Zhou, A. M. Hallas, H. J. Silverstein, Y. Qiu, J. R. D. Copley, J. S. Gardner, and C. R. Wiebe, "$Yb_2Sn_2O_7$: A magnetic Coulomb liquid at a quantum critical point," *Physical Review B*, vol. 87, p. 134408, 2013.

[180] L. Savary and L. Balents, "Spin liquid regimes at nonzero temperature in quantum spin ice," *Physical Review B*, vol. 87, p. 205130, 2013.

[181] L. Savary and L. Balents, "Quantum spin liquids: a review," *Reports on Progress in Physics*, vol. 80, no. 1, p. 016502, 2017.

[182] L. Pan, N. J. Laurita, K. A. Ross, B. D. Gaulin, and N. P. Armitage, "A measure of monopole inertia in the quantum spin ice $Yb_2Ti_2O_7$," *Nature Physics*, vol. 12, no. 4, pp. 361–366, 2016.

[183] Y. Tokiwa, T. Yamashita, M. Udagawa, S. Kittaka, T. Sakakibara, D. Terazawa, Y. Shimoyama, T. Terashima, Y. Yasui, T. Shibauchi, and Y. Matsuda, "Possible observation of highly itinerant quantum magnetic monopoles in the frustrated pyrochlore $Yb_2Ti_2O_7$," *Nature Communications*, vol. 7, p. 10807, 2016.

[184] F. R. Foronda, F. Lang, J. S. Möller, T. Lancaster, A. T. Boothroyd, F. L. Pratt, S. R. Giblin, D. Prabhakaran, and S. J. Blundell, "Anisotropic Local Modification of Crystal Field Levels in Pr-Based Pyrochlores: A Muon-Induced Effect Modeled Using Density Functional Theory," *Physical Review Letters*, vol. 114, p. 017602, 2015.

[185] G. F. Koster, J. O. Dimmock, R. G. Wheeler, and H. Statz, *Properties of the thirty-two point groups*. Cambridge, Massachusetts: MIT Press, 1963.

Publications related to the dissertation

V. Peçanha-Antonio, E. Feng, X. Sun, D. Adroja, H. C. Walker, A. S. Gibbs, F. Orlandi, Y. Su, and T. Brückel, "Intermultiplet transitions and magnetic long-range order in Sm-based pyrochlores," *Physical Review B*, vol. 99, p. 134415, 2019.

V. Peçanha-Antonio, E. Feng, Y. Su, V. Pomjakushin, F. Demmel, L.-J Chang, R. J. Aldus, Y. Xiao, M. R. Lees, and T. Brückel, "Magnetic excitations in the ground state of $Yb_2Ti_2O_7$," *Physical Review B*, vol. 96, p. 214415, 2017.

Acknowledgements

You may have noticed, dear reader, that the pronoun of choice in this thesis was “we”. There is an obvious reason for that: I had the privilege of *not* being alone at any stage during the development of this work.

First of all, if you reached this point in your reading, I must say thanks to you, person who trusted (or evaluated) my work. I must also mention (before you give up reading these acknowledgements) how much I owe to my mom and my husband. These two people are, since I can remember, the biggest loves of my life, no matter how far apart we live from each other. Just thank you, you two, for being my summer, my autumn, my winter and my spring, simply for being who you are.

The next one is the “Familienvater” of our expats group in JCNS-2, my supervisor Yixi Su. I cannot figure anyone who would bring a young girl from a small (and unknown) University in Brasil directly to Germany, and give her the opportunity that he gave me. I myself probably wouldn’t. Only for that, Yixi already deserves my eternal gratitude. He did much more, though. Yixi, thank you for not being, in any moment, even minimally unsupportive to any of my crazy ideas. We worked hard and fought hard. Thank you for being there, always fighting along with me.

Together with Yixi, another person had to take charge of my stay in JCNS-2. Prof. Brückel is maybe one of the most generous persons I’ve met in Germany, and also in my life. A wise man, certainly. As I said some time ago, thank you for not giving up on me, even when I deserved.

I must also mention the long list of friends I made during the last four years. Among them, the instrument scientists and technicians with whom I had the opportunity to work. Franz Demmel, Fabio Orlandi, Alex Gibbs, and Adroja, thank you for your support, overtime and company during my neutron scattering experiments. To the cryostat guys Chris, Jeff, Heiner, Helga, Berthold, Andi and Alex: thank you for making (or at least trying to make) the dilution fridges work. We all definitely know how much fun one can have, even when the experiment fails.

To those friends that shared a bit of this everyday journey with me, and made me feel as if Munich and Jülich were an extension of my own home: be sure, I will cary a bit of you with me, wherever I go. My colleagues, friends and current officemates (Beni, Tobi, and, why not, Patrick), my former officemates (Manuchar), my very cooperative and kind Doktorvater (Joachim Wuttke), our dear secretaries (Franziska, Monika and Barbara) and directors (Stefan and Rainer “Bruchi”), Anto, Bob, Maddi, Inês, Luca, Paulo, my Chinese siblings (Erxi, Fengfeng, Xiao Wang, Junda, Xiao Sun, Wenhai, Lei, Liming) and Jülich friends, those I didn’t name (you know who you are): I hope I did already thank any of you for being unconditionally by my side in these last 1460 days.

Luckily, we live in a small world. I’m sure we all will have the pleasure to meet again along one of these bright beamlines of life.

Com amor,

Vivi